

Technical University of Denmark



Low Power DEAP Actuator Drive for Heating Valves

Huang, Lina; Andersen, Michael A. E.; Zhang, Zhe

Publication date:
2014

Document Version
Publisher's PDF, also known as Version of record

[Link back to DTU Orbit](#)

Citation (APA):
Huang, L., Andersen, M. A. E., & Zhang, Z. (2014). Low Power DEAP Actuator Drive for Heating Valves. Technical University of Denmark, Department of Electrical Engineering.

DTU Library
Technical Information Center of Denmark

General rights

Copyright and moral rights for the publications made accessible in the public portal are retained by the authors and/or other copyright owners and it is a condition of accessing publications that users recognise and abide by the legal requirements associated with these rights.

- Users may download and print one copy of any publication from the public portal for the purpose of private study or research.
- You may not further distribute the material or use it for any profit-making activity or commercial gain
- You may freely distribute the URL identifying the publication in the public portal

If you believe that this document breaches copyright please contact us providing details, and we will remove access to the work immediately and investigate your claim.

Lina Huang

Low Power DEAP Actuator Drive for Heating Valves

PhD Thesis, October 2014

Lina Huang

Low Power DEAP Actuator Drive for Heating Valves

PhD Thesis, October 2014

Low Power DEAP Actuator Drive for Heating Valves,

This report was prepared by

Lina Huang

Supervisors

Michael A. E. Andersen

Zhe Zhang

| | |
|---------------|------------------------------------------------------------------------------------------------------------------------------------------|
| Release date: | 31st October 2014 |
| Category: | 1 (public) |
| Edition: | Draft |
| Comments: | This thesis is submitted in partial fulfillment of the requirements for obtaining the PhD degree at the Technical University of Denmark. |
| Rights: | ©Lina Huang, 2014 |

Department of Electrical Engineering
Electronics Group (ELE)
Technical University of Denmark
Oersteds Plads Building 349
DK-2800 Kgs. Lyngby
Denmark

www.ele.elektro.dtu.dk

Tel: (+45) 45 25 38 00

Fax: (+45) 45 93 16 34

Preface and Acknowledgment

This PhD project "Low Power DEAP Actuator Drive for Heating Valves" is carried out at the PhD school, Department of Electrical Engineering, Technical University of Denmark (DTU). Funded by the Danish National Advanced Technology Foundation (HTF), the project has been part of the WP8 involved in the HTF project "Highly efficient low cost energy generation and actuation using disruptive DEAP technology". Close collaboration with Danfoss PolyPower A/S and Danfoss A/S Heating Solutions has been achieved throughout the project. An external research visit was carried out at the "Laboratory for Power Management and Integrated Switch-Mode Power Supplies (SMPS)" in University of Toronto, Canada.

During the PhD studies, I have become deeply indebted and grateful to all of those who has stood by me and helped me throughout this project. My special thanks and deeply appreciation goes to:

- My supervisors Prof. Michael A. E. Andersen and Assoc. Prof. Zhe Zhang for providing me this opportunity and for their inspiration, encouragement and endless confidence in me during the project.
- The colleagues involved in WP8 and WP4 of the HTF project "Highly efficient low cost energy generation and actuation using disruptive DEAP technology" for their constructive discussions, suggestions and comments.
- All the colleagues at Electronics Group for their support, help and constructive discussions. Special thanks to Henriette and Bertil, for the kindly assistance and care.
- Prof. Aleksandar Prodić at University of Toronto, for accepting me as a visiting PhD student at his research group, and all the colleagues and students in the group for their help and support.
- My dear parents Shangguang Huang and Qingyu Wang and my partner Hengzhuang Wang, for their deeply love and endless support and encouragements.

Abstract

Modern heating systems play a key role in providing comfortable living environment and saving energy. The radiator heating valve and thermostat are essential elements to achieve the temperature control in the dwelling space. The existing actuator inside the thermostat either suffers from the operation noise issue, or cannot realize the accurate temperature regulation and remote control. Due to the advancement of the material science, in recent years, a new type of smart material, called DEAP (Dielectric Electro Active Polymer), gradually attracts the attention of researchers. The superior performances of DEAP actuator, such as noise free operation, high energy density, quick response time, etc, make it a possible solution to replace the conventional actuators inside the thermostat.

To operate the DEAP actuator in the heating system and considering its intrinsic properties, a driver featuring high output voltage and capacitive load charging ability has been investigated. High voltage flyback converter is proved to be an applicable solution in the heating valve application. The conventional flyback topology and the multiple transformers based primary parallel secondary series flyback converter (PPSSFC) featuring the unidirectional energy flow are investigated in terms of fundamental working principle and practical implementation. The converter with bidirectional energy flow functionality is desired to improve the overall efficiency and has been studied as well. The design guidelines of the high voltage flyback transformer in capacitive load charging and discharging application are proposed. In order to achieve the thorough understanding of the converter, a switching cycle based analytical model for both charging mode and discharging mode have been established. Based on this, the energy efficiency analysis has been carried out to achieve efficiency calculation model. Moreover, two system level control schemes are proposed to achieve the corresponding temperature control. The functionality and energy consumption of the high voltage driver have been verified through the test in the practical heating system with the radiator heating valve and the implemented DEAP actuator.

The implemented high voltage flyback converters can achieve relatively low volume and satisfactory efficiencies. In addition, the switching cycle based analytical model and the energy efficiency analysis can be used to well predict the behaviour and efficiency in both charging and discharging mode. The system level energy consumption is relatively low when the burst mode control scheme is applied. If 2.5 Ah batteries are employed, the high voltage driving system with bidirectional converter can run for around 2.1 years.

Resumé

Moderne varmeanlæg spiller en central rolle i at give komfortable omgivelser og sparer energi. Radiatorvarmeventiler og termostater er væsentlige elementer for at opnå god temperaturkontrol i boligens rum. Den eksisterende aktuator inde i termostaten lider enten fra støjproblemer når den regulerer, den kan ikke bruges til at realisere den nøjagtige regulering temperatur eller den kan ikke fjernbetjenes. Som følge af udviklingen af materialevidenskab i de seneste år, har en ny type intelligent materiale, kaldet DEAP (Dielektrisk ElektroActive Polymer) efterhånden tiltrukket sig opmærksomhed fra forskere. DEAP aktuatoren fordele såsom støjfri drift, høj energitæthed, hurtig responstid, etc., gør det til en mulig løsning til at erstatte de konventionelle aktuatorer inde i termostaterne.

For at udnytte DEAP aktuator og dens egenskaber i varmesystemet, er en elektronisk konverter med høj udgangsspænding til opladning af en kapacitiv belastning blevet undersøgt. Højspændings flyback-konverteren viste sig at være en anvendelig løsning i varmeventilen. Den konventionelle flyback-topologi og multiple transformer-baserede primær parallel, sekundær serie flyback-konverter (PPSSFC) med det envejs energiflow er undersøgt i form af grundlæggende funktionsprincipper og den praktiske implementering. Konverteren med tovejs energiflow funktionalitet, der foretrækkes for at forbedre den samlede effektivitet er også blevet undersøgt. Der foreslås designretningslinjer for højspændings flyback-transformeren til anvendelser med kapacitive belastningsopladninger og -afladninger. For at opnå en grundig forståelse af konverteren, er en detaljeret analytisk model for både opladnings- og afladningsfunktionerne blevet lavet. Baseret på dette er en analyse af energieffektiviteten også blevet udført. Endvidere foreslås der to systemniveau reguleringsmetoder for at opnå en forbedret temperatur kontrol i et varmeanlæg. Funktionalitet og energiforbruget i højspændings konverteren er blevet verificeret gennem test i et varmesystem med radiatorvarme ventil og implementeret DEAP aktuator.

Den udførte højspænding flyback-konverter kan opnå relativt lav volumen og tilfredsstillende effektivitet. Desuden kan kredsløbsanalysen og analysen af energieffektiviteten anvendes til godt forudsige virkemåde og effektivitet i både opladnings- og afladningstilstandene. Systemet energiforbrug er relativt lav, når burst-mode kontrolordningen anvendes. Hvis en 2,5 Ah batteri benyttes, kan den bidirektionale højspænding konverter køre i ca. 2,1 år inden et batteriskift er nødvendigt.

Contents

| | |
|--------------------------------------------------|-------------|
| Preface | i |
| Abstract | iii |
| Resumé | v |
| Contents | vii |
| List of Figures | xi |
| List of Tables | xiii |
| 1 Introduction | 1 |
| 1.1 Scope | 1 |
| 1.2 Scope of Project | 1 |
| 1.3 Background and Motivation | 3 |
| 1.4 Project Objectives | 4 |
| 1.5 Thesis Structure and Content | 4 |
| 2 Overview and State-of-the-Art | 7 |
| 2.1 Heating System | 7 |
| 2.1.1 Overview | 7 |
| 2.1.2 Heating Valve and Specifications | 9 |
| 2.1.3 Radiator Thermostat | 10 |
| 2.2 Dielectric Electro Active Polymer | 11 |
| 2.2.1 Structure | 11 |
| 2.2.2 Capacitive Property | 12 |

| | | |
|----------|----------------------------------------------------------------------------------------|-----------|
| 2.2.3 | Working Principle | 14 |
| 2.2.4 | Application Fields | 15 |
| 2.3 | High Voltage Driver Solutions | 17 |
| 2.3.1 | System Configuration | 17 |
| 2.3.2 | High Voltage Converter | 18 |
| 2.3.3 | Sensing and System Level Control Discussion | 23 |
| 2.3.4 | Power Source and Auxiliary Power Supplies Solution | 25 |
| 2.4 | Summary | 25 |
| 3 | High Voltage Flyback Converter Investigation | 27 |
| 3.1 | Unidirectional Energy Flow | 27 |
| 3.1.1 | Traditional Topology Discussion | 27 |
| 3.1.2 | New Topology Investigation | 30 |
| 3.2 | Bidirectional Energy Flow | 33 |
| 3.2.1 | Topology Configuration | 33 |
| 3.2.2 | Working Principle | 34 |
| 3.2.3 | Transformer Investigation | 35 |
| 3.2.4 | Prototype | 36 |
| 3.3 | Analytical Switching Cycle Modelling | 37 |
| 3.3.1 | Core Loss Consideration and Detailed Configuration of Fly- back Converter | 38 |
| 3.3.2 | Charging Mode | 39 |
| 3.3.3 | Discharging Mode | 40 |
| 3.4 | Energy Efficiency Investigation | 42 |
| 3.4.1 | Charging Efficiency | 42 |
| 3.4.2 | Discharging Efficiency | 42 |
| 3.4.3 | Loss Distribution | 43 |
| 3.5 | Summary | 43 |
| 4 | DEAP Actuator Driving System | 45 |
| 4.1 | System Level Control Scheme | 45 |
| 4.1.1 | Voltage Tracking Control | 46 |
| 4.1.2 | Burst Mode Control | 48 |
| 4.2 | System Level Integration | 49 |

| | | |
|----------|---------------------------------------------------------------------------------------------------------------------------------------------------------------------|------------|
| 4.2.1 | Mechanical Coupling | 49 |
| 4.2.2 | Electrical Connection | 50 |
| 4.3 | System Level Test | 50 |
| 4.3.1 | Functionality Verification | 50 |
| 4.3.2 | Energy Consumption Analysis | 51 |
| 4.4 | Summary | 51 |
| 5 | Conclusion and Future Works | 53 |
| 5.1 | Conclusion | 53 |
| 5.2 | Future Work | 55 |
| | Bibliography | 57 |
| | List of Publications | 65 |
| | Appendix | 67 |
| A | A Review of High Voltage Drive Amplifiers for Capacitive Actuators | 67 |
| B | Analysis of Dielectric Electro Active Polymer Actuator and its High Voltage Driving Circuits | 75 |
| C | Battery Powered High Output Voltage Bidirectional Flyback Converter for Cylindrical DEAP Actuator | 81 |
| D | Primary Parallel Secondary Series Flyback Converter (PPSSFC) with Multiple Transformers for Very High Step-Up Ratio in Capacitive Load Charging Applications | 87 |
| E | High Voltage Bidirectional Flyback Converter Driving DEAP Actuator for Automotive Applications | 97 |
| F | Investigation of transformer winding architectures for high voltage capacitor charging applications | 103 |
| G | Detailed Behavior Analysis for High Voltage Bidirectional Flyback Converter Driving DEAP Actuator | 113 |
| H | Analytical Switching Cycle Modeling of Bidirectional High Voltage Flyback Converter for Capacitive Load Considering Core Loss Effect | 121 |

| | | |
|----------|------------------------------------------------------------------------------------------------------------------|------------|
| I | Efficiency of Capacitively Loaded Converters | 165 |
| J | Energy Efficiency Investigation of Bidirectional High Voltage Fly-back Converter for DEAP Actuator | 173 |
| K | Design and Development of Autonomous High Voltage Driving System for DEAP Actuator in Radiator Thermostat | 201 |
| L | Design Comparison of Autonomous High Voltage Driving System for DEAP Actuator | 211 |
| M | DEAP actuator and its high voltage driver for heating valve application | 219 |

List of Figures

| | | |
|------|----------------------------------------------------------------------------------------------|----|
| 1.1 | The configuration of DEAP platform project. | 2 |
| 1.2 | PhD thesis structure. | 5 |
| 2.1 | The diagram of a simplified heating system. | 8 |
| 2.2 | Energy usage before and after renovation of heating system. | 9 |
| 2.3 | The commonly used two types of radiator heating valve. | 9 |
| 2.4 | The commonly used two types of radiator thermostat. | 11 |
| 2.5 | DEAP structure and deformation when voltage is applied. | 12 |
| 2.6 | DEAP film impedance and phase versus frequency. | 12 |
| 2.7 | Capacitance versus voltage characteristic of DEAP material, film capacitor and MLCC. | 13 |
| 2.8 | Proposed in-line heating valve with embedded DEAP actuator. . . . | 15 |
| 2.9 | Proposed DEAP film based golfer's swing monitoring device. | 16 |
| 2.10 | Conceptual DEAP film based generator for wave energy. | 16 |
| 2.11 | Block diagram of high voltage driver of DEAP actuator for radiator heating valve. | 17 |
| 2.12 | Two types of commonly used PT. | 19 |
| 2.13 | Schematic diagrams of PT based converters. | 20 |
| 2.14 | Schematic diagrams of flyback converters. | 21 |
| 2.15 | Stroke versus voltage characteristic of DEAP actuator. | 24 |
| 2.16 | High voltage measurement circuit. | 25 |
| 3.1 | Operating principle of unidirectional flyback converter for capacitive actuator. | 28 |
| 3.2 | Implemented unidirectional high voltage flyback converter for capacitive actuator. | 29 |

| | | |
|------|------------------------------------------------------------------------------------------------------------------------|----|
| 3.3 | Experimental verification of unidirectional flyback converter for capacitive actuator. | 30 |
| 3.4 | The configuration of multiple transformer based PPSSFC. | 31 |
| 3.5 | The prototype and entire charging phase of PPSSFC. | 32 |
| 3.6 | Experimental waveforms of successive charging cycles of PPSSFC for capacitive actuator. | 33 |
| 3.7 | Operating principle of energy recovery phase of bidirectional flyback converter for capacitive actuator. | 34 |
| 3.8 | Implemented bidirectional high voltage flyback converter for capacitive actuator. | 36 |
| 3.9 | Experimental verification of bidirectional high voltage flyback converter for capacitive actuator. | 37 |
| 3.10 | Detailed configuration of bidirectional high voltage flyback converter for capacitive actuator. | 39 |
| 3.11 | High voltage operating waveforms of charging mode. | 40 |
| 3.12 | High voltage operating waveforms of discharging mode. | 41 |
| 3.13 | Efficiency of bidirectional high voltage flyback converter for capacitive actuator. | 42 |
| 3.14 | Loss distribution of bidirectional high voltage flyback converter for capacitive actuator. | 43 |
| 4.1 | Flow chart of the voltage tracking control. | 47 |
| 4.2 | Experimental verification of voltage tracking control scheme. | 47 |
| 4.3 | Flow chart of the burst mode control. | 48 |
| 4.4 | The mechanical coupling between the DEAP actuator and the heating valve. | 49 |
| 4.5 | The pictures of heating valve, DEAP actuator and high voltage driver integrated in the testing heating system. | 50 |
| 4.6 | Experimental curve between the voltage and water flow rate. | 50 |
| 4.7 | Energy loss of high voltage driver based on PPSSFC and burst mode control. | 51 |

List of Tables

| | | |
|-----|------------------------------------------------------------------------------------------------------------------|----|
| 2.1 | Specifications and actuation requirements of radiator valves | 10 |
| 2.2 | Design specifications and requirements of high voltage converter . . . | 19 |
| 2.3 | Comparison of transformer applied in PT based and flyback high voltage converter | 22 |
| 2.4 | Comparison of power stage and control scheme applied in PT based and flyback high voltage converter | 23 |

Introduction

1.1 Scope

The scope of this thesis is to present the research work carried out in the PhD project “Low Power DEAP Actuator Drive for Heating Valves” during the period from November 2011 through October 2014. Most of the scientific results of the research have been published or submitted in form of peer reviewed conference and journal papers. The publications form a major part of this thesis and are included in Appendix A - M.

The objective of this thesis is to supplement the already published information and thereby present a more coherent and complete overview of the research work and results obtained in the project.

Traditionally, power electronics converters are mainly used to process power for energy dissipation elements, such as resistive heater, resistive-inductive motors, etc. The advancement of the smart material science and engineering claim the increasing demand for the power conversion devices which can efficiently process electrical energy to feed the capacitive elements. The thesis addresses the research work in this emerging field. It is also a hope that the thesis can attract more researchers and engineers to be interested in this promising research direction.

1.2 Scope of Project

Since the early 1990s, as a type of smart material, DEAP (Dielectric Electro Active Polymer) is gradually attracting the attention of scientists and investigators from various disciplines. Danfoss Group perceived the bright prospect of DEAP and started the research within this field since 1995. A separate company within Danfoss Group, called Danfoss PolyPower A/S, was established in 2008 to design and manufacture the DEAP film and elements for customers. In order to further improve the performance and reliability of the DEAP material, to build up the simulation and computer supported engineering tools based design platform for

1.2. Scope of Project

DEAP solutions and to penetrate and validate the application of DEAP solutions in selected domains, a platform project entitled “Highly efficient low cost energy generation and actuation using disruptive DEAP technology” was proposed by Danfoss PolyPower A/S and gained the great support from the Danish National Advanced Technology Foundation (HTF). 7 companies, 3 universities and 8 PhD students are involved in this platform project, which is organized with 9 work packages (WPs).

In WP1, Department of Chemical Engineering of Technical University of Denmark (DTU) and Danfoss PolyPower A/S are cooperating to optimize the characteristics of DEAP film. Polyteknik A/S, ESS Technology A/S, Danfoss PolyPower A/S and DTU Chemical Engineering are involved in WP2 to improve the production processes. In WP3, DTU Department of Management of Engineering and Danfoss PolyPower A/S are focusing on investigating DEAP elements with various configurations and building high-level block diagrams for 4 application work packages. DTU Department of Electrical Engineering and Aalborg University (AAU) Department of Energy Technology and Noliac A/S are working together to provide electrical solutions inside the platform project. University of Southern Denmark (SDU) Mads Clausen Institute and Danfoss PolyPower A/S are trying to develop design and simulations tools for DEAP film and elements. WP6 to WP9 are 4 work packages based on applications and are led by WP4. DTU Electrical Engineering and Danfoss PolyPower A/S are demonstrating an incremental motor in WP6. AAU and Wave Star A/S are investigating a wave energy harvester with DEAP technology. DTU Electrical Engineering and Danfoss A/S Heating Solutions are investigating the potential DEAP based in-line heating valve. In WP9, a flat screen loudspeaker is under development by DTU Electrical Engineering and Bang & Olufsen A/S. The platform project structure with the information of corresponding work packages is illustrated in Figure 1.1.

This PhD project “Low Power DEAP Actuator Drive for Heating Valves” is based on WP8 and the goal is to develop the electrical part for this work package. While the DEAP element is taken care by Danfoss Polypower A/S and the heating valve design is carried out in Danfoss A/S Heating Solutions.

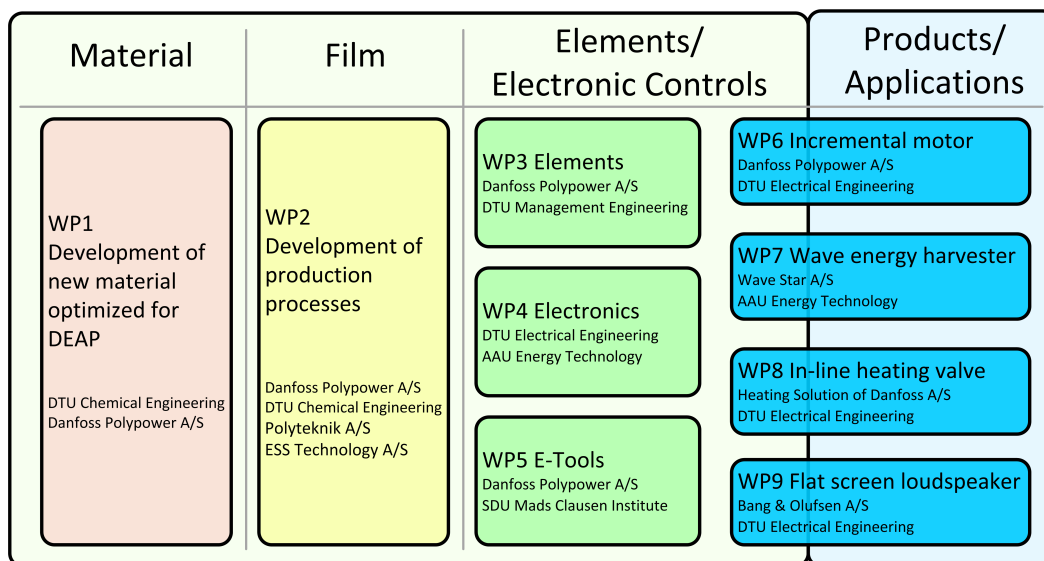


Figure 1.1: The configuration of DEAP platform project.

1.3 Background and Motivation

Over the past few decades, people increasingly attaches great importance to the energy conservation technology and development of renewable energy due to the growing energy crisis caused by the serious shortage of natural resources. As a part of energy system in a modern city, efficient heating system is utilized to heat the rooms of a building by means of radiators connected by pipes to a source of heat. Efficient heating system plays an important role in saving energy. One critical part involved in this heating network tends to be the heating valve, which can be applied to regulate the room temperature by controlling the hot water flow in the pipe according to the ambient temperature. Compared to the fixed stream flow in the pipe, this automatic and dynamic regulation of hot water is unquestionably beneficial for avoiding the waste of thermal energy.

As a device without intrinsic actuation mechanism, the heating valve cannot work alone. Thus an external actuator needs to be employed to adjust the position of the valve in order to control the hot water flow. Currently, there are two types of commonly used heating valve actuators on the market. One is the self-actuating element, typically consists of the liquid or gas which can expand or contract according to the surrounding temperature. This purely mechanical actuator, however, suffers from the inaccurate temperature control as well as the impossibility of the remote control. The other actuating device is the step motor based actuator, which is inherently prone to noise issues and relatively short battery life.

Generally, polymer has many attractive properties, such as lightweight, inexpensive, fracture tolerant and pliable [1]. When the dielectric polymer is placed between two compliant electrodes, the DEAP material is to be constituted. An electrostatic force is induced to compress the polymer in thickness and expand the material in area when a voltage is applied over the electrodes. This electrical to mechanical conversion thus enables the DEAP film based actuator [2], [3], [4]. The detailed information related to DEAP material will be addressed in section 2.2. Compared to traditional hydraulic, pneumatic and electromagnetic counterparts, the DEAP actuator is superior in terms of weight, noise issues, force density and response speed [5]. Considering the limitations of current heating valve actuators, the actuator formed of DEAP film can be an excellent candidate to replace the conventional counterparts since it can easily overcome the noise issue and achieve the accurate and remote temperature control if an electrical driver is employed.

The intrinsic property of DEAP film implies that a relatively high voltage is needed in order to generate a certain amount of mechanical force [6]. For the current version film, the voltage to fully elongate the actuator needs to reach 2-2.5 kV. One type of energy source to power the current actuator in heating valve applications is the small volume AA battery. To provide the required voltage for DEAP film, an interface between the energy source and the actuator needs to be applied, i.e. a high voltage DC-DC converter. In order to compete with the products already on the market, a highly efficient, small volume and low cost DEAP actuator based driving system for heating valves needs to be investigated. Not only a compact and energy efficient design of the heating valve and actuator is needed, also a highly efficient and small size high voltage DC-DC driving system is desired, which forms the main topic of this thesis.

1.4 Project Objectives

As mentioned in section 1.2, the primary objective of this PhD project is to develop the electrical part of WP8 in DEAP platform project, i.e. to investigate an energy efficient and space saving high voltage DC-DC driving system for DEAP actuator in heating valve applications. To achieve the main objective of the research, the following sub-goals are proposed:

- The battery powered high output voltage converter tends to be the most critical part in the entire high voltage driving system. Potential high voltage converting solutions need to be proposed and compared in terms of efficiency, volume and cost. The most beneficial converter configuration needs to be figured out to meet the demands in the specific heating valve application. A transformer involved in the high voltage converter plays a key role in boosting the low voltage from battery to the voltage required by the actuator. The theoretical design and the practical implementation of the high voltage transformer as well as the corresponding power stage need to be carried out to achieve a high voltage DC-DC converter.
- The configuration of the DEAP film leads to the intrinsic capacitive property. The operational principle of the converter feeding the capacitive load differs from that of the converter powering the resistive load. In order to thoroughly understand the working modes of the converter with capacitive load, the analytical behaviour model thus needs to be established. Furthermore, the energy loss and efficiency of the high voltage converter need to be analysed in order to have an overview for the loss distribution and to further optimize the design.
- In this low power high voltage driving system, the energy consumption by the control and auxiliary parts cannot be neglected. The proper control scheme therefore needs to be investigated to achieve energy conservation and to extend battery life. In order to validate the functionality of this high voltage driving device, a system level test together with DEAP actuator and heating valve needs to be carried out in Danfoss A/S Heating Solutions.

1.5 Thesis Structure and Content

The structure and contents of this PhD project is visualized in the flow chart shown in Figure 1.2. The first chapter briefly introduces the scope, background and motivation as well as the objectives of the project. The overview and state-of-the art are discussed in Chapter 2. Chapter 3 addresses the research related to the high voltage flyback converter, including the practical design and implementation as well as the theoretical modelling and analysis. The control scheme and system level integration of the entire high voltage DEAP actuator driving system are addressed in Chapter 4. The thesis is finalized with a conclusion and future work. Furthermore, the published or submitted conference and journal papers are illustrated in the flow

chart as well. The purpose of this thesis is to provide a condensed and coherent overview of the research and the results obtained in the project.

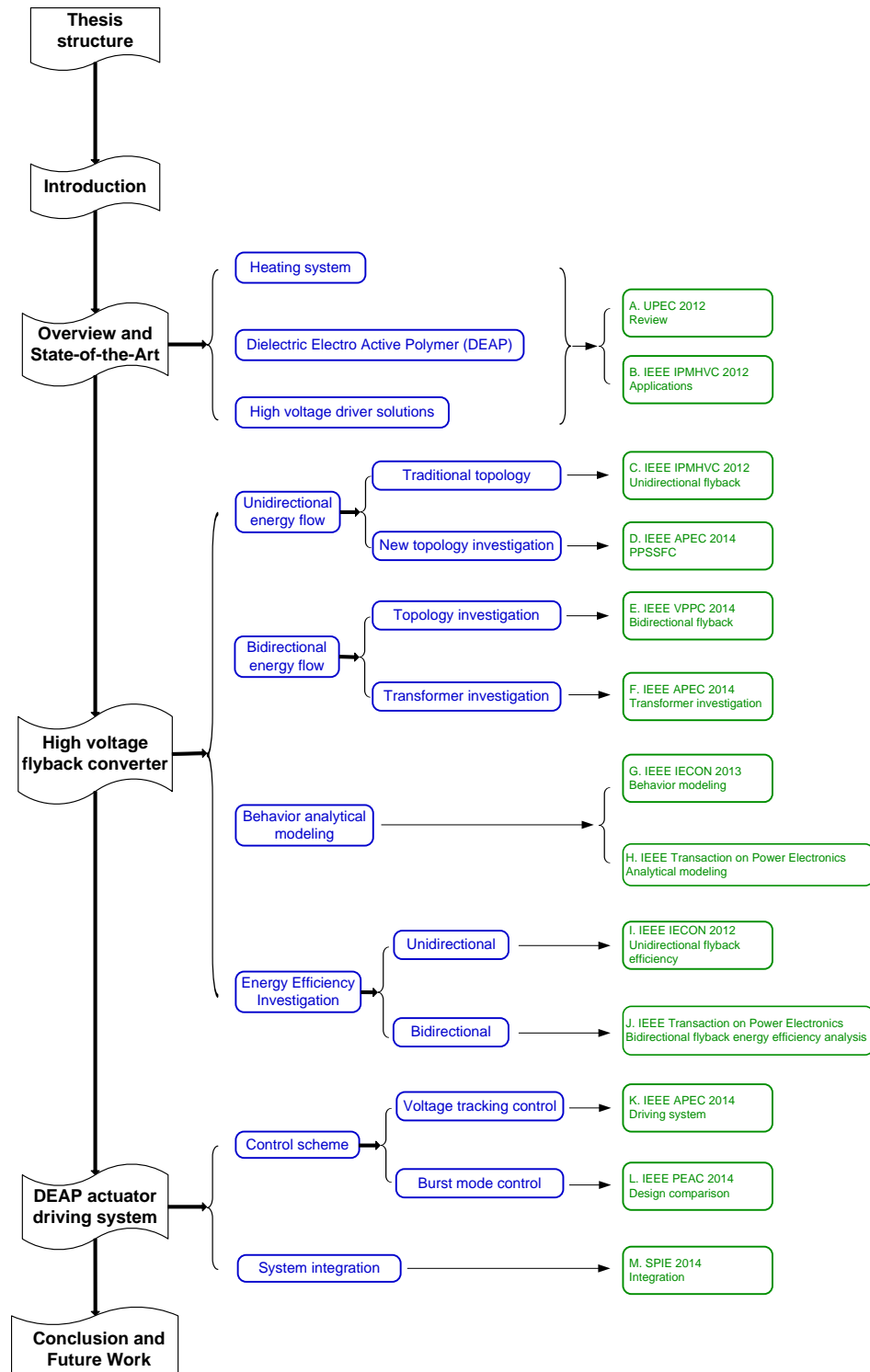


Figure 1.2: PhD thesis structure.

Overview and State-of-the-Art

The research subject of the project is the high voltage driver for DEAP actuator in the heating system. In this chapter, an overview and state-of-the-art discussion for the heating system, DEAP film and actuator and the high voltage driving solutions are presented. The detailed information related to the application of DEAP actuator and high voltage driver can refer to Appendix A and B.

2.1 Heating System

2.1.1 Overview

A large amount of heat energy is utilized to keep the indoor temperature in the range of comfort, especially in the winter time and in cold regions. In the old heating system, the absence of the temperature closed loop control leads to either the overheating of the room, which corresponds to the waste of thermal energy, or low room temperature, which makes dwellers feel uncomfortable. In order to save energy and increase comfort, the existing inefficient heating systems need to be renovated to their modern counterparts with advanced temperature regulating devices. Danfoss A/S Heating Solutions involved in this project is the world's leading heating system solutions provider and associated equipments supplier.

A simplified two pipe water based modern heating system is illustrated in Figure 2.1 [7]. The red pipes stand for the hot water supply while the blue ones correspond to the cold water return. A heat exchanger is applied to reduce the operating cost by transferring heat between two fluids [8]. A water pump plays the role in raising the hot water to the desired height using pressure. In each dwelling unit, one or more radiators are applied to transfer thermal energy of hot water inside to the surrounding air in order to heat the room [9]. A heating valve is the device to adjust the water flow in the pipe and thermostat with internal actuators and a closed loop temperature control is applied to drive the valve [10], [11]. The detailed discussion related to heating valve and thermostat are presented in subsection 2.1.2 and 2.1.3, respectively. While in some dwelling space, floor heating is preferred by

2.1. Heating System

the residents to achieve an evenly distribution of temperature and to avoid cold spots. Automatic Balancing Pressure Controller (ABPC) is used to optimize water flow through automatically compensating for system pressure changes in order to maximize energy efficiency. Obviously, in Figure 2.1, the hot water comes from the heat source and goes through exchanger and pump to reach the radiators or floor heating equipments and then goes back to the heat source again through the cold water pipe, which forms a water circulation of the heating system.

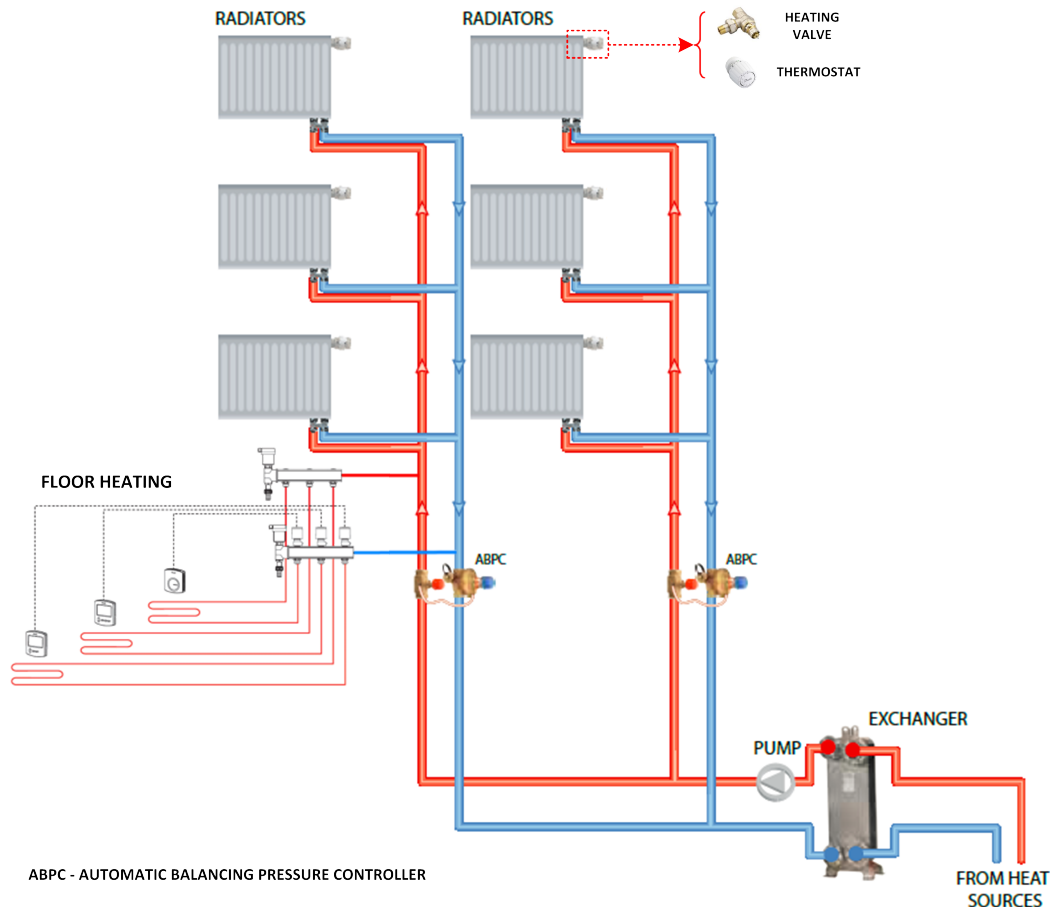


Figure 2.1: The diagram of a simplified heating system.

Due to the good performance of energy saving and short payback time, the two pipe water based modern heating system with advanced heating valve and thermostat has been widely used to replace the existing inefficient counterpart in old buildings. During the period from 2000 to 2008, the real energy consumption of three buildings in Eastern Europe before and after renovation of heating system are collected by Danfoss A/S Heating Solutions and are illustrated in Figure 2.2 [7]. The energy usage data before and after renovation are expressed with dash and solid lines, respectively. Obviously, the energy consumption decrease sharply after modern heating valves and thermostats were installed in the system. By comparing the energy usage of 2000 and 2008, it is easy to be aware that the energy consumption for three buildings are reduced by 35%, 57% and 38%, respectively. Furthermore, the data from Danfoss A/S Heating Solutions indicate that the payback time for three buildings are 1.6, 1.0 and 1.0 years, respectively.

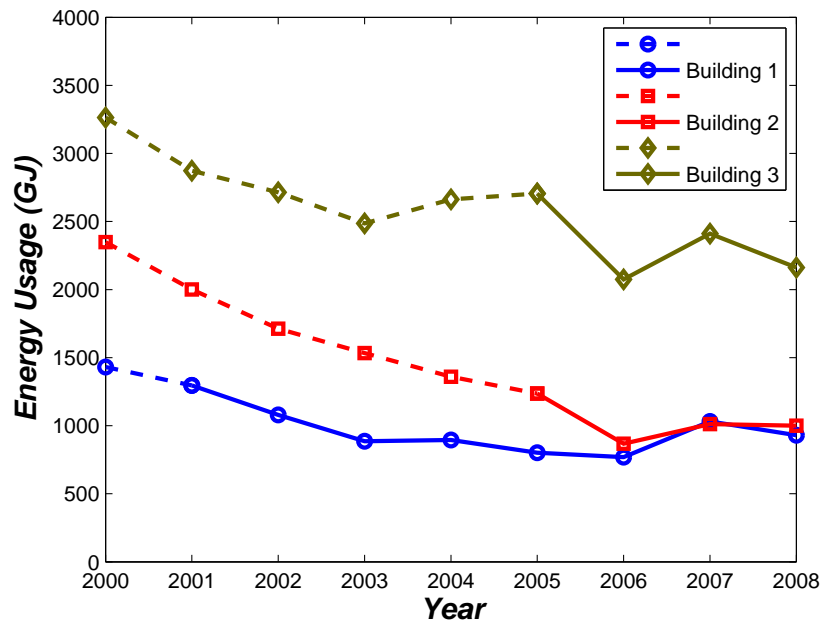


Figure 2.2: Energy usage before and after renovation of heating system.

2.1.2 Heating Valve and Specifications

Similar to other type of mechanical valves, radiator heating valves employed in the two pipe water based heating system are used to control the flow of hot water by opening, closing or partially obstructing a variety of passageways [12]. Nowadays, two types of radiator valves are widely used in the heating system. One is the straight version valve and the other type is the angle version, which are displayed in Figure 2.3a and 2.3b, respectively [10]. The straight heating valve is applied when the flow direction does not need to change while the radiator valve with angle design incorporate a 90° bend to achieve a flow in the perpendicular direction. As a purely mechanical device without intrinsic mechanical power, heating valve cannot work independently. Only when the radiator valve's pressure pin, the outside terminal of which can easily be observed in Figure 2.3, is pressed by the external force, the water flow can be regulated.



Figure 2.3: The commonly used two types of radiator heating valve.

2.1. Heating System

As the mechanical load of the actuator inside thermostat, radiator heating valves need to be understood in terms of specifications and actuation demands, which are summarized in Table 2.1 [10]. Most parts of the valve are made up of brass, which can guarantee its normal operation even when water temperature goes up to 120 °C and working pressure increases to 10 bars. In order to actuate the valve, 25 N needs to be provided to the pressure pin, whose maximum stroke is limited to 1 mm. In general, heating systems with large thermal inertia constant do not set strict dynamic targets. In the worst case, the radiator heating valve still allows up to 5 s actuation time.

Table 2.1: Specifications and actuation requirements of radiator valves

| Specifications / Actuation requirements | Values |
|-----------------------------------------|---------|
| Valve body and other metal parts | Brass |
| Max. ambient temperature | 60 °C |
| Max. water temperature | 120 °C |
| Max. working pressure | 10 bar |
| Max. differential pressure | 0.6 bar |
| Actuation force | 25 N |
| Max. actuation frequency | 0.2 Hz |
| Max. stroke | 1 mm |

2.1.3 Radiator Thermostat

The radiator thermostat with internal actuators is used to provide mechanical force to adjust the position of the pressure pin of radiator heating valve in order to regulate the water flow in the pipe. Currently, two types of thermostats are commonly available on the market. One is the purely mechanical thermostat with internal self-actuating thermal actuator, which is shown in Figure 2.4a. The other is the battery supplied step motor actuator based radiator thermostat, which is shown in Figure 2.4b [9].

The principle of thermal expansions and contractions enables the self-actuating thermal actuator, which is placed inside the radiator thermostat. The absence of electrical parts limit the possibility of remote control for this type of thermostat. However, with the increasing penetration of smart home system, the household appliances and devices are desired to be controlled remotely. Furthermore, the accurate temperature control can be hard to reach since the temperature closed loop control is not applied.

The highly reliable and inexpensive step motor, which converts the digital pulses to linear motion, can be accommodated in the thermostat to actuate the radiator heating valve. The remote control can easily be achieved due to the employment of the electromagnetic actuation device. However, this kind of thermostat normally introduces the noise issue, which is not desired in the dwelling space. In addition, the battery life tends to be relatively short due to the low system level efficiency. The current product generally can continuously operate for around 2 years with the same batteries.

Due to the disadvantages of the existing actuators, a new type of actuating device needs to be proposed, which needs to feature accurate temperature control, remote control feasibility, noise free operation and high system level efficiency. The new actuator will be discussed in detail in subsection 2.2.4.



Figure 2.4: The commonly used two types of radiator thermostat.

2.2 Dielectric Electro Active Polymer

The investigation of Dielectric Electro Active Polymer (DEAP) can be traced back to an experiment carried out by Roentgen in 1880, through which the actuation mechanism of DEAP material was observed [6]. This discovery had been verified by Sacerdote in 1899, who also established the relationship between strain response and electric field excitation [13]. Over the past two decades, the research related to DEAP has obtained considerable progress in investigating and improving material performance and developing potential mechanical configurations, which enables the commercialization of this technology.

As an emerging type of smart material, DEAP has already demonstrated superior performance over a variety of evaluation parameters, such as light weight, low manufacturing cost, large elastic strain, fast electromechanical response speed, etc, and thus can be applied in a wide range of applications [1]. This section is organized to illustrate DEAP in terms of structure, capacitive characteristic, operating principle as well as application fields.

2.2.1 Structure

DEAP is configured with dielectric polymer in the middle and two compliant electrodes on both sides of the polymer. The structure of DEAP film is illustrated

2.2. Dielectric Electro Active Polymer

in Figure 2.5a. Currently, silicone polymer is widely applied due to low loss characteristic under high frequency operation and wide operating temperature range compared to other potential dielectric material [14]. After exploring large number of electrode material, carbon grease has been validated to be a good solution since it has good conductive capability even at high strains and it can easily be adhered to most dielectric polymer material. In addition to carbon grease, other potential electrode material can be metallic paints, graphite and carbon powder, etc [6].

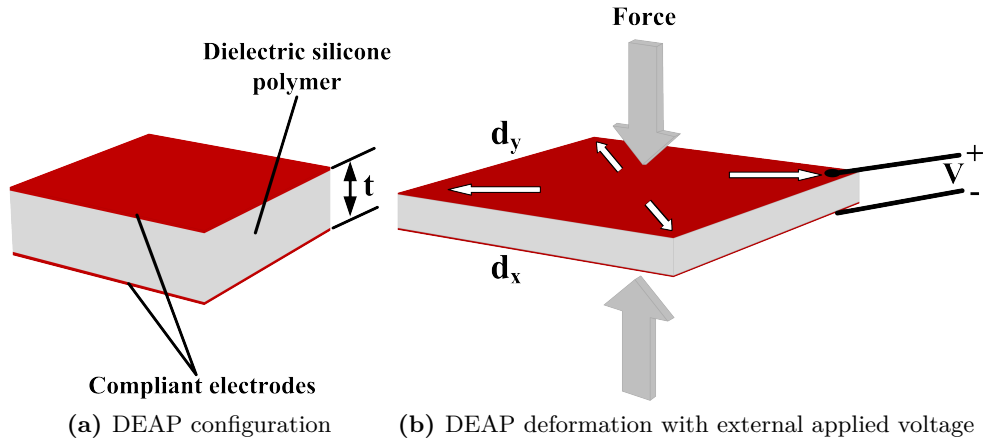


Figure 2.5: DEAP structure and deformation when voltage is applied.

2.2.2 Capacitive Property

DEAP film exhibit similar sandwich structure to that of the parallel plate capacitor, which implies the capacitive property of the material [15], [16]. The impedance measurement has been carried out in the low operating frequency and the results are shown in Figure 2.6, which indicate the pure capacitive characteristic through the -90° phase angle and the declining impedance value with increased frequency.

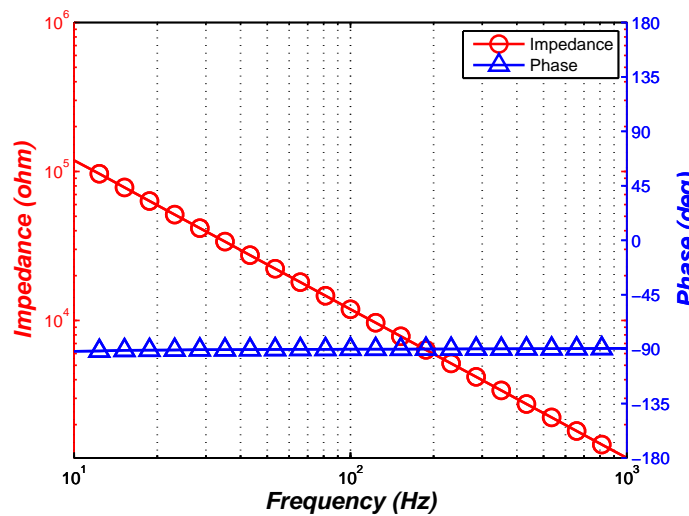


Figure 2.6: DEAP film impedance and phase versus frequency.

As mentioned in section 1.3, a voltage in the range of kilovolt needs to be applied for the current version DEAP film to have a deformation. The investigation related to capacitive property under high voltage operation can be beneficial for better understanding the material itself and providing detailed load information for high voltage driving system design.

Currently, two types of low volume high voltage capacitor in the range of nano farad are commonly used [17]. As one of this type, film capacitor also has the sandwich configuration as described for the standard parallel plate capacitor. The dielectric material are normally the insulating plastic film while metallized aluminium or zinc are widely applied to form electrodes. Over a wide temperature range, normally from -55°C to $+150^{\circ}\text{C}$, film capacitor exhibits good performance in terms of temperature independence. In addition, like the electrolytic capacitor, its capacitance nearly does not change with the applied voltage, even under the high voltage operation. These two merits enable the broad application of film capacitor in the field of high voltage and high power energy conversion. The small size high operating voltage Class 2 Multiple-Layer Ceramic Capacitor (MLCC), in general, employs ceramic material to constitute the dielectric layer and applies metal to be the electrodes. Compared to film capacitor, Class 2 MLCC normally presents weak performance in terms of temperature and voltage independence.

In order to investigate the high voltage capacitive property, the DEAP film with nominal capacitance 134 nF has been measured in terms of capacitance versus voltage characteristic. For comparison study, the same experiments have been carried out for the similar nominal capacitance film capacitor and Class 2 MLCC. 9 parallel 15 nF film capacitor were employed to be a 135 nF capacitor and nominal 132 nF MLCC consists of 4 parallel 33 nF capacitor. The experimental results are presented in Figure 2.7, which indicate that the property similarity between DEAP and film capacitor. Therefore, it can be concluded that, if the polymer deformation is within the limits, the capacitance of DEAP material almost does not change in the high voltage operation.

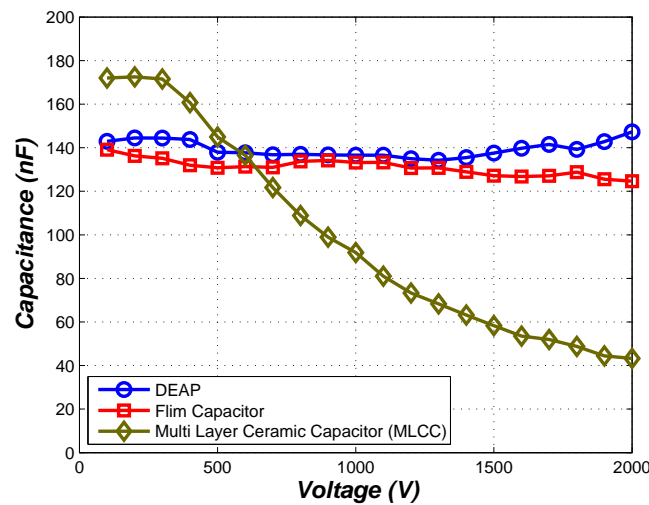


Figure 2.7: Capacitance versus voltage characteristic of DEAP material, film capacitor and MLCC.

2.2.3 Working Principle

When a certain amount of electric field is applied for the flexible dielectric polymer of DEAP, the material tends to compress in thickness and expand in the perpendicular direction due to the electrostatic force. This mechanism is illustrated in Figure 2.5b and enables the DEAP film based actuator. The generated mechanical force can be derived from Coulomb's law and can be expressed as

$$F_{e.static} = \varepsilon_0 \cdot \varepsilon_r \cdot d_x \cdot d_y \cdot E_{static}^2 = \varepsilon_0 \cdot \varepsilon_r \cdot d_x \cdot d_y \cdot \frac{V^2}{t^2} \quad (2.1)$$

where ε_0 and ε_r are the vacuum permittivity and relative permittivity of DEAP film, respectively. d_x and d_y are the x-axis and y-axis dimensions, respectively, as shown in Figure 2.5b. While $F_{e.static}$ stands for the electrostatic force, E_{static} , V and t are the electric field, applied voltage over electrodes and thickness of the dielectric polymer, respectively [6].

The capacitive property of the DEAP film has already been verified in the circumstances of low frequency and high voltage operation in subsection 2.2.2. Referring to the capacitance derivation of parallel plate capacitor, the capacitance of DEAP film can be represented as

$$C = \varepsilon_0 \cdot \varepsilon_r \cdot \frac{d_x \cdot d_y}{t} \quad (2.2)$$

where C is the capacitance value of the DEAP film with thickness t , length d_x and width d_y , as shown in Figure 2.5.

Obviously, the intrinsic flexible property of silicone polymer results in large strain capability of DEAP film. When an external force is applied to stretch the material, the significant deformation leads to the change of the capacitance value. The variation relationship between the shape and the capacitance, thus, indicates the possibility of DEAP film based capacitive sensor [18], [19], [20].

One of capacitor's application is to store energy electrostatically in an electric field. Likewise, the electrical energy can be stored in the DEAP film with purely capacitive characteristic in the low frequency operation. The stored energy E_{stored} can be calculated by

$$E_{stored} = \frac{1}{2} \cdot C \cdot V^2 \quad (2.3)$$

Eq. 2.3 indicates that if the capacitance value of the DEAP film increases due to the deformation caused by external mechanical force while the applied voltage keeps constant, the energy stored in the film correspondingly tends to become larger, which enables the energy transformation from mechanical to electrical. By utilizing this mechanism, a new type of generator and energy harvester have been proposed. More detailed information in this field can refer to [21], [22], [23].

2.2.4 Application Fields

2.2.4.1 Actuator in Heating System

The good performance parameters of DEAP actuator, such as high energy density, light weight and noise free operation, enable it to be a potential candidate to replace the current existing pneumatic, hydraulic and electromagnetic actuators in aerospace and automotive electronics industries, in which weight is normally with a high priority, and in dwelling space, which is sensitive to noise issues [24].

To overcome the shortcomings of the commonly used actuators in radiator thermostat, which are mentioned in subsection 2.1.3 and to further improve the compactness, a conceptual in-line heating valve with embedded DEAP actuator, which integrates the heating valve and actuator inside radiator thermostat together, is proposed by Danfoss A/S Heating Solutions. The configuration is shown in Figure 2.8. The light yellow part is the hollow DEAP actuator, which is totally involved inside the valve body and is used to adjust the position of the integrated pin in order to control the water flow. The high voltage converter and associated components are situated in the black box with the dimensions as $27\text{ mm} \times 16\text{ mm} \times 10\text{ mm}$.

Currently, several critical challenges related to the material performance and mechanical parameter limit the application of the in-line heating valve. Figure 2.8 indicates that the hot water needs to pass through the hollow DEAP actuator. The water absorption of silicone polymer cannot be neglected in the long running, which leads to the decrease of the dielectric properties and the corrosion of the material. Low volume is one of the critical factors to enable the in-line heating valve design. In order to regulate the water flow, a certain amount of actuation force is needed, as illustrated in Table 2.1, while Eq. 2.1 indicates that the mechanical force is proportional to the size of the DEAP film. Thus the trade off between the volume and force needs to be evaluated to achieve the feasible design. The close point detection is a key function of the radiator heating valve and it can be achieved by the intrinsic current property of step motor actuator involved in the thermostat. The intrinsic sensor functionality of DEAP film has been proposed to realize the close point detection while detailed means of implementation need to be discussed. Although the high voltage driver for in-line heating valve with embedded DEAP actuator is set to be the ultimate goal for this project, due to the unsettled challenges, this report is only focusing on the high voltage driver for DEAP actuator used to replace the current actuators inside the radiator thermostat.

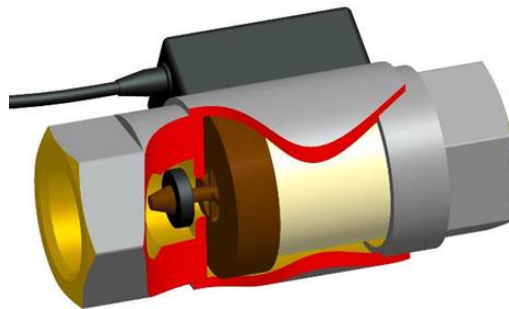


Figure 2.8: Proposed in-line heating valve with embedded DEAP actuator.

2.2.4.2 Sensor

The light weight property and large strain capability enable the DEAP film based sensor to compete with the existing technologies in the emerging wearable devices field. Danfoss Polypower A/S has launched several versatile and compliant wearable sensors to be applied in the field of monitoring the shape change of surfaces. One specific case is to form a golfer's swing monitoring device, which is illustrated in Figure 2.9 [25]. When the DEAP material is stretched, the capacitance changes correspondingly. A module with the function to transfer the capacitance to voltage needs to be implanted in order to obtain the voltage signal, which can be transmitted to the PC or data centre through wireless connection for further analysis.

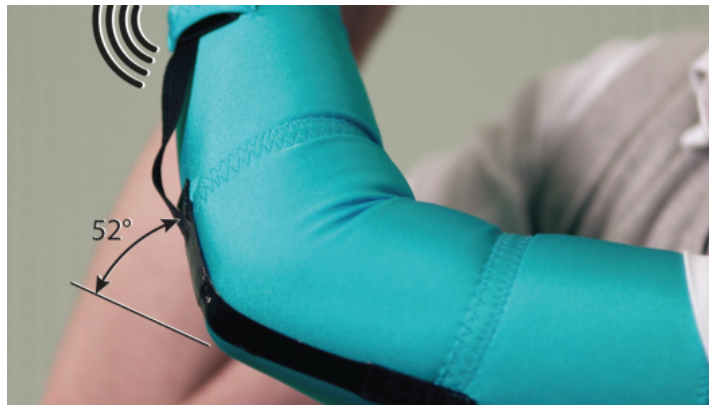


Figure 2.9: Proposed DEAP film based golfer's swing monitoring device.

2.2.4.3 Energy harvester

The transformation mechanism of mechanical force to electrical energy of DEAP material, mentioned in subsection 2.2.3, enables the DEAP film based generator, which can be applied in the ocean to collect the wave energy. The conceptual idea is illustrated in Figure 2.10 [26]. When the float is moved by the waves, the linear motion over DEAP film can be directly transformed to electrical energy, thus eliminating the complex conversion systems, such as hydraulics.

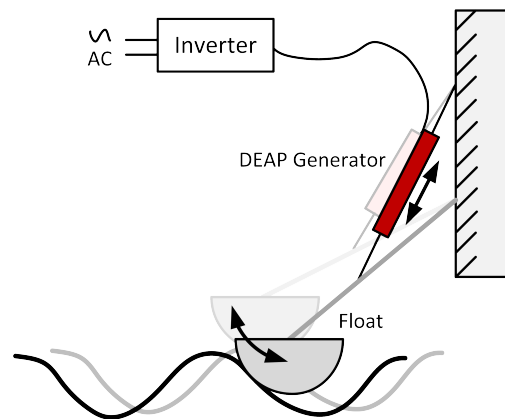


Figure 2.10: Conceptual DEAP film based generator for wave energy.

2.3 High Voltage Driver Solutions

2.3.1 System Configuration

Due to the good performance in terms of noise level and energy density, the DEAP actuator has been selected by Danfoss A/S Heating Solutions to be the potential replacement of the current self-actuating and step motor actuators involved in the radiator thermostat. The high driving voltage demand of DEAP film and accurate temperature control requirement of thermostat necessitate the investigation of high voltage driving system of DEAP actuator for radiator heating valve, whose block diagram is presented in Figure 2.11. The high voltage converter, the sensing and system level control unit as well as the power source and auxiliary power supplies constitute the high voltage driver, as indicated in Figure 2.11. While the DEAP actuator as the electrical load of the high voltage converter and the radiator heating valve as the terminal mechanical load have already been discussed in detail in section 2.1 and 2.2, respectively.

The most critical part involved in the high voltage driving system tends to be the high voltage converter, which is responsible for generating high output voltage to elongate the DEAP actuator from low input voltage power source. The potential solutions for high voltage converter will be discussed and compared in detail in subsection 2.3.2.

In order to accurately regulate the indoor room temperature, the direct temperature closed loop control can be applied with the help of temperature sensor and analog or digital controller. Alternatively, the indirect temperature regulation based on the control of the converter output voltage can be achieved when high voltage sensing circuits and voltage controller are employed. Detailed information will be presented in subsection 2.3.3.

As an indispensable part in the driving system, the power source and auxiliary power supplies will be briefly addressed in subsection 2.3.4.

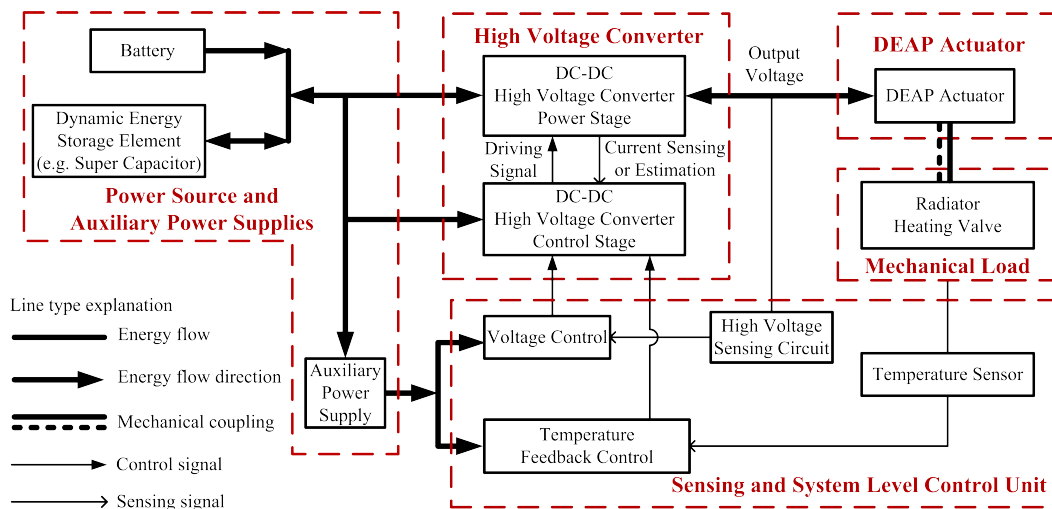


Figure 2.11: Block diagram of high voltage driver of DEAP actuator for radiator heating valve.

2.3.2 High Voltage Converter

2.3.2.1 Specifications

Before evaluating the power stage and control stage involved in the high voltage converter, the design specifications and requirements need to be confirmed first.

Currently, the step motor inside radiator thermostat is powered by two 1.5 V AA batteries connected in series. In order to keep consistent for the next generation product with DEAP actuator, Danfoss A/S Heating Solutions has decided to apply the same power source. That means the high voltage converter is going to be powered by 3 V batteries.

Radiator heating valve, as the terminal load, needs to be actuated by 25 N external force, as summarized in Table 2.1. As the driving source for the mechanical load, DEAP actuator needs to be capable of providing this 25 N force to drive the heating valve through mechanical coupling. Eq. 2.1 indicates the relationship between the force and material parameters as well as applied voltage. Normally, the relative permittivity ϵ_r cannot be changed when the recipe for the polymer is determined while the thickness of the film t is dependent on fabrication process and can be considered to be a fixed value for the material available. Thus the electrostatic force only depends on the size of the film and the applied voltage. In order to achieve low volume actuator to compete with existing actuators, the maximum applicable voltage is decided to be applied. That is 2 kV for the current version film. As a critical load parameter for the high voltage converter, the capacitance of DEAP actuator can be calculated by Eq. 2.2 with the determined film size.

The DEAP film has been validated with constant capacitance value if the deformation is within the limits during the high voltage operation in subsection 2.2.2. Although DEAP actuator has the ability to transfer the electrical energy to mechanical motion, the transformation efficiency is extremely low, which is about 2% as verified in [5]. This low electromechanical coupling coefficient indicates that most electrical energy is still stored in the capacitive actuator. When the actuator needs to be released, the energy can either be dissipated in consumption components or be recovered to the energy source in order to achieve high system level efficiency [27]. While the application of energy recovery normally introduces extra energy consumption and space occupation for the applied control and measurement components, which tends to weaken the benefits of the energy recycling. In fact, whether to dissipate or to recover the energy needs to be evaluated in the specific situation.

Even though dynamic characteristic is not with high priority in the indoor heating system which is normally with high thermal time constant. The heating valve is still desired to be controlled open or close in a relatively short time. The DEAP actuator with fast electromechanical response speed, theoretically, can be considered as an ideal component without any time delay. Thus the output voltage of the converter immediately corresponds to the motion of the heating valve. So the open or close time of the valve is determined by the continuous charging and discharging time of the high voltage converter for DEAP actuator. Table 2.1 indicates the maximum actuation frequency for current heating valves is 0.2 Hz, which means the actuator needs to reach the maximum applicable voltage within 5 s.

In order to be accommodated in the low volume capsule of the radiator thermostat, shown in Figure 2.4, the entire high voltage driving system needs to be designed as low volume as possible without sacrificing the required functionalities. As the critical part of driving system, high voltage converter needs to be applied with the same design rule. As general guidelines, if the normal operations are not affected, the converter is desired to be designed with high efficiency and low cost. All the specifications and requirements of high voltage converter design are summarized in Table 2.2.

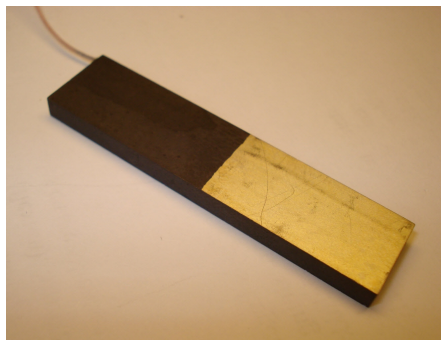
Table 2.2: Design specifications and requirements of high voltage converter

| Parameters | Specifications |
|---------------------------------------------|----------------------|
| Input voltage | 3 V |
| Max. output voltage | 2 kV |
| Capacitance of DEAP actuator | 200 nF |
| Stored energy in DEAP actuator | Dissipate or recover |
| Max. continuous charging / discharging time | 5 s |
| Size | As small as possible |

The low input voltage and high output voltage indicate that the converter needs to feature high step-up ratio, in this case, it needs to reach as high as 667. If size and high step-up ratio are taken into account with higher priority over other demands, the emerging piezoelectric transformer (PT) based converter and the traditional magnetic transformer based flyback converter are potential candidates for the high voltage energy conversion interface.

2.3.2.2 Piezoelectric Transformer Based Proposal

Piezoelectric transformer (PT) is a device, which utilizes the conversion between the electrical and mechanical energy to achieve the voltage transformation [28], [29]. PT is constituted of both primary and secondary side. The primary element transforms the electrical energy to mechanical vibration. Through the joint structure, the vibration is transferred to secondary side and then transformed back to an electrical output voltage. Two type of commonly used PTs are shown in Figure 2.12 [30].



(a) Rosen type of PT



(b) Radial type of PT

Figure 2.12: Two types of commonly used PT.

To apply PT to an energy conversion system and predict the system level performance, an electrical circuit model with lumped parameters needs to be derived [31]. The model depicted in the grey dash boxes of Figure 2.13a and 2.13b is normally used to represent the behaviour of the PT in a narrow band near a single resonance frequency [32], [33], [34]. The lumped parameter values of the model can be acquired in the datasheet of the PT or through practical measurements [35].

In the primary side, the half bridge topology without magnetic components has been proved to be a good driving solution for PT in terms of component count, size and EMI performance [30], [36], [37]. The capacitive property of the actuator needs to be taken into account when developing the PT based converter for DEAP film. As discussed before, energy recovery is not desired for the high voltage converter in some cases, where the unidirectional energy flow PT based converter with diode rectifier, shown in Figure 2.13a, can be applied. Otherwise, if the stored energy in actuator needs to be transferred back to the primary power source, it is necessary to employ the bidirectional energy flow PT based converter with active rectifier in the secondary side, shown in Figure 2.13b [38].

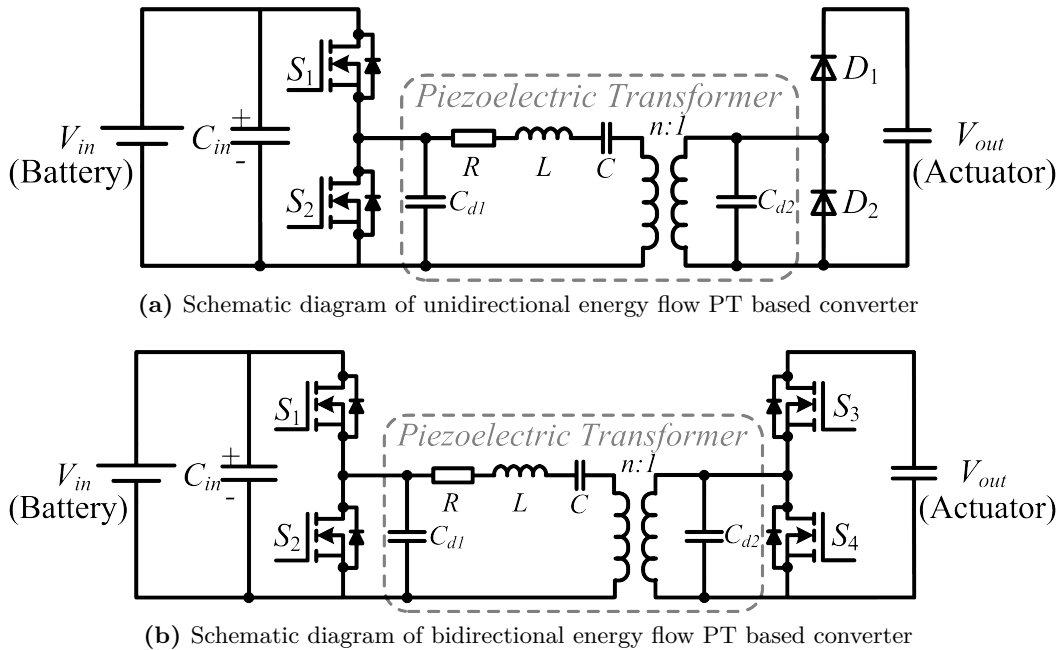


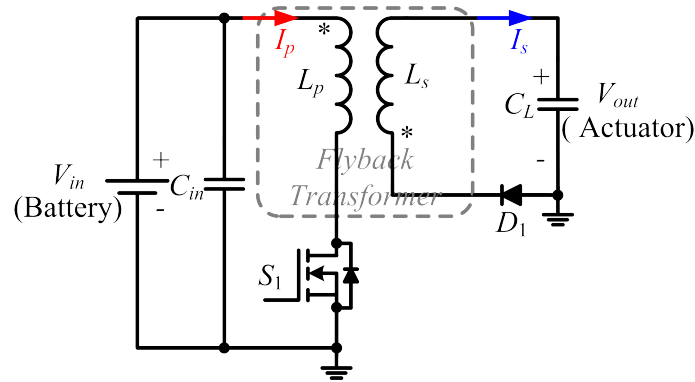
Figure 2.13: Schematic diagrams of PT based converters.

An efficient transfer of the mechanical energy from the primary to the secondary side can be achieved when the PT is operated in the resonance mode [30]. While the resonance of PT is normally with high quality factor, which leads to the narrow band of efficient operation. In addition, the resonance frequency also varies with the temperature, load, ageing, etc. In order to enable the efficient energy transfer as well as the strict operating frequency control, a complex control scheme is difficult to be avoided. One feasible solution tends to be the self-oscillating control with voltage or current feedback [39]. In general, the realization of the control for bidirectional energy transfer exhibit more complexity compared to that in unidirectional converter.

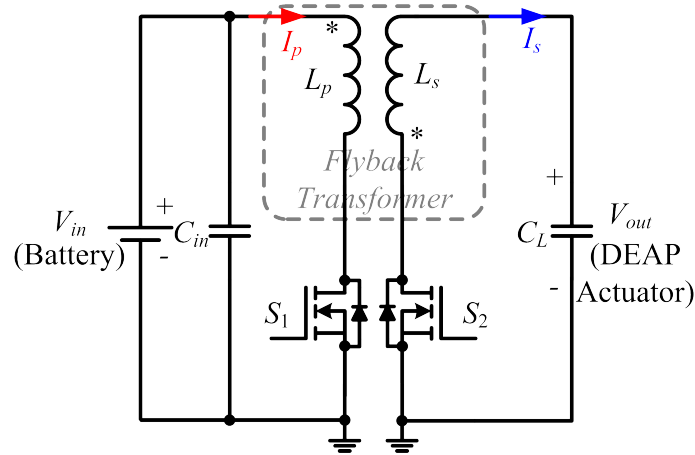
2.3.2.3 Magnetic Transformer Based Proposal

As a simple topology, magnetic transformer based flyback converter can be easily found in the consumer electronics products, telecommunication system as well as household appliances [40], [41]. Moreover, flyback topology has been applied in the cathode ray tube (CRT) TVs to generate high voltage for electron tubes [42], [43].

Likewise, two applicable flyback based configurations can be used to achieve the unidirectional or bidirectional energy flow between the energy source and the capacitive load. One is the unidirectional flyback converter with diode rectifier in the secondary side, which is shown in Figure 2.14a [44]. By replacing the diode with active semiconductor component, the bidirectional flyback converter, shown in Figure 2.14b, is formed to achieve the energy recovery when system level efficiency is with the highest priority [45], [46], [47], [48].



(a) Schematic diagram of unidirectional flyback converter



(b) Schematic diagram of bidirectional flyback converter

Figure 2.14: Schematic diagrams of flyback converters.

As a well developed topology, flyback converter can operate efficiently with the help of appropriate control strategies. In the conventional flyback converters, the output voltage regulation and the dynamic load characteristic are of most concern to designers, which necessitate the employment of the outer voltage closed loop control as well as the inner current loop control. When flyback is used in the high voltage application with only capacitive load, the peak current control with

boundary conduction mode (BCM) or discontinuous conduction mode (DCM) can ensure the effective energy transfer in each switching cycle [44], [49], [50]. While the output voltage can be regulated by hysteresis control, which will be discussed in system level control in subsection 2.3.3.

2.3.2.4 Proposals Comparison

In order to select the solution with maximum overall benefits in terms of size, efficiency and cost, which are normally contradictory evaluation criteria, comparison of the PT based and flyback high voltage converter proposals need to be carried out in the aspect of transformer itself, power stage configuration as well as control schemes.

Compared to flyback transformer, the absence of winding for PT can provide a great potential in achieving low volume high voltage transformer [51],[52]. After long term development, conventional flyback transformer can be fabricated with very low expenses. The cost of manufacture for PT can be kept low as well if the automatic mass production can be achieved. The mechanism of electromechanical energy transfer makes PT be superior over magnetic transformer, which normally operate based on the electromagnetic transfer, in terms of EMI performance [53], [54], [55]. Although high step-up ratio can be achieved by PT, the current situation of PT research indicates that it is quite difficult to reach extremely high step-up ratio, such as 667 mentioned before [28], [52]. The capacitive property of the load enables the flyback transformer based topology to achieve a high step-up ratio with relatively less effort. The design methodologies of magnetic transformer have been systematically developed for decades, whilst as an emerging field, PT is still under preliminary investigation and expects the easy and feasible design proposals. The compared items of PT and flyback transformer are summarized in Table 2.3.

Table 2.3: Comparison of transformer applied in PT based and flyback high voltage converter

| Comparison category | Comparison item | PT based converter | Flyback converter |
|---------------------|--------------------------------|--------------------|------------------------|
| Transformer | Size | Small | Large |
| | Cost | Low | Low |
| | EMI | Low | High |
| | High step-up ratio realization | Difficult | Relatively easy |
| | Design complexity | High | Low |

As presented in Figure 2.13, the half bridge topology applied in the primary side of both unidirectional and bidirectional PT based converter requires two MOSFETs and one high side gate driver for controlling the high side MOSFET to be switched on and off. By contrast, only one low side MOSFET needs to be employed in the primary side of unidirectional or bidirectional flyback converter, as indicated in Figure 2.14. If unidirectional configuration is decided to be applied, the PT based converter needs two high voltage diodes to form the rectifier in the secondary side whilst one diode is sufficient in the flyback case. Likewise, two high voltage MOSFETs and one high voltage high side gate driver tend to be unavoidable in

the secondary side for bidirectional operation of the PT based converter. This high side gate driver to drive the high voltage MOSFET rated at 2 kV is not available on the market yet and it is not so easy to achieve this high voltage gate driver.

As discussed in subsection 2.3.2.2, PT needs to be controlled tightly within the narrow band of resonance frequency to ensure the efficient operation. Otherwise the energy loss as well as the temperature rise will be caused by the inefficient running. While the variation of the temperature tends to change the resonance frequency of PT to be even further away from the controlled switching frequency. This positive feedback mechanism finally leads to the failure of the PT [53], [56]. In fact, the resonance frequency of the operating PT cannot be measured, so indirect estimation approaches need to be applied, which absolutely increase the complexity of control scheme [57], [58], [59], [60], [61]. In comparison, the flyback converter can easily be controlled to achieve peak current detection and BCM or DCM operation with commercial control ICs. The compared items for power stage and control scheme of PT based and flyback high voltage converter are listed in Table 2.4.

Table 2.4: Comparison of power stage and control scheme applied in PT based and flyback high voltage converter

| Comparison category | Comparison item | PT based converter | Flyback converter |
|----------------------------|---------------------------------|--------------------|-------------------|
| Unidirectional power stage | Primary MOSFET | 2 | 1 |
| | Primary high side gate driver | 1 | 0 |
| | Secondary high voltage diode | 2 | 1 |
| Bidirectional power stage | Primary MOSFET | 2 | 1 |
| | Primary high side gate driver | 1 | 0 |
| | Secondary high voltage MOSFET | 2 | 1 |
| | Secondary high side gate driver | 1 | 0 |
| Control scheme | Complexity | High | Low |
| | Commercial control IC | No | Yes |

As indicated in Table 2.3, PT itself features lower volume compared to the flyback transformer in high voltage applications. Even so, it cannot be concluded that PT based converter is more advantageous in terms of volume than flyback converter, since the former has more disadvantages in terms of components count in power stage. Thus it is critical to carry out the overall evaluation of the proposals based on the specific case. In fact, PT based converter is especially suitable to be applied in the EMI sensitive situation, such as magnetic resonance imaging (MRI) scanner. If heating valve application is taken into account, the employment of the mature high voltage flyback converter enables the reliable high voltage driving system with low overall volume and cost.

2.3.3 Sensing and System Level Control Discussion

As stated in subsection 2.3.1, two potential system level control solutions can be used to regulate the ambient temperature in the dwelling space. If direct temperature control is feasible, the temperature sensor needs to be applied to achieve the temperature closed loop control. In general, there are three types of electrical tem-

perature sensors, including thermistor, thermocouple and resistance thermometer [62]. Considering the working temperature range, accuracy and difficulty level of achievement of voltage signal, the thermocouple is selected to be the most commonly used temperature sensor in the radiator thermostat application. In order to achieve the advanced algorithm for temperature feedback control and to increase the control flexibility, the closed loop control is desired to be realized in the digital controller, such as microcontroller or digital signal processor (DSP).

In some cases, direct temperature control cannot be easily achieved. As an actuation device for the radiator heating valve, DEAP actuator can regulate the motion of the pressure pin involved in the valve in order to control the water flow by adjusting the applied voltage. For a specific actuator, the voltage versus motion stroke characteristic can be measured when the actuator is available. The typical curve of this property is illustrated in Figure 2.15 [63]. The temperature estimation model based on the motion of valve pin and the water flow flux needs to be built up to predict the ambient temperature in this voltage control based temperature regulation solution.

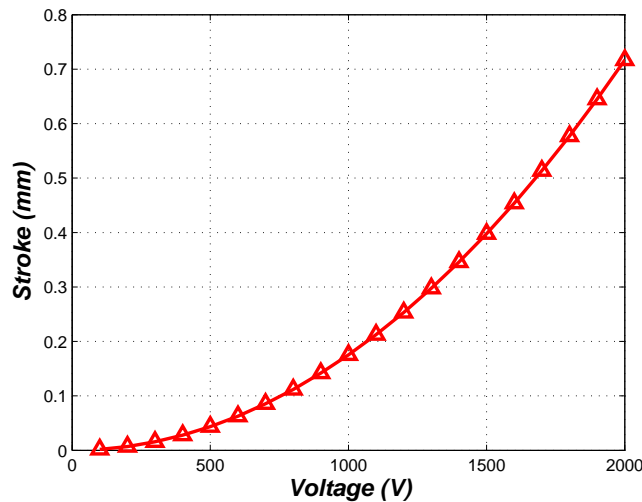


Figure 2.15: Stroke versus voltage characteristic of DEAP actuator.

In order to achieve the voltage control, the high voltage applied over actuator needs to be sensed accurately. The resistive divider normally tends to be an effective solution, while in the high voltage case, the parasitic parameters considerably affect its normal operation which necessitates the employment of capacitive divider. Before sending the high voltage measurement signal to control loop, an operational amplifier buffer with high input impedance needs to be applied. The described high voltage measurement circuit is shown in Figure 2.16 [35]. Similar to temperature control, the voltage closed loop control is expected to be achieved with digital controller as well to ensure the control flexibility.

The accuracy of indirect temperature control greatly depends on the practical stroke response of DEAP actuator, the accuracy of the temperature estimation model and the high voltage measurement. While the hysteresis phenomenon has already been proved to exist in the DEAP actuator, which asks for more efforts to thoroughly investigate its motion response to achieve a more accurate model.

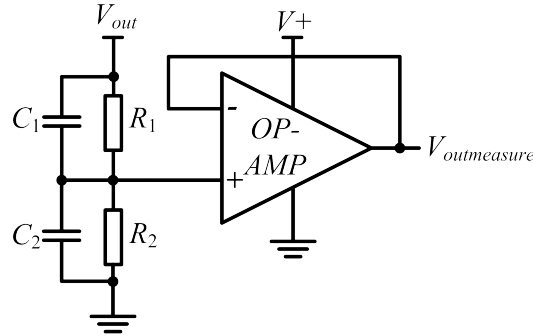


Figure 2.16: High voltage measurement circuit.

2.3.4 Power Source and Auxiliary Power Supplies Solution

In the cases that energy needs to be recycled from the capacitive actuator to the primary power source, one type of dynamic energy storage element featuring high energy density, such as super capacitor, needs to be applied in parallel with power source in order to store energy for non-chargeable batteries as well as to ensure the stabilization of the input voltage during the energy transfer and recycle phases.

As the sole energy source for the entire driving system, two series 1.5 V AA batteries cannot provide sufficiently high voltage to supply the control ICs, the sensing circuits as well as to drive the MOSFETs. Thus the auxiliary power supplies which can boost the input voltage to desired values need to be used. In order to achieve the balance between volume, efficiency and cost, commercial highly integrated switched mode power supplies (SMPS) with very few external passive components can be a feasible solution.

2.4 Summary

In this chapter, the heating system, Dielectric Electro Active Polymer (DEAP) and the high voltage driver solutions for DEAP actuator involved in the heating valve applications have been described to give an overview of the research subjects. By reviewing the state-of-the-art solutions for the high voltage converter, flyback topology is selected as the interface circuit between the energy source and the actuator. The investigation of the high voltage flyback converter will be the main focus of Chapter 3, while the entire DEAP actuator high voltage driving system will be emphasized on Chapter 4.

High Voltage Flyback Converter Investigation

The topology comparison presented in section 2.3.2 indicates the high voltage flyback converter tends to be a good solution as an energy interface between energy source and DEAP actuator in the heating valve application. In this chapter, the unidirectional and bidirectional energy flow as well as the analytical switching cycle model and energy efficiency will be investigated to achieve the design considerations and thorough understanding of the high voltage energy conversion interface.

3.1 Unidirectional Energy Flow

In the investigation of unidirectional high voltage flyback converter, two potential solutions are proposed to achieve the high step-up ratio. One is the conventional flyback topology, which will be discussed in subsection 3.1.1, while the other is the multiple flyback transformer based primary parallel secondary series flyback converter (PPSSFC), which will be the subject of subsection 3.1.2. These subsections only provide brief summary and more detailed information can refer to Appendix C and D.

Either BCM or DCM current mode control can be applied to achieve the complete energy transfer in one switching cycle, as stated in subsection 2.3.2.3. The charging speed for capacitive actuator is a critical criteria even in the heating system with low dynamic performance. These considerations enable the application of BCM control scheme in the unidirectional energy flow flyback converter.

3.1.1 Traditional Topology Discussion

3.1.1.1 Topology Configuration

The conventional unidirectional flyback converter has been depicted in Figure 2.14a. In practical application, one current sensing resistor needs to be employed to achieve

the current mode control. Moreover, in order to suppress the voltage spike over MOSFET caused by the leakage inductance of flyback transformer when S_1 is switched off, RC or RCD snubber circuits need to be applied in the primary side [64]. This kind of protection circuit is not desired in the secondary side, since the introduction of extra capacitance tends to affect the charging ability and efficiency. The feasible solution is to utilize the high voltage diode with sufficient voltage margin. The detailed configuration information is provided in Appendix C.

3.1.1.2 Working Principle

The objective of the unidirectional energy flow converter is to charge the capacitive actuator to the pre-set voltage. This is achieved by the voltage accumulation through a series of successive charging switching cycles. In each cycle, when S_1 is switched on, the energy is transferred from the power source to the flyback transformer, which corresponds to the increase of the primary current I_p , as indicated in Figure 2.14a. Until the current reaches the peak value which is set by the current control IC, the primary MOSFET is controlled to switch off. Afterwards, the energy stored in the flyback transformer can be released to the capacitive actuator through the freewheeling path in the secondary side. This energy transfer indicates the decrease of the secondary current I_s , as indicated in Figure 2.14a as well as the rise of the output voltage. In the entire charging phase, the key waveforms of three successive switching cycles are illustrated in Figure 3.1. The application of BCM current mode control implies that, when the secondary side current drops to zero, the next switching cycle starts immediately.

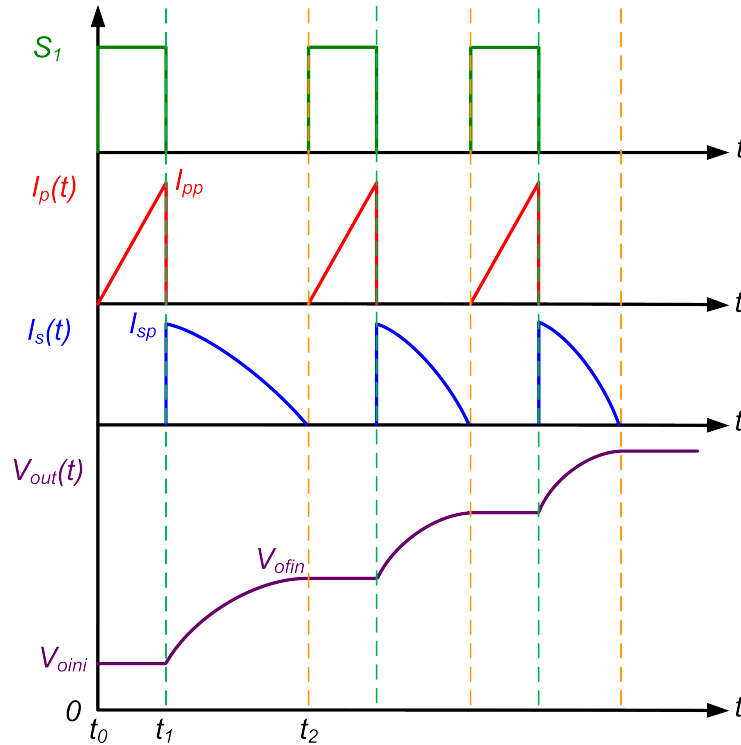


Figure 3.1: Operating principle of unidirectional flyback converter for capacitive actuator.

In one switching cycle, the on time of S_1 and the freewheeling time of D_1 can be achieved to evaluate the overall charging time in the design stage. The starting time for one switching cycle is denoted as t_0 and S_1 is turned off at time point t_1 , while the entire cycle completes at t_2 . Theoretically, t_1 and t_2 can be derived as

$$t_1 = t_0 + \frac{I_{pp} \cdot L_p}{V_{in}} \quad (3.1)$$

$$t_2 = t_1 + \arctan\left(\frac{I_{sp} \cdot \sqrt{L_s}}{V_{oini} \cdot \sqrt{C_L}}\right) \cdot \sqrt{L_s \cdot C_L} \quad (3.2)$$

where I_{pp} and I_{sp} stand for the primary and secondary peak current respectively. $I_{sp} = \frac{I_{pp}}{N}$ and N is the turns ratio of the flyback transformer, defined as secondary winding turns divided by primary winding turns. The primary and secondary inductances are denoted as L_p and L_s , respectively. V_{in} is the input voltage of the converter and V_{oini} represents the initial output voltage of the converter at the beginning of this switching cycle. C_L is the capacitance of the actuator.

If the potential losses are not taken into account, according to the law of conservation of energy, the energy stored in the flyback transformer tends to be totally released to the capacitive actuator. The final output voltage of the current cycle V_{ofin} , therefore, can be derived as

$$V_{ofin} = \sqrt{V_{oini}^2 + I_{sp}^2 \cdot \frac{L_s}{C_L}} \quad (3.3)$$

3.1.1.3 Prototype

The implemented unidirectional high voltage flyback converter with the corresponding dimensions is shown in Figure 3.2. In addition to the unidirectional flyback configuration, high voltage resistors and MOSFET are applied to dissipate the stored energy in the actuator when it needs to be released [65].

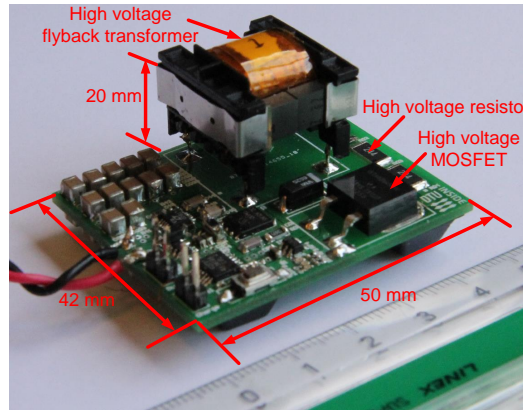


Figure 3.2: Implemented unidirectional high voltage flyback converter for capacitive actuator.

3.1. Unidirectional Energy Flow

The high voltage converter shown in Figure 3.2 has been validated in terms of charging ability as well as the operating principle through experiments. The waveforms in Figure 3.3a indicate that the converter is able to charge the capacitive actuator to 2 kV in 300 ms. The operation mode of peak current and BCM control are confirmed in Figure 3.3b. The current signals I_p and I_s are represented by the voltages over the current sensing resistors, which leads to the negative current signal in the secondary side.

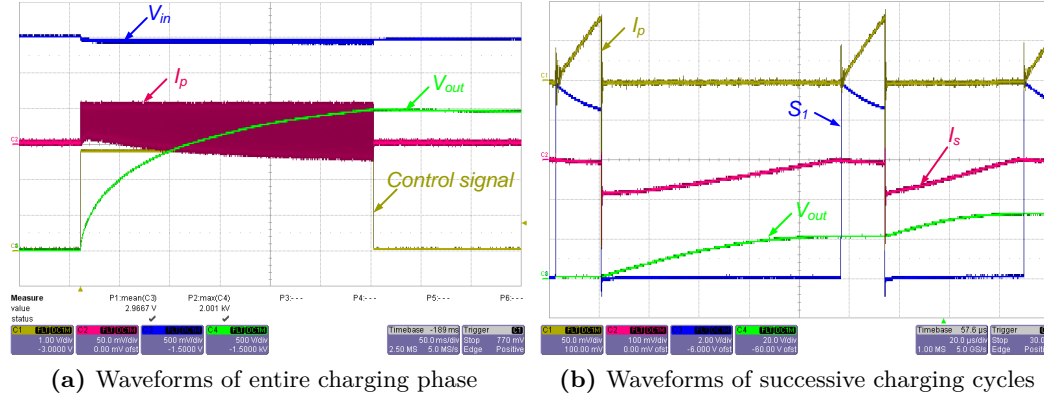


Figure 3.3: Experimental verification of unidirectional flyback converter for capacitive actuator.

3.1.2 New Topology Investigation

3.1.2.1 Topology Configuration

As displayed in Figure 3.2, the high voltage flyback transformer tends to occupy a large fraction of total volume of the converter, which is not desired in terms of volume distribution. In addition, the large number of winding turns in the secondary side of transformer leads to non-negligible parasitic capacitance, which significantly affect the charging ability as well as the efficiency [66], [67]. Furthermore, the special requirements of the high voltage flyback transformer prevents the application of the commercially available flyback transformer, which inevitably increases the design and development cost.

The drawback of the conventional flyback topology calls for a more flexible configuration. Thus a multiple transformer based primary parallel secondary series flyback converter (PPSSFC) is proposed, which is depicted in Figure 3.4. Compared to the configuration with only one transformer, if the same peak current in each transformer is assumed, the parallel connection of primary windings enables the transformers to store more energy in each switching cycle. The series connection of secondary windings can significantly reduce the equivalent parasitic capacitance due to the intrinsic property of series capacitors. If multiple transformers and one single transformer has similar volume, the layout flexibility can be achieved in PPSSFC configuration by reasonably arranging the small transformers to optimal place based on the overall picture. The small volume and relatively low voltage of the transformers in PPSSFC enable the off-the-shelf flyback transformer to be

applied in order to save cost in terms of design and development.

Although the PPSSFC configuration can overcome some issues existing in the conventional flyback topology, the proposed topology also inevitably induces some other problems. One potential issue tends to be the high voltage spike over S_1 due to the parallel connection of the leakage inductor in each transformer. Moreover, the series connection of the secondary winding leads to large winding resistance, which is especially severe when transformer has a small volume. Similar to secondary winding parasitic capacitance, the winding resistance also considerably affects the charging ability and efficiency.

The discussion related to the benefits and drawbacks of the traditional and the proposed topologies indicated that the selection of the proper configuration needs to be dependent on the requirements in the specific case. If small volume and flexibility is set with high priority, the PPSSFC configuration tends to be more desired. While the conventional flyback topology can be beneficial in achieving higher efficiency.

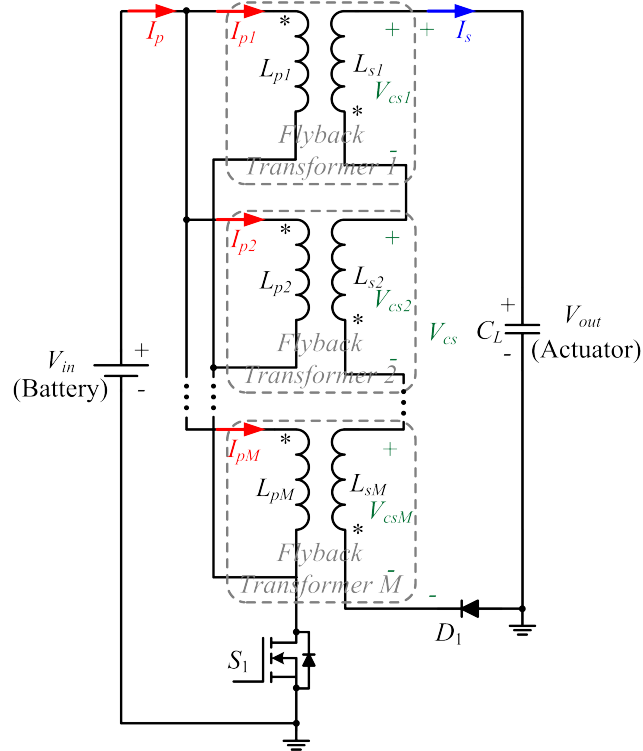


Figure 3.4: The configuration of multiple transformer based PPSSFC.

3.1.2.2 Working Principle

The fundamental operating principle of PPSSFC is similar to that in conventional flyback converter. The flyback transformers still play the role of intermediate energy transfer medium between the power source and capacitive load. In each switching cycle, the energy is transferred to the transformers first and then can be released to the capacitive actuator.

3.1. Unidirectional Energy Flow

The working principle of PPSSFC can also be represented with Figure 3.1. Assuming M flyback transformers are involved in the PPSSFC configuration, the total primary current I_p is actually the sum of all transformers primary current $I_{px(x=1..M)}$ and yields

$$I_p = \sum_{x=1}^M I_{px} \quad (3.4)$$

Supposing all the transformers are identical, secondary side series connection can force to achieve the current sharing of the primary peak current, which can be expressed as

$$I_{pp1} = I_{pp2} = \dots = I_{ppM} = \frac{I_{pp}}{M} \quad (3.5)$$

where $I_{ppx(x=1..M)}$ stands for the peak current in each transformer and I_{pp} is the total peak current in the primary side.

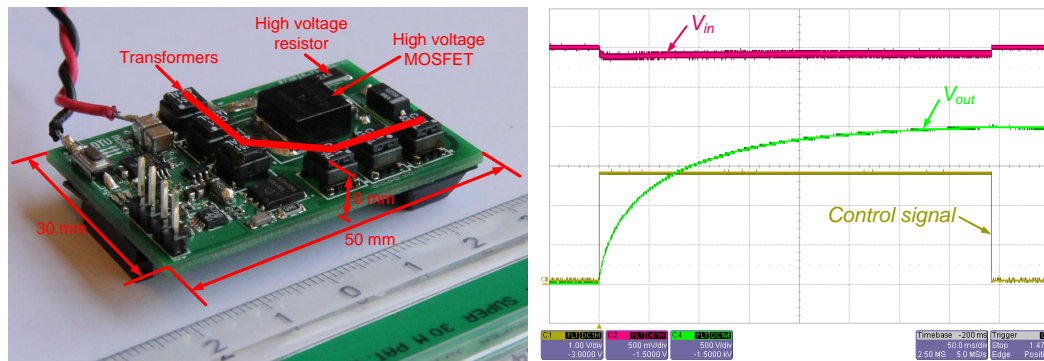
Similarly, the voltage sharing in the secondary side can be guaranteed by the parallel connection of the primary windings, which can be expressed as

$$V_{cs1} = V_{cs2} = \dots = V_{csM} = \frac{V_{cs}}{M} \quad (3.6)$$

where $V_{csx(x=1..M)}$ represents the secondary winding voltage of each transformer and V_{cs} stands for the voltage over all secondary windings. Both $V_{csx(x=1..M)}$ and V_{cs} are illustrated in Figure 3.4 with positive direction.

3.1.2.3 Prototype

A PPSSFC with 6 low volume commercial flyback transformers has been designed and implemented in order to verify the proposed topology in the capacitive load charging application. The prototype is displayed in Figure 3.5a with corresponding dimensions. Similar to the traditional flyback converter illustrated in Figure 3.2, the high voltage resistor and MOSFET here are used to discharge the actuator when necessary. By comparison with conventional flyback prototype, the PPSSFC illustrated in Figure 3.5a features lower volume and higher flexibility in placing the components with small volume.



(a) Implemented PPSSFC for capacitive actuator (b) Waveforms of entire charging phase

Figure 3.5: The prototype and entire charging phase of PPSSFC.

The charging ability of the implemented PPSSFC is validated through experiments. Figure 3.5b indicates that the converter is capable of driving the actuator to 2 kV within 400 ms from a 3 V battery source. In addition, the operating principle is experimentally verified in terms of peak current mode and BCM control, which can be confirmed through Figure 3.6a and 3.6b.

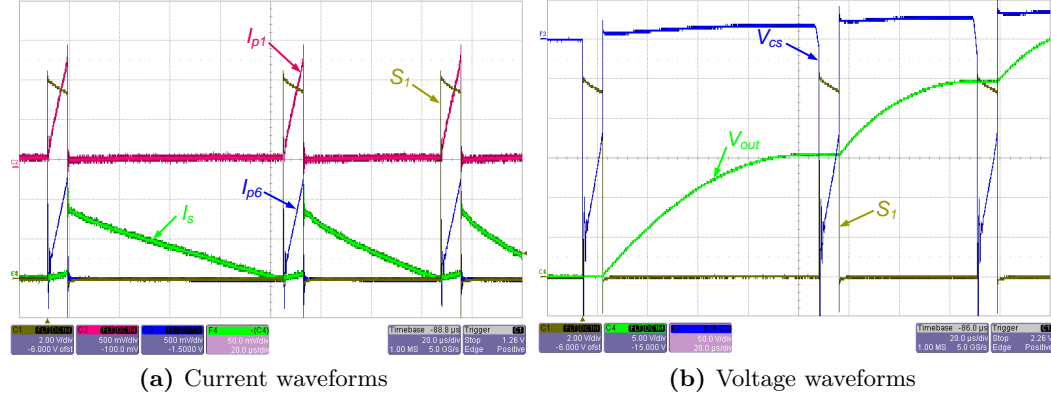


Figure 3.6: Experimental waveforms of successive charging cycles of PPSSFC for capacitive actuator.

3.2 Bidirectional Energy Flow

As indicated in subsection 2.3.2, the intrinsic capacitive property of DEAP actuator and its poor transformation characteristic of electrical energy to mechanical force necessitate the high voltage converter with bidirectional energy flow functionality in some cases. In this section, the high voltage bidirectional flyback converter for capacitive actuator will be discussed briefly and the detailed investigation is provided in Appendix E, F and K.

3.2.1 Topology Configuration

The high voltage bidirectional flyback topology has been illustrated in Figure 2.14b. Similar to the considerations mentioned in subsection 3.1.1.1, the current sensing resistors need to be applied in both primary and secondary side of the bidirectional converter to achieve the peak current control. Likewise, the RCD snubber is only applied in the primary side to perform the protection for the primary semiconductor device. The voltage rating is set with the highest priority when selecting the secondary high voltage MOSFET, since no snubber circuit is employed in the secondary side due to the considerations related to the charging ability as well as the efficiency.

More importantly, two additional high voltage diodes must be used to prevent the current passing through the body diode of high voltage MOSFET, which normally features poor performance in terms of reverse recovery, and to provide the free-wheeling path for the secondary side current in the charging phase. The practical configuration is provided in Appendix E.

3.2.2 Working Principle

Normally, the bidirectional flyback converter for capacitive load operates in either charging mode or discharging mode to achieve the energy transfer to the actuator or the energy recovery from the capacitive load. In fact, the working principle of charging phase is the same as in the unidirectional flyback converter, which is only responsible for charging the capacitive actuator to the pre-set voltage, and is not necessary to be repeated again. So this subsection will only focus on the operating principle of discharging phase.

As described in subsection 2.3.2.3, BCM or DCM can be applied in the flyback converter for capacitive load in order to achieve the fully energy transfer in each switching cycle. The charging phase has been analysed with BCM operation mode in subsection 3.1.1.2. The energy recovery phase, which is not sensitive to the entire operation time, can therefore be operated with DCM.

Similar to the charging phase in the unidirectional energy flow converter, the energy recovery phase in bidirectional converter also consists of a series of successive switching cycles. In each cycle, when S_2 is switched on, the energy is transferred to the flyback transformer from the capacitive load, which corresponds to the rise of the secondary side current and the drop of the output voltage. Once the secondary current reaches the peak value, S_2 is controlled to switch off. The energy stored in the transformer will be recovered to the energy source through the freewheeling channel formed by the body diode of S_1 . The key waveforms of three successive switching cycles, during the whole discharging phase, are shown in Figure 3.7.

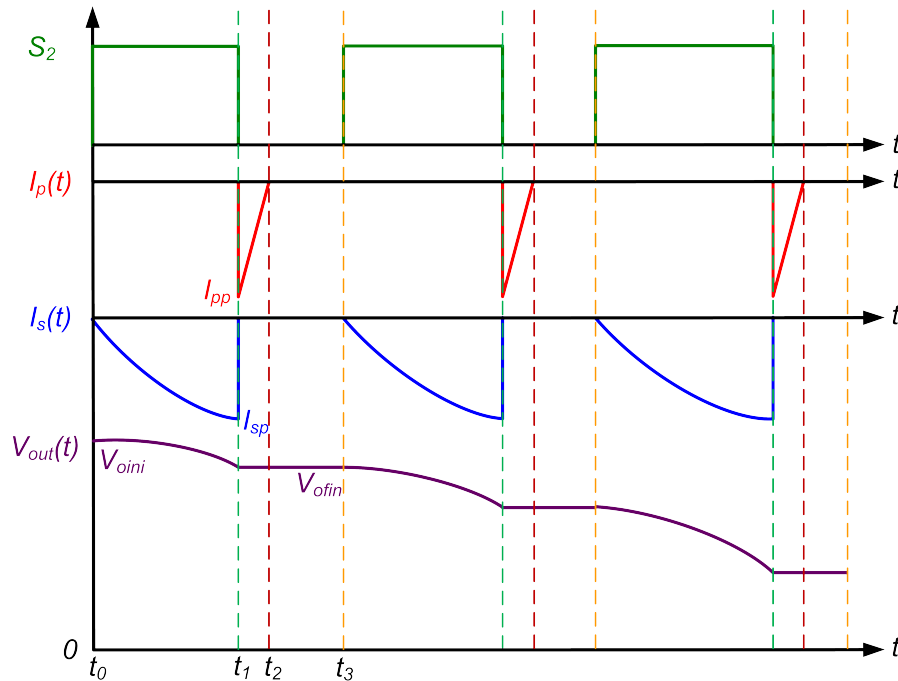


Figure 3.7: Operating principle of energy recovery phase of bidirectional flyback converter for capacitive actuator.

If one switching cycle starts from t_0 , theoretically, the time point to reach the secondary peak current t_1 and the primary current freewheeling complete time

point t_2 can be derived as

$$t_1 = t_0 + \arcsin\left(\frac{-I_{sp} \cdot \sqrt{L_s}}{V_{oini} \cdot \sqrt{C_L}}\right) \cdot \sqrt{L_s \cdot C_L} \quad (3.7)$$

$$t_2 = t_1 + \frac{-I_{pp} \cdot L_p}{V_{in}} \quad (3.8)$$

In the discharging phase, a fixed switching frequency $f_{discharge}$ is applied to ensure the DCM operation mode, thus the end time of the whole cycle t_3 can be expressed as

$$t_3 = t_0 + \frac{1}{f_{discharge}} \quad (3.9)$$

If neglecting the component losses, the final output voltage of the current cycle V_{ofin} theoretically yields

$$V_{ofin} = \sqrt{V_{oini}^2 - I_{sp}^2 \cdot \frac{L_s}{C_L}} \quad (3.10)$$

3.2.3 Transformer Investigation

As a critical component in the bidirectional flyback topology for capacitive load, high voltage flyback transformer needs to be investigated in terms of design methodology as well as the architecture optimization to achieve low parasitic parameters. The related research is addressed in detail in Appendix E, F and K.

The secondary inductance of flyback transformer L_s is subject to the bandwidth of the IC, which is used to realize the peak current control in the secondary side. Even when the converter operates in the highest output voltage, the core saturation is not allowed. To ensure this, the secondary inductance needs to be sufficiently large. If the minimum response time of IC is T_{min} , the secondary inductance needs to satisfy

$$L_s > \frac{T_{min} \cdot V_{omax}}{|I_{sp}|} \quad (3.11)$$

where V_{omax} stands for the maximum operating voltage of the high voltage converter.

Compared to the magnetic resistance of the air gap, normally, the magnetic resistance determined by the magnetic material can be neglected. Thus the secondary inductance can be given by

$$L_s = \frac{N_{sec}^2 \cdot \mu_0 \cdot A}{l_{gap}} \quad (3.12)$$

where N_{sec} is the number of turns of the secondary winding, μ_0 , A and l_{gap} represent the vacuum permeability, the cross-sectional area of the magnetic core and the length of the air gap, respectively.

Eq. 3.12 indicates, the solutions to achieve large value of secondary inductance include: 1) have more winding turns in the secondary side; 2) use larger core which generally features larger cross-sectional area; 3) reduce the air gap length. The

3.2. Bidirectional Energy Flow

first two methods are not desired due to the space limitation and the parasitic component consideration. While the reduction of the air gap can introduce the saturation risk to the core. The maximum flux density can be expressed as

$$B_{max} = \frac{N_{sec} \cdot |I_{sp}|}{l_{gap}} \quad (3.13)$$

In the design phase, the feasible values of L_s , I_{sp} , N_{sec} , A and l_{gap} need to be achieved to ensure the magnetizing time larger than the minimum response time of the control IC and to guarantee the B_{max} below the saturation point of the core material even in the worst case.

The architecture of the transformer significantly affect the parasitic parameters of the transformer [68], [69], [70], [71]. One critical parameter tends to be the stray capacitance paralleled to the secondary winding C_s , which considerably influences the charging ability and efficiency in the charging phase and the reliability in the discharging phase. The calculation methodology of the secondary parasitic capacitor has been summarized in Appendix F. In order to charge the capacitive actuator to the pre-set maximum voltage, the energy stored in the transformer in each switching cycle needs to be sufficient larger than the energy absorbed by the stray capacitor, which can be expressed as

$$\frac{1}{2} \cdot L_s \cdot I_{sp}^2 > \frac{1}{2} \cdot C_s \cdot V_{omax}^2 \quad (3.14)$$

3.2.4 Prototype

The implemented bidirectional high voltage flyback converter is displayed in Figure 3.8 with corresponding dimensions. Compared to the unidirectional converter prototype, the employment of the primary dynamic energy storage component, i.e. the super capacitor in this case, leads to the increase of the converter height. Moreover, the secondary side control related devices also contribute to the dimension increase. The volume comparison among the three prototypes, including the unidirectional and bidirectional flyback converters and the PPSSFC, indicates that if the size is with first priority, the PPSSFC prototype tends to be a desired solution.

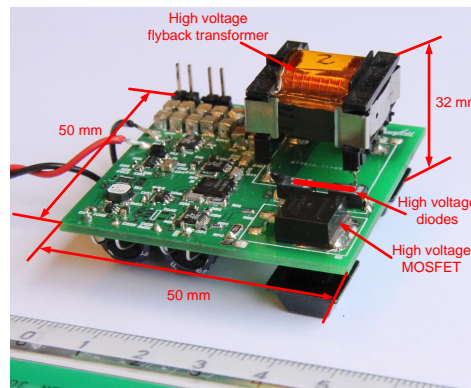
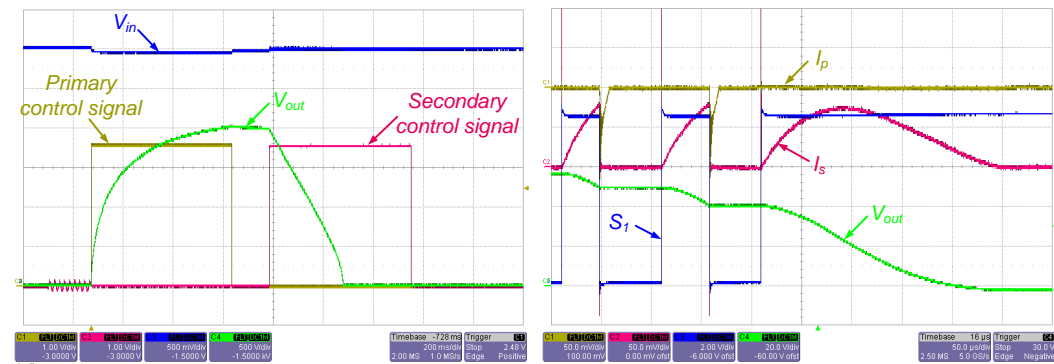


Figure 3.8: Implemented bidirectional high voltage flyback converter for capacitive actuator.

The energy transfer and recovery capabilities of the bidirectional high voltage flyback prototype have been verified with experiments. The entire charging and discharging phase is illustrated in Figure 3.9a, which indicates the converter is able to reach 2 kV in 600 ms and the entire discharge time is around 300 ms. Compared to the charging time in unidirectional converter, the much longer time for the bidirectional prototype is primarily caused by the introduction of extra stray capacitance of secondary high voltage MOSFET. During the discharge phase, the operating mode of peak current and DCM control is confirmed in Figure 3.9b. The current signals here are also represented by the voltage over the current sensing resistors, thus resulting in the positive value in the secondary side and negative value in the primary side.



(a) Waveforms of charging and discharging phase (b) Waveforms of successive discharging cycles

Figure 3.9: Experimental verification of bidirectional high voltage flyback converter for capacitive actuator.

3.3 Analytical Switching Cycle Modelling

The fundamental working principle has been addressed for converters with both unidirectional and bidirectional energy flow in subsection 3.1.1.2 and 3.2.2, respectively. While the discussion in these subsections mainly focuses on the theoretical analysis without taking the influence of the parasitic components into account. In practice, the operating behaviour of the converter is considerably affected by the parasitic parameters, especially in the high voltage operation. The thorough understanding of the high voltage flyback converter for capacitive load needs to be achieved to provide the optimal design guideline for this type of converter in the future design. As an important criteria, efficiency normally tends to attract attention when evaluating the power electronics converters. The analysis concerning the efficiency thus needs to be carried out to figure out the components losses and for the future improvement of charging as well as discharging phase efficiency. In order to achieve these goals, the first step is to derive the switching cycle based analytical behaviour model in both charging and discharging phase with the consideration of all potential parasitic parameters as well as core loss, which greatly affect the accuracy of the analysis in the capacitive actuator driving application. The detailed analytical switching cycle model has been achieved in Appendix H for both charging and discharging modes.

3.3.1 Core Loss Consideration and Detailed Configuration of Flyback Converter

The Steinmetz equation has been extensively applied to evaluate the core loss in the sinusoidal excitation cases, which can be expressed as [68], [72]

$$P_v = k \cdot f^\alpha \cdot \left(\frac{\Delta B}{2}\right)^\beta \quad (3.15)$$

where P_v stands for the power loss per unit volume, f represents the switching frequency and ΔB is the peak-to-peak flux density. α , β and k are dependent on the core material and can be obtained from the datasheet of core manufacturer.

In order to obtain more accurate core loss in the non-sinusoidal and high voltage slew rate situation, the improved generalized Steinmetz equation (iGSE) had been proposed [73], [74], [75], [76]. The core loss calculation based on iGSE can be expressed as

$$P_v = \frac{1}{T} \int_0^T k_i \left| \frac{dB}{dt} \right|^\alpha (\Delta B)^{\beta-\alpha} dt \quad (3.16)$$

$$k_i = \frac{k}{(2\pi)^{\alpha-1} \int_0^{2\pi} |\cos \theta|^\alpha 2^{\beta-\alpha} d\theta} \quad (3.17)$$

where T is the switching period, $\left| \frac{dB}{dt} \right|$ represents the absolute value of change rate of flux density.

Generally, resistive component can be utilized to represent the effect of loss. Thus a core loss equivalent resistance can be introduced to model the influence of the core loss [77]. If considering the equivalent resistance from the secondary side, one obtains

$$R_{ceqs} = \frac{U_{sw}^2}{P_v} \quad (3.18)$$

where R_{ceqs} stands for the secondary side core loss equivalent resistance and U_{sw} is the secondary winding voltage.

Apart from the core loss, the parasitic elements also need to be taken into account in order to achieve the accurate model. As previously mentioned, the most critical parasitic component tends to be the secondary side stray capacitance C_s , which is paralleled to the secondary winding of the flyback transformer.

The effect caused by the leakage inductances needs to be considered as well. The primary and secondary side leakage inductances are denoted as L_{pl} and L_{ps} , respectively. While it should be noted that the primary and secondary side leakage inductance cannot exist at the same time. When the energy is transferred from the primary side to the secondary side, L_{pl} is utilized to stand for the untransferrable energy stored in the flyback transformer. The same concept applies to L_{ls} .

If establishing the accurate model is set to be the ultimate goal, the winding resistances of both primary and secondary side (R_{pw} and R_{sw}) also need to be taken into account. In fact, they are frequency dependent parameters and need to be paid more attention when integrating into the analytical model.

After taking the core loss equivalent resistor and the essential parasitic elements into account, the detailed configuration of the bidirectional high voltage flyback converter is depicted in Figure 3.10. The RP_1 , RP_2 and RP_3 are the current sensing resistors, which can help to realize the current mode control. The voltages over these resistors are employed to represent the current signals in both primary and secondary side. The magnetizing inductances are represented with L_{pm} and L_{sm} in the primary and secondary side, respectively. Thus the primary and secondary total inductances can be given by

$$L_p = L_{pm} + L_{pl} \quad (3.19)$$

$$L_s = L_{sm} + L_{sl} \quad (3.20)$$

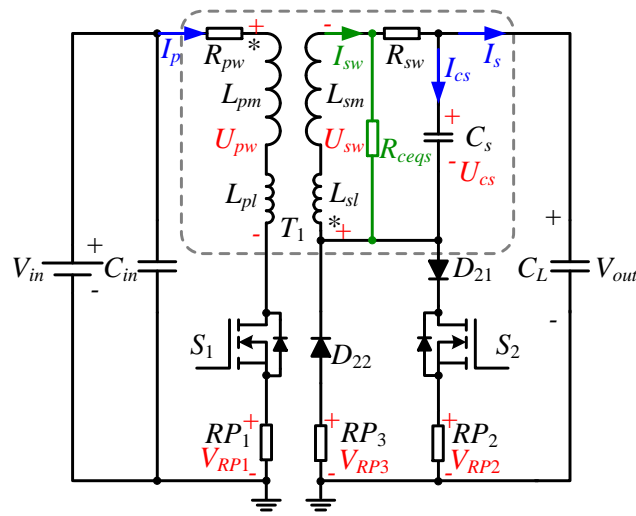


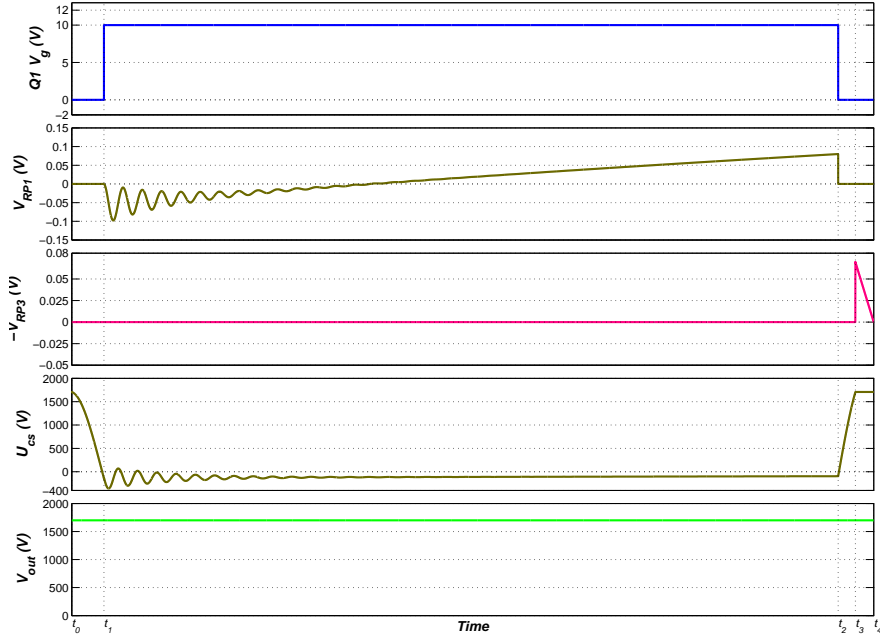
Figure 3.10: Detailed configuration of bidirectional high voltage flyback converter for capacitive actuator.

3.3.2 Charging Mode

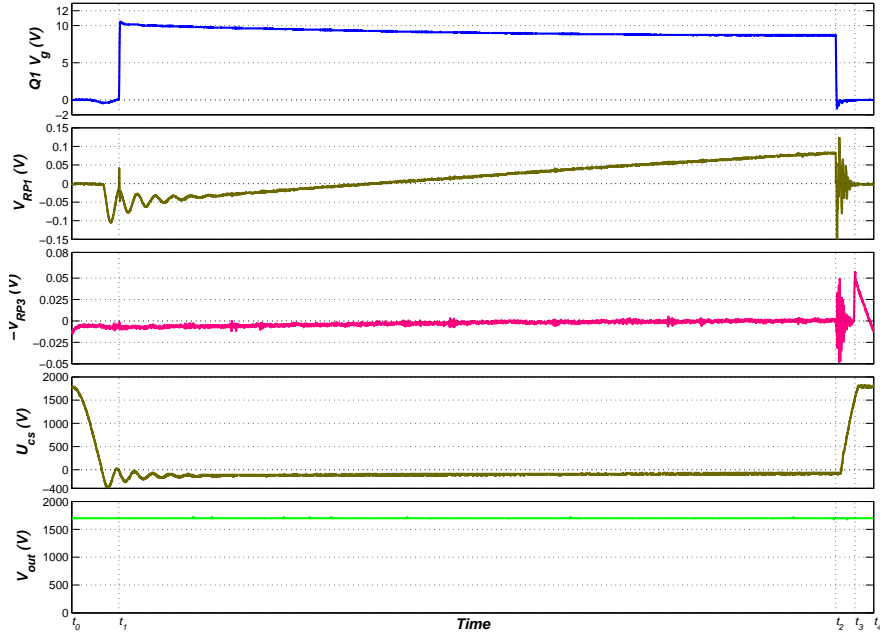
Due to the adoption of the BCM operation mode, one switching cycle of the charging mode consists of 4 intervals, denoted as $[t_0 \ t_1]$, $[t_1 \ t_2]$, $[t_2 \ t_3]$ and $[t_3 \ t_4]$ respectively. During $[t_0 \ t_1]$, the secondary side stray capacitor C_s resonates with secondary inductance L_s with the initial energy stored in the stray capacitor. The stage $[t_1 \ t_2]$ corresponds to the magnetization behaviour in the primary side when S_1 is switched on. In order to force the freewheeling diode D_{22} to conduct, the secondary side stray capacitor needs to be charged to the current output voltage during $[t_2 \ t_3]$. $[t_3 \ t_4]$ is the actual freewheeling stage.

The established analytical model can be applied to predict the behaviour in one charging cycle for both low and high voltage operation. The analytical model based calculated key waveforms for one cycle under high voltage operation and the corresponding measured waveforms are shown in Figure 3.11a and 3.11b, respectively. The comparison between the calculated and measured results indicates that the analytical model of charging mode can well represent the practical behaviour in one switching cycle.

3.3. Analytical Switching Cycle Modelling



(a) Analytical model based calculated waveforms



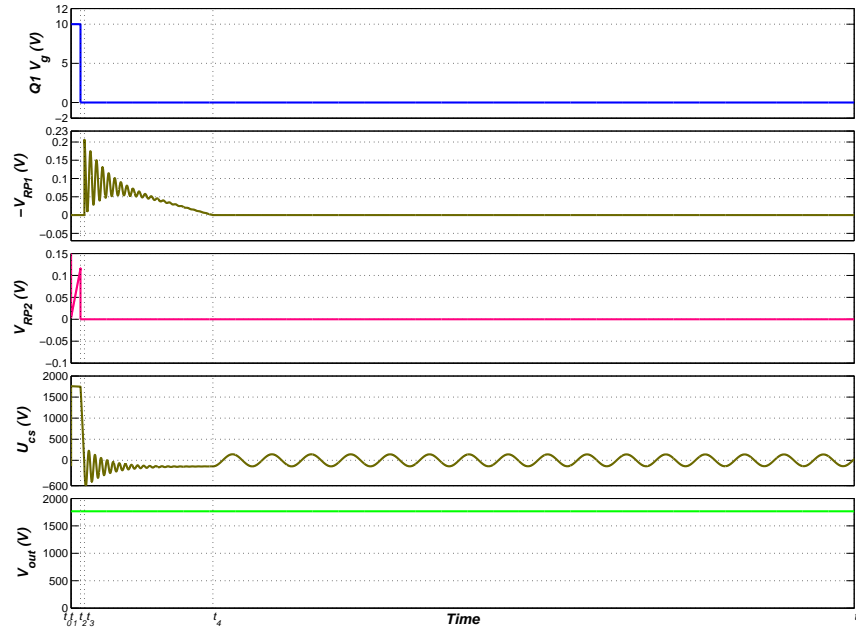
(b) Experimental waveforms

Figure 3.11: High voltage operating waveforms of charging mode.

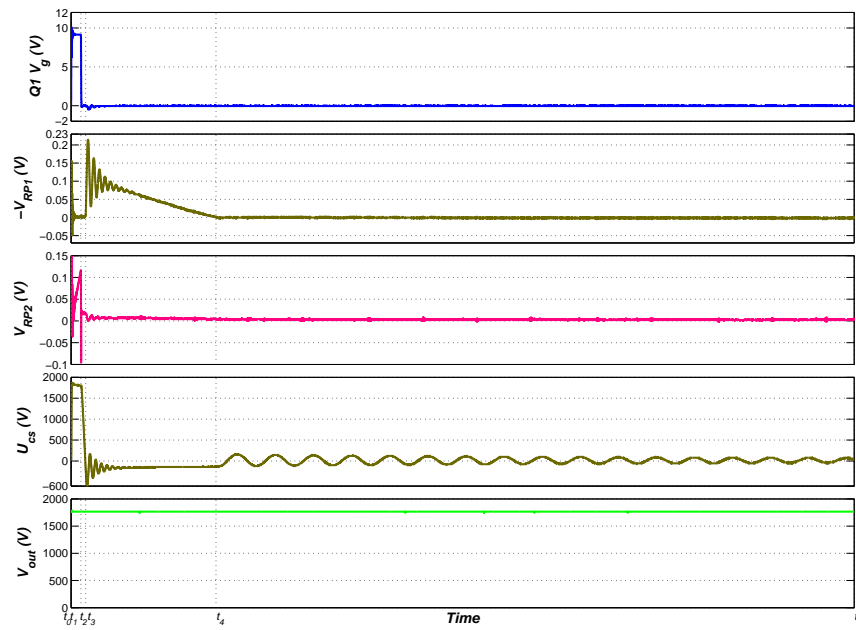
3.3.3 Discharging Mode

The DCM operation mode in the discharging phase leads to 5 intervals in one discharging cycle and are denoted as $[t_0 t_1]$, $[t_1 t_2]$, $[t_2 t_3]$, $[t_3 t_4]$ and $[t_4 t_5]$ respectively. When S_2 is switched on, the secondary side parasitic capacitor C_s is charged first in stage $[t_0 t_1]$. Afterwards, the secondary side magnetization behaviour occurs during

the interval $[t_1 \ t_2]$. In stage $[t_2 \ t_3]$, the behavior is the same as that in the stage $[t_0 \ t_1]$ of the charging mode. The energy stored in the flyback transformer recovers to the primary source in the interval $[t_3 \ t_4]$. The last stage $[t_4 \ t_5]$ corresponds to the discontinuous conduction phase in the discharging mode. By comparing the calculated key waveforms of one cycle in Figure 3.12a and the corresponding measured waveforms in Figure 3.12b, it can be summarized the analytical model of discharging mode can well predict the practical behaviour.



(a) Analytical model based calculated waveforms



(b) Experimental waveforms

Figure 3.12: High voltage operating waveforms of discharging mode.

3.4 Energy Efficiency Investigation

Based on the achieved analytical behavioural model, the efficiency can be analysed in both charge and discharge phases. In the analysis, it is more reasonable to consider the energy efficiency rather than power efficiency, since the converter only supplies the capacitive load. The detailed investigation of the efficiency in the high voltage bidirectional flyback converter can refer to Appendix J.

3.4.1 Charging Efficiency

As mentioned in subsection 3.1.1.2, the charge process of the high voltage converter contains a series of successive switching cycles. For each switching cycle, the input energy to the converter can be achieved by calculating the integral of the input current and voltage in the energy transfer period. Summing up the input energy for all the switching cycles involved in the charge phase can achieve the total input energy E_{in} . The final energy stored in the actuator is denoted as E_{stored} , thus the charging efficiency can be expressed as

$$\eta_{charging} = \frac{E_{stored}}{E_{in}} \quad (3.21)$$

The calculated efficiencies are compared to the measured ones in Figure 3.13a, which indicates the validity of the efficiency calculation model for charge phase.

3.4.2 Discharging Efficiency

Likewise, the recovered energy in each cycle can be obtained through the integral of the primary recovered current and input voltage in the energy recovery period. The total recovery energy and the stored energy can determine the discharging efficiency. The match between the calculated and measured efficiency curves in Figure 3.13b verifies the discharging efficiency calculation model.

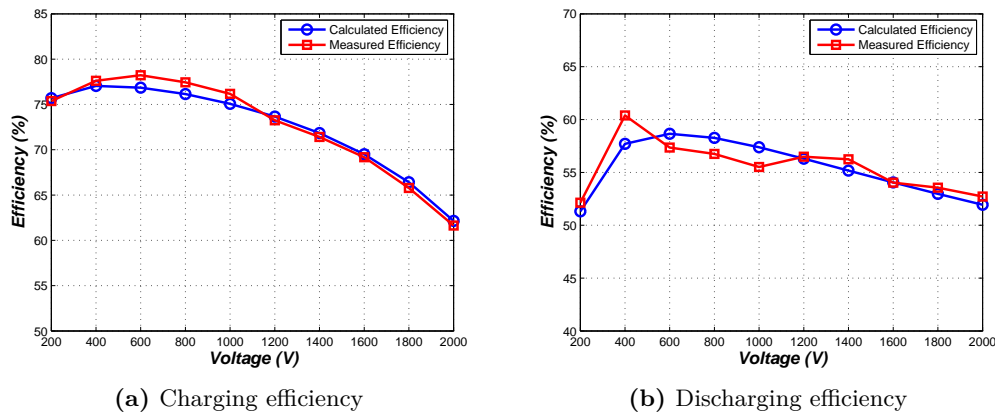


Figure 3.13: Efficiency of bidirectional high voltage flyback converter for capacitive actuator.

3.4.3 Loss Distribution

In the charge phase, the elements which contribute to the losses include the primary winding, primary leakage inductor, S_1 , primary current sensing resistor RP_1 , secondary winding, secondary leakage inductor, freewheeling diode D_{22} and secondary current sensing resistor RP_3 and core. The loss distribution corresponding to these elements for charge phase is shown in Figure 3.14a. Obviously, the losses in the primary side and magnetic core dominates the total energy consumption.

Similarly, the loss elements in discharge phases are secondary winding, secondary leakage inductor, S_2 , high voltage diode D_{21} , secondary current sensing resistor RP_2 , primary current sensing resistor RP_1 , primary winding, body diode of S_1 and core. The discharge phase loss distribution is illustrated in Figure 3.14b. It can be observed that the losses are mainly distributed in the primary side and the magnetic core.

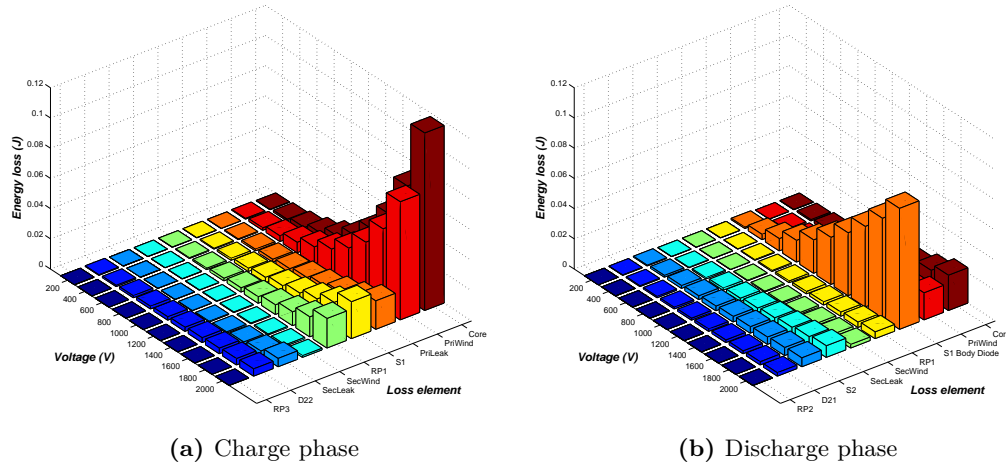


Figure 3.14: Loss distribution of bidirectional high voltage flyback converter for capacitive actuator.

3.5 Summary

The high voltage flyback converter with unidirectional or bidirectional energy flow functionality for capacitive load has been investigated in terms of working principle, transformer design and practical implementation. The PPSSFC topology with the possibility of achieving low volume and high layout flexibility has been proposed. The switching cycle based analytical behavioural model has been established for both charge and discharge mode in the bidirectional flyback converter. Moreover, the energy efficiency calculation model has been verified through the comparison with the measured efficiency. Finally, the loss distribution for both charge and discharge phase are achieved.

DEAP Actuator Driving System

High voltage converters are mainly responsible for boosting the low input voltage from the battery to the high voltage required by the DEAP actuator. In order to achieve the normal operation of the entire high voltage driving system, the system level control scheme needs to be investigated. When the driving system is ready, the high voltage driver, DEAP actuator and radiator heating valve can be connected electrically or mechanically in order to be integrated into a small heating system for testing purposes. Thus the functionality of the high voltage driving system can be validated in the practical heating system. Moreover, the energy consumption analysis can be carried out based on the operating efficiency of the power stage and energy loss of the control stage and auxiliary power supplies. The detailed contents discussed in this chapter can refer to Appendix K, L and M.

4.1 System Level Control Scheme

One critical objective of the heating system is to provide a comfortable temperature in the dwelling space. In the DEAP actuator and radiator heating valve involved heating system, the temperature regulation in the living space can be achieved by the indirect or direct temperature control, which are proposed by Danfoss A/S Heating Solutions and have already been introduced in subsection 2.3.3.

Taking the relationship between the applied voltage and the stroke of the DEAP actuator and the temperature estimation model based on the actuator motion and the hot water flow rate into account, the indirect temperature control can be realized through regulating the output voltage of the high voltage converter for the capacitive actuator. The reverse application of the temperature estimation model can help to determine the reference voltage for the driving system. The output voltage of the high voltage converter then needs to be controlled to follow the reference voltage to achieve the temperature control, which will be discussed in subsection 4.1.1.

The direct temperature control, to some extent, can release the pressure of the high

voltage closed loop control of the driver. In this control methodology, the radiator heating valve is controlled to be fully open or closed. The hot water volume into the radiator which is related to the temperature change can be controlled by the time of opening and closing the valve. Correspondingly, following the high level control signals from the temperature feedback loop, the high voltage converter needs to charge the load to the maximum voltage in order to ensure the fully open status of the valve or to fully discharge the actuator to achieve the blocking of hot water in the pipe. This type of burst mode control will be presented in subsection 4.1.2.

Analog control normally features high dynamic response range and robustness and tends to be particularly applicable for the current loop control involved in the high voltage converter. In comparison, for system level control, digital controller with high flexibility and easy implementation is a desired solution [78], [79], [80]. In this section, both the output voltage control and burst mode control will be designed and implemented digitally.

4.1.1 Voltage Tracking Control

In the indirect temperature control, in order to ensure the output voltage continuously follows the reference signal, the tracking control strategy can be applied with the help of the high voltage measurement circuit which has been addressed in subsection 2.3.3 and the tracking algorithm which can be achieved in a digital controller.

The capacitive property of the actuator makes the voltage hysteresis control more applicable rather than the voltage regulation control which are normally employed in the converter powering the resistive load [35]. When selecting the hysteresis band, the trade-off between the voltage accuracy and status switching frequency needs to be taken into account to achieve a feasible output voltage range.

The voltage tracking control scheme can easily be implemented with a small size and low cost microcontroller [81]. Similar to most of control programs, the first step is to initialize the parameters and registers which will be used in the program. A certain amount of time delay needs to be applied in some cases to ensure the completion of the start up for the specific circuits. In the bidirectional converter case, this time delay tends to be necessary to guarantee the fully charge of the super capacitor in the primary side. Afterwards, the reference voltage and the measured output voltage need to be acquired through the internal ADC involved in the microcontroller. After obtaining the sampling data, a hysteresis band based on reference voltage can be achieved. If the output voltage is within this range, the high voltage converter does not need to work. If the output voltage is lower than the minimum reference signal, the energy transfer function needs to be enabled to charge the capacitive load. Otherwise, it is necessary to enable the energy recovery function in the bidirectional converter or discharge circuits in the unidirectional converter to discharge the capacitive actuator. The flow chart of the voltage tracking control methodology to achieve the hysteresis control is illustrated in Figure 4.1. In this control strategy, although the charge and discharge control ICs do not need to work all the time, the auxiliary power supplies and the high voltage measurement circuit always need to stay in the working condition, which is not beneficial in saving energy in this battery powered case.

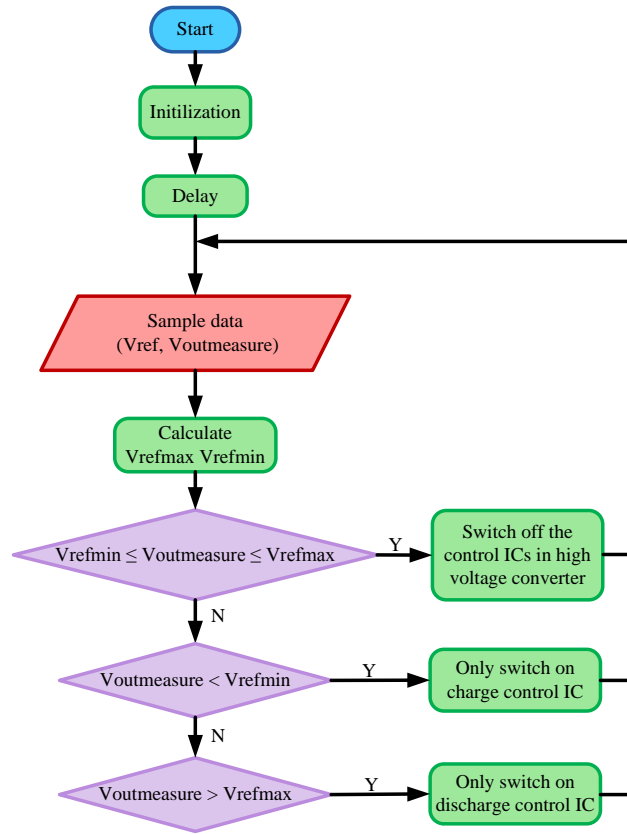


Figure 4.1: Flow chart of the voltage tracking control.

In order to verify the voltage tracking control scheme in the high voltage driver, the experiments has been carried out with the external reference signal. The experimental waveform shown in Figure 4.2 indicates that, although the tracing accuracy declines as the output voltage increases, on the whole, the output voltage of the converter can well follow the reference signal within the allowed range of accuracy. In addition, the comparison between the measured and the practical output voltage can prove that the good performance is achieved for the high voltage measurement circuit.

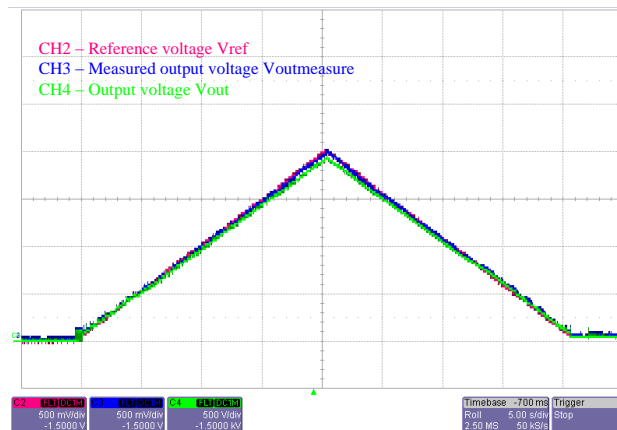


Figure 4.2: Experimental verification of voltage tracking control scheme.

4.1.2 Burst Mode Control

As stated before, the output voltage of the converter only switches between the maximum value and zero in the direct temperature control strategy. In fact, from the perspective of high voltage converter for capacitive load charging application, the output voltage is directly dependent on the charging time. Therefore, by adjusting the working time of the charge control IC, the output voltage can be controlled [82]. The same concept is applicable to the discharging process of the bidirectional converter. The high voltage resistors are used to dissipate the energy of the actuator in the unidirectional case. The time to fully discharge the load $T_{discharge}$ depends on the capacitance of the actuator C_L and the resistance value of the high voltage resistors R_{HV} and can be expressed as

$$T_{discharge} > 3 \cdot R_{HV} \cdot C_L \quad (4.1)$$

The outcome of the temperature feedback control is the trigger signals to enable the fully charge or discharge of the actuator. The microcontroller tends to be a desired tool to capture the trigger signals and to control the working time of charge and discharge ICs or the discharging circuits in the unidirectional converter. After capturing the trigger signal for charge, the control program jumps to the corresponding interrupt service routine, the auxiliary power supplies is switched on to work first. Afterwards, the charge control IC is enabled for a period of time to achieve the fully charge for the actuator. Then all the ICs need to be shut down and the microcontroller returns to the sleep mode to save energy. The similar process is used to achieve the fully discharge of the actuator. The flow chart of this type of burst mode control is illustrated in Figure 4.3. The absence of the high voltage measurement circuit in this control scheme makes it a more desired solution when energy consumption is with highest priority.

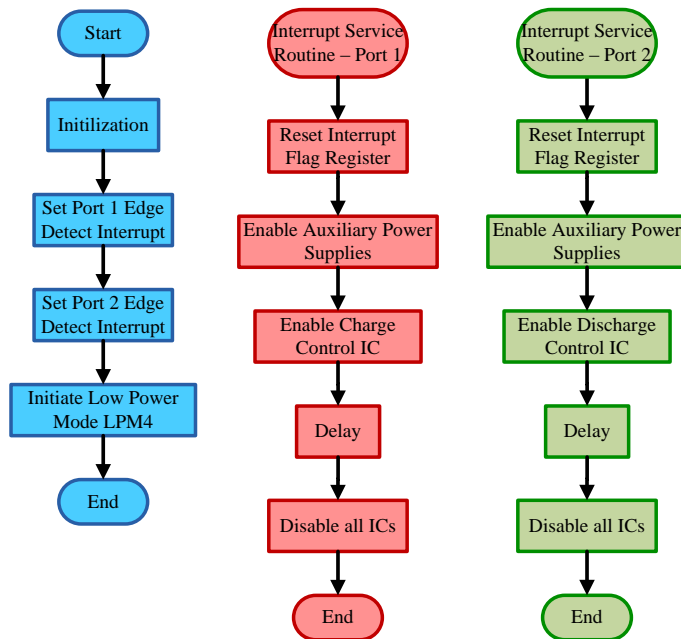


Figure 4.3: Flow chart of the burst mode control.

4.2 System Level Integration

In order to conduct the system level test, the high voltage driver, DEAP actuator and radiator heating valve need to be integrated. Figure 2.11 indicates that the DEAP actuator is mechanically coupled to the heating valve and the high voltage converter is electrically connected to the actuator, which will be addressed in the subsection 4.2.1 and 4.2.2, respectively.

4.2.1 Mechanical Coupling

The integration of the DEAP actuator and the heating valve is depicted in Figure 4.4. When fixing the actuator on a heating valve, the center rod of the actuator tends to press against the valve pin. The counterforce from the spring of the valve is capable of stretching the actuator, thus leading to the initial downward force of the DEAP actuator to close the valve. After applying a high voltage over the actuator, the electrostatic force generated by the actuator tends to counteract the initial force, hence resulting in the opening of the valve.

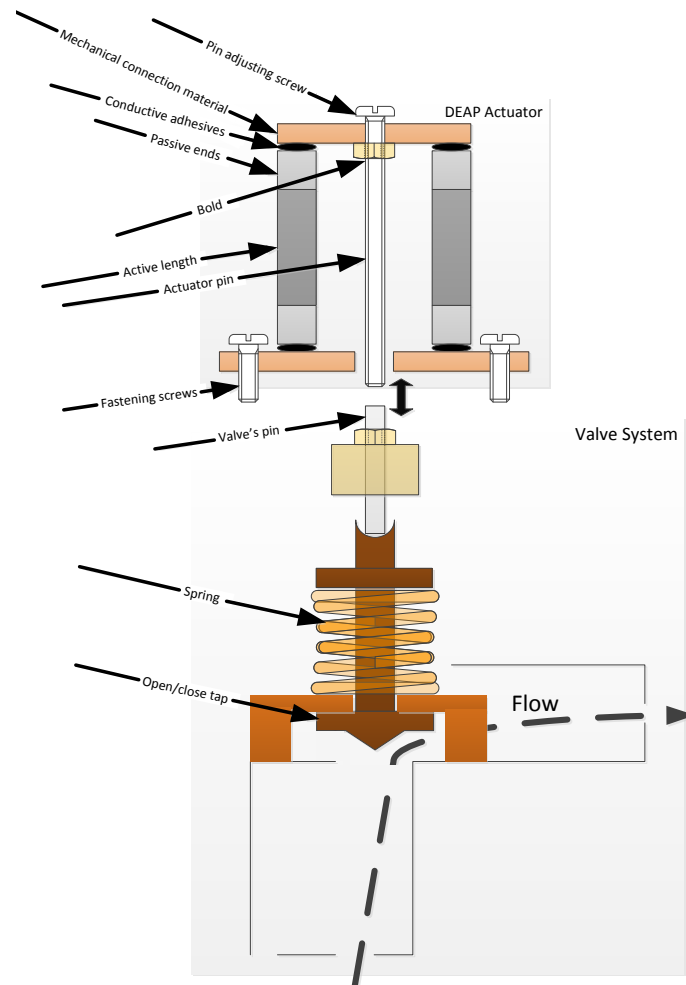


Figure 4.4: The mechanical coupling between the DEAP actuator and the heating valve.

4.2.2 Electrical Connection

After integrating the DEAP actuator to the heating valve in the practical heating system for testing purposes, the high voltage driver can be easily connected to the actuator through high voltage wires, which is shown in Figure 4.5.

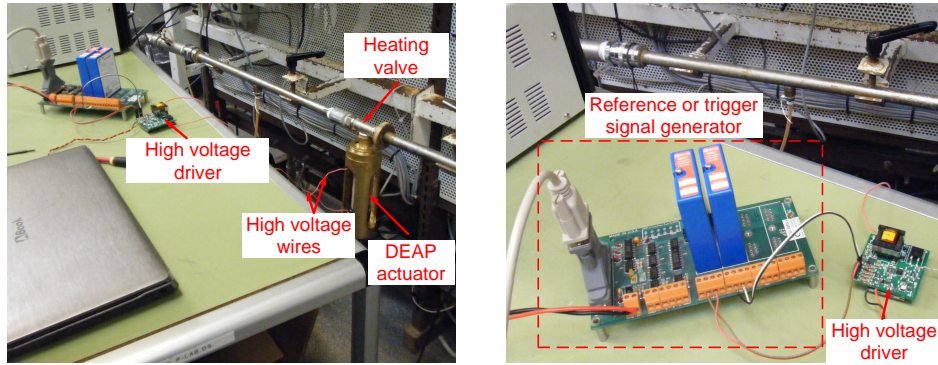


Figure 4.5: The pictures of heating valve, DEAP actuator and high voltage driver integrated in the testing heating system.

4.3 System Level Test

4.3.1 Functionality Verification

The bidirectional high voltage driving system with the voltage tracking control is selected to be one solution to drive the DEAP actuator in the testing heating system. The experiments have been performed to verify the functionality of the high voltage driver and the entire testing system. The experimental data were collected to achieve the curve of the applied voltage over the actuator versus the water flow rate in the pipe, which is shown in Figure 4.6 and can validate the performance of the whole system.

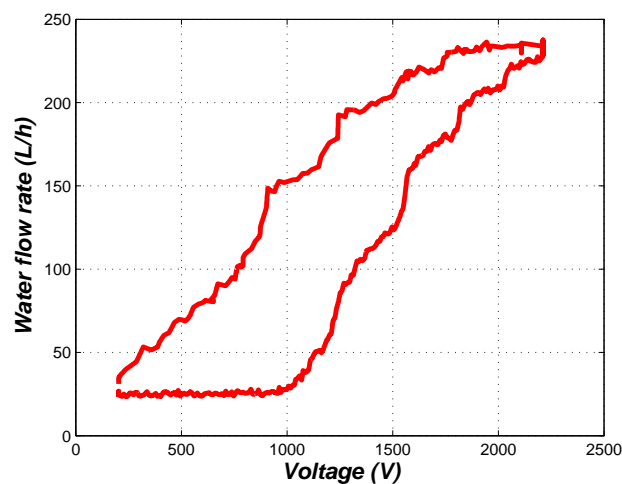


Figure 4.6: Experimental curve between the voltage and water flow rate.

Obviously, the entire system exhibit hysteresis characteristic, which is primarily due to the intrinsic property of the valve. To some extent, the DEAP actuator also contributes to the phenomenon of the hysteresis.

4.3.2 Energy Consumption Analysis

The high voltage driver with PPSSFC and burst mode control is a desired solution in the situation with limited space. In order to evaluate the energy consumption for each charging and discharging phase, the operating efficiency of the power stage as well as the working time of control ICs and auxiliary power supplies need to be measured. After processing the measurement based data, corresponding to different output voltages, the energy losses per charging and discharging phase can be achieved, which are shown in Figure 4.7. Obviously, with the increase of the output voltage, the energy consumption tends to rise rapidly. One reason for explaining this phenomenon tends to be the parasitic capacitance of the high voltage flyback transformer. Figure 4.7 also indicates that, compared to the energy loss involved in the power stage, the consumption from the control circuits and auxiliary power supplies can be neglected. In general, if the yearly times of fully charging and discharging the actuator can be estimated, the battery life can roughly be calculated.

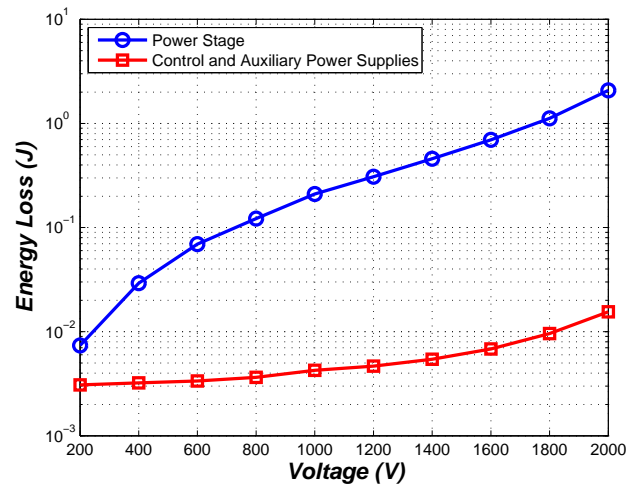


Figure 4.7: Energy loss of high voltage driver based on PPSSFC and burst mode control.

4.4 Summary

Corresponding to the direct and indirect temperature control, two types of control scheme involved in the high voltage driving system have been proposed, i.e. the voltage tracking control and the burst mode control. The system level integration based on the high voltage driver, DEAP actuator and the radiator heating valve has been carried out. The experiments have been performed in the practical testing heating system in order to verify the functionality of the driver as well as the system and to measure the efficiency for analysing the energy consumption.

Conclusion and Future Works

5.1 Conclusion

This work addresses the battery powered high voltage driver solution for DEAP actuator and radiator heating valve in the modern heating system.

This thesis first describes the motivation and background of the research work. As a new type of smart material, DEAP has been researched and developed by Danfoss Polypower A/S for years. In addition to improving the material performance and developing DEAP based various mechanical configurations, the researchers involved in this field also need to figure out the potential application situations in order to penetrate the existing markets and to explore new ones with the technology. This research is based on the possibility of replacing the conventional self-actuating or step-motor actuators in the radiator thermostat with DEAP material based actuator in order to achieve noise free operation and accurate as well as remote temperature control in the dwelling space.

Before investigating the potential high voltage driver solutions for DEAP actuator, the efficient and energy saving modern heating system with radiator heating valves and thermostats has been addressed. The DEAP material has been presented in terms of structure, working principle and potential application fields. To better understand the material, the investigation of its capacitive versus frequency property as well as the capacitive characteristic under high voltage operation has been carried out. The configuration of the high voltage driving system for the capacitive DEAP actuator gives an overview of the research objects. Two types of feasible solutions of high voltage converter has been compared in terms of size, cost and other evaluation criteria. In the heating valve application, the comparison indicates that the high voltage flyback topology based solution tends to be more applicable rather than the piezoelectric transformer based converter and has been selected to be the primary research subject. Moreover, the system level control schemes which corresponds to the direct and indirect temperature control in the heating system are discussed. The power source for the high voltage driver and the auxiliary power supplies solution are briefly introduced.

The major parts of this thesis and the associated publications correspond to the following contributions.

- The fundamental operating principle and the feasible current control schemes of the unidirectional high voltage flyback topology featuring high step-up ratio and powering the pure capacitive load are analysed. Based on the theoretical analysis, a 3 V battery powered high output voltage flyback converter with 667 step-up ratio for charging the DEAP actuator is achieved.
- To reduce the volume of the conventional high voltage flyback converter as well as to increase the flexibility in the transformer layout, a multiple flyback transformers based PPSSFC topology is proposed. In this configuration, the primary windings of the transformers are connected in parallel to enhance the energy storage ability in each switching cycle. The secondary windings are in series connection to achieve lower parasitic capacitance. A low volume commercial flyback transformers based unidirectional PPSSFC with 667 step-up ratio is achieved for capacitive load charging application.
- The high voltage flyback topology with bidirectional energy flow functionality is investigated in terms of practical configuration and basic working principle. Moreover, the design guidelines of the high voltage flyback transformer are proposed for the capacitive load charging and energy recovery application. The theoretical analysis and the design guidelines lead to the achievement of an bidirectional high voltage converter with 70% charging efficiency and 50% discharging efficiency under 2 kV operation.
- The operating principle of the converter for capacitive load is different from that of the steady-state operation converter. To achieve the thorough understanding of the operating mechanism, the analytical modelling for switching cycles is needed to be carried out. As a critical loss, especially in the high voltage operation, the core loss is needed to be taken into account to achieve the more accurate model. The proposed models for both charging and discharge mode are verified through the comparison to the measured results.
- Based on the proposed analytical model, the efficiency for charging and discharging phases are achieved. All the potential losses are considered in the efficiency analysis, including the winding losses, leakage inductance, core loss, etc. The comparison between the calculated efficiencies and the measured ones validate the analytical model of efficiency calculation.
- In the system level, the voltage tracking control as well as the burst mode control are proposed to achieve the indirect or direct temperature control in the heating system. Burst mode control tends to be a desired solution in a battery powered system due to its superior performance in terms of energy saving. If 2.5 Ah batteries are employed, the high voltage driving system with bidirectional converter can run for around 2.1 years.
- The implemented DEAP actuator and the radiator heating valve are integrated to a heating system for testing purposes. The high voltage driver

are electrically connected to the actuator and the system level test has been carried out to verify the functionality as well as the energy consumption.

5.2 Future Work

The research conducted in this work investigates the flyback topology based high voltage driver for DEAP actuator in heating valve application. In order to achieve more efficient driver with small volume and low cost, further investigations can focus on the following subjects:

- The parasitic capacitance of the secondary winding not only affects the charging ability and efficiency in the charging phase, but also can induce an inrush current to fail the control IC, thus reducing the reliability in the discharging phase. In order to achieve more efficient energy transfer in each switching cycle, the low leakage inductance is also desired. However, normally, these two parameters are contradictory. The optimal design approach is expected to achieve the optimum trade-off between the parasitic capacitance and the leakage inductance.
- Normally, efficiency, volume and cost are contradictory requirements for transformers. It is difficult to achieve the highest efficiency with lowest volume and cost. The trade-off analysis of transformer is worthy to be investigated to achieve the optimal design guidelines.
- The power stage can be optimized to achieve a relative small size with satisfactory efficiency. To further reduce the volume of the high voltage driver, it is reasonable to propose an IC to integrate the functions of the current discrete PWM controller in the high voltage converter, the auxiliary power supplies and the microcontroller which is responsible for the system level control.

Bibliography

- [1] Y. Bar-Cohen, *Electroactive polymer (EAP) actuators as artificial muscles : reality, potential, and challenges*. SPIE Press, 2004.
- [2] D. De Rossi, R. Pelrine, F. Carpi, and R. Kornbluh, *Dielectric elastomers as electromechanical transducers*. Elsevier Science, 2008.
- [3] M. Tryson, H.-E. Kiil, and M. Benslimane, “Powerful tubular core free dielectric electro activate polymer (DEAP) push actuator,” in *Proceedings of SPIE*, vol. 7287, pp. 72871F–1 – 72871F–11, March 2009.
- [4] M. Y. Benslimane, H.-E. Kiil, and M. J. Tryson, “Dielectric electro-active polymer push actuators: performance and challenges,” *Polymer International*, vol. 59, no. 3, pp. 415–421, 2010.
- [5] M. J. Tryson, R. Sarban, and K. P. Lorenzen, “The dynamic properties of tubular DEAP actuators,” in *Proceedings of SPIE*, vol. 7642, pp. 76420O–1–76420O–10, March 2010.
- [6] P. Brochu and Q. Pei, “Advances in dielectric elastomers for actuators and artificial muscles,” *Macromolecular Rapid Communications*, vol. 31, no. 1, pp. 10–36, 2010.
- [7] Danfoss A/S Heating Solutions, “Energy saving solutions for renovation of heating and cooling systems.” http://heating.danfoss.com/PCMPDF/VZA6E302_Sep2014Lowres.pdf, September 2014.
- [8] “Heat exchanger.” http://en.wikipedia.org/wiki/Heat_exchanger, October 2014.
- [9] “Radiator.” <http://en.wikipedia.org/wiki/Radiator>, October 2014.
- [10] Danfoss A/S Heating Solutions, “Radiator valves.” <http://www.danfoss.com/Products/Categories/Group/HE/Radiator-Thermostats/Radiator-Valves/20c1f5e4-1043-4848-be0e-fc36f7fd8136.html>, October 2014.
- [11] Danfoss A/S Heating Solutions, “Radiator thermostats.” <http://www.danfoss.com/Products/Categories/Group/HE/Radiator-Thermostats/Radiator-Sensors/31992cd7-0eab-48d2-a1b5-d2fb06219e6d.html>, October 2014.

- [12] “Valve.” <http://en.wikipedia.org/wiki/Valve>, October 2014.
- [13] Y. Bar-Cohen, “Electroactive polymers as artificial muscles - reality and challenges,” *Collection of Technical Papers - AIAA/ASME/ASCE/AHS/ASC Structures, Structural Dynamics and Materials Conference*, vol. 4, pp. 2313–2321, 2001.
- [14] M. Andriot, S. Chao, A. Colas, S. Cray, F. deBuyl, J. DeGroot, A. Dupont, T. Easton, J. Garaud, E. Gerlach, *et al.*, “Silicones in industrial applications,” *Silicon-Based Inorganic Polymers*, vol. 84, pp. 1–106, 2009.
- [15] R. Jones, P. Wang, B. Lassen, and R. Sarban, “Dielectric elastomers and compliant metal electrode technology,” in *MELECON 2010 - 2010 15th IEEE Mediterranean Electrotechnical Conference*, pp. 368–373, April 2010.
- [16] M. Benslimane, H.-E. Kiil, and M. J. Tryson, “Electromechanical properties of novel large strain polypower film and laminate components for deap actuator and sensor applications,” in *Proceedings of SPIE*, vol. 7642, pp. 764231–1 – 764231–11, March 2010.
- [17] “Types of capacitor.” http://en.wikipedia.org/wiki/Types_of_capacitor, October 2014.
- [18] Y. Iskandarani and H. Karimi, “Pressure sensor development based on dielectric electro active polymers,” in *Industrial Electronics and Applications (ICIEA), 2012 7th IEEE Conference on*, pp. 530–535, July 2012.
- [19] Y. Iskandarani and H. Karimi, “Sensing capabilities based on dielectric electro active polymers-feasibility and potential state-of-the-art application,” *Sensors Journal, IEEE*, vol. 12, pp. 2616–2624, Aug 2012.
- [20] S. Seelecke and A. York, “Towards self-sensing of deap actuators: Capacitive sensing experimental analysis,” *ASME 2010 Conference on Smart Materials, Adaptive Structures and Intelligent Systems, SMASIS 2010*, vol. 1, pp. 307–314, 2010.
- [21] R. Pelrine, R. D. Kornbluh, J. Eckerle, P. Jeuck, S. Oh, Q. Pei, and S. Stanford, “Dielectric elastomers: generator mode fundamentals and applications,” in *Proceedings of SPIE*, vol. 4329, pp. 148–156, 2001.
- [22] E. Dimopoulos, I. Trintis, and S. Munk-Nielsen, “Energy harvesting cycles of dielectric electro active polymer generators,” in *IECON 2012 - 38th Annual Conference on IEEE Industrial Electronics Society*, pp. 374–381, Oct 2012.
- [23] E. Dimopoulos, I. Trintis, and S. Munk-Nielsen, “Comparison of the dielectric electroactive polymer generator energy harvesting cycles,” in *Proceedings of SPIE*, pp. 868700–1 – 868700–13, March 2013.
- [24] R. Sarban, B. Lassen, and M. Willatzen, “Dynamic electromechanical modeling of dielectric elastomer actuators with metallic electrodes,” *Mechatronics, IEEE/ASME Transactions on*, vol. 17, pp. 960 –967, October 2012.

-
- [25] “Wireless golf training sensor.” <http://www.polypower.com/products/sensors/cases+collection/Wireless+golf+training+sensor.htm>, October 2014.
 - [26] “DEAP generator.” <http://www.polypower.com/products/Generators/>, October 2014.
 - [27] O. Gomis-Bellmunt, D. Montesinos-Miracle, S. Galceran-Arellano, and A. Sudria-Andreu, “A buck-boost bidirectional converter to drive piezoelectric actuators,” in *Power Electronics and Applications, 2007 European Conference on*, pp. 1–7, Sept 2007.
 - [28] E. Horsley, M. Foster, and D. Stone, “State-of-the-art piezoelectric transformer technology,” in *Power Electronics and Applications, 2007 European Conference on*, pp. 1–10, Sept 2007.
 - [29] C.-Y. Lin, *Design and analysis of piezoelectric transformer converters*. PhD thesis, Virginia Polytechnic Institute and State University, 1997.
 - [30] M. S. R. dgaard, *Piezoelectric transformer based power converters; design and control*. PhD thesis, Technical University of Denmark, Department of Electrical Engineering, 2012.
 - [31] E. Horsley, A. Carazo, M. Foster, and D. Stone, “A lumped equivalent circuit model for the radial mode piezoelectric transformer,” in *Applied Power Electronics Conference and Exposition, 2009. APEC 2009. Twenty-Fourth Annual IEEE*, pp. 1747–1753, Feb 2009.
 - [32] Y. Liu, D. Vasic, F. Costa, and D. Schwander, “Improvement of burst-mode controlled piezoelectric transformers,” in *Power Electronics and Motion Control Conference (EPE/PEMC), 2012 15th International*, pp. DS2c.7–1–DS2c.7–6, September 2012.
 - [33] M. S. Rø dgaard, T. Andersen, K. S. Meyer, and M. A. E. Andersen, “Design of interleaved multi layer rosen type piezoelectric transformer for high voltage dc/dc applications,” in *Power Electronics, Machines and Drives (PEMD 2012), 6th IET International Conference on*, pp. 1 –6, March 2012.
 - [34] E. Baker, W. Huang, D. Chen, and F. Lee, “Radial mode piezoelectric transformer design for fluorescent lamp ballast applications,” *Power Electronics, IEEE Transactions on*, vol. 20, pp. 1213–1220, Sept 2005.
 - [35] T. Andersen, M. S. Rø dgaard, O. C. Thomsen, and M. A. E. Andersen, “Low voltage driven dielectric electro active polymer actuator with integrated piezoelectric transformer based driver,” in *Proceedings of SPIE*, pp. 79762N–1 – 79762N–12, March 2011.
 - [36] T. Andersen, *Piezoelectric transformer based power supply for dielectric electro active polymers*. PhD thesis, Technical University of Denmark, Department of Electrical Engineering, 2012.
 - [37] E. Horsley, N. Nguyen-Quang, M. Foster, and D. Stone, “Achieving zvs in inductor-less half-bridge piezoelectric transformer based resonant converters,”

- in *Power Electronics and Drive Systems, 2009. PEDS 2009. International Conference on*, pp. 446–451, Nov 2009.
- [38] K. S. Meyer, M. S. Rø dgaard, M. A. E. Andersen, and T. Andersen, “Piezo-electric power converter with bi-directional power transfer,” 2014. Patent WO2013083679.
 - [39] M. S. Rø dgaard, M. A. E. Andersen, and K. S. Meyer, “Self-oscillating loop based piezoelectric power converter,” 2013. Patent WO2013083678 A3.
 - [40] A. Abramovitz, C.-S. Liao, and K. Smedley, “State-plane analysis of regenerative snubber for flyback converters,” *Power Electronics, IEEE Transactions on*, vol. 28, pp. 5323–5332, Nov 2013.
 - [41] J.-H. Jung and S. Ahmed, “Flyback converter with novel active clamp control and secondary side post regulator for low standby power consumption under high-efficiency operation,” *Power Electronics, IET*, vol. 4, pp. 1058–1067, November 2011.
 - [42] P. Davari, F. Zare, A. Ghosh, and H. Akiyama, “High-voltage modular power supply using parallel and series configurations of flyback converter for pulsed power applications,” *Plasma Science, IEEE Transactions on*, vol. 40, pp. 2578–2587, Oct 2012.
 - [43] A. Rahimi, F. Rahimi, and I. Hassanzadeh, “Analysis of high-voltage flyback converter in color tvs, and its regulation,” in *Power Electronics and Drive Systems, 2003. PEDS 2003. The Fifth International Conference on*, vol. 1, pp. 353–358 Vol.1, Nov 2003.
 - [44] R. Erickson and D. Maksimovic, *Fundamentals of Power Electronics*. Power electronics, Springer, 2001.
 - [45] G. Chen, Y.-S. Lee, S. Hui, D. Xu, and Y. Wang, “Actively clamped bidirectional flyback converter,” *Industrial Electronics, IEEE Transactions on*, vol. 47, pp. 770–779, Aug 2000.
 - [46] J. Park, Y.-S. Roh, Y.-J. Moon, and C. Yoo, “A ccm/dcm dual-mode synchronous rectification controller for a high-efficiency flyback converter,” *Power Electronics, IEEE Transactions on*, vol. 29, pp. 768–774, Feb 2014.
 - [47] H.-H. Chung, W.-L. Cheung, and K. Tang, “A zcs bidirectional flyback dc/dc converter,” *Power Electronics, IEEE Transactions on*, vol. 19, pp. 1426–1434, Nov 2004.
 - [48] L. Eitzen, C. Graf, and J. Maas, “Cascaded bidirectional flyback converter driving deap transducers,” in *IECON 2011 - 37th Annual Conference on IEEE Industrial Electronics Society*, pp. 1226–1231, Nov 2011.
 - [49] P. Thummala, Z. Zhang, and M. Andersen, “High voltage bi-directional fly-back converter for capacitive actuator,” in *Power Electronics and Applications (EPE), 2013 15th European Conference on*, pp. 1–10, Sept 2013.

-
- [50] P. Thummala, Z. Zhang, M. Andersen, and S. Rahimullah, "Dielectric electro active polymer incremental actuator driven by multiple high-voltage bi-directional dc-dc converters," in *Energy Conversion Congress and Exposition (ECCE), 2013 IEEE*, pp. 3837–3844, Sept 2013.
- [51] E. Wells, *Comparing magnetic and piezoelectric transformer approaches in CCFL applications*. Analog Applications Journal, Texas Instruments Incorporated, 2009.
- [52] A. Flynn and S. Sanders, "Fundamental limits on energy transfer and circuit considerations for piezoelectric transformers," *Power Electronics, IEEE Transactions on*, vol. 17, pp. 8–14, Jan 2002.
- [53] C.-H. Lin, Y. Lu, H.-J. Chiu, and C.-L. Ou, "Eliminating the temperature effect of piezoelectric transformer in backlight electronic ballast by applying the digital phase-locked-loop technique," *Industrial Electronics, IEEE Transactions on*, vol. 54, pp. 1024–1031, April 2007.
- [54] T. Kim, S. Choi, S. Lee, and B. Cho, "New piezoelectric transformer adapter with universal input voltage range," in *Power Electronics and Drives Systems, 2005. PEDS 2005. International Conference on*, vol. 2, pp. 1223–1227, Nov 2005.
- [55] S. Hamamura, T. Zaitzu, T. Ninomiya, and M. Shoyama, "Noise characteristics of piezoelectric-transformer dc-dc converter," in *Power Electronics Specialists Conference, 1998. PESC 98 Record. 29th Annual IEEE*, vol. 2, pp. 1262–1267 vol.2, May 1998.
- [56] T. Andersen, M. Andersen, O. Thomsen, M. Foster, and D. Stone, "Nonlinear effects in piezoelectric transformers explained by thermal-electric model based on a hypothesis of self-heating," in *IECON 2012 - 38th Annual Conference on IEEE Industrial Electronics Society*, pp. 596–601, Oct 2012.
- [57] D. Vasic, Y.-P. Liu, F. Costa, and D. Schwander, "Piezoelectric transformer-based dc/dc converter with improved burst-mode control," in *Energy Conversion Congress and Exposition (ECCE), 2013 IEEE*, pp. 140–146, Sept 2013.
- [58] Y. Liu, D. Vasic, F. Costa, and D. Schwander, "Improvement of burst-mode controlled piezoelectric transformers," in *Power Electronics and Motion Control Conference (EPE/PEMC), 2012 15th International*, pp. DS2c.7–1–DS2c.7–6, Sept 2012.
- [59] S. Yun, J. Sim, J. Park, S. Choi, and B. H. Cho, "Adaptive phase control method for load variation of resonant converter with piezoelectric transformer," in *Power Electronics and Drive Systems, 2007. PEDS '07. 7th International Conference on*, pp. 164–168, Nov 2007.
- [60] J. Alonso, C. Ordiz, and M. Dalla Costa, "A novel control method for piezoelectric-transformer based power supplies assuring zero-voltage-switching operation," *Industrial Electronics, IEEE Transactions on*, vol. 55, pp. 1085–1089, March 2008.

- [61] J. Martin, M. Prieto, F. Nuno, and J. Diaz, "A new full-protected control mode to drive piezoelectric transformers in dc-dc converters," in *Power Electronics Specialists Conference, 2001. PESC. 2001 IEEE 32nd Annual*, vol. 1, pp. 378–383 vol. 1, 2001.
- [62] "Temperature sensors." http://en.wikipedia.org/wiki/List_of_temperature_sensors, October 2014.
- [63] R. Sarban, R. W. Jones, B. R. Mace, and E. Rustighi, "A tubular dielectric elastomer actuator: Fabrication, characterization and active vibration isolation," *MECHANICAL SYSTEMS AND SIGNAL PROCESSING*, vol. 25, no. 8, pp. 2879–2891, 2011.
- [64] Fairchild Semiconductor Corporation, *Design Guidelines for RCD Snubber of Flyback Converters*. Application Note AN-4147, 2006.
- [65] IXYS CORPORATION, *High Voltage Power MOSFETs IXTA02N450HV IXTT02N450HV*, October 2013.
- [66] J. Biela and J. Kolar, "Using transformer parasitics for resonant converters - a review of the calculation of the stray capacitance of transformers," in *Industry Applications Conference, 2005. Fourtieth IAS Annual Meeting. Conference Record of the 2005*, vol. 3, pp. 1868–1875, 2005.
- [67] L. Dalessandro, F. da Silveira Cavalcante, and J. Kolar, "Self-capacitance of high-voltage transformers," *Power Electronics, IEEE Transactions on*, vol. 22, no. 5, pp. 2081–2092, 2007.
- [68] E. Snelling, *Soft ferrites : Properties and applications*. Butterworths, 1988.
- [69] W. Hurley and D. Wilcox, "Calculation of leakage inductance in transformer windings," *Power Electronics, IEEE Transactions on*, vol. 9, pp. 121–126, Jan 1994.
- [70] F. Blache, J.-P. Keradec, and B. Cogitore, "Stray capacitances of two winding transformers: equivalent circuit, measurements, calculation and lowering," in *Industry Applications Society Annual Meeting, 1994., Conference Record of the 1994 IEEE*, pp. 1211–1217 vol.2, Oct 1994.
- [71] A. Massarini and M. Kazimierczuk, "Self-capacitance of inductors," *Power Electronics, IEEE Transactions on*, vol. 12, pp. 671–676, Jul 1997.
- [72] Z. Ouyang, *Advances in Planar and Integrated Magnetics*. PhD thesis, Technical University of Denmark, Department of Electrical Engineering, 2012.
- [73] J. Li, T. Abdallah, and C. Sullivan, "Improved calculation of core loss with non-sinusoidal waveforms," in *Industry Applications Conference, 2001. Thirty-Sixth IAS Annual Meeting. Conference Record of the 2001 IEEE*, vol. 4, pp. 2203–2210 vol.4, Sept 2001.
- [74] K. Venkatachalam, C. Sullivan, T. Abdallah, and H. Tacca, "Accurate prediction of ferrite core loss with nonsinusoidal waveforms using only steinmetz parameters," in *Computers in Power Electronics, 2002. Proceedings. 2002 IEEE Workshop on*, pp. 36–41, June 2002.

-
- [75] J. Muhlethaler, J. Kolar, and A. Ecklebe, "Loss modeling of inductive components employed in power electronic systems," in *Power Electronics and ECCE Asia (ICPE ECCE), 2011 IEEE 8th International Conference on*, pp. 945–952, 2011.
- [76] J. Muhlethaler, J. Biela, J. Kolar, and A. Ecklebe, "Improved core-loss calculation for magnetic components employed in power electronic systems," *Power Electronics, IEEE Transactions on*, vol. 27, no. 2, pp. 964–973, 2012.
- [77] J. Muhlethaler, J. Biela, J. Kolar, and A. Ecklebe, "Core losses under dc bias condition based on steinmetz parameters," in *Power Electronics Conference (IPEC), 2010 International*, pp. 2430–2437, 2010.
- [78] L. Jakobsen, H. Schneider, and M. Andersen, "Comparison of state-of-the-art digital control and analogue control for high bandwidth point of load converters," in *Applied Power Electronics Conference and Exposition, 2008. APEC 2008. Twenty-Third Annual IEEE*, pp. 1440–1445, Feb 2008.
- [79] L. Barreto, M. Sebastiao, L. de Freitas, E. Alves Coelho, V. Farias, and J. Vieira, "Analysis of a soft-switched pfc boost converter using analog and digital control circuits," *Industrial Electronics, IEEE Transactions on*, vol. 52, pp. 221–227, Feb 2005.
- [80] L. Torok and S. Munk-Nielsen, "Efficiency and hardware comparison of analog control-based and digital control-based 70 w two-stage power factor corrector and dc-dc converters," in *Power Electronics and Applications (EPE 2011), Proceedings of the 2011-14th European Conference on*, pp. 1–8, Aug 2011.
- [81] Texas Instruments Incorporated, *Mixed Signal Microcontroller MSP430G2231*, February 2010.
- [82] Linear Technology Corporation, *Capacitor Charger Controller LT3750*, February 2006.

List of Publications

Overview of publications accomplished during this PhD study. The publications are located in Appendix A - M.

- A: **Lina Huang**, Zhe Zhang and Michael A. E. Andersen, “A Review of High Voltage Drive Amplifiers for Capacitive Actuators”, 47th International Universities’ Power Engineering Conference (UPEC 2012), 2012.
- B: Prasanth Thummala, **Lina Huang**, Zhe Zhang and Michael A. E. Andersen, “Analysis of Dielectric Electro Active Polymer Actuator and its High Voltage Driving Circuits”, 2012 IEEE International Power Modulator and High Voltage Conference (IPMHVC 2012), 2012.
- C: **Lina Huang**, Zhe Zhang and Michael A. E. Andersen, “Battery Powered High Output Voltage Bidirectional Flyback Converter for Cylindrical DEAP Actuator”, 2012 IEEE International Power Modulator and High Voltage Conference (IPMHVC 2012), 2012.
- D: Riccardo Pittini, **Lina Huang**, Zhe Zhang and Michael A. E. Andersen, “Primary Parallel Secondary Series Flyback Converter (PPSSFC) with Multiple Transformers for Very High Step-Up Ratio in Capacitive Load Charging Applications”, 2014 IEEE Applied Power Electronics Conference and Exposition (APEC 2014), 2014.
- E: **Lina Huang**, Rahimullah Sarban, Zhe Zhang and Michael A. E. Andersen, “High Voltage Bidirectional Flyback Converter Driving DEAP Actuator for Automotive Applications”, The 9th IEEE Vehicle Power and Propulsion Conference (VPPC 2013), 2013.
- F: Henrik Schneider, Prasanth Thummala, **Lina Huang**, Ziwei Ouyang, Arnold Knott, Zhe Zhang and Michael A. E. Andersen. “Investigation of transformer winding architectures for high voltage capacitor charging applications”, 2014 IEEE Applied Power Electronics Conference and Exposition (APEC 2014), 2014.
- G: **Lina Huang**, Zhe Zhang and Michael A. E. Andersen, “Detailed Behavior Analysis for High Voltage Bidirectional Flyback Converter Driving DEAP

Actuator”, 39th Annual Conference of the IEEE Industrial Electronics Society (IECON 2013), 2013.

- H: **Lina Huang**, Zhe Zhang and Michael A. E. Andersen, “Analytical Switching Cycle Modeling of Bidirectional High Voltage Flyback Converter for Capacitive Load Considering Core Loss Effect”, Submitted to Transactions on Power Electronics, 2014.
- I: Thomas Andersen, **Lina Huang**, Zhe Zhang and Michael A. E. Andersen, ‘Efficiency of Capacitively Loaded Converters”, 38th Annual Conference of the IEEE Industrial Electronics Society (IECON 2012), 2012.
- J: **Lina Huang**, Zhe Zhang and Michael A. E. Andersen, “Energy Efficiency Investigation of Bidirectional High Voltage Flyback Converter for DEAP Actuator”, Submitted to Transactions on Power Electronics, 2014.
- K: **Lina Huang**, Zhe Zhang and Michael A. E. Andersen, “Design and Development of Autonomous High Voltage Driving System for DEAP Actuator in Radiator Thermostat”, 2014 IEEE Applied Power Electronics Conference and Exposition(APEC 2014), 2014.
- L: **Lina Huang**, Riccardo Pittini, Zhe Zhang and Michael A. E. Andersen, “Design Comparison of Autonomous High Voltage Driving System for DEAP Actuator”, 2014 International Power Electronics and Application Conference and Exposition (PEAC 2014), 2014.
- M: **Lina Huang**, Lars. F. Nørmølle, Rahimullah Sarban, Ebbe N. Christiansen, Zhe Zhang and Michael A. E. Andersen, “DEAP actuator and its high voltage driver for heating valve application”, SPIE Smart Structures/NDE on Electroactive Polymer Actuators and Devices (EAPAD) 2014, 2014.

APPENDIX A

A Review of High Voltage Drive Amplifiers for Capacitive Actuators

47th International Universities' Power Engineering Conference (UPEC 2012)

A Review of High Voltage Drive Amplifiers for Capacitive Actuators

Lina Huang

Zhe Zhang

Michael A.E. Andersen

Technical University of Denmark, DTU Elektro,
Oersteds Plads, Building 349, DK-2800 Kgs. Lyngby, Denmark

huang@elektro.dtu.dk

zz@elektro.dtu.dk

ma@elektro.dtu.dk

Abstract—This paper gives an overview of the high voltage amplifiers, which are used to drive capacitive actuators. The amplifiers for both piezoelectric and DEAP (dielectric electro-active polymer) actuator are discussed. The suitable topologies for driving capacitive actuators are illustrated in detail, including linear as well as switched mode amplifiers. In the past much attention has been paid on the driver for piezoelectric actuator. As DEAP is a type of new material, there is not much literature reference for it.

Index Terms—capacitive actuator, DEAP actuator, driver, high voltage, review, linear amplifier, piezoelectric actuator, switched mode amplifier

I. INTRODUCTION

With the emerging of various smart materials, such as piezoelectric ceramic and dielectric electro-active polymer (DEAP), the capacitive actuator has gained increasing attention in both academia and industry. There is no uniform definition for capacitive actuator, in general, if an actuator principally performs the property of capacitor and is actuated by electrostatic forces or electric field, it could be considered as capacitive actuator. Currently, electrostatic, electrostrictive, piezoelectric and DEAP actuators are common types of capacitive actuators.

Compared to traditional electro-magnetic, pneumatic or hydraulic actuator, the capacitive actuators possess many advantages, such as high power density, fast and direct actuation, high actuating precision, extremely low steady-state power consumption, etc. Therefore, capacitive actuators have been widely used in Micro Electro Mechanical Systems (MEMS) or highly precise actuation occasions.

However, one of the difficult issues facing the capacitive actuators is the relative high driving voltage. For example, the stimulating voltage to drive DEAP actuator should reach several thousand volts for the current DEAP material; this potential can be several hundred volts when driving piezoelectric actuator, since multilayer ceramic structure is employed [1]. The situation is much better in electrostatic actuators, which normally need relative low driving voltage for operation [2]. In fact, electrostrictive actuators exhibit similar electromechanical characteristics as piezoelectric actuators in many aspects, but with low hysteresis and narrow operation temperature range, and several papers discuss the amplifiers design for electrostrictive actuators [3-6].

Therefore, in this paper, only high voltage drivers for piezoelectric and DEAP actuators will be considered.

II. HIGH VOLTAGE DRIVE AMPLIFIERS FOR PIEZOELECTRIC ACTUATOR

As a new type of smart material actuator, piezoelectric actuator has attracted extensive concern in recent decades. However, most focus is on the research of new geometries, search of new applied field, development of new actuation scheme, etc. By contrast, the literature related to the drive circuits is few and far between. However, it is still necessary to summarize the available drivers for piezoelectric actuators for the future reference, as they behave like a capacitive load.

A. Linear Amplifiers for Piezoelectric Actuator

In the early development period of drive amplifiers for piezoelectric actuator, the linear amplifiers took the dominant position because they had been readily available and easy to use. The most commonly used implementation for linear amplifier is shown in Fig. 1. In general, class A, class B or class AB linear amplifiers are always employed to drive piezoelectric actuators [7]. An improve class A drive amplifier is proposed in [8], and [9] discusses the linear working optocoupler based linear driver for scanning tunnelling microscope piezoactuators. It is well known that class A amplifiers suffer from severe low efficiency. However, linear power drivers have distinct advantages, e.g. low signal distortion, good static performance, high integration level, simple structure and low electromagnetic interference [10]. Therefore, in some electromagnetic field sensitive applications, relatively high efficient class B amplifiers are adopted [11, 12]. In order to increase the output peak current and power, a paralleled class AB quasi-complementary symmetry power amplifier circuits are described and analyzed in [10].

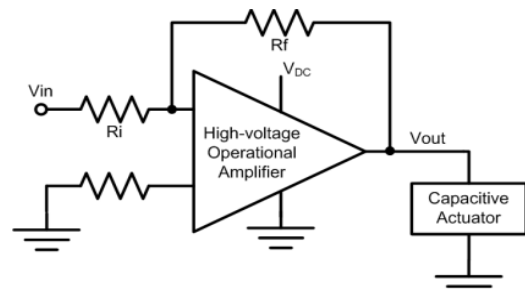


Fig. 1. Schematic diagram of a linear amplifier driving piezoelectric actuator

For a variety of linear driving amplifiers as well as their improved versions, the common issues are high energy dissipation and low efficiency. Reference [13] analyzes the maximum ratio of stored energy to dissipated energy is 50%, which means the highest energy efficiency is only 33%. According to [14-16], the power loss for the driving circuit in Fig. 1 is

$$P_{Dissipate} = 4 \cdot C \cdot V_p^2 \cdot f. \quad (1)$$

where C is capacitance of piezoelectric actuator, V_p is the peak sinusoidal driving voltage and f is its frequency. The example in [14] shows that, if a piezoelectric actuator with $1\mu F$ effective capacitance needs $100V_{p,p}$ $2kHz$ sinusoidal signal to drive, the power dissipation of driving amplifier is $80W$; whereas the maximum effective mechanical work is only $0.6W$.

Owing to the huge power loss of the driver, the bulky heat sink or other auxiliary heat dissipation devices cannot be neglected, which will entirely submerge the advantages of piezoelectric actuations.

B. Switched Mode Amplifiers for Piezoelectric Actuator

For driving piezoelectric actuator, a promising alternative to linear amplifier is the switched mode amplifier, which can easily be achieved in relative high efficiency, small size as well as low weight. In recent years, switching mode drivers has already become the research focus.

1) Switching Mode Driving Stage

A variety of switching mode topologies had been employed to actuate piezoelectric elements, such as buck, half bridge, flyback, buck-boost and converters based on piezoelectric transformers [17].

In fact, piezoelectric actuators only need several hundred volts stimulating voltage, which can easily be achieved through commercial power supplies. Therefore, more focus has been paid on the design of output driving stage, which is responsible for amplifying voltage signal based on the actuation demand. After reading related literatures, it can be concluded that the most common topologies for driving stage are bidirectional buck [16, 18-27] and full bridge [28-33], shown in Fig. 2 and Fig. 3, respectively.

For bidirectional buck converter, when S_1 is on, piezoelectric actuator is charged through inductor L and L is also magnetized in this period to accumulate magnetic energy. Then S_1 is off, the stored energy in L will be

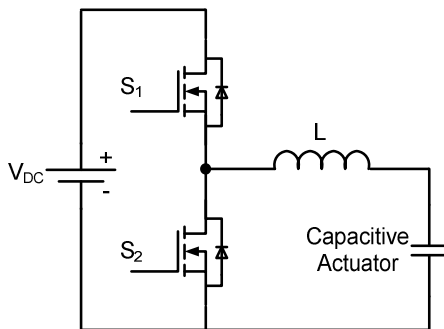


Fig. 2. Basic configuration of bidirectional buck topology

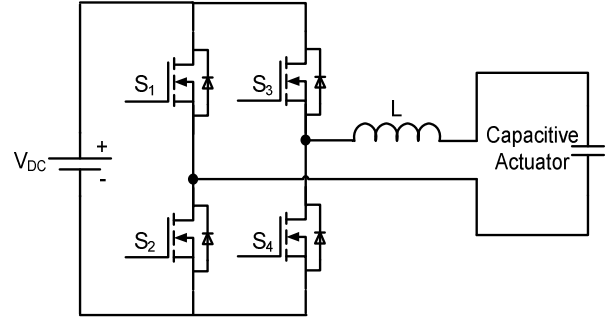


Fig. 3. Basic configuration of full bridge topology

transferred to actuator through the body diode of S_2 . In the energy recovery process, S_2 is on first, L is magnetized by capacitive actuator, after that, it will release the magnetic energy to DC power supply by the body diode of S_1 .

Similar to the operation of bidirectional buck topology, in full bridge topology, S_2 , S_3 and body diodes of S_1 , S_4 work for the charge process. And energy recovery period is contributed by S_1 , S_4 and body diodes of S_2 , S_3 .

Generally, the piezoelectric actuator needs relative low frequency signal to drive, whereas the switching frequency of current semiconductors that can be achieved much higher in value. That is to say, it is easy to realize the low frequency actuation requirement with high frequency switched mode amplifiers.

2) Switching Mode Voltage Boost Stage

In some portable or autonomous operation occasions, a boost stage, which is used to generate high voltage, also needs to be considered. As in these cases, it is normally the battery or low voltage power source provides the electrical energy. In order to improve the overall efficiency, it is also necessary to recycle the stored reactive energy to power source.

The bidirectional boost, buck-boost and flyback are always adopted to achieve the set up of voltage as well as the energy recovery to the power supply. If the piezoelectric actuators do not put strict constraints on the driving signal, such as extremely low harmonic distortion for sinusoidal drive voltage, the switched mode boost stage can directly be used to drive the capacitive actuator. Otherwise, a switching mode driving stage should be used to realize the high quality actuation demand.

a) Bidirectional Boost Converter

The topology configuration for bidirectional boost converter is shown in Fig. 4.

When S_1 is on, the inductor L absorbs energy from DC power supply. When S_1 is turned off, the inductor and DC source will release energy to the capacitive actuator together through body diode of S_2 .

When recycling the reactive energy stored in actuator, S_2 will work first to magnetize L as well as transfer partial energy to power source. Then when S_2 is off, magnetic energy in L will be totally recovered to the DC source. The operation waveforms are displayed in Fig. 5.

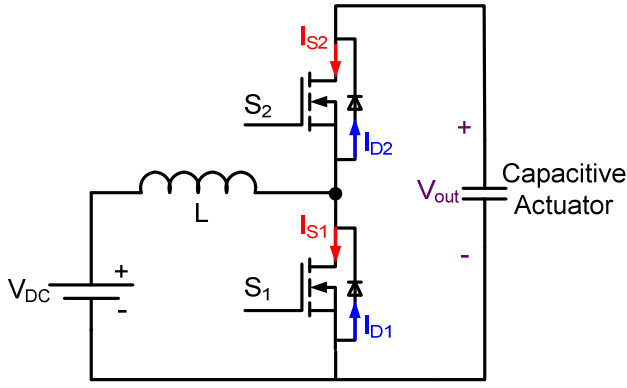


Fig. 4. Bidirectional boost topology

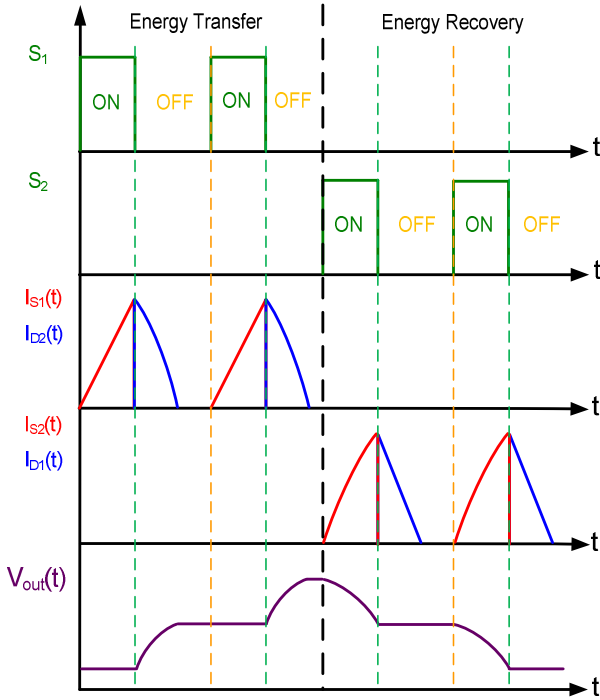


Fig. 5. Working waveforms of bidirectional boost converter

b) Bidirectional Buck-Boost and Flyback Converter

Bidirectional buck-boost and flyback topologies have earned much attention for driving capacitive actuators [17, 21, 22, 34].

Actually, flyback converter is the isolated version of buck-boost converter; therefore, it is reasonable to discuss them together. The topology structures of bidirectional buck-boost and flyback converter are shown in Fig. 6 and Fig. 7, respectively.

In the energy transfer process, only S_1 and body diode of S_2 work. When S_1 is on, energy is transferred to inductor L or primary coupled inductor for flyback converter. When S_1 is off, the energy of inductor will pass to the capacitive actuator through LC resonance. For flyback, it is the secondary coupled inductor that constitutes the resonant circuit.

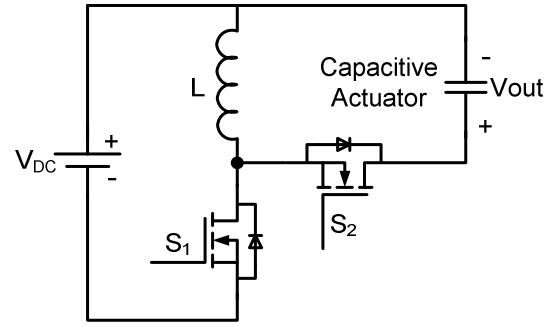


Fig. 6. Bidirectional Buck-Boost Topology

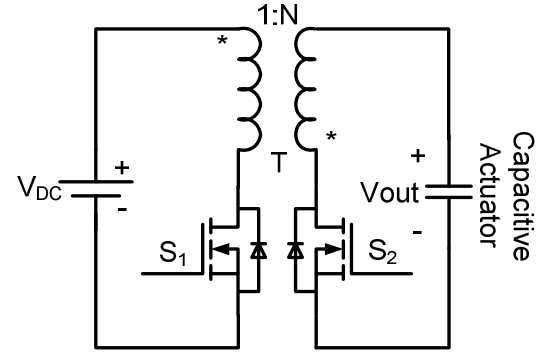


Fig. 7. Bidirectional Flyback Topology

For discharge process of piezoelectric actuator, only S_2 and body diode of S_1 operate. It is like the reverse operation of charge process. That means, LC resonant circuit works first in order to magnetize inductor, then the energy of inductor will be recovered to DC power supply. The typical operating waveforms are much like the waveforms for bidirectional boost converter. To avoid repetition, they will not be shown here again.

c) Topology Comparison

In order to provide guideline in choosing the appropriate topology, the critical characteristics for each converter are summarized in Table I.

The choice of topology primarily depends on the application conditions. For example, if the V_{DC} is very low while the output voltage needs to be very high, it is not worthy to select boost or buck-boost converter. Because the high voltage MOSFETs are not inexpensive, if two high voltage MOSFETs are needed, it costs too much. If flyback is chosen, this problem can be avoided, as the step up transformer can let the primary MOSFET to be a low voltage one. Also in some isolation occasions, flyback will be the only option.

However, if the output voltage is relatively low, boost or buck-boost will be good choices because of the easy design and manufacture for magnetic component.

In fact, it is difficult to draw a conclusion that which topology is most suitable in a certain application. When choosing the topology, the design difficulty, cost as well as size should be evaluated at the same time.

TABLE I CHARACTERISTICS SUMMARY FOR THREE BIDIRECTIONAL TOPOLOGIES

| Topology | MOSFETs | | | Magnetic components | | | | |
|------------|---------------------------|---------------------------|--------|---------------------|---------|-----------------------------------|-----------|-------|
| | Voltage stress | | Cost | | | | | |
| | S1 | S2 | | Core | Winding | Design and manufacture difficulty | Isolation | Size |
| Boost | Vout | Vout | Medium | Yes | 1 | Easy | No | Small |
| Buck-Boost | Vout+V _{DC} | Vout+V _{DC} | High | Yes | 1 | Easy | No | Small |
| Flyback | V _{DC} +(Vout/N) | Vout+(V _{DC} *N) | Low | Yes | 2 | Difficult | Yes | Large |

C. Control Strategies of Switched Mode Amplifiers

Normally, the control schemes need to be considered with the actuation demand for the whole piezoelectric system. Combing with the concrete application, many control strategies are proposed in the literatures. [17], [20] and [34] discuss the sliding mode control, and digital control methods are presented in [35] and [36].

At present, most of piezoelectric actuator drive amplifiers adopt voltage control, because it can be easily achieved. However, in the high precise actuation occasions, the intrinsic hysteresis between applied voltage and displacement will greatly affect the resolution [37, 38]. For reducing the hysteresis effect of voltage control, the charge control or current control can be employed [39].

Much research has been done in the current or charge control field. Current pulse drive is proposed in [40-43]. This control method needs many current sources and sinks with various values to achieve the high resolution of displacement. In addition, charge control also attracts much attention in recent years. This control scheme is presented detailedly in [39, 44-49].

III. ULTRA HIGH VOLTAGE DRIVE AMPLIFIERS FOR DEAP ACTUATOR

Compared to piezoelectric ceramic, dielectric electro-active polymer (DEAP) is a newer type of smart material, which is actually a very thin elastomer film with a compliant electrode layer on both sides. When a voltage is applied to DEAP material, the polymer will compress in thickness and expand in area due to the electric field [50]; therefore, DEAP can be used as an actuator. A cylindrical DEAP actuator is shown in Fig. 8 [51]. Its stroke-voltage response is demonstrated in Figure 9 [52]. It is obvious that DEAP actuator needs high voltage to be fully elongated.

From 1999, the DEAP material has gained immense development. Despite a large number of papers focus on investigating the characterization of DEAP material, improving the performance and applying it towards a rich variety of applications, the situation of researching into the drive circuits for DEAP actuator is quite different. There is only one paper related to the design of drive circuits [51], which demonstrates the Piezoelectric Transformer (PT) based power converter to drive DEAP actuator.

However, several low power ultra high output voltage drive amplifiers for DEAP actuator have emerged in the lab of university or on the market, which could be a compensation for lacking of literatures. According to [53], the efficiency of

one commercial high voltage product can only be approximately 45%. And most products on the market do not pay much attention to recover the stored energy in capacitive actuators, which is very critical to improve the total efficiency of the system. In addition, the price and size for the current products also have a great optimization space. Therefore, deep research concerning the low cost, small size and high efficiency driving amplifiers for DEAP actuator deserves being carried out.

IV. Conclusion and Future Work

This paper summarizes the high voltage drive circuits for capacitive actuators, including piezoelectric actuator and DEAP actuator. The main focus is on the piezoelectric actuator, as there are very few literature references for driver of DEAP actuator. Both linear and switched mode amplifiers are discussed in detail. For switched mode amplifiers, the topology configurations and operating principles are illustrated. Compared to DEAP actuator, piezoelectric actuator only needs relative low driving voltage, however, the



Figure 8. Cylindrical DEAP actuator

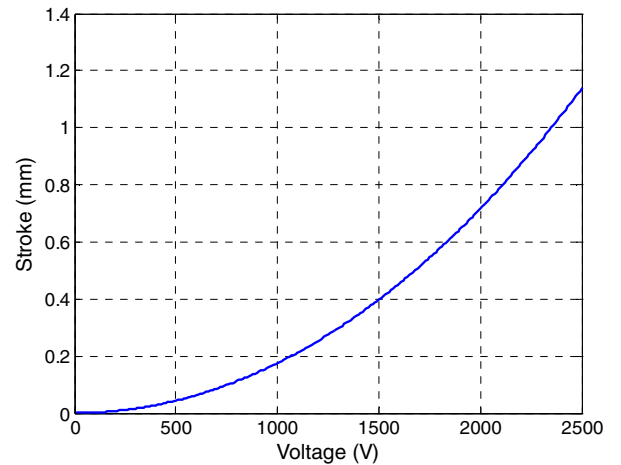


Figure 9. Stroke-voltage characteristic of cylindrical DEAP actuator

fundamental idea of driving capacitive actuator will be referenced for the future research of DEAP driver.

REFERENCES

- [1] E. Montane, P. Miribel-Catala, J. Lopez-Sanchez, M. Puig-Vidal, S. Bota, and J. Samitier, "High-voltage smart power integrated circuits to drive piezoceramic actuators for microrobotic applications," *IEE Proceedings - Circuits, Devices and Systems*, pp. 343-347, 2001.
- [2] N.I. Maluf, R.J. Reay and G.T.A. Kovacs, "High-voltage devices and circuits fabricated using foundry CMOS for use with electrostatic MEM actuators," *The 8th International Conference on Solid-State Sensors and Actuators*, pp. 158-161, 1995.
- [3] G. A. Zvonar, J. Luan, F.C. Lee, D.K. Lindner, S. Kelly, D. Sable and T. Schelling, "High-frequency switching amplifiers for electrostrictive actuators," *Proc. SPIE*, vol. 2721, pp. 465-475, 1996.
- [4] G. A. Zvonar and D. K. Lindner, "Nonlinear electronic control of an electrostrictive actuator," *Proc. SPIE*, vol. 3044, pp. 448-458, 1997.
- [5] G. A. Zvonar and D. K. Lindner, "Power flow analysis of electrostrictive actuators driven by switchmode amplifiers," *Journal of Intelligent Material Systems and Structures*, vol. 9, no. 3, pp. 210-222, March 1998.
- [6] G. A. Zvonar, D. K. Lindner and R. M. Goff, "Power flow through amplifiers controlling electrostrictive actuators," *Proc. SPIE*, vol. 3326, pp. 479-488, 1998.
- [7] G. Powers, Q. Xu, T. Guidarelli and J. Smith, "High-power inchworm actuators for extended-range precision positioning," *Proc. SPIE*, vol. 5762, pp. 287-298, 2005.
- [8] S. Reynolds "A high-voltage, high-frequency linear amplifier/driver for capacitive loads," *Measurement Science & Technology*, vol. 3, no. 3, pp. 283-288, March 1992.
- [9] V. Strom, R. D. Gomez, J. Nogues, B. Rodell and K. V. Rao, "Inexpensive high-voltage low-current amplifier for driving long-range scanning tunneling microscope piezoactuators," *Measurement Science & Technology*, vol. 6, no. 7, pp. 1072-1077, July 1995.
- [10] D. V. Newton, J. A. Main, E. Garcia and L. Massengill, "Piezoelectric Actuation Systems: Optimization of Driving Electronics," *Proc. SPIE*, vol. 2717, pp. 259-266, 1996.
- [11] C. Wallenhauer, A. Kappel, B. Gottlieb, T. Schwebel and T. Luth, "Efficient class-B analog amplifier for a piezoelectric actuator drive," *Mechatronics*, vol. 19, no. 1, pp. 56-64, February 2009.
- [12] C. Wallenhauer, B. Gottlieb, R. Zeichfussl and A. Kappel, "Efficiency-improved high-voltage analog power amplifier for driving piezoelectric actuators" *IEEE Trans. Circuits and Systems*, vol. 57, no. 1, pp. 291-298, January 2010.
- [13] D. J. Leo, "Energy analysis of piezoelectric-actuated structure driven by linear amplifiers," *Journal of Intelligent Material Systems and Structures*, vol. 10, no. 1, pp. 36-45, January 1999.
- [14] J. A. Main, D. V. Newton, L. Massengill and E. Garcia, "Efficient power amplifiers for piezoelectric applications," *Smart Materials and Structures*, vol. 5, pp. 766-775, 1996.
- [15] D. V. Newton, J. A. Main, E. Garcia and L. Massengill, "Piezoelectric Actuation Systems: Optimization of Driving Electronics," *Proc. SPIE*, vol. 2717, pp. 259-266, 1996.
- [16] D. J. Clingman, "Drive electronics for large piezo actuators," *Proc. SPIE*, vol. 3044, pp. 459-467, 1997.
- [17] O. Gomis-Bellmunt, D. Montesinos-Miracle, S. Galceran-Arellano and A. Sudria-Andreu, "A buck-boost bidirectional converter to drive piezoelectric actuators," *Proc. 12th European Conference on Power Electronics and Applications*, pp. 3213-3219, September 2007.
- [18] H. Janocha and C. Stiebel, "New approach to a switching amplifier for piezoelectric actuators," *Actuator 98*, pp. 189-192.
- [19] C. Stiebel and H. Janocha, "New concept of a hybrid amplifier for driving piezoelectric actuators," *Proceedings of the 1st IFAC-Conference on Mechatronic Systems, Germany*, pp. 379-384, 2000.
- [20] O. Gomis-Bellmunt, J. Rafecas-Sabate, D. Montesinos-Miracle, J. M. Fernandez-Mola and J. Bergas-Jane, "Design and control of a half-bridge converter to drive piezoelectric actuators," *Power Electronics and Motion Control Conference 2008 (EPE-PEMC 2008)*, pp. 731-733, 2008.
- [21] M. Karpelson, J. P. Whitney, G. Y. Wei and R. J. Wood, "Design and fabrication of ultralight high-voltage power circuits for flapping-wing robotic insects," *26th Annual IEEE Applied Power Electronics Conference and Exposition (APEC)*, pp. 2070-2077, March 2011.
- [22] M. Karpelson, G. Y. Wei and R. J. Wood, "Milligram-scale high-voltage power electronics for piezoelectric microrobots," *2009 IEEE International Conference on Robotics and Automation*, pp. 2217-2224, May 2009.
- [23] D. K. Lindner, M. Zhu, N. Vujic and D. Leo "Comparison of linear and switching drive amplifiers for piezoelectric actuators," *Proceedings of the AIAA/ASME/ASCE/AHS/ASC 43th Structures, Structural Dynamics, and Materials Conference*, April 2002.
- [24] C. P. Song, M. M. Abdalla, D. K. Lindner and Z. Gurdal, "Combined optimization of active structural systems and drive circuits," *Proc. SPIE*, vol. 4693, pp. 136-147, 2002.
- [25] D. K. Lindner, H. Y. Zhu, C. P. Song, W. X. Huang and D. L. Cheng, "Low input voltage switching amplifiers for piezoelectric actuators," *Proc. SPIE*, vol. 4698, pp. 282-292, 2002.
- [26] J. Y. Luan and F. C. Lee, "Design of a high frequency switching amplifier for smart material actuators with improved current mode control," *29th Annual IEEE Power Electronics Specialists Conference*, pp. 59-64, 1998.
- [27] W. P. Robbins, "Simplified unipolar, quasisquare wave energy recovery drive circuits for piezoelectric actuators," *IEEE Trans. Ultrasonics, Ferroelectrics, and Frequency Control*, vol. 52, no. 8, pp. 1420-1426, August 2005.
- [28] S. Chandrasekaran, D. K. Lindner and R. C. Smith, "Optimized design of switching amplifiers for piezoelectric actuators," *Journal of Intelligent Material Systems and Structures*, vol. 11, no. 11, pp. 887-901, November 2000.
- [29] S. Chandrasekaran, D. K. Lindner and R. C. Smith, "Optimization of switching amplifiers for piezoelectric actuators," *Proc. SPIE*, vol. 3991, pp. 418-429, 2000.
- [30] D. K. Lindner and S. Chandrasekaran, "Power system design issues for smart materials," *Proc. SPIE*, vol. 3668, pp. 805-813, 1999.
- [31] R. Y. Li, N. Frohlike and J. Bocker, "LLCC-PWM Inverter for driving high-power piezoelectric actuators," *Power Electronics and Motion Control Conference 2008 (EPE-PEMC 2008)*, pp. 159-164, 2008.
- [32] R. Y. Li, M. Loenneker, N. Froehleke and J. Boecker, "Design of power supply for driving high power piezoelectric actuators," *2008 IEEE Industry Applications Society Annual Meeting*, pp. 1254-1259, 2008.
- [33] P. Sente, C. Vloebergh, F. Labrique and P. Alexandre, "Control of a direct-drive servo-valve actuated by a linear amplified piezoelectric actuator for aeronautic applications," *2008 International Conference on Electrical Machines*, pp. 1491-1496, 2008.
- [34] O. Gomis-Bellmunt, D. Montesinos-Miracle, S. Galceran-Arellano and J. Rull-Duran, "Sliding mode control based buck-boost bidirectional converter to drive piezoelectric loads," *Electrical Engineering*, vol. 90, no. 2, pp. 115-125, December 2007.
- [35] G. Gnadt and R. Kasper, "VHDL-AMS model of piezoelectric actuators for simulations in mechatronics and in power electronics," *International Conference on Computer as a Tool (EUROCON 2001)*, pp. 783-788, September 2007.
- [36] G. Gnadt and R. Kasper, "A power drive control for piezoelectric actuators," *IEEE International Symposium on Industrial Electronics* pp. 963-967, May 2004.
- [37] H. J. M. T. A. Adriaens, W. L. d Koning and R. Banning, "Modeling piezoelectric actuators," *IEEE/ASME Trans. Mechatronics*, vol. 5, no. 4, pp. 331-341, December 2000.
- [38] B. Jaffe, W. R. Cook and H. Jaffe, *Piezoelectric Ceramics*, Academic Press, 1971.
- [39] A. J. Fleming and S. O. R. Moheimani, "Improved current and charge amplifiers for driving piezoelectric loads," in *Proc. SPIE*, vol. 5052, 2003, pp. 242-252.
- [40] K. Furutani and A. Furuta, "Evaluation of driving performance of piezoelectric actuator with current pulse," *10th International Workshop on Advanced Motion Control*, pp. 387-392, March 2008.
- [41] K. Furutani and A. Furuta, "Comparison of driving performance of piezoelectric actuator - current pulse drive and voltage linear drive," *7th International Conference on Machine Automation (ICMA 2008)*, pp. 183-188, 2008.
- [42] K. Furutani and Iidag, "A driving method of piezoelectric actuator by using current pulses," *Measurement Science & Technology*, vol. 17, no. 9, pp. 2387-2394, September 2006.
- [43] K. Furutani and Iidag, "Performance of driving method of piezoelectric actuator by using current pulse," *9th International Workshop on Advanced Motion Control*, pp. 506-511, March 2006.

- [44] A. J. Fleming and S. O. R. Moheimani, "Improved current and charge amplifiers for driving piezoelectric loads, and issues in signal processing design for synthesis of shunt damping circuits," *Journal of Intelligent Material Systems and Structures*, vol. 15, no. 2, pp. 77-92, February 2004.
- [44] A. J. Fleming and S. O. R. Moheimani, "Precision current and charge amplifiers for driving highly capacitive piezoelectric loads," *Electronics Letter*, vol. 39, no. 3, pp. 282-284, February 2003.
- [45] K. A. Yi and R. J. Veillette, "A charge controller for linear operation of a piezoelectric stack actuator," *IEEE Trans. Control Systems Technology*, vol. 13, no. 4, pp. 517-526, July 2005.
- [46] A. J. Fleming and S. O. R. Moheimani, "A grounded-load charge amplifier for reducing hysteresis in piezoelectric tube scanners," *Review of Scientific Instruments*, vol. 76, no. 7, July 2005.
- [47] A. J. Fleming and K. K. Leang, "Charge drives for scanning probe microscope positioning stages," *Ultramicroscopy*, vol. 108, no. 12, pp. 1551-1557, November 2008.
- [48] M. Spiller and Z. Hurak, "Hybrid charge control for stick-slip piezoelectric actuators" *Mechatronics*, vol. 21, no. 1, pp. 100-108, February 2011.
- [49] A. J. Fleming and K. K. Leang, "Evaluation of charge drives for scanning probe microscope positioning stages," *American Control Conference 2008*, pp. 2028-2033, June 2008.
- [50] M. Y. Benslimane, H. E. Kiil and M. J. Tryson, "Dielectric electro-active polymer push actuators: performance and challenges", *Polymer International*, vol. 59, no. 3, pp. 415-421, 2010.
- [51] T. Andersen, M. S. Rødgaard, O. C. Thomsen and M. A. E. Andersen, "Low voltage driven dielectric electro active polymer actuator with integrated piezoelectric transformer based driver," *Proc. SPIE*, vol. 7976, pp. 79762N-1-79762N-12, 2011.
- [52] R. Sarban, R. W. Jones, B. R. Mace and E. Rustighi, "A tubular dielectric elastomer actuator: fabrication, characterization and active vibration isolation", *Mechanical Systems and Signal Processing*, vol.25 no. 8, , pp. 2879-2891, 2011.
- [53] O. Bilgen, K. B. Kochersberger, D. J. Inman and O. J. Ohanian III, "Lightweight High Voltage Electronic Circuits for Piezoelectric Composite Actuators," *Journal of Intelligent Material Systems and Structures*, vol. 21, no. 14, pp. 1417-1426, September 2010.

APPENDIX B

Analysis of Dielectric Electro Active Polymer Actuator and its High Voltage Driving Circuits

*2012 IEEE International Power Modulator and High Voltage Conference (IPMHVC
2012)*

Analysis of Dielectric Electro Active Polymer Actuator and its High Voltage Driving Circuits

Prasanth Thummala, Lina Huang, Zhe Zhang and Michael A. E. Andersen

Technical University of Denmark, Department of Electrical Engineering, DK-2800 Kongens Lyngby, Denmark

Email: {pthu, huang, zz, ma}@elektro.dtu.dk

ABSTRACT

Actuators based on dielectric elastomers have promising applications in artificial muscles, space robotics, mechatronics, micro-air vehicles, pneumatic and electric automation technology, heating valves, loud speakers, tissue engineering, surgical tools, wind turbine flaps, toys, rotary motors, and grippers for material handling, etc. This paper focuses on the application of Dielectric Electro Active Polymer (DEAP) technology as an actuation mechanism for different applications. The DEAP material requires very high voltage (~2.5 kV DC) to fully utilize it as an actuator. In this paper the DEAP actuator is analyzed in detail and the actuator structures, for the wind turbine flap and the heating valve applications are shown. Different high voltage switch mode power supply topologies for driving the DEAP actuator are discussed. The simulation and experimental results are discussed.

Index Terms — Dielectric electro active polymer (DEAP), actuator, high voltage (HV), dc-dc converter, power electronics, heating valves, wind turbine flaps, PolyPower

1 INTRODUCTION

Smart materials which respond to external stimuli like light, temperature, pressure, pH, magnetic and electric fields by changing their shape or size have been a particular focus in the past decade [1]. The intelligent materials include, shape memory alloys, piezoelectric materials, etc. and deforming active polymers include hydro gels, dielectric elastomers, carbon-nano tubes and liquid crystalline elastomers. Electro Active Polymers (EAPs) that undergoes force and deformation when electrically stimulated were strongly focused in the last years.

An actuator is a mechanical device for moving or controlling a mechanism or a system. EAPs can be used as actuators in active structures, in particular when large deformations are required. Such EAP actuators convert electrical energy into mechanical energy and produce large strains. Several applications of dielectric elastomer actuators were discussed in [2]. From the electrical standpoint, DEAP actuators are capacitive loads. In [3] a low voltage driven DEAP actuator was developed using piezoelectric transformer. A novel activation strategy for dielectric elastomer actuators was proposed in [4]. Section 2 discusses the detailed analysis of the DEAP actuator and its electrical, mechanical, and

electromechanical modeling, and the actuator structures for the heating valves and wind turbine flaps applications. We discuss the high voltage DC-DC converter topologies in Section 3, followed by the conclusion in Section 4.

2 DIELECTRIC ELASTOMERS AS ACTUATORS

Electro Active Polymers (EAPs) are categorized into two major classes: ionic and electronic. An electric field or coulomb forces drive electronic EAPs, while the actuation mechanism for ionic EAPs is through the diffusion or mobility of ions. The electronic EAPs generally require high electric fields ($>100 \text{ V}/\mu\text{m}$) and the ionic EAPs requires low driving voltages, nearly equal to 1-5V. Typical driving voltages for dielectric elastomer actuators lie in the range between 2 kV and 4 kV, depending on the polymer breakdown field and thickness of the polymer film. The operating principle of a dielectric elastomer actuator is shown in Figure 1. The DEAP material is a very thin ($\sim 40 \mu\text{m}$) incompressible elastomer film with a compliant electrode layer on both sides [5]. A dielectric elastomer is basically a compliant capacitor. The electrodes are designed to be able to comply with the deformations of the elastomer. As for any capacitor, when an electric field is applied to the electrodes, positive charges appear on one electrode, and negative charges on the other. This gives rise to coulomb forces between opposite charges, generating a pressure, known as the Maxwell stress. The Maxwell stress forces the electrodes to move closer, thereby squeezing the polymer. As the polymer is thinned, it elongates in the directions perpendicular to the applied force [6]. The electro static pressure (or stress) σ generated by the actuator is

$$\sigma = \epsilon_o \epsilon_r \left(\frac{v_{DEAP}}{x} \right)^2 = \epsilon_o \epsilon_r E^2 \quad (1)$$

where E is the imposed electrical field, x is the final thickness, v_{DEAP} is the voltage across the DEAP material, and ϵ_o and ϵ_r are the permittivity of the free space ($8.85 \times 10^{-12} \text{ F/m}$) and the relative permittivity of the polymer, respectively. The mechanical strain S of the DE is given by

$$S = -\frac{\epsilon_o \epsilon_r}{Y} \left(\frac{v_{DEAP}}{x_o / (1+S)} \right)^2 = -\frac{\epsilon_o \epsilon_r}{Y} \left(\frac{v_{DEAP} (1+S)}{x_o} \right)^2 \quad (2)$$

where Y is the Young's modulus and d_o is the initial thickness of the material. Using the capacitive behavior of the polymer, DEAP can be used as an actuator, mechano-electrical sensor, as well as energy harvester to generate electricity. When operated as an actuator DEAP show unique properties, such as very low electrical power consumption, high specific elastic energy density, high speed of response, no noise, flexibility, high power density, large bandwidth, higher performance than competing technologies and light weight, hence it has the potential to be an effective replacement for conventional actuators.

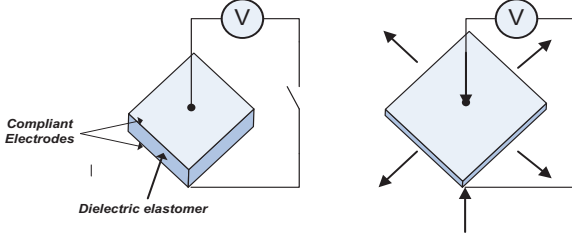


Figure 1. Schematic showing the principle of operation of DEAP actuator. Right: Voltage is ON; Left: Voltage is OFF;

1.1 POLYPOWER DEAP ACTUATOR



Figure 2. PolyPower DE tubular actuator

PolyPower™ dielectric elastomer (DE) is a silicone DE manufactured by Danfoss PolyPower A/S, Denmark. PolyPower DEAP actuator (Figure 2) is produced in thin sheets of 40 μm thickness. Table 1 shows the properties of the Danfoss PolyPower DEAP material. A DE sheet can be modeled as a strain dependent variable plate capacitor (3). For the unidirectional actuation shown in Figure 3, the capacitance of the DEAP actuator as a function of strain S is

$$C = \epsilon_o \epsilon_r \frac{A}{x} = \epsilon_o \epsilon_r \frac{A_o (1+S)}{x_o / (1+S)} = \epsilon_o \epsilon_r \frac{A_o}{x_o} (1+S)^2 \quad (3)$$

Table 1. Material properties of Danfoss PolyPower DEAP material

| | |
|---------------------------|---------------------|
| Film thickness | 40 μm |
| Dielectric field strength | 40 V/ μm |
| Dielectric constant | 3.1 |

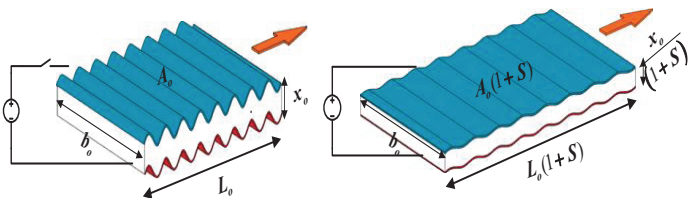


Figure 3. Left: A laminate of PolyPower DE material with corrugated surface and electrode, Right: Actuation direction of the DE material.

1.2 DEAP ELECTRICAL MODELLING

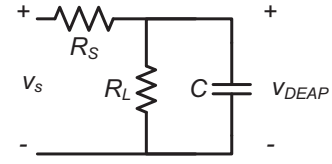


Figure 4a. Electric-circuit model of DEAP actuator

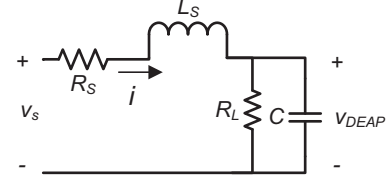


Figure 4b. Electric-circuit model of DEAP actuator including the inductance of the high voltage cables and the compliant electrodes

Figures 4a and 4b show the circuit representation of the electrical model for the DE system employed in this paper. In the figures, R_s is the resistance of the electrodes and the wiring, R_L is the resistance of the DE material, C is the capacitance of the DE sheet, L_s is the equivalent inductance of the electrodes and the high voltage cables, v_s is the voltage of the power source, and v_{DEAP} is the voltage over the DE sheet.

For the circuit shown in Figure 4a, the quasi-electrostatic pressure (1) at the surface of the DE sheet is induced by v_{DEAP} , which is given by

$$\frac{dv_{DEAP}(t)}{dt} + \left(\frac{R_L + R_s}{R_L R_s C} \right) v_{DEAP}(t) = \left(\frac{1}{R_s C} \right) v_s(t) \quad (4)$$

Similarly for the circuit shown in Figure 4b, the differential equations are given as,

$$v_s(t) = R_s i + L_s \frac{di}{dt} + v_{DEAP}(t) \quad (5)$$

$$i = \frac{v_{DEAP}(t)}{R_L} + C \frac{dv_{DEAP}(t)}{dt} \quad (6)$$

Figures 5a and 5b are the block diagram representations for the electrical equivalents of the DEAP actuator.

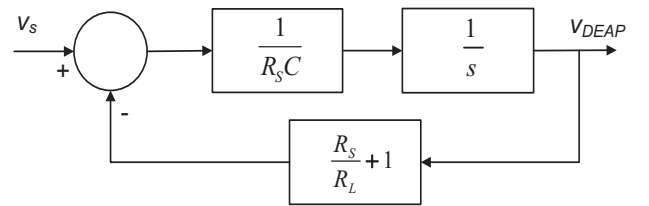


Figure 5a. Block diagram for the electrical circuit of the EAP actuator shown in Figure 4a

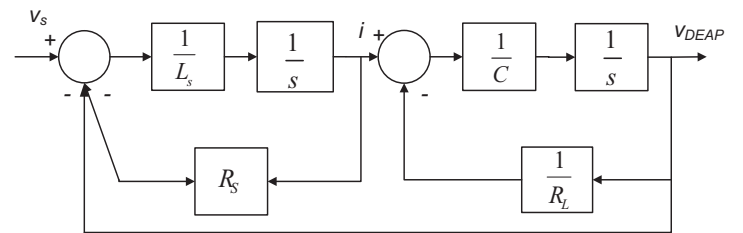


Figure 5b. State block diagram for the electrical circuit of the EAP actuator shown in Figure 4b

1.3 DEAP MECHANICAL MODELLING

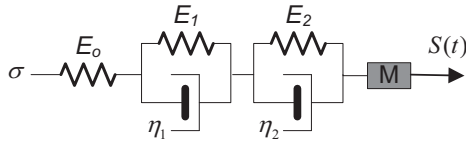


Figure 6. Voigt-Kelvin's viscoelastic model with inertial force.

Dielectric polymers exhibit both elastic solid and viscous fluid characteristics. The viscoelastic behavior of the polymers can be modeled as linear elastic spring (E_0 , E_1 and E_2) and dashpot networks (η_1 and η_2). The viscoelastic behavior of the DE actuators can be predicted by a Voigt-Kelvin five-parameter model (Figure 6) [7]. The strain response $S(t)$ to a step-stress input σ of the five-parameter Voigt-Kelvin model is

$$S(t) = \sigma \left(\frac{1}{E_0} + \sum_{n=1}^2 \frac{1}{E_n} \left(1 - \exp\left(-\frac{t}{\tau_n}\right) \right) \right) \quad (7)$$

where $\tau_n = \eta_n / E_n$ are the retardation time constants.

1.4 DEAP ELECTRO-MECHANICAL MODELLING

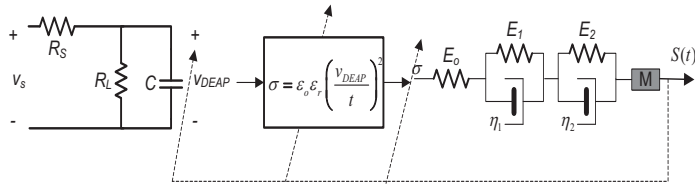


Figure 7. Electro-mechanical modeling of DEAP actuator

Figure 7 shows the electro-mechanical model of DEAP actuator. The input voltage v_s generate a voltage across the DEAP capacitor v_{DEAP} , which induces an electrostatic pressure σ . The mechanical part input viz., the electrostatic pressure σ is the input that results in a mechanical strain S . If the actuation strain S is large, it changes the capacitance C , thickness t , and the stiffness of the material

2.5 DIFFERENT STRUCTURES OF DEAP ACTUATORS

In this paper we focus on the application of DEAP actuator technology to two challenging applications, viz., heating valves and wind turbine flaps. The actuator structures for the two applications are discussed below.

2.5.1 WIND TURBINE FLAP APPLICATION

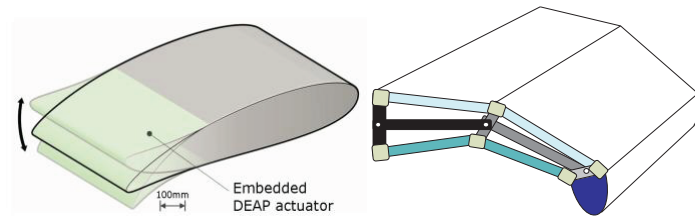


Figure 8. Left: Embedded DEAP actuator into the wing flap; Right: actuated flap structure with DEAP actuators.

Implementing DEAP actuator in the wind turbine flaps will result in improved blade efficiency, reduced loads and fatigues

on the blades and turbine. Figure 8 shows the typical structure of the wind turbine flap with embedded DEAP actuators.

2.5.2 HEATING VALVE APPLICATION

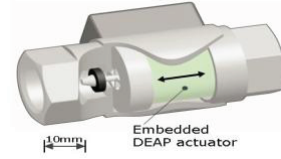


Figure 9. The heating valve containing the DEAP actuator

The current heating valve actuators in the market are thermal actuators, being noiseless but consuming significant power, and electrical gear motors which are relatively energy efficient, but inherently prone to noise issues. The compact in-line heating valves based on DEAP actuator will make better, cheaper and noiseless valves without mechanical parts.

3 HIGH VOLTAGE POWER CONVERTERS TO DRIVE THE DEAP ACTUATOR

To drive the DEAP actuator a high voltage in the range of kilovolts is required [3, 4]. For the systematic control of the DEAP actuators that are implemented in a specific application, special high voltage power electronic (HVPE) converters with advanced control techniques are required. Simulation and experimental results for a unidirectional flyback converter are shown.

3.1 DIFFERENT TOPOLOGIES

Flyback and full bridge converters shown in Figures 10a and 10b, are some of the suitable DC-DC converter topologies for high voltage applications. However, the choice of the converter topology depends on the specific requirements of the application, which are shown in Table 2.

Table 2. Specifications of the applications and choice of converter topology

| Application | Input voltage | Charging Time of Actuator |
|-------------------|---------------------------|---------------------------|
| Wind turbine flap | 24 V (from battery) | 50-100 ms |
| | 400 V (from wind turbine) | |
| Heating valve | 3 V (from battery) | 5-10 min |

Table 3. Parameters of the flyback converter used in the experiment

| Parameters | Values |
|------------------------------|------------|
| Rated input voltage | 24 V |
| Rated output voltage | 2.5 kV |
| Magnetizing inductance L_p | 35 μ H |
| Flyback transformer core | EF20, N87 |
| Primary turns/ Turns ratio | 10/ 20 |
| Leakage inductance L_{lk} | 800 nH |
| Capacitance of DEAP actuator | 145 nF |
| Primary peak current | 5.3 A |

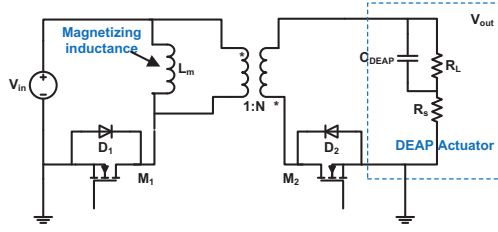


Figure 10a. Schematic of bi-directional flyback converter

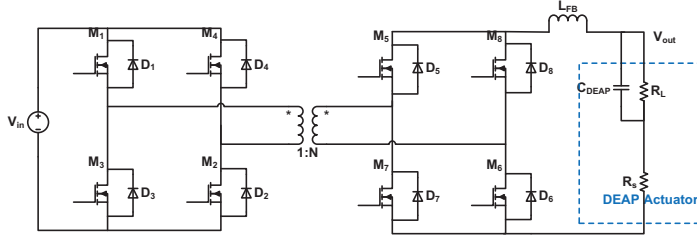


Figure 10b. Schematic of isolated bi-directional full bridge converter.

In this paper we focus only on the flyback topology, for both applications. We used LT3751 capacitor charger controller to generate high voltage. However, for wind turbine flap application, if the output power requirement is too high, isolated full bridge converter is the good choice.

3.2 SIMULATION AND EXPERIMENTAL RESULTS

The simulation has been done using LTSpice software. The simulation results for a uni-directional flyback are shown below for different input voltages ($V_{in} = 3V$, $24V$ and $400V$).

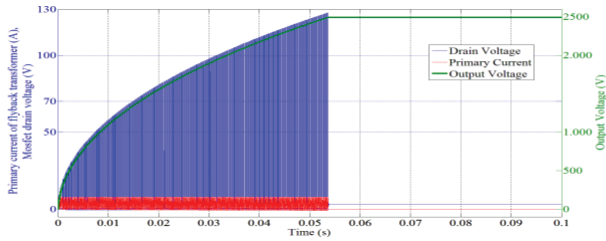


Figure 11. Simulation results of flyback converter for $V_{in} = 3 V$

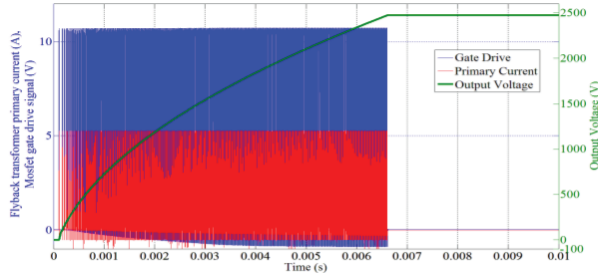


Figure 12. Simulation results of flyback converter for $V_{in} = 24 V$

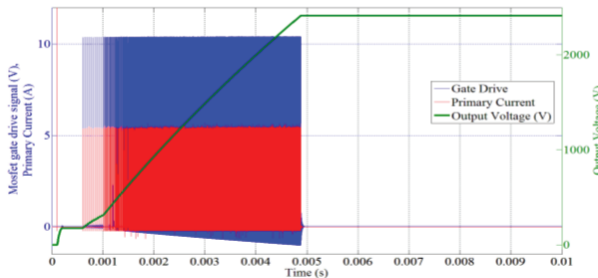


Figure 13. Simulation results of flyback converter for $V_{in} = 400 V$

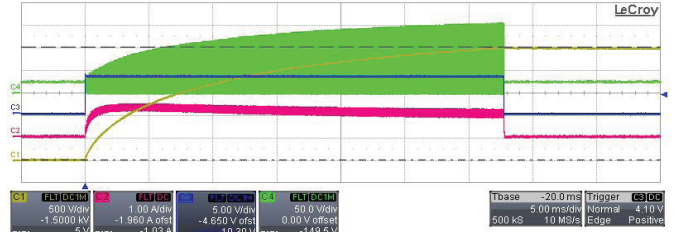


Figure 14. Experimental waveforms (CH1-Output voltage; CH2-Input current; CH3-Charge signal to the converter; CH4-Mosfet drain voltage)



Figure 15. Experimental waveforms (CH1-Output voltage; CH2-Flyback primary current; CH3-Charge signal to the converter; CH4-Mosfet gate voltage)

Figures 14 and 15 are the experimental results for the uni-directional flyback converter.

4 CONCLUSION

The DEAP actuator is analyzed in detail. And the modeling of the DEAP actuator is presented. Different structures of the DEAP actuators that can be implemented in two different applications are shown. Some high voltage converter topologies for driving the capacitive loads are presented. Finally, simulation and experimental results are shown for a uni-directional flyback converter.

REFERENCES

- [1] Y. Bar-Cohen, *Electroactive Polymer (EAP) Actuators as Artificial Muscles: Reality, Potential, and Challenges*. SPIE Press, Bellingham, Washington, USA, 2001.
- [2] R. Pelrine, P. Sommer-Larsen, R. Kornbluh, R. Heydt, G. Kofod, Q. Pei, P. Gravesen, "Applications of dielectric elastomer actuators", Proc. of SPIE, Smart structures and materials 2001: Electroactive polymer actuators and devices, Vol. 4329, pp. 335-349, 2001.
- [3] T. Andersen, M. S. Rødgaard, O. C. Thomsen and M. A. E. Andersen, "Low voltage driven dielectric electro active polymer actuator with integrated piezoelectric transformer based driver," *Proceedings of SPIE*, vol. 7976, p. 79762N, 2011.
- [4] M. Babič, R. Versteck, G. Berselli, J. Lenarčič, V. Parenti Castelli, G. Vassura, "An electronic driver for improving the open and closed loop electro-mechanical response of Dielectric Elastomer actuators", *Mechatronics*, Vol. 20, pp. 201-212, 2010.
- [5] M. Benslimane, P. Gravesen, P. Sommer-Larsen, "Mechanical properties of dielectric elastomers with smart metallic compliant electrodes", In. Proc. of SPIE Int Soc. Opt. Eng., 4695, pp. 150-157, 2002.
- [6] R.E. Pelrine, R.D. Kornbluh, J.P. Joseph, "Electrostriction of polymer dielectrics with compliant electrodes as a means of actuation," *Sensors and Actuators*, Vol. A 64, pp. 77-85, 1998.
- [7] R. Sarban, B. Lassen, M. Willatzen, "Dynamic Electromechanical Modeling of Dielectric Elastomer Actuators With Metallic Electrodes," *IEEE/ASME Transactions on Mechatronics*, Vol. PP, no.99, pp.1-8, 2011.

APPENDIX C

Battery Powered High Output Voltage Bidirectional Flyback Converter for Cylindrical DEAP Actuator

*2012 IEEE International Power Modulator and High Voltage Conference (IPMHVC
2012)*

Battery Powered High Output Voltage Bidirectional Flyback Converter for Cylindrical DEAP Actuator

Lina Huang, Prasanth Thummala, Zhe Zhang, Michael A. E. Andersen

huang@elektro.dtu.dk, pthu@elektro.dtu.dk, zz@elektro.dtu.dk, ma@elektro.dtu.dk

Technical University of Denmark, Department of Electrical Engineering, DK-2800 Kgs. Lyngby, Denmark

ABSTRACT

DEAP (Dielectric Electro Active Polymer) actuator is essentially a capacitive load and can be applied in various actuation occasions. However, high voltage is needed to actuate it. In this paper, a high voltage bidirectional flyback converter with low input voltage is presented. The fundamental operating principle for both energy transfer process and energy recovery process is analyzed in detail. In order to verify the analysis, critical simulation results are provided. So far, a unidirectional flyback converter, which can realize the energy transfer process, has been implemented in the lab. The design parameters for flyback transformer and snubber circuits are illustrated. Moreover, the experimental waveforms are provided.

Index Terms — DEAP actuator, high voltage, flyback, bidirectional

1 INTRODUCTION

DEAP (Dielectric Electro Active Polymer) is a new type of polymer material, which consists of a soft silicone polymer, sandwiched between two compliant metallic electrodes [1]. The similar structure to a capacitor enables DEAP to be fundamentally considered as a capacitive load. Figure 1 shows the measured impedance of DEAP material at low frequency. The -90 degrees phase angle can sufficiently illustrate the capacitive property of DEAP.

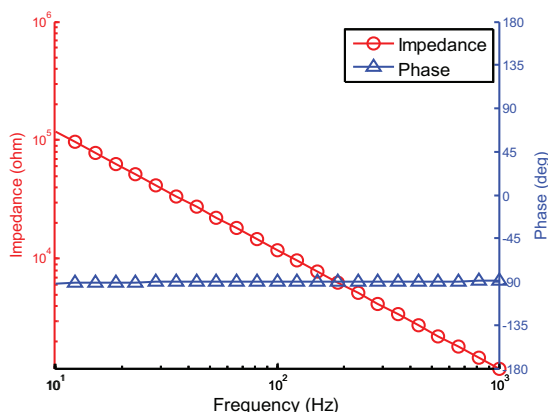


Figure 1. Impedance measurement of DEAP material

When a voltage is applied to DEAP material, the polymer will

compress in thickness and expand in area due to the electric field [2]; therefore, DEAP can be used as an actuator. Compared to traditional electro-magnetic, pneumatic or hydraulic actuators, capacitive actuator possesses many advantages, such as high power density, low weight, fast and direct actuation, high actuating precision, extremely low steady-state power consumption, low noise, etc.

Because of the simple design and immense applicable occasions, cylindrical DEAP actuator, which only performs linear motion, will be an effective replacement for many conventional actuators. Figure 2 shows a cylindrical DEAP actuator [3].



Figure 2. Cylindrical DEAP actuator

The stroke-voltage response of cylindrical DEAP actuator shown in Figure 2, is demonstrated in Figure 3 [4]. It is obvious that DEAP actuator needs high voltage to be fully elongated.

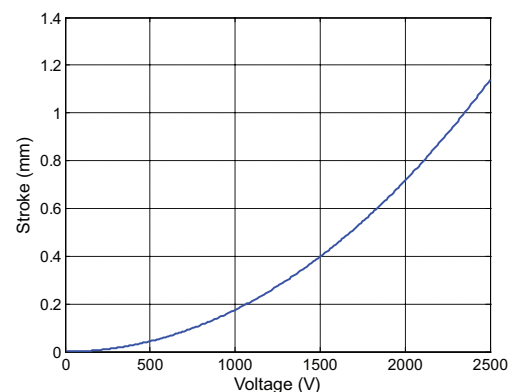


Figure 3. Stroke-voltage characteristic of cylindrical DEAP actuator

Owing to the low weight of DEAP actuator, it can be used in the portable or autonomous systems, where the battery will be the only power source. Therefore, for stimulating DEAP, a DC-DC converter which can convert low input voltage to high output voltage will be necessary. Combined with the capacitive property

of DEAP material and the objective to extend the lifetime of battery, a bidirectional flyback converter can be a good choice, which can not only boost the low voltage to several thousand volts, but also can recover the stored electrical energy when DEAP actuator is released. Furthermore, due to the simple topology of flyback, the converter can be realized in small size, which is vital in the portable or autonomous applications.

This paper analyzes the working principle of bidirectional flyback converter to drive cylindrical DEAP actuator and validates the feasibility through simulation in Section 2. Until now, only the unidirectional flyback converter was realized in the lab, which can boost the output voltage to 2.5kV from a 3V battery and will be addressed in Section 3. And conclusion is drawn in Section 4.

2 BIDIRECTIONAL FLYBACK ANALYSIS

For DEAP actuator, only a small portion of stored electrical energy is converted into mechanical response [5]; therefore, it can approximately be considered as a pure capacitor load in order to simplify the analysis.

2.1 TOPOLOGY AND WORKING PRINCIPLE

The bidirectional flyback converter is shown in Figure 4, consisting of coupled inductors in the middle and active power switches in both primary and secondary side.

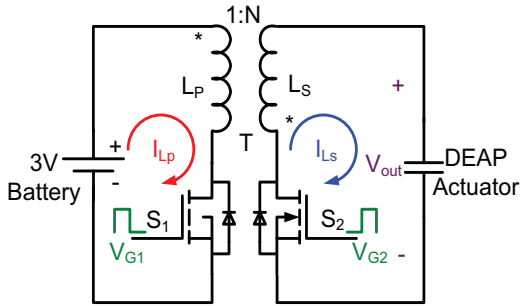


Figure 4. The topology of bidirectional flyback converter

a) Energy transfer process analysis

When driving DEAP actuator, the electrical energy is transferred to capacitive load from battery. Actually, the energy transfer process includes a series of switching cycles. For each cycle, the primary inductor L_p is magnetized in the on-time of S_1 to accumulate magnetic energy. Then in the off-time of S_1 , through body diode of S_2 , the stored energy will be transferred to DEAP actuator from coupled secondary inductor L_s . Ideally, the magnetic energy of L_s is totally transformed into electrical energy in the capacitive actuator. Moreover, based on the basic principle of LC resonant circuit, in every off-time of S_1 , inductor current of L_s and output voltage V_{out} can be expressed in (1) and (2), respectively.

$$i_{L_s}(t) = i_{L_s}(0) \cdot \cos\left(\frac{t}{\sqrt{L_s \cdot C_{DEAP}}}\right) - V_{out}(0) \cdot \sqrt{\frac{C_{DEAP}}{L_s}} \cdot \sin\left(\frac{t}{\sqrt{L_s \cdot C_{DEAP}}}\right) \quad (1)$$

$$V_{out}(t) = V_{out}(0) \cdot \cos\left(\frac{t}{\sqrt{L_s \cdot C_{DEAP}}}\right) + i_{L_s}(0) \cdot \sqrt{\frac{L_s}{C_{DEAP}}} \cdot \sin\left(\frac{t}{\sqrt{L_s \cdot C_{DEAP}}}\right) \quad (2)$$

where L_s is the inductance of secondary coupled inductor, C_{DEAP} is the capacitance of DEAP actuator, and $i_{L_s}(0)$, $V_{out}(0)$ are the initial current and voltage for inductor and actuator, respectively.

In order to reduce the charge time of fully elongating DEAP actuator and completely transfer the energy stored in the flyback transformer in each cycle, a boundary mode control strategy can be used [6]. When the current through the body diode of S_2 accomplishes freewheeling in the previous cycle, the next cycle immediately starts. In addition, primary peak current control is employed to guarantee the sufficient utilization of magnetic core as well as to avoid its saturation. The fixed input voltage from battery and the application of peak current control make primary conduction time a constant value. However, with the increasing of output voltage, the freewheeling time in secondary side will decrease. That means the switching frequency is variable, and in the early stage of charge, the converter operates in low frequency, whereas at the end, the working frequency becomes high. Although the unfixed operating frequency accelerates the charging process, it also brings some challenges in designing the transformer and analyzing the power loss. The waveforms of first several cycles in charging process are shown in Figure 5.

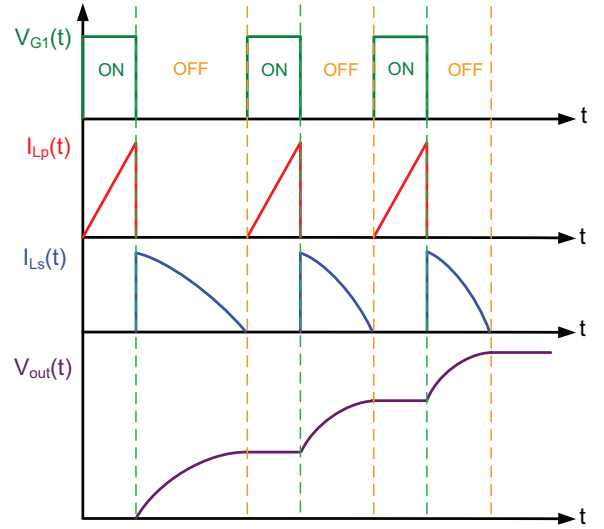


Figure 5. Waveforms in the energy transfer process

b) Energy recovery process analysis

For the purpose of increasing the service life of battery, it is pivotal to recover the energy stored in DEAP actuator when it is released. Like the charge process, the energy recovery process also consists of many successive switching cycles. Only S_2 and the body diode of S_1 work in the discharging process. In each cycle, L_s obtains magnetic energy from DEAP actuator in the on-time of S_2 and releases the stored energy to primary side in the off-time of S_2 .

Similar to energy transfer stage, boundary mode control scheme and secondary peak current control are also adopted in discharge process. The waveforms of first several cycles in the energy recovery process are shown in Figure 6.

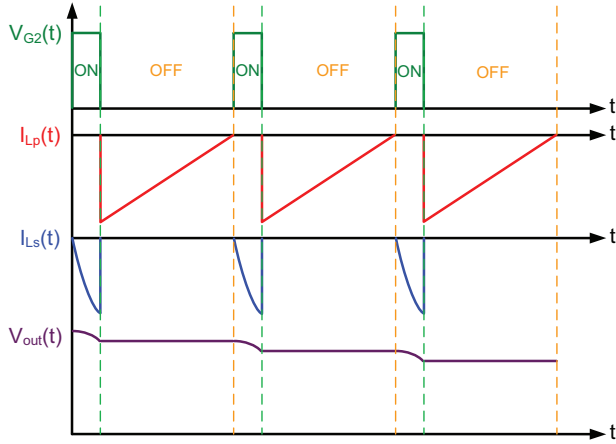


Figure 6. Waveforms in energy recovery process

2.2 SIMULATION VERIFICATION

For validating the analysis mentioned above, a bidirectional flyback converter simulation model has been established with PLECS (Piecewise Linear Electrical Circuit Simulation) software. In addition, a boundary operation mode and peak current control module is also built up. The detailed simulations parameters are shown in Table 1.

Table 1. Simulation parameters for bidirectional flyback converter

| Simulation Parameters | Values |
|------------------------------|-----------|
| L_p | 9 μ H |
| L_s | 21.36 mH |
| Capacitance of DEAP actuator | 142 nF |
| V_{in} | 3 V |
| Primary peak current | 3.9 A |
| Secondary peak current | 80 mA |
| N | 48.7 |

a) Energy transfer process simulation

Figure 7 shows the whole charge process, in which the output voltage increases from 0 to 2.5kV.

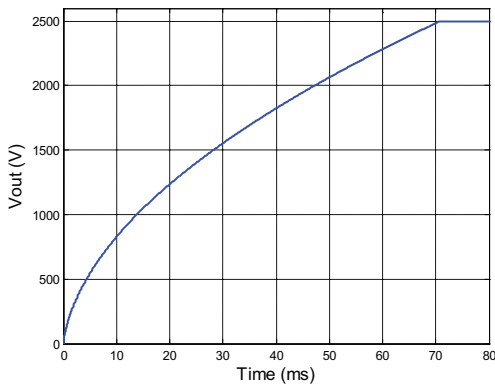


Figure 7. Simulated output voltage waveform in the energy transfer process

In the first several cycles, the current waveforms for both primary and secondary side are shown in Figure 8, which indicates that the boundary mode operation is achieved. Owing to the employment of boundary mode, the charge time is short, only less than 80ms.

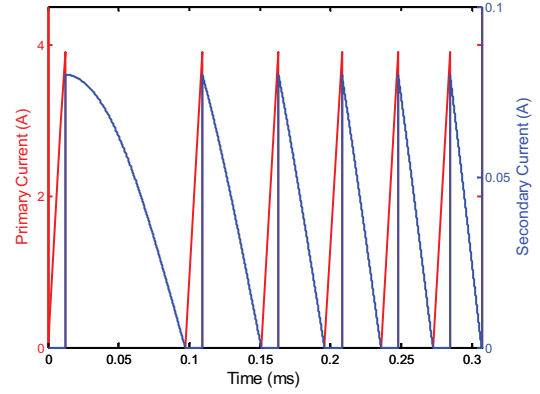


Figure 8. Simulated current waveform in the energy transfer process

b) Energy recovery process simulation

The output voltage decreases from 2.5kV to 0 in the energy recovery process, shown in Figure 9. And the current waveforms are provided in Figure 10, which also demonstrates the realization of boundary mode in discharge process.

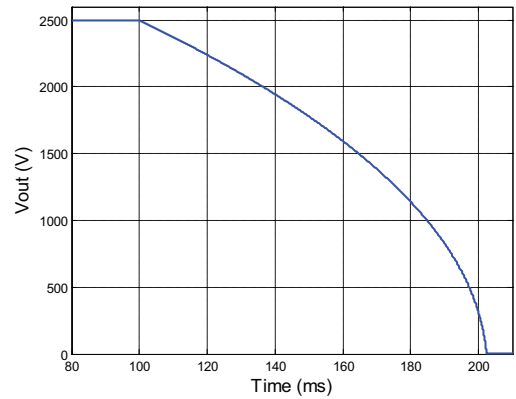


Figure 9. Simulated output voltage waveform in the energy recovery process

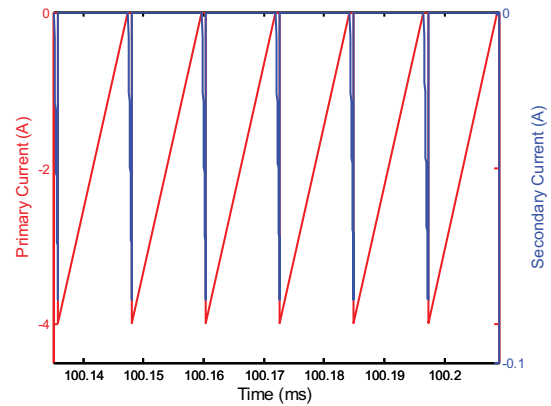


Figure 10. Simulated current waveform in the energy recovery process

3 UNIDIRECTIONAL FLYBACK DESIGN AND REALIZATION

A unidirectional flyback converter to drive DEAP actuator, shown in Figure 11, has been realized in the lab. Because of the voltage stress issue of S_1 , a RC snubber and a RCD clamp circuits are employed [7].

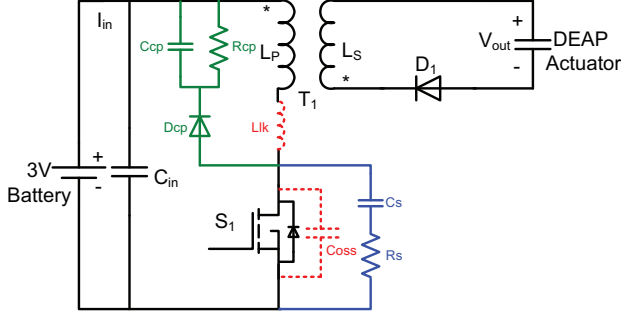


Figure 11. Unidirectional flyback converter

3.1 DESIGN PARAMETERS

The detailed design parameters are shown in Table 2, including the parameters of transformer, RC and RCD circuit.

Table 2. Design parameters for unidirectional flyback converter

| Parameters | Values |
|-----------------------------------------------|-------------------|
| Turns ratio (primary turns : secondary turns) | 7:341 |
| Core type (Core material) | EF20 (N67) |
| Air gap length | 250 μm |
| L_p | 9 μH |
| L_s | 21.36 mH |
| Leakage inductance L_{lk} | 750 nH |
| Capacitance of DEAP actuator | 142 nF |
| R_s of RC snubber circuit | 68.1 Ω |
| C_s of RC snubber circuit | 220 pF |
| R_{cp} of RCD clamp circuit | 20 k Ω |
| C_{cp} of RCD clamp circuit | 1 μF |

3.2 EXPERIMENTAL WAVEFORMS

The experimental waveforms are shown in Figure 12, Figure 13 and Figure 14. From Figure 12, it is clear to see the variable switching frequency which is caused by the boundary mode operation.

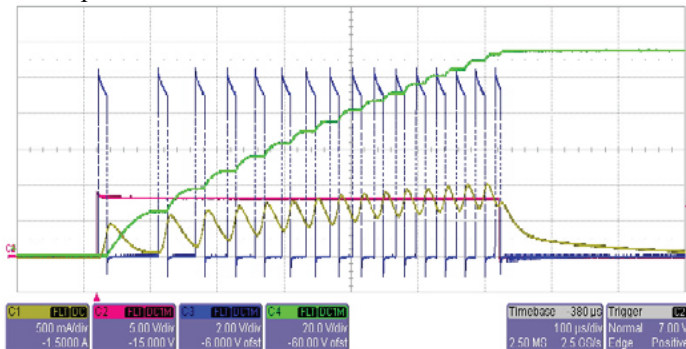


Figure 12. Experimental waveforms (CH1-input current I_{in} ; CH2-charge control signal for converter; CH3-gate signal of S_1 ; CH4-output voltage)

The peak current control can be validated in Figure 13 and the whole energy transfer process is shown in Figure 14.

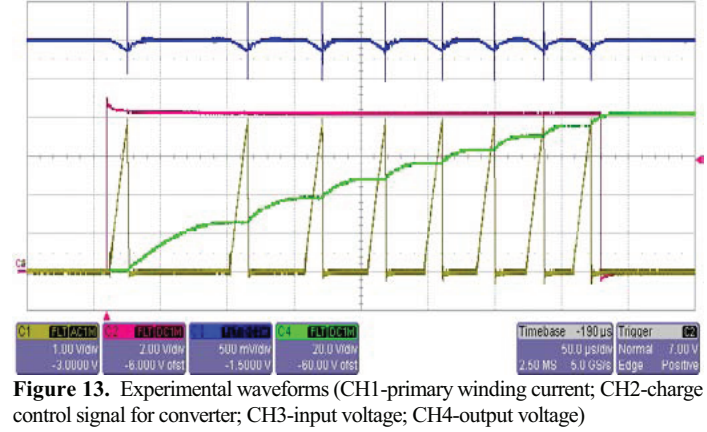


Figure 13. Experimental waveforms (CH1-primary winding current; CH2-charge control signal for converter; CH3-input voltage; CH4-output voltage)

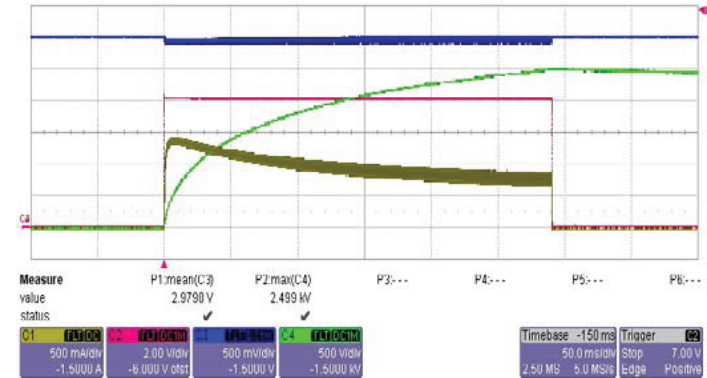


Figure 14. Experimental waveforms (CH1-input current I_{in} ; CH2-charge control signal for converter; CH3-input voltage; CH4-output voltage)

4 CONCLUSION

A high voltage bidirectional flyback converter driving DEAP actuator is presented. The detailed analysis for both the energy transfer and the recovery process is discussed. The simulation results are provided to support analysis. In addition, a unidirectional flyback prototype has been implemented in the lab, which can charge DEAP actuator to 2.5kV.

REFERENCES

- [1] M. Y. Benslimane, H. E. Kiil and M. J. Tryson, "Electro-mechanical properties of novel large strain PolyPower film and laminate components for DEAP actuator and sensor applications", Proceedings of SPIE, Vol. 7642, 2010.
- [2] M. Y. Benslimane, H. E. Kiil and M. J. Tryson, "Dielectric electro-active polymer push actuators: performance and challenges", Polymer International, Vol. 59, No. 3, pp. 415-421, 2010.
- [3] T. Andersen, M. S. Rødgaard, O. C. Thomsen and M. A. E. Andersen, "Low voltage driven dielectric electro active polymer actuator with integrated piezoelectric transformer based driver", Proceedings of SPIE, Vol. 7976, 2011.
- [4] R. Sarban, R. W. Jones, B. R. Mace and E. Rustighi, "A tubular dielectric elastomer actuator: Fabrication, characterization and active vibration isolation", Mechanical Systems and Signal Processing, Vol.25 No. 8, , pp. 2879-2891, 2011.
- [5] M. J. Tryson, R. Sarban, K. P. Lorenzen, "The dynamic properties of tubular DEAP actuators", Proceedings of SPIE, Vol. 7642, 2010.
- [6] "LT3750 Capacitor Charger Controller Datasheet", Linear Technology Corporation, USA.
- [7] "Application Note AN-4147 Design Guidelines for RCD Snubber of Flyback Converters", Fairchild Semiconductor Corporation, USA, 2006.

APPENDIX D

Primary Parallel Secondary Series Flyback Converter (PPSSFC) with Multiple Transformers for Very High Step-Up Ratio in Capacitive Load Charging Applications

2014 IEEE Applied Power Electronics Conference and Exposition(APEC 2014)

Primary Parallel Secondary Series Flyback Converter (PPSSFC) with Multiple Transformers for Very High Step-Up Ratio in Capacitive Load Charging Applications

Riccardo Pittini, Lina Huang, Zhe Zhang and Michael A. E. Andersen

Department of Electrical Engineering

Technical University of Denmark

Oersteds Plads, Building 349, Kgs. Lyngby, Denmark

Email: ripit@elektro.dtu.dk, huang@elektro.dtu.dk, zz@elektro.dtu.dk, ma@elektro.dtu.dk

Abstract— Flyback converters are widely used in several applications, however, with this topology it is very challenging to achieve high voltage operation especially with very high step-up ratio (>500) within limited space. This paper presents a new flyback-based topology which utilizes primary parallel and secondary series transformer connection in order to achieve very high step-up ratio (up to 650) as well as high voltage operation (~ 2 kV) in a small volume. The topology is presented and analyzed. The advantages and disadvantages of the proposed topology are discussed. A prototype used to verify the proposed topology has been implemented. Finally, experimental results are used to validate the performance of the proposed topology.

I. INTRODUCTION

Power electronics converters are used in an increasing number of fields and applications. The improvements in power electronic devices and semiconductor materials have significantly reduced the cost of power converters and increased their efficiency. The research concerning the power converters, however, is mostly focus on processing the power for resistive or resistive-inductive load. In recent years, capacitive load applications have been gradually brought into the view of researchers as well as engineers. One successful application is the photoflash capacitor inside the camera [1]. In addition, capacitive smart material, such as piezoelectric material and Dielectric Electro Active Polymer (DEAP) [2][3], have gained extensive attention from academia and industry and they can be potentially used in a variety of applications [4][5]. The major advantage given by these materials is that it is possible to have non-magnetic actuator which can be applied in some magnetic sensitive occasions, e.g. in magnetic resonance imaging (MRI). These types of actuators have a capacitor-like structure where the dielectric material is confined between two electrodes. By applying a

voltage difference between the electrodes, charge is stored in the device. Then the induced electrostatic force creates an attraction between the two electrodes and causes a displacement of the dielectric material. This movement can be used to create a non-magnetic linear actuator that behaves as a variable capacitor in electrical terms. One common issue for above-mentioned capacitive loads is that they require relatively high voltage to be operated [6]. In the case of photoflash and piezoelectric material applications, this voltage is in the range of hundred volts. However, in the case of DEAP actuators, the voltage level is in the multi-kV range (typically 2.5 kV) [7].

Flyback converters are widely used in a large variety of industrial and consumer applications, such as laptop chargers, mobile phone chargers, standby power supplies for computers and other low power (<250 W) switch mode power supplies (SMPSs). The success of the flyback topology is due to its simplicity, low component count and cost. In fact, flyback converters are also often used for achieving high step-up ratios. However, in low power high voltage applications, the converter design becomes challenging mostly due to parasitic elements and component stresses. In high voltage applications [8] one of the major factors that affects converter performance is the flyback transformer. The transformer leakage inductance causes significant stresses over the primary power semiconductors. In addition, the transformer end-to-end capacitance (or stray capacitance) becomes one of the main concerns for high voltage applications (>1 kV) [4][9][10]. This is mostly due to the large amount of energy that is stored in this stray capacitance at high voltages. Limiting the energy stored in this interwinding stray capacitance can significantly improve the converter performance in terms of efficiency as well as increasing the working voltage. One solution to achieve this is to have an optimized transformer winding

configuration which results in a higher manufacturing cost. Besides, a small value of stray capacitance can be easily achieved by using a large core volume which would provide flexibility in the winding arrangement and in the selection of the wire diameter.

In this paper, in order to have a high voltage converter within a small converter volume, a new topology based on primary parallel secondary series flyback converter (PPSSFC) is presented. The new topology uses series and parallel connection of multiple transformers to achieve very high step-up ratio (up to 650) and low energy stored in the transformer output stray capacitance. A low-power high-voltage converter prototype has been designed for DEAP actuator (capacitive load) in heating valve applications. The converter is characterized by an input voltage of 3 V and an output voltage of 2 kV with a size of $\sim 3.5 \times 2.5$ cm. Experimental results validate the proposed topology achieving a step-up ratio of ~ 650 times (from a 3 V battery up to 2 kV).

II. PROPOSED TOPOLOGY: PRIMARY PARALLEL SECONDARY SERIES FLYBACK CONVERTER (PPSSFC)

It is challenging to achieve a low winding stray capacitance for a high voltage flyback transformer without applying complex winding configurations or without a highly optimized transformer design. This is especially true in the case of small transformers.

It is well known that capacitors series connection results in a smaller equivalent total capacitance. Based on this basic principle, the series connection of several transformer secondary windings is beneficial for reducing the equivalent secondary winding stray capacitance. In capacitive load charging applications, the energy stored in flyback transformer

during each charging cycle can be used as criteria for evaluating the capacitive load charging capability. That means, the more energy the transformer can store, the higher output voltage the converter can achieve in the case of same winding stray capacitance. For this reason, the parallel connection instead of series connection for primary windings tends to be beneficial in increasing the transferable energy to the secondary side.

The primary in parallel secondary in series based flyback converter has been derived and depicted in Fig. 1. Assuming N transformers, each transformer has a secondary winding stray capacitance C_s , then the secondary equivalent stray capacitance (C_{seq}) can be obtained through (1), which results in a capacitance is reduced by a factor of N .

$$C_{seq} = \frac{C_s}{N} \quad (1)$$

Similarly, the total primary equivalent inductance (L_{prieq}) can be calculated through the following equation

$$L_{prieq} = N \cdot (L_{p_m} + L_{p_l}) \quad (2)$$

where L_{p_m} and L_{p_l} are the primary magnetizing inductance and the leakage inductance, respectively. Considering the same peak current as in the single transformer case, the energy stored in the PPSSFC configuration will be N times larger than the energy stored in only one transformer.

Minimizing the energy stored in the windings stray capacitance is extremely beneficial for high voltage applications. However, this advantage is reduced by the increased secondary series resistance. In fact, the windings series connection at the transformers secondary sides results in higher winding losses since the total secondary winding

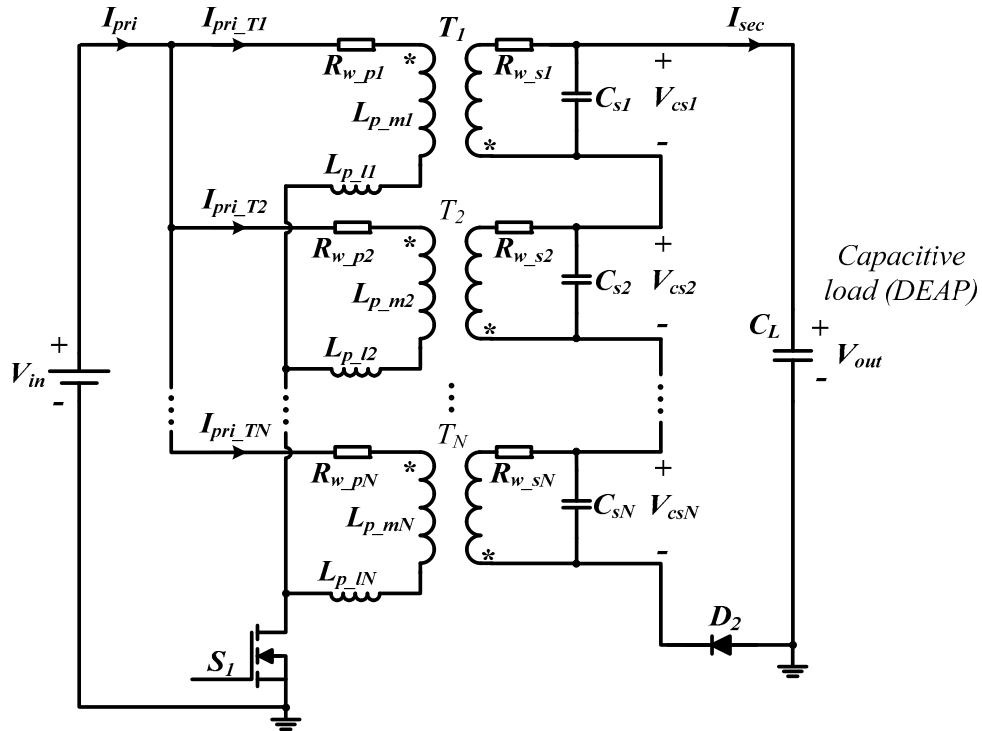


Fig 1. Circuit scheme of the proposed primary parallel secondary series flyback converter (PPSSFC) topology.

resistance (R_{w_seq}) is N times the single transformer secondary winding resistance (R_{w_s}), as in (3). Therefore, there will always be a trade-off between the energy stored in the output capacitance and the total secondary winding resistance.

$$R_{w_seq} = N \cdot R_{w_s} \quad (3)$$

III. OPERATING PRINCIPLES AND ANALYSIS

A. Assumption and General Information

In this investigation, the N -transformers are supposed to be identical. Possible mismatches of primary inductances due to parameters variation in the transformer production will cause different peak current in each transformer but, the secondary series connection forces the current in the transformers to be equal. Therefore, to simplify the analysis, the current in each transformer stage can be considered to be equal. Similarly, the mismatches of secondary stray capacitances will result in the unbalanced voltage sharing. The primary parallel connection forces the voltage over winding to be equal. For this reason, it is reasonable to assume that the voltage is balanced for the secondary windings.

Commonly, converters used in charging capacitive load applications stops working when the pre-set output voltage is reached and do not regulate the output voltage like in regular converters operating in steady state. In fact, the entire charging process consists of a series of consecutive charging cycles. In order to improve the charging efficiency, reduce the overall duration of the charging process and effectively limit the maximum flux density, the boundary mode control as well as primary peak current control methodology are the most suitable candidates and they have been widely employed in ongoing capacitive load charging applications [11-13]. Another advantage of these control modes is that it is possible to operate the converter in closed loop by using feedback from the converter primary side. This does not require a feedback loop that crosses the converter galvanic insulation barrier.

It is possible to analyze the working principle based on one charging cycle with the initial output voltage $V_{outInitial}$ due to the similarity in behavior for all charging cycles during the entire charging period. The behavior under high voltage condition represents the general case for the analysis. To some extent, the low voltage operation can be considered as a special case of high voltage operation. For these reasons, the high output voltage operation will be investigated in detail and the difference between high voltage and low voltage operation will be discussed briefly later.

B. Operation Modes Under High Output Voltage

The operation modes in one charging cycle under high output voltage condition can be expressed in four time intervals, presented on Fig. 2. And the corresponding critical operating waveforms are shown in the right side of Fig. 3.

Mode 1 [$t_0' \leq t \leq t_1'$: Fig. 2(a)]: At the beginning of this time interval, primary MOSFET S_1 is switched on. Due to the resonance between the secondary winding inductance and stray capacitance during the last operation mode [t_3' t_4'] of previous charging cycle, a negative minimum primary winding current is induced at time instant t_0' , which can be roughly estimated through the following equation

$$I_{pri_min} = -\sqrt{\frac{C_s}{L_{p_m}+L_{p_l}}} \cdot \frac{V_{outInitial}}{N} \quad (4)$$

where $V_{outInitial}$ not only represents the initial output voltage for the current charging cycle, but also stands for the final output voltage of previous cycle. C_s , L_{p_m} and L_{p_l} are the secondary winding stray capacitance, primary magnetizing inductance and primary leakage inductance for one transformer. N represent the total transformer number in the PPSSFC configuration.

In this operation mode the primary winding current increases from I_{pri_min} until it reaches the pre-set peak current I_{pri_p} . Considering the influence of the on-resistance of S_1 (R_{dson}), this current for each transformer I_{pri_T} can be expressed as

$$I_{pri_T}(t) = \frac{V_{in}}{N \cdot R_{dson}} + (I_{pri_min} - \frac{V_{in}}{N \cdot R_{dson}}) \cdot e^{-\frac{N \cdot R_{dson}}{L_{p_m}+L_{p_l}}(t-t_0')} \quad (5)$$

where V_{in} is the input voltage for the proposed converter.

Correspondingly, the on-time of S_1 can be calculated through the following equation

$$t_{0-1}' = -\left[\ln\left(\frac{I_{pri_p} \cdot N \cdot R_{dson} - V_{in}}{I_{pri_min} \cdot N \cdot R_{dson} - V_{in}}\right)\right] \cdot \frac{L_{p_m}+L_{p_l}}{N \cdot R_{dson}} \quad (6)$$

For this interval, neglecting the impact of winding resistances, the secondary winding voltage for each transformer can be expressed as

$$V_{cs}(t) = -(V_{in} - N \cdot I_{pri_T}(t) \cdot R_{dson}) \cdot n_{ratio} \quad (7)$$

where n_{ratio} stands for the turns ratio for one transformer and it is equal to the secondary winding turns divided by the primary winding turns.

Mode 2 [$t_1' \leq t \leq t_2'$: Fig. 2(b)]: When S_1 is switched off at time t_1' , the stored energy in the transformers cannot be transferred instantaneously to the capacitive load due to the influence of C_s . The voltage over C_s needs to build up until it reaches $V_{outInitial}/N$ before the current freewheeling period can start; this assumes that the voltage drop of freewheeling diode D_2 is negligible. The energy used for charging C_s comes from the energy stored in the transformers. This also means that the secondary peak current I_{sec_p} cannot be obtained through the direct reflection from I_{pri_p} , and can be approximately estimated by

$$I_{sec_p} = \sqrt{\frac{I_{pri_p}^2}{n_{ratio}^2} + \frac{C_s \cdot V_{cs}(t_1')^2}{n_{ratio}^2 \cdot L_{p_m}} - \frac{C_s \cdot V_{outInitial}^2}{n_{ratio}^2 \cdot N^2 \cdot L_{p_m}}} \quad (8)$$

where $V_{cs}(t_1')$ is the voltage over C_s at the time instant t_1' . In this time interval, the circuit is driven by the resonance between the secondary magnetizing inductance and C_s . The initial energy comes from the secondary peak current.

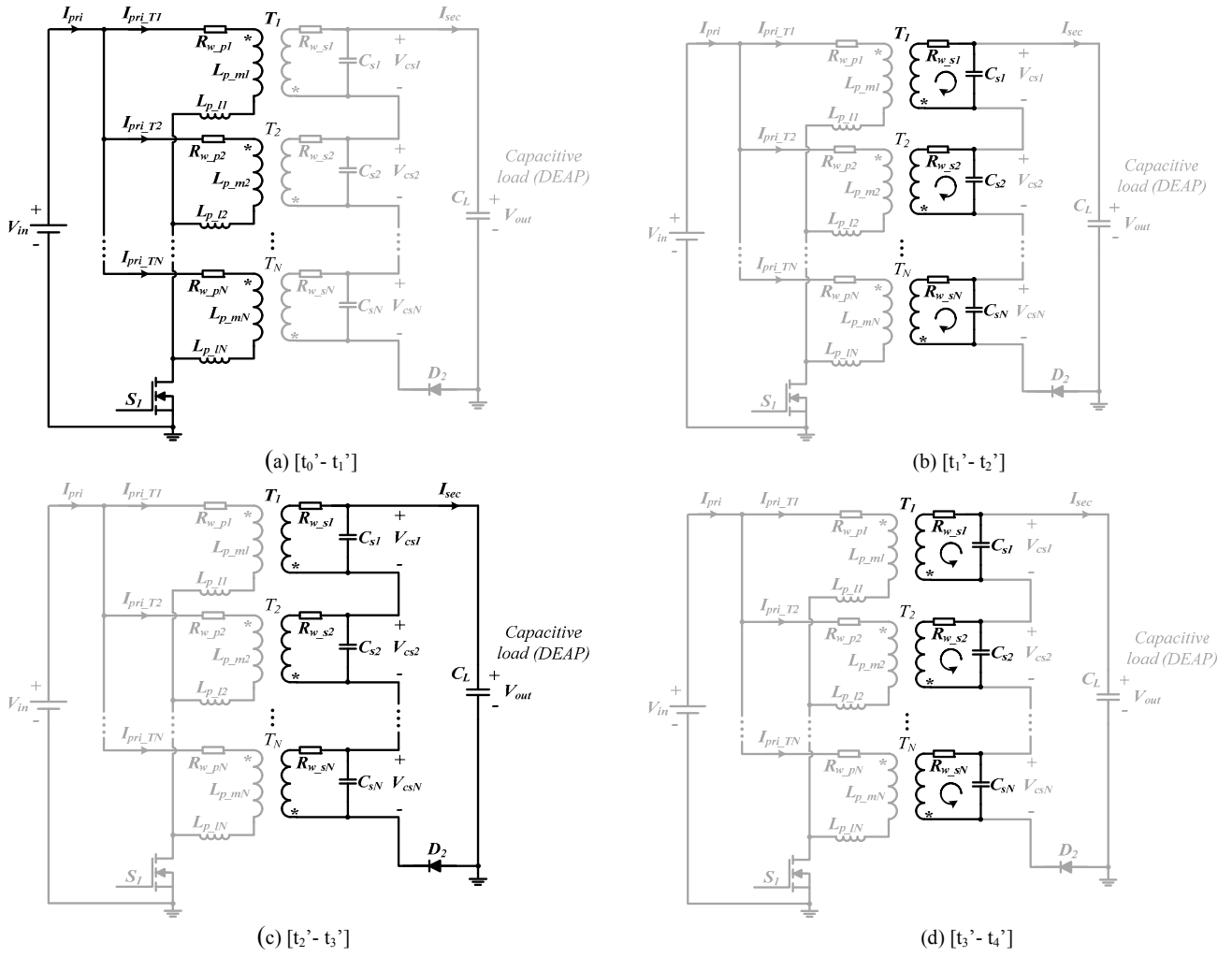


Fig. 2. Equivalent circuit schemes of the operation modes in PPSSFC under high output voltage condition.

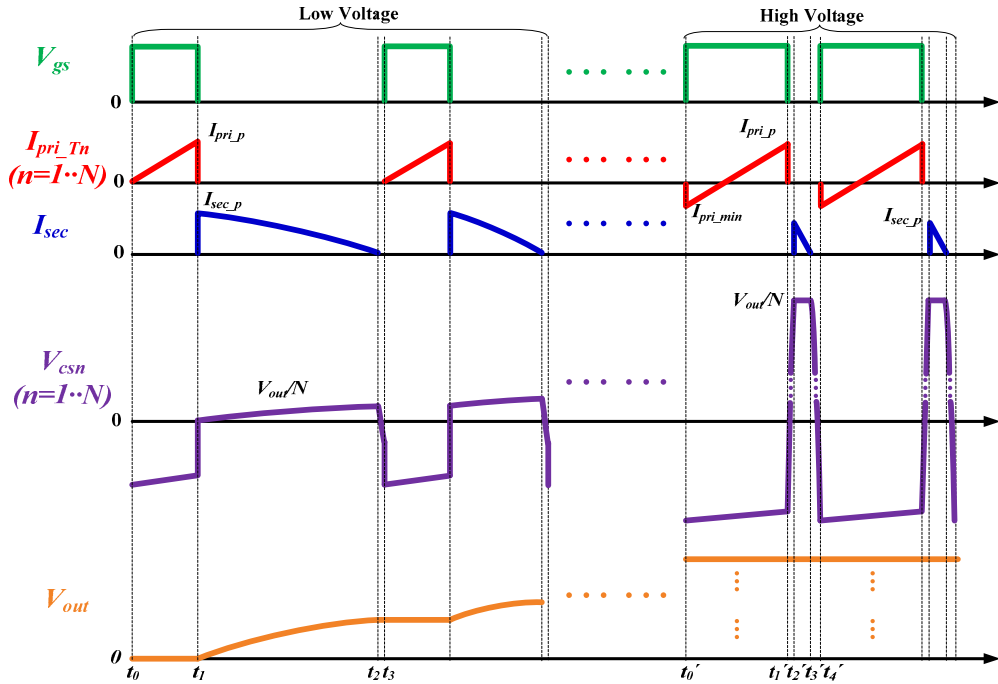


Fig 3. Converter critical operating waveforms at low voltage (left side) and at high voltage (right side).

Assuming negligible the influence of resistance and core losses, the voltage over C_s can be roughly estimated as in (9).

$$V_{cs}(t) = V_{cs}(t_1') \cdot \cos[\omega_r \cdot (t - t_1')] + I_{pri,p} \cdot \sqrt{\frac{L_{p,m}}{C_L}} \cdot \sin[\omega_r \cdot (t - t_1')] \quad (9)$$

where ω_f is the resonant angular frequency of secondary magnetizing inductance and C_s and can be calculated as

$$\omega_r = \frac{1}{n_{ratio} \cdot \sqrt{L_{p,m} \cdot C_s}} \quad (10)$$

Mode 3 [$t_2' \leq t \leq t_3'$: Fig. 2(c)]: When V_{cs} reaches $V_{outInitial}/N$ at the time instant t_2' , the secondary current freewheeling starts. If neglecting the impact of resistances in the secondary side and the voltage drop of D_2 , the freewheeling current can be expressed as

$$I_{sec}(t) = I_{sec,p} \cdot \cos[\omega_f \cdot (t - t_2')] - \frac{V_{outInitial} \cdot C_L}{\omega_f} \cdot \sin[\omega_f \cdot (t - t_2')] \quad (11)$$

where C_L is the capacitance of the capacitive load and ω_f is the resonant angular frequency of secondary magnetizing inductance and C_L , which can be calculate by (12).

$$\omega_f = \frac{1}{n_{ratio} \cdot \sqrt{L_{p,m} \cdot C_L}} \quad (12)$$

Correspondingly, output voltage for this time interval can be calculated as in (13).

$$V_{out}(t) = V_{outInitial} \cdot \cos[\omega_f \cdot (t - t_2')] + I_{sec,p} \cdot n_{ratio} \cdot \sqrt{\frac{L_{p,m}}{C_L}} \cdot \sin[\omega_f \cdot (t - t_2')] \quad (13)$$

This time interval ends when $I_{sec}(t)$ reaches 0, then the duration time for this period can be calculated through

$$t_{2-3}' = \frac{1}{\omega_f} \cdot \left[\arctan\left(\frac{I_{sec,p} \cdot \omega_f}{V_{outInitial} \cdot C_L}\right) \right] \quad (14)$$

Mode 4 [$t_3' \leq t \leq t_4'$: Fig. 2(d)]: After the secondary freewheeling current reaches 0 at the time t_3' , due to the stored energy in C_s , the drain voltage of S_1 is still larger than V_{in} , based on the basic principle of boundary mode control, S_1 cannot be switched on at this time instant. In fact, similar to *Mode 2*, at this time interval the circuit is driven by the resonance between secondary magnetizing inductance and C_s however in this case, with the initial energy from C_s .

The voltage over C_s in this period can be calculated through

$$V_{cs}(t) = \frac{V_{out}(t_3')}{N} \cdot \cos[\omega_r \cdot (t - t_3')] \quad (15)$$

where $V_{out}(t_3')$ is the voltage over C_s at the time t_3' .

Neglecting the impact of the body diode in S_1 , this time interval ends when V_{cs} reaches $-n_{ratio} \cdot V_{in}$, then the duration time can be calculated as

$$t_{3-4}' = \frac{1}{\omega_r} \cdot \left[\arccos\left(\frac{-n_{ratio} \cdot V_{in} \cdot N}{V_{out}(t_3')}\right) \right] \quad (16)$$

The presented analysis is simplified, a more detailed analysis of the time intervals is presented on [14].

C. Low Output Voltage Operation Discussion

At low output voltages, the key operating waveforms are presented in the left side of Fig. 3.

In *Mode 1*, the current starts from 0 and not from negative. This happens because of the small amount of energy stored in C_s at low output voltage, this is not sufficient to force the energy be transferred back to the primary creating a negative peak current.

In the case of low output voltage, the time used to charge C_s tends to be really short, therefore, the *Mode 2* does not need to be considered and the secondary peak current is the primary peak current divided by the transformer turns ratio, as illustrated in (17).

$$I_{sec,p} = \frac{I_{pri,p}}{n_{ratio}} \quad (17)$$

Furthermore, in *Mode 4*, at low output voltage, V_{cs} cannot reach $-n_{ratio} \cdot V_{in}$, the time interval can be estimated by half of the resonance period of secondary magnetizing inductance and C_s , shown in (18).

$$t_{2-3} = \frac{\pi}{\omega_r} \quad (18)$$

IV. PPSSFC TOPOLOGY DISCUSSION

A. Topology Advantages

Conventional flyback converters for high voltage capacitive charging applications require an optimized transformer design or large volume core in order to limit the secondary winding stray capacitance (C_s). As the converter output voltage (V_{out}) increases, the energy stored in the secondary stray capacitance ($E_{s,stray\,cap.}$) increases with the quadratic of the converter output voltage, shown in (19). This will limit the maximum achievable output voltage for the converter.

$$E_{s,stray\,cap.} = \frac{1}{2} \cdot C_s \cdot V_{out}^2 \quad (19)$$

The proposed topology is derived from a flyback topology by replacing the flyback transformer with two or more primary parallel secondary series connected transformers. In this case the converter output voltage is shared between the series connection of N secondary windings. This results that the energy stored in the winding stray capacitance is halved in case of $N = 2$, it is 1/3 in case of $N = 3$ and so on, as in equation

$$E_{s,stray\,cap.,PPSSFC} = N \cdot \frac{1}{2} \cdot C_s \cdot \left(\frac{V_{out}}{N}\right)^2 \quad (20)$$

where $E_{s,stray\,cap.,PPSSFC}$ stands for the total energy stored in the winding stray capacitances of N transformers. This characteristic greatly improves the charging ability of the converter.

Assuming an ideal flyback converter topology loss-less and without any parasitic elements, using peak current and boundary mode control schemes, the energy transferred by the flyback transformer in every charging cycle is constant, shown in (21).

$$E_{cycle} = \frac{1}{2} \cdot L_{p,m} \cdot I_{pri,p}^2 \quad (21)$$

Assuming a complete charging process for output voltage from 0 V up to V_{out} , the total energy required to charge the capacitive load is expressed as

$$E_{CL} = \frac{1}{2} \cdot C_L \cdot V_{out}^2 \quad (22)$$

Therefore, for a conventional flyback topology, the number of successive charging cycles, $N_{charging\ cycles}$, required to complete the entire charging process can be calculated as

$$N_{charging\ cycles} = \frac{C_L \cdot V_{out}^2}{L_{p,m} \cdot I_{pri,p}^2} \quad (23)$$

In the presented PPSSFC topology, assuming the primary current is maintained constant for each transformer, then in each charging cycle, the energy transferred by the flyback transformers increases by N times, as shown in (24).

$$E_{cycle\ PPSSFC} = \frac{1}{2} \cdot N \cdot L_{p,m} \cdot I_{pri,p}^2 \quad (24)$$

This eventually results that the PPSSFC topology requires N times less cycles for charging the capacitive load under same conditions, illustrated in (25).

$$N_{charging\ cycles\ PPSSFC} = \frac{C_L \cdot V_{out}^2}{N \cdot L_{p,m} \cdot I_{pri,p}^2} \quad (25)$$

Moreover, with PPSSFC configuration, the major advantages are that it is possible to achieve a high voltage converter within limited space and with a low price by employing small size off-the-shelf transformers. A large transformer with optimized for low stray capacitance can also be used to obtain high output voltage. This can normally be achieved by separating the windings in different sectors in a coil former or applying complex winding configurations, which will result in high transformer manufacturing cost. Small off-the-shelf transformers are not required to be highly optimized and therefore, they can be manufactured with very low cost. Besides, the PPSSFC with small transformers can provide higher flexibility in the PCB layout compared to the flyback configuration based on a single large transformer. This tends to be especially useful when converter power density optimization is required or large transformer cores are not available in the desired size.

B. Topology Disadvantages

Compared to one single transformer operated at the same peak current, like the transferrable energy stored in the transformer magnetizing inductance increases by N times, the non-transferrable energy stored in the leakage inductance will increase by N as well, illustrated in (26) and (27).

$$E_{leak} = \frac{1}{2} \cdot L_{p,l} \cdot I_{pri,p}^2 \quad (26)$$

$$E_{leak\ PPSSFC} = \frac{1}{2} \cdot N \cdot L_{p,l} \cdot I_{pri,p}^2 \quad (27)$$

where E_{leak} is the energy stored in the leakage inductance for one transformer, and E_{leak} represents the total leakage inductance energy in the PPSSFC configuration. The N times larger leakage inductance energy will bring much more pressure for the voltage stress of S_l . Fortunately, a variety of low-voltage power MOSFETs are available on the market. The impact of this disadvantage can be minimized by carefully calculating the voltage stress caused by the energy

stored in the leakage inductance and selecting the power semiconductors with suitable voltage rating.

Assuming identical current sharing between all the transformers primary stages, the current through S_l can be expressed as

$$I_{S1}(t) = N \cdot I_{pri,T}(t) \quad (28)$$

This means the power MOSFET S_l has higher current stress compared with one transformer case. However, low voltage MOSFETs are available with very low on-resistances and for these reasons, this disadvantage has very limited impact.

The series connection of the transformers on the high voltage side provides increased loss due to the series connection of the secondary winding resistances, which will, to some extent, limit the benefit from reducing stray capacitance. The increased number of components (transformers) is another disadvantage of the PPSSFC configuration.

V. PROTOTYPE IMPLEMENTATION

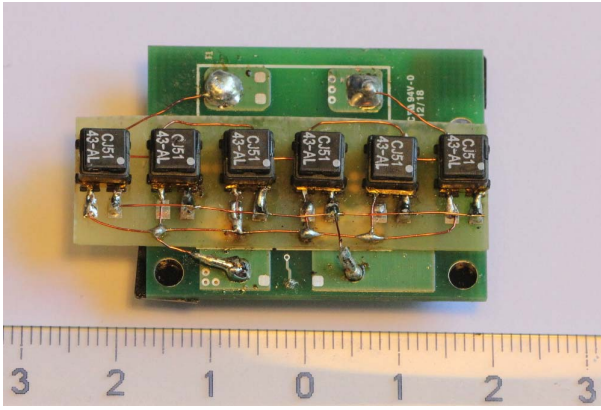
In order to validate the proposed topology, a small size prototype with the ability to charge the capacitive load to a high voltage has been implemented, as shown in Fig. 4 (a) and (b). An off-the-shelf flyback transformer CJ5143-AL from Coilcraft is employed in this prototype [15]. The critical parameters for the converter, capacitive load as well as the flyback transformer are summarized in Table I. Peak current as well as boundary mode control schemes are implemented by the capacitor charger controller LT3750 from Linear Technology [13]. An optimized design and layout can furthermore reduce the converter volume.

VI. EXPERIMENTAL RESULTS

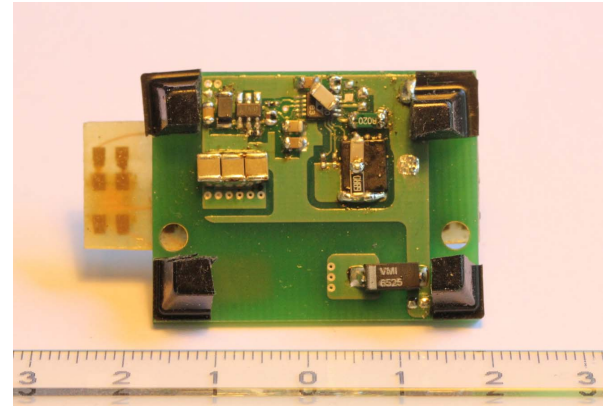
The experiments have been carried out to verify the proposed topology as well as the implementation of the prototype. The overall charging process for a 220 nF capacitive load is shown in Fig. 5. The maximum output voltage (2 kV) is achieved through a 3 V input voltage within 400 ms continuous charging time.

TABLE I.
PARAMETERS OF PPSSFC PROTOTYPE, DEAP ACTUATOR AND
FLYBACK TRANSFORMER

| Parameters | Values |
|--------------------|-------------|
| V_{in} | 3 V |
| Maximum V_{out} | 2 kV |
| Transformer number | 6 |
| Converter size | 3.5x2.5 cm |
| C_L | 220 nF |
| n_{ratio} | 15 |
| $L_{p,m}$ | 15 μ H |
| $L_{p,l}$ | 250 nH |
| C_s | 18.5 pF |
| $R_{w,p}$ | 1 Ω |
| $R_{w,s}$ | 25 Ω |
| $I_{pri,p}$ | 1.2 A |



(a) Top view



(b) Bottom view

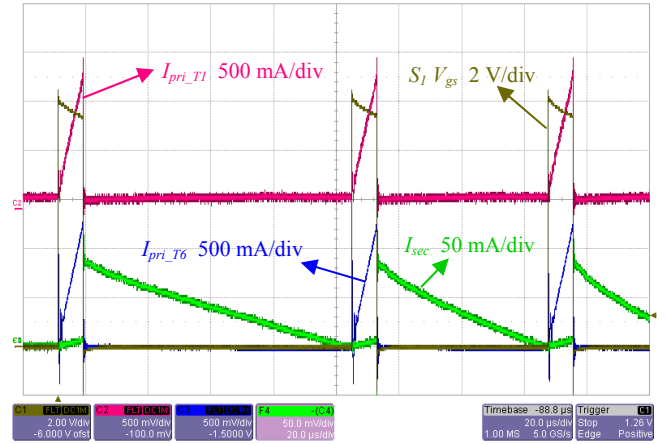
Fig. 4. Converter prototype (reference scale in cm).

The detailed operating waveforms for three successive charging cycles at low voltage are shown in Fig. 6 (a) and (b), including both current and voltage waveforms. From the primary winding currents in transformer T_1 and T_6 , it can be seen that good current sharing between transformers is achieved. Moreover, it also can be observed that the peak current and the boundary mode control are achieved. At low output voltage, the resonance current at the beginning of each switching cycle is caused by the primary leakage inductance and secondary winding stray capacitance. Due to the impact of parasitic capacitors in the secondary side, it is difficult to measure the real voltage waveform over C_s for one of the transformers. Instead, the overall transformers secondary voltage is measured. These voltage waveforms are presented on Fig. 6 (b), where the three operation modes at low output voltage can be observed.

In a similar way, the experimental waveforms for three charging cycles at high voltage operation are shown on Fig. 7. The realization of current sharing between transformers can be confirmed through the winding current waveforms in Fig. 7 (a). Moreover, at the beginning of each charging cycle a negative current spike can be observed. This was mentioned in the analysis and it is also verified in the current waveforms. At

high output voltage, a resonance is observed at the beginning of every switching cycle due to the secondary winding leakage inductance and secondary winding stray capacitance. In the voltage waveforms on Fig. 7 (b), the charging of the intra winding capacitance C_s can be observed.

The experimental results verify that the converter prototype operates accordingly to the analysis performed in the previous section.



(a) Current waveforms

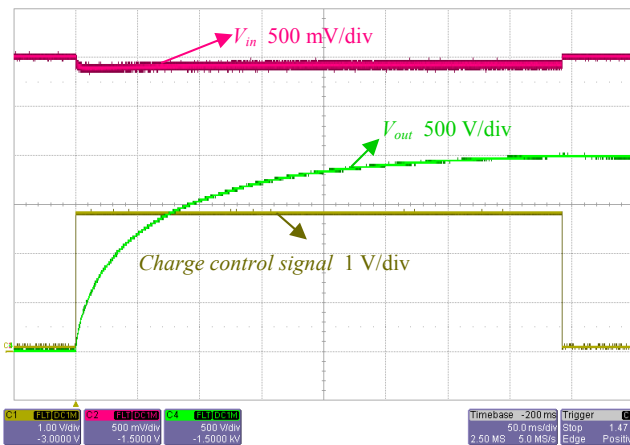
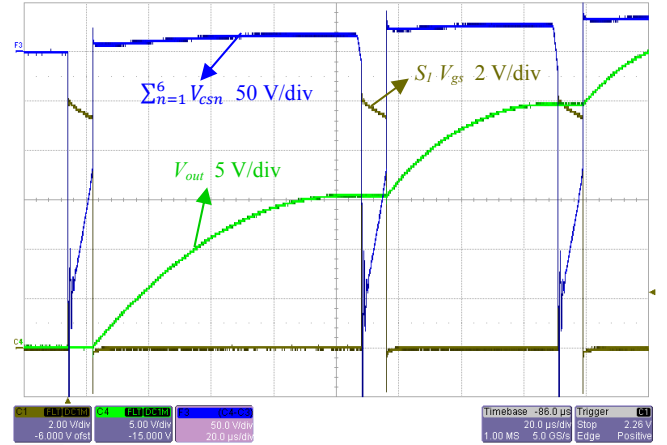
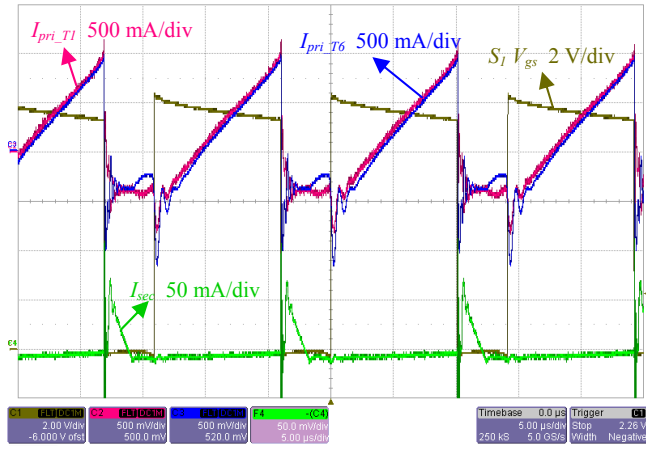


Fig. 5. Overall experimental waveform for the entire charging process.

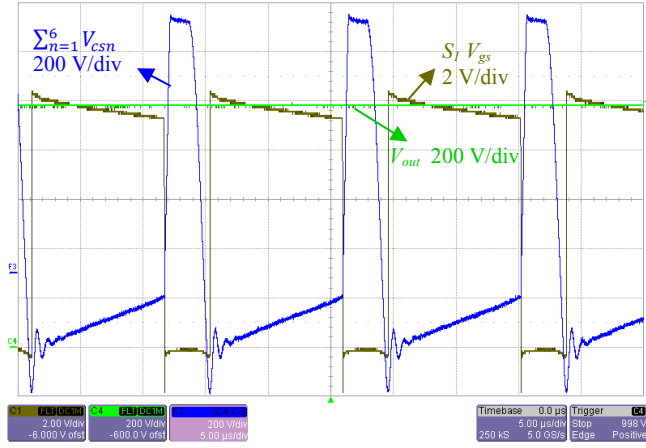


(b) Voltage waveforms

Fig. 6. Detailed experimental waveforms for charging cycles at low output voltage.



(a) Current waveforms



(b) Voltage waveforms

Fig. 7. Detailed experimental waveforms for charging cycles at high output voltage.

VII. CONCLUSIONS

The paper presents a primary parallel secondary series flyback converter (PPSSFC). The new topology is derived from the conventional flyback converter and uses multiple transformers to mitigate the effects of the secondary stray capacitance. The topology is very suitable for applications which require very large step-up ratios, low end-to-end capacitance and high output voltage within limited space.

The operating principles and switching cycle based analysis are presented for both high and low voltage operation. The advantages and disadvantages for the proposed topology are discussed in terms of energy stored in the secondary stray capacitance, transferrable and non-transferrable energy stored in the flyback transformers as well as the voltage and current stress for semiconductor components. Compared to a single large transformer case, the proposed topology can be beneficial for reducing the transformer winding complexity and for providing high flexibility in PCB layout.

The proposed PPSSFC topology has been verified on a converter for a DEAP actuator (capacitive load). The PPSSFC achieved very high step-up ratio (650x) and high voltage operation (2 kV) and it is based on six off-the-shelf transformers. It is observed that the switching cycle based

operating analysis of the proposed converter is exactly validated by the experimental results.

REFERENCES

- [1] Sokal, N.O.; Redl, R., "Control algorithms and circuit designs for optimal flyback-charging of an energy-storage capacitor (e.g., for flash lamp or defibrillator)," IEEE Transactions on Power Electronics, vol.12, no.5, pp.885-894, Sep 1997.
- [2] Das-Gupta, D.K.; Doughty, K., "Electro-Active Polymers in Non-Destructive Dielectric Evaluation," IEEE Transactions on Electrical Insulation, vol.EI-20, no.1, pp.20,28, Feb. 1985.
- [3] Shankar, Ravi, Tushar K. Ghosh, and Richard J. Spontak. "Dielectric elastomers as next-generation polymeric actuators." Soft Matter 3.9 (2007): 1116-1129.
- [4] D. Campolo, M. Sitti, and R. S. Fearing, "Efficient charge recovery method for driving piezoelectric actuators with quasi-square waves," IEEE Transactions on Ultrasonics, Ferroelectrics and Frequency Control, vol. 50, pp. 237-244, 2003.
- [5] R. Sarban, B. Lassen, and M. Willatzen, "Dynamic Electromechanical Modeling of Dielectric Elastomer Actuators With Metallic Electrodes," IEEE/ASME Transactions on Mechatronics, vol. 17, pp. 960-967, 2012.
- [6] Eitzen, L.; Graf, C.; Maas, J., "Cascaded bidirectional flyback converter driving DEAP transducers," IECON 2011 - 37th Annual Conference on IEEE Industrial Electronics Society, pp.1226-1231, 7-10 Nov. 2011.
- [7] L. Huang, Z. Zhang, and M. A. E. Andersen, "A review of high voltage drive amplifiers for capacitive actuators," in 47th International Universities Power Engineering Conference (UPEC), 2012, pp. 1-6.
- [8] S.E. Thomas; C. W. Tipton, and D. Porschet, "Fabrication and Practical Considerations of a Flyback Transformer for Use in High Pulsed-Power Applications," Thirty-Eighth Southeastern Symposium on System Theory (SSST), 2006, pp.406-409.
- [9] S.-K. Chung, "Transient characteristics of high-voltage flyback transformer operating in discontinuous conduction mode," IEEE Proceedings - Electric Power Applications, vol. 151, pp. 628-634, 2004.
- [10] Dalessandro, L.; da Silveira Cavalcante, F. and Kolar, J. "Self-Capacitance of High-Voltage Transformers," IEEE Transactions on Power Electronics, vol.22, no.5, pp.2081-2092, Sep. 2007.
- [11] Sokal, N.O.; Redl, R., "Control algorithms and circuit designs for optimally flyback-charging an energy-storage capacitor (e.g. for a flash lamp)," Fifth Annual Applied Power Electronics Conference and Exposition, APEC '90 Conference Proceedings, pp.295-302, 11-16 March 1990.
- [12] Wong, K., "Energy-Efficient Peak-Current State-Machine Control With a Peak Power Mode," IEEE Transactions on Power Electronics, vol.24, no.2, pp.489-498, Feb. 2009.
- [13] "LT3750 Capacitor Charger Controller Datasheet," Linear Technology Corporation, USA.
- [14] L. Huang, Z. Zhang, and M. A. E. Andersen, " Detailed Behavior Analysis for High Voltage Bidirectional Flyback Converter Driving DEAP Actuator," IECON 2013 - 39th Annual Conference on IEEE Industrial Electronics Society, pp.623-628, Nov. 2013.
- [15] "CJ5143-AL flyback transformer datasheet", Coilcraft Incorporated, USA.

APPENDIX E

High Voltage Bidirectional Flyback Converter Driving DEAP Actuator for Automotive Applications

The 9th IEEE Vehicle Power and Propulsion Conference (VPPC 2013)

High Voltage Bidirectional Flyback Converter Driving DEAP Actuator for Automotive Applications

Lina Huang, Zhe Zhang, Michael A. E. Andersen
Technical University of Denmark, Ørsted Plads,
Building 349, 2800 Kgs. Lyngby, Denmark
huang@elektro.dtu.dk, zz@elektro.dtu.dk,
ma@elektro.dtu.dk

Rahimullah Sarban
Danfoss PolyPower A/S, Nils Koppel Allé,
Building 404 – 221, 2800 Kgs. Lyngby, Denmark
sarban@danfoss.com

Abstract— DEAP (Dielectric Electro Active Polymer) is a new type of smart material. The actuator based on DEAP material tends to be applied in a variety of occasions. It will have prosperous future when employed in automotive field. This paper is focused on the design and implementation of a low input voltage and high output voltage bidirectional converter for driving the DEAP actuator. The detailed design and implemented parameters have been summarized, especially for the high voltage transformer. The experiments have been performed to validate the design and implementation.

Keywords—DEAP actuator; high voltage; flyback; bidirectional; automotive application

I. INTRODUCTION

In recent years, with the continuous emergence of various new smart materials, DEAP (Dielectric Electro Active Polymer) material was brought into the view of researchers. Dielectric elastomer material is sandwiched between two compliant electrodes, which constitutes the fundamental structure of DEAP material [1]. When voltage is applied to the electrodes, because of the electrostatic pressure, the elastomer is compressed in thickness and expands in the plane perpendicular to the thickness direction [2]. Therefore DEAP material can be made into actuators.

Smart material based actuators in automotive applications have gained increasing attentions from researchers and engineers over the last decades, especially shape memory alloy and piezoelectric material based actuators [3]–[6]. In addition, piezoelectric actuator based fuel injector has already been marketed by world's leading automotive electronics suppliers.

DEAP actuators are constructed by rolling, stacking, or folding multiple layers of a thin (10 – 100 μm) polymer sheets. Mechanical suspenders and electrical connectors are subsequently applied to the rolled or stacked structure. DEAP, due to its polymeric nature, is 7 times lighter than steel. This results the corresponding actuators to be lighter than conventional metal based actuators and motors. In addition, DEAP actuators are noiseless as their mechanical constructions do not contain gearings, bearings, joint, and sliding as is the case with conventional actuators and motors. Furthermore, the DEAP material has a fast electromechanical response with a rise time in μs .

All the aforementioned properties of DEAP material make the corresponding actuators light, silent, and fast. Actuators

with such properties are of high interest in automotive applications to improve vehicles efficiency and comfort. DEAP actuators can potentially be used for automotive loudspeakers, active vibration damping of switchboards and other sensitive parts, mirror positioning, seat adjustment, headlight adjustment, window adjustment to mention a few.

The car battery is the common power source for the actuators in automotive applications [6]. However, the stimulating voltage for DEAP actuators is relatively very high, normally in the range of kilovolts [7]. Therefore, when DEAP actuators are used in automotive products, a low input voltage and high output voltage DC-DC converter is required, which is actually the main focus of this paper.

Two important considerations need to be pointed out here. 1) The basic configuration of DEAP material is similar to the structure of capacitor, which means DEAP actuator is fundamentally a capacitive load. The design methodology of a DC-DC converter driving capacitive load is different from the normal converter powering resistive load. 2) The efficiency of DEAP actuator is defined as mechanical work divided by input energy to actuator. It had been validated that this efficiency is very low and most energy is stored in the actuator [9]. Therefore, a bidirectional operation converter which can recover the energy to the power source must be a suitable choice in terms of energy utilization [8], [9].

II. HIGH VOLTAGE BIDIRECTIONAL CONVERTER DESIGN

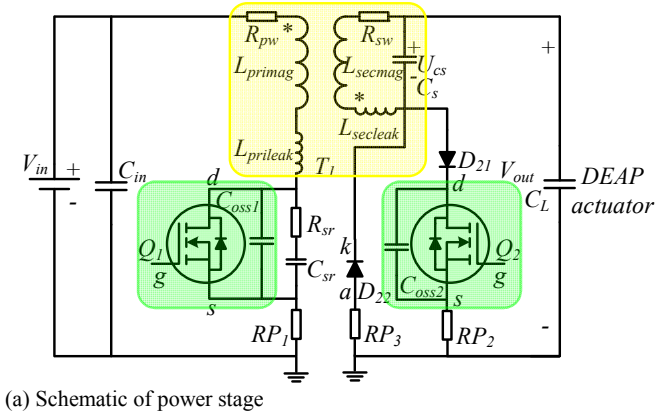
In order to drive DEAP actuator, a battery powered high output voltage converter has been proposed to implement. The detailed specifications for driving device are summarized in table I.

In this low power and high voltage case, flyback or piezoelectric transformer based converter tends to be good

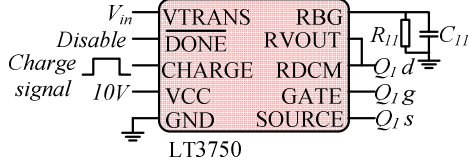
TABLE I. SPECIFICATIONS FOR BATTERY POWERED HIGH VOLTAGE CONVERTER

| Parameters | Specifications |
|-----------------------------|--------------------------------------------------------------------------------------------------|
| Input voltage | 3 V * |
| Output voltage | 0-2.4 kV |
| Capacitance of actuator | 220 nF |
| Function | Have the ability to charge capacitive actuator from 0V to 2.4 kV and discharge from 2.4 kV to 0V |
| Charge and discharging time | 300 ms~5 s |

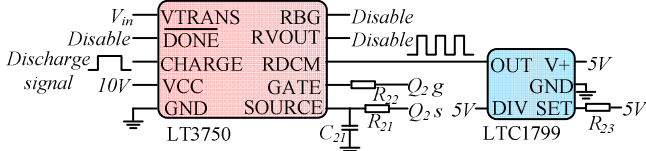
* 3V is used in these tests, but it can as well be designed for 12V nominal automotive battery.



(a) Schematic of power stage



(b) Schematic of charge control



(c) Schematic of discharge control

Fig. 1. Schematic of high voltage bidirectional flyback converter.

choice. Hence, a high voltage bidirectional flyback converter has been designed to fulfill the specifications. The schematic for the whole converter is shown in Fig. 1 and the fundamental working principles have been investigated in [10].

The power stage is shown in Fig. 1 (a). In addition, some critical parasitic elements, such as primary leakage inductor $L_{primeleak}$, secondary winding stray capacitor C_s as well as the output capacitor of primary MOSFET C_{oss1} etc., are depicted as well. In fact, the primary and secondary leakage inductors cannot exist at the same time. When energy flow is from power source to secondary side, we use primary leakage inductor to describe the untransferable energy stored in flyback transformer, and vice versa. Due to the poor performance of body diode in high voltage MOSFET Q_2 , a blocking diode D_{21} is employed in order to prevent the current passing through the body diode and a high voltage diode D_{22} is adopted to provide the freewheeling path for the secondary current. Normally, RC snubber or RCD clamp circuit is required to suppress the ringing associated with the leakage inductance in order to protect the MOSFET. For the purpose of saving space, only simple RC snubber circuit is employed in the primary side. Owing to the efficiency issue, any extra capacitor must be avoided in the high voltage side. Hence, neither RC nor RCD circuit is employed in the secondary side. However, it is essential to select the MOSFET with higher breakdown voltage in order to make sure that the extra stress voltage caused by the energy stored in the leakage inductance will not damage the Q_2 . With the aim of realizing peak current control, the current sensing resistors RP_1 and RP_2 are employed to transform the

TABLE II. POWER STAGE COMPONENTS AND PARASITIC PARAMETERS

| Component name | Device | |
|-----------------------|----------|--------------------------------------|
| Q_1 | INFINEON | BSC320N20NS3 G ($V_{DSS}=200V$) |
| Q_2 | IXYS | IXTV03N400S ($V_{DSS}=4000V$) |
| D_{21} and D_{22} | VMI | VMI6525 ($V_{RWM}=5000V$) |
| RP_1 | OHMITE | LVK12R020FER (1206 20mΩ 1%) |
| RP_2 and RP_3 | YAGEO | RC1206FR-101RL (1206 1Ω 1%) |
| R_{sr} | YAGEO | RE1206DR-0768RL (1206 68Ω 0.5%) |
| C_{sr} | AVX | 12062A221JAT2A (1206 220pF 200V C0G) |
| C_{oss1} | | 135pF @ $V_{ds}=100V$ |
| C_{oss2} | | 19pF @ $V_{ds}=25V$ |

current signal into voltage. Yet, RP_3 is just used to measure the current through diode D_{22} without any purpose concerning control. The critical components employed in the power stage are listed in Table II.

Fig. 1 (b) and (c) illustrate the charging and discharging control circuits, respectively. The capacitor charger controller LT3750 from Linear Technology is employed to realize the charging process control. It operates in the boundary conduction mode, which is beneficial in terms of improving the charging efficiency as well as reducing the total charging time [11]. It is not straightforward to apply LT3750 for discharging capacitive load. Indeed, more issues must be taken into consideration. The discharging LT3750 cannot directly connect to the power stage owing to the issues of maximum rating. Hence, another oscillator IC LTC1799, from Linear Technology as well, is employed to implement the fixed frequency operation for LT3750 instead of the default boundary mode operation. In addition, due to the huge influence of secondary winding stray capacitor C_s , an additional driving resistor R_{22} needs to be utilized in order to limit the switching speed. Furthermore, the huge spike on current sensing resistor RP_2 caused by charging C_s must be filtered through RC circuit (R_{21} and C_{21}) before entering the SOURCE pin of LT3750. In fact, two boost ICs are employed to achieve the stable 5V and 10V from 3V input voltage as well, which are not depicted in the schematic.

III. HIGH VOLTAGE FLYBACK TRANSFORMER IMPLEMENTATION

The most important part in the converter must be the high voltage flyback transformer. Because of the special application, no commercial transformer fulfilling the demands is available. Therefore, a high voltage flyback transformer must be designed and implemented by ourselves.

A pair of E 20/10/6 cores with the material ferrite N27 from EPCOS has been selected. One EF20 core has 90μm air gap with core part number B66311G90X127 and the other does not have air gap with core part number B66311GX127. The EF20 bobbin also from EPCOS has been employed to place the windings. There are in total 6 layers for the secondary winding and the adjacent layers have been insulated with 0.1mm kapton tape. In addition, 0.15mm margin tapes are adopted to guarantee the enough insulation strength at the edge of the bobbin. In order to reduce the stray capacitance of the winding, the z-winding method has been employed. AWG32 wire is used for the secondary winding and AWG29 wire for primary

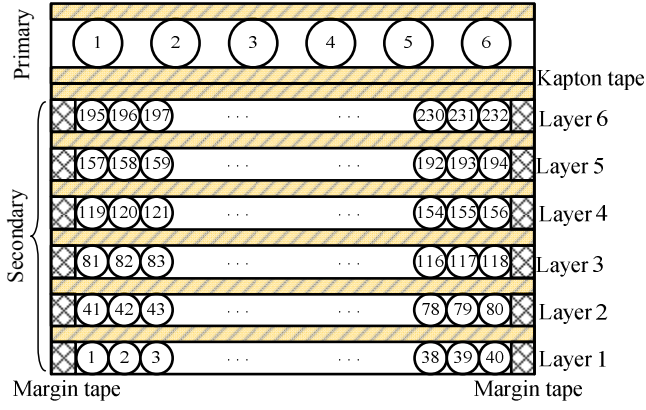


Fig. 2. The configuration of the high voltage flyback transformer.

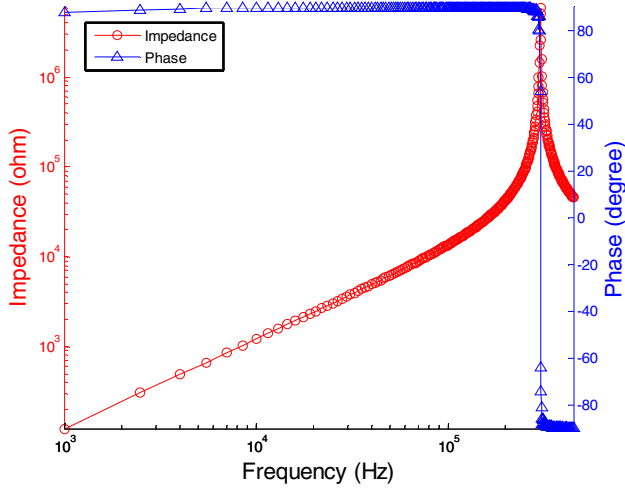


Fig. 3. Impedance measurement of secondary winding.

TABLE III. HIGH VOLTAGE FLYBACK DESIGN PARAMETERS

| Parameters | Values |
|---------------------------------------|--------------------------------------------------------|
| Primary turns | 6 |
| Secondary turns | 240 |
| Core type | EF20 |
| Core material | Ferrite N27 |
| Core air gap | 90 μ m |
| Primary peak current | 4A |
| Secondary peak current | 103mA |
| Core reluctance | 533019.9A/Wb |
| Air gap reluctance | 2057447A/Wb |
| Total reluctance | 2590467A/Wb |
| Used peak flux density (B_{peak}) | 266mT |
| Primary inductance | 13 μ H |
| Primary leakage inductance | 300nH |
| Secondary inductance | 18.85mH |
| Secondary leakage inductance | 450 μ H |
| Secondary stray capacitance | 14.2pF |
| Primary AC resistance | 79.4m Ω -106.81m Ω @ f =1kHz-100kHz |
| Secondary AC resistance | 4.99 Ω -29.92 Ω @ f =1kHz-100kHz |

winding because of higher current. Two layers of kapton tape are employed between primary and secondary winding to provide a reinforced insulation. The detailed configuration for the implemented transformer is depicted in Fig. 2.

After implementing the transformer, all the parameters, such as the magnetizing inductance, leakage inductance and

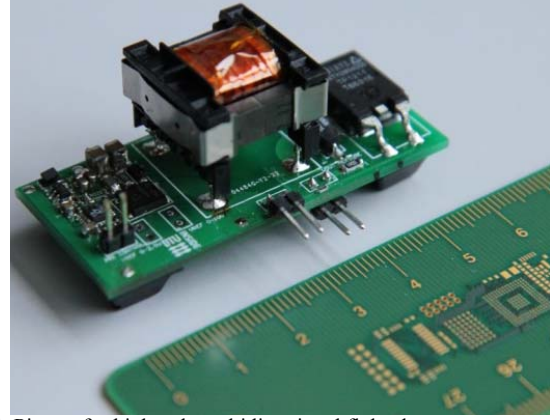


Fig. 4. Picture for high voltage bidirectional flyback converter.

winding stray capacitance, can be measured using N4L PSM1735 frequency response analyzer with its impedance analysis interface. Concerning the efficiency as well as reliable operation issues, it is essential to know the value of C_s , which can be calculated through the first resonance frequency in impedance measurement of secondary winding, shown in Fig. 3 [12]. All the parameters concerning the transformer are summarized in Table III and the final implemented converter is shown in Fig. 4.

IV. EXPERIMENTAL VALIDATION AND EFFICIENCY MEASUREMENT

In order to validate the design and implementation, experiments have been performed. The overall waveform for charging capacitive load to 2.4kV and discharging to 0 is shown in Fig. 5, which indicates the converter can satisfy the design specifications. In addition, for verifying the normal operation of charging process in detail, the critical waveforms for first three charging cycle and three successive cycles when output voltage is charged to around 2kV are shown in Fig. 6 and 7, respectively. Similarly, in discharging process, the critical waveforms of one single cycle when output voltage is discharged to around 2kV and the last three discharging cycles are shown in Fig. 8 and 9, respectively. An efficiency measurement has been carried out as well in order to have a

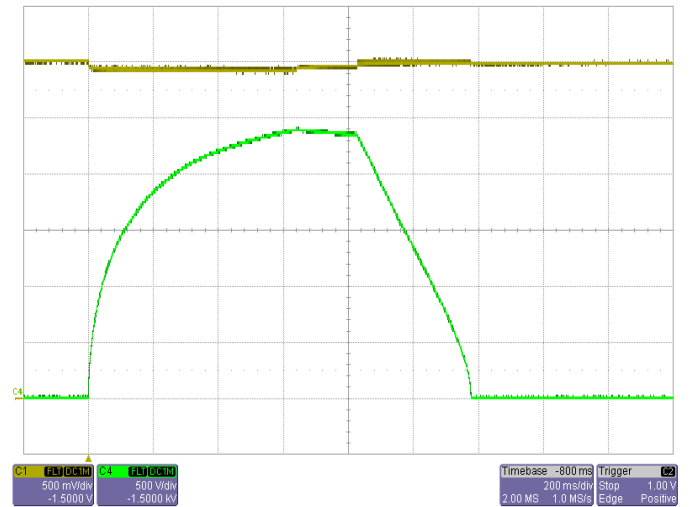


Fig. 5. Overall waveform for charging and discharging processes (CH1- V_{in} CH4- V_{out}).

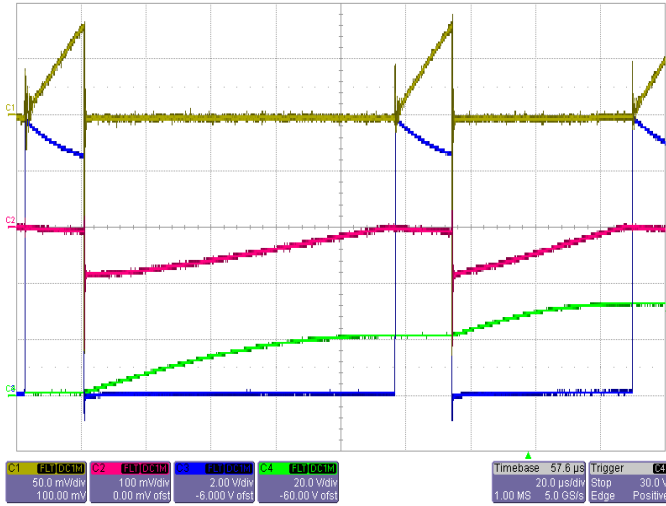


Fig. 6. Critical waveforms for low output voltage operation in charging process (CH1-VRP1 CH2-VRP3 CH3-Q1 Vg CH4-V_{out}).

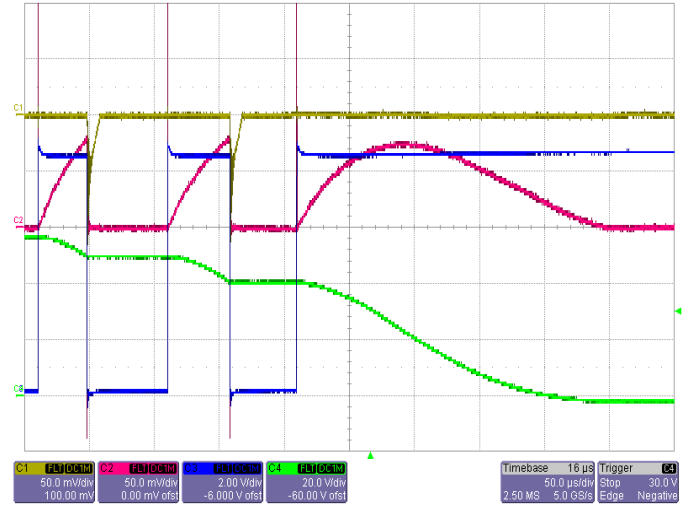


Fig. 9. Waveforms for low output voltage operation in discharging process (CH1-VRP1 CH2-VRP2 CH3-Q₂ Vg CH4-V_{out}).

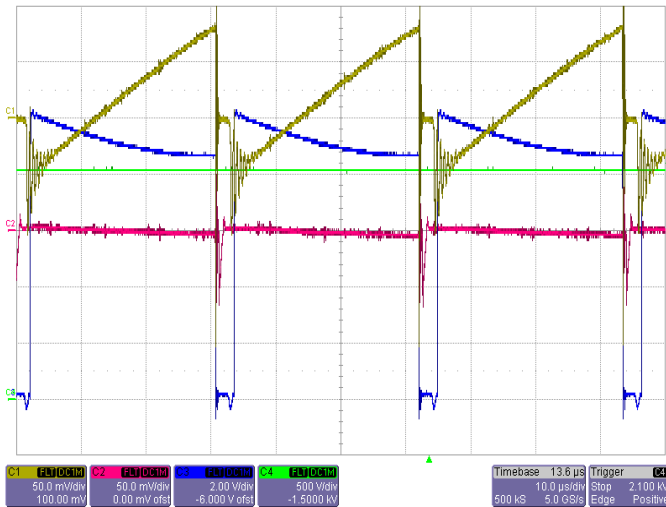


Fig. 7. Waveforms for high output voltage operation in charging process (CH1-VRP1 CH2-VRP3 CH3-Q1 Vg CH4-V_{out}).

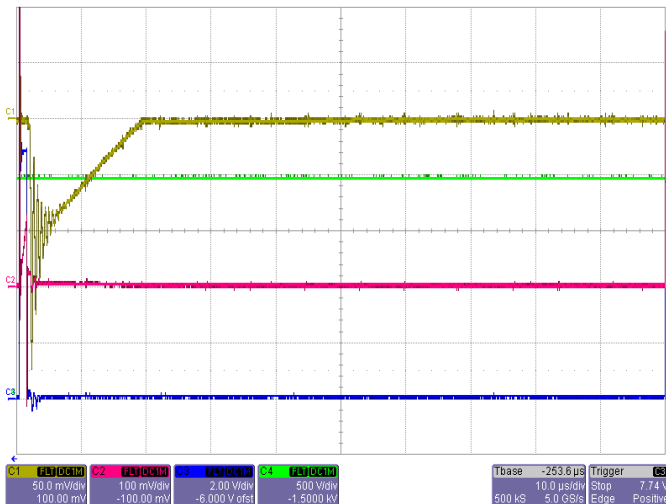


Fig. 8. Waveforms for high output voltage operation in discharging process (CH1-VRP1 CH2-VRP2 CH3-Q₂ Vg CH4-V_{out}).

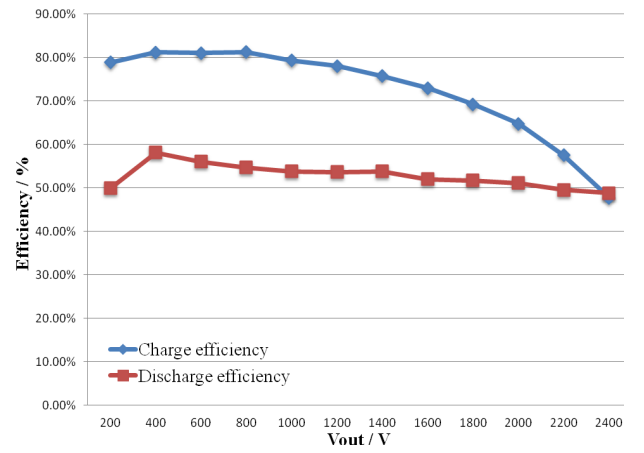


Fig. 10. Efficiency curves for both charging and discharging process.

better understanding for the converter. The charging and discharging efficiency curves are shown in Fig. 10.

V. CONCLUSION

As a new type of smart material, DEAP material as well as its potential applications in automotive field are introduced. A low voltage input bidirectional flyback based converter for driving DEAP actuator has been designed and implemented. The design parameters, selected components as well as the critical parasitic parameters are provided in detail, especially for the high voltage flyback transformer. The experiments have been carried out to validate the design and implementation. The efficiency curve has been measured in order to have a better understanding for the converter.

REFERENCES

- [1] R. Jones; P. Wang; B. Lassen, and R. Sarban, "Dielectric elastomers and compliant metal electrode technology," 2010 15th IEEE Mediterranean Electrotechnical Conference (MELECON), 2010, pp. 368 -373.
- [2] R. Sarban, B. Lassen, and M. Willatzen, "Dynamic electromechanical modeling of dielectric elastomer actuators with metallic electrodes," IEEE/ASME Transactions on Mechatronics, vol. 17, no. 5, pp. 960-967, October 2012.

- [3] E. A. Williams, G. Shaw and M. Elahinia, "Control of an automotive shape memory alloy mirror actuator," *Mechatronics*, vol. 20, pp. 527-534, 2010.
- [4] M. Collado, F. Alvarez, R. Cabas, I. Gabikaetxebarria and J. Ugalde, "SMA Pin Puller Actuator for an Automotive Application," *Conference proceeding Actuator*, pp. 216-219, 2010.
- [5] G. Gnad and R. Kasper, "Power drive circuits for piezo-electric actuators in automotive applications," *IEEE International Conference on Industrial Technology*, pp. 1558-1561, 2006.
- [6] V. A. Neelakantan, G. N. Washington and N. K. Bucknor, "Model predictive control of a two stage actuation system using piezoelectric actuators for controllable industrial and automotive brakes and clutches," *Journal of Intelligent Material Systems and Structures*, vol. 19, pp. 845-857, 2008.
- [7] R. Shankar, T. K. Ghosh and R. J. Spontak, "Dielectric elastomers as next-generation polymeric actuators," *Soft Matter*, The Royal Society of Chemistry, vol. 3, pp. 1116-1129, 2007.
- [8] Y. Bar-Cohen, *Electroactive Polymer [EAP] Actuators as Artificial Muscles: Reality, Potential, and Challenges*, 2nd ed. Washington, DC: SPIE, 2004.
- [9] M. J. Tryson, R. Sarban and K. P. Lorenzen, "The dynamic properties of tubular DEAP actuators," *Electroactive Polymer Actuators and Devices (EAPAD)*, vol. 7642, 2010.
- [10] L. Huang, P. Thummala, Z. Zhang and M. A. E. Andersen, "Battery powered high output voltage bidirectional flyback converter for cylindrical DEAP actuator," *IEEE International Power Modulator and High Voltage Conference (IPMHVC)*, 2012.
- [11] LT3750 datasheet, "LT3750 Capacitor Charger Controller Datasheet," Linear Technology Corporation, USA.
- [12] L. Dalessandro, F. da Silveira Cavalcante, and J. Kolar, "Self-Capacitance of High-Voltage Transformers," *IEEE Transactions on Power Electronics*, vol. 22. No. 5, pp. 2081-2092, 2007.

APPENDIX F

Investigation of transformer winding architectures for high voltage capacitor charging applications

2014 IEEE Applied Power Electronics Conference and Exposition(APEC 2014)

Investigation of transformer winding architectures for high voltage capacitor charging applications

Henrik Schneider, Prasanth Thummala, Lina Huang, Ziwei Ouyang, Arnold Knott, Zhe Zhang, Michael A. E. Andersen

Electronics Group, Department of Electrical Engineering

Technical University of Denmark

2800 Kongens Lyngby, Denmark

hensc@elektro.dtu.dk, pthu@elektro.dtu.dk, huang@elektro.dtu.dk

Abstract—Transformer parameters such as leakage inductance and self-capacitance are rarely calculated in advance during the design phase, because of the complexity and huge analytical error margins caused by practical winding implementation issues. Thus, choosing one transformer architecture over another for a given design is usually based on experience or a trial and error approach. This work presents equations regarding calculation of leakage inductance, self-capacitance and AC resistance in transformer winding architectures, ranging from the common non-interleaved primary/secondary winding architecture, to an interleaved, sectionalized and bank wound architecture. The analytical results are evaluated experimentally and through FEM simulations. Different transformer winding architectures are investigated in terms of the losses caused by the transformer parasitics for a bi-directional high-voltage (~1500 V) flyback converter used to drive a dielectric electro active polymer based incremental actuator. The total losses due to the transformer parasitics for the best transformer architectures is reduced by more than a factor of ten compared to the worst case transformer architectures.

I. INTRODUCTION

Dielectric electro active polymer (DEAP) is an emerging smart material that has experienced significant development and has gained increasing attention over the last decade [1], [2]. DEAP, when used as actuators, has the potential to be an effective replacement for many conventional actuators due to its unique properties such as high strain, light weight, low noise operation, low power consumption. However, a compact high voltage driver is required to charge and discharge the DEAP from 0 V to 2500 V DC supplied from a 24 V battery. The DEAP actuator applications require a bi-directional energy transfer capability, to increase the life time of the battery. The flyback converter topology is suitable for low power (< 150 W), and high voltage capacitor charging applications, as it can be made very compact with a low number of components.

The flyback transformer is the most critical component in terms of driver performance. The high voltage requirement

demands a high turns ratio which calls for a large number of secondary turns. This may lead to a high winding self-capacitance resulting in severe capacitive switching loss and undesirable, resonating current spikes in the leading edge of the current waveform, which could lead to false triggering of the current limit during the turn-on process.

The leakage inductance of the transformer may cause undesirable voltage spikes on the drains of the primary and secondary MOSFETs during the charge and the discharge processes, respectively, which lead to use of active or passive snubber circuits in the converter. With active snubbers high energy efficiency can be achieved, at the expense of a higher cost and added control complexity whereas the passive snubbers result in switching loss due to the leakage inductance. The AC resistance is also an important parameter to consider, since the AC conduction loss is caused by high frequency skin and proximity effects in a flyback converter operating in boundary conduction mode (BCM) or in discontinuous conduction mode (DCM).

Thus, accurate estimation of the transformer parameters and their associated losses are required, to evaluate different transformer winding architectures (TWAs) from which the best TWA is selected to achieve high energy efficiency. Extensive research has been done on calculating the leakage inductance in conventional transformers [3]-[6], [17], and in [7]-[17], the capacitance calculation methods have been proposed for inductors, power, planar, and high voltage transformers. The influence of transformer parasitics for the low power flyback converter has been discussed in [24]. This paper investigates a number of TWAs providing a deep insight into transformer design and its impact on the total loss contribution of a bi-directional high-voltage flyback converter.

The paper is organized as follows: the TWAs are described and then calculations of self-capacitance, leakage inductance and AC resistance for different TWAs are provided. The calculated transformer parameters are evaluated via FEA simulation using ANSOFT Maxwell and

This work was sponsored by Danish National Advanced Technology Foundation.

the transformer paracitics for all TWAs are presented, followed by the conclusion.

II. TRANSFORMER WINDING ARCHITECTURES

This paper investigates the four known winding schemes (A, B, C and D) as shown in Fig. 1 [14], [16], [26], [27]. Winding scheme A is the most simple to implement since the next layer starts where the previous layer ended. In winding scheme B, the next layer starts just above the starting point of the previous layer. Winding scheme C split the winding into a number of sections that is individually wound like winding scheme A. In winding scheme D, the turns progress in a vertical back angled way where turns are built on top of previous turns. It seems like winding scheme D achieves as many angled sections as there are turns in a layer without the penalty of reducing the fill factor due to the thickness of the section walls. Another advantage is that winding scheme D can be easily interleaved which is not the case for winding scheme C since it is hard to add section walls in-between windings. The difference in self-capacitance due to the winding schemes is severe because the voltage potentials between the turns in the winding are changed.

Several winding buildups (S/P, S/P/S, S/P/S/P/S/P/S; where S and P are the secondary and primary windings, respectively) are investigated - see Fig. 2. Based on these configurations, seven high voltage transformer winding architectures (W_1 - W_7) are derived and the winding information is summarized in Table 1. In order to simplify the implementation of the windings a low turns ratio of 10 is selected. The TWAs W_1 - W_6 are wound with 10 primary turns

and 100 secondary turns. W_7 deviates since it is only implemented with 9 primary turns due to the nature of the winding architecture.

Winding scheme A is employed for the primary winding of all architectures. Moreover, all winding space of the bobbin is utilized to improve the fill factor and to reduce the winding resistance. Equal space allocation for primary and secondary winding is adopted for this investigation, thus the primary winding is wound with a number of parallel wires.

III. SELF-CAPACITANCE

High voltage transformers tend to have a large number of turns in the high voltage side, which introduces a non-negligible parasitic self-capacitance. It is important to predict the self-capacitance in the design phase in order to avoid severe switching loss. In fact, the winding self-capacitance is a parameter representing the electric field energy stored in the winding and is considered as a shunt lumped element in most cases [14]. Due to a large number of turns per layer, the effect of the turn-to-turn capacitance can be neglected and the main

TABLE I. HIGH VOLTAGE TRANSFORMER ARCHITECTURES

| Design | Winding buildup | Secondary winding | | Primary winding |
|------------------------------------------------------------------------------------------------------------------------------------------------------------------------------------------------------------------------------------------------------------------------------------------------------------------------------------------------------------------------------------------------------------------------------------------------------------------------------------------------------------------------------------------------------------------------------------|-----------------|-------------------|-----------------------------------------------------------------------------------------------------------------------------------------------------------------------|----------------------------------------------------------------------------------------------------------|
| | | Scheme | Parameters | Parameters |
| W_1 | S/P | A | $N_s = 100$ $d_{is} = 0.3 \text{ mm}$ $d_{os} = 0.32 \text{ mm}$ $p_{TT} = 0.355 \text{ mm}$ $p_{LL} = 0.34 \text{ mm}$ $n_{ls} = 4$ $n_{pars} = 1$ | $N_p = 10$ $*d_{ip} = 0.7 \text{ mm}$ $*d_{op} = 0.8 \text{ mm}$ $n_{lp} = 2$ $n_{parp} = 2$ |
| W_2 | S/P | B | | |
| W_3 | S/P | C | | |
| W_4 | S/P | D | | |
| W_5 | S/P/S | B | | |
| W_6 | S/P/S | D | | |
| W_7 | S/P/S/P/S/P/S | B | Core / Material used: RM8 / N41 | $N_p = 9$ $*d_{ip} = 0.48 \text{ mm}$ $*d_{op} = 0.5 \text{ mm}$ $n_{lp} = 3$ $n_{parp} = 5$ |
| Parameters interpretation | | | | |
| N_s / N_p - number of secondary / primary turns; n_{ls} / n_{lp} - number of secondary / primary winding layers; n_{pars} / n_{parp} - number of secondary / primary parallel windings; d_{is} / d_{os} - inner / outer diameter of secondary winding; d_{ip} / d_{op} - inner / outer diameter of primary winding; p_{TT} / p_{LL} - turn-to-turn / layer-to-layer pitch of secondary winding; $*$ In the practical transformer implementation triple insulated (TEX) windings are not used for the primary due to the unavailability of the wires; | | | | |

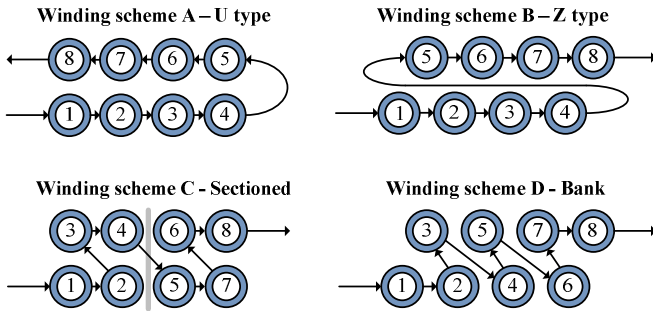


Figure 1. An overview of different winding schemes.

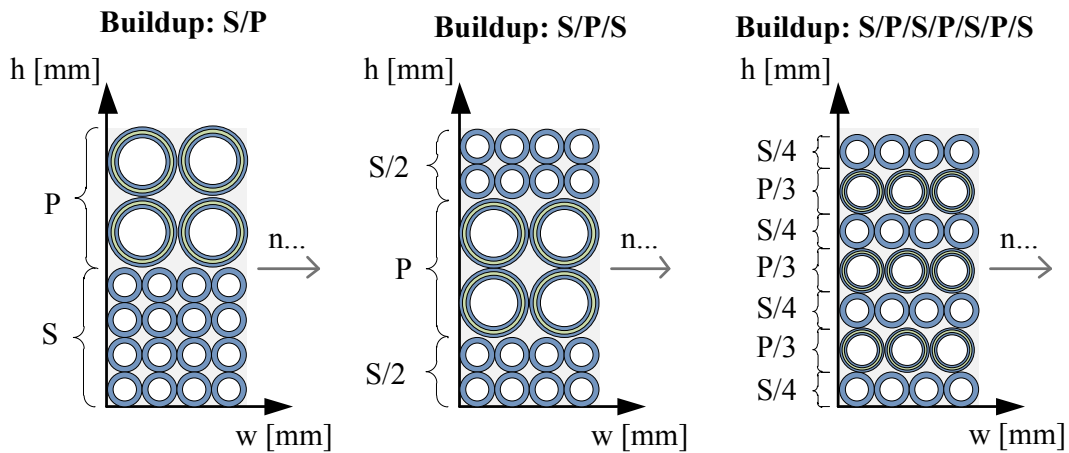


Figure 2. An overview of different winding buildups.

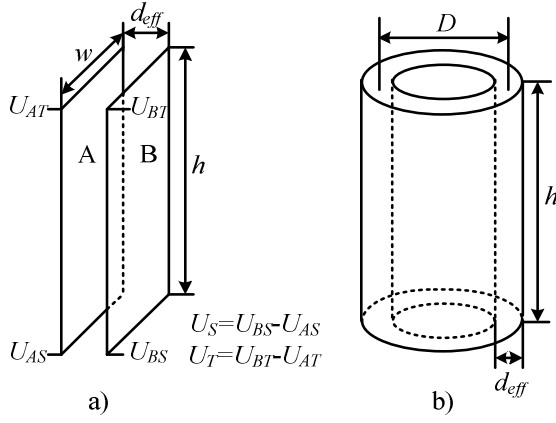


Figure 3. a) Two parallel plates with a linear potential distribution, b) Cylindrical capacitor model

contribution to the self-capacitance comes from the layer-to-layer capacitance, which can be calculated based on the simple parallel-plate or cylindrical capacitor model [14]-[16].

The self-capacitance in the transformer windings can be calculated using the electro static energy stored in the volume between the conductors [14], [16] and is given by

$$E_{Electric} = \frac{1}{2} \iiint_{Vol} \epsilon E^2 dv = \frac{1}{2} C_S U_W^2 \quad (1)$$

where ϵ is the equivalent dielectric constant of the winding, E is the electric field strength, C_S is the self-capacitance, and U_W is the total voltage across the winding.

The energy stored in two adjacent conductive layers with a linear potential distribution, shown in Fig. 3a, can be calculated by (2), which is derived in [16]. The total stored energy is

$$E_{Stored} = \frac{C_l}{6} (U_S^2 + U_S U_T + U_T^2) \quad (2)$$

where U_S and U_T are the potential difference between the two surfaces at the bottom and top respectively, and C_l is the capacitance between the two surfaces and is considered as a parallel plate capacitance and can be calculated using (3)

$$C_l = \epsilon_r \epsilon_0 \frac{hw}{d_{eff}} \quad (3)$$

where ϵ_0 is the vacuum permittivity and is 8.854×10^{-12} F/m, ϵ_r is the relative permittivity of the dielectric material. The parameters h , w represents the dimensions of the plate and d_{eff} is the effective distance between two layers (which needs to be calculated for each TWA) and is given by

$$d_{eff} = p_{LL} - 1.15d_{is} + 0.26p_{TT} \quad (4)$$

where p_{LL} , d_{is} and p_{TT} are the layer to layer pitch, inner diameter, and turn to turn pitch, of the secondary winding, respectively. According to the methods given in [16], the expressions for calculating the self-capacitance for all above mentioned TWAs have been derived and are summarized in Table 2. Normally, the cylindrical shape, shown in Fig. 3b, is desired for most winding layers due to the simple winding

TABLE II. SELF-CAPACITANCE EXPRESSIONS FOR DIFFERENT TWAS

| TWA | Self-capacitance expression |
|---------------------------------------------------------------------------------------------------------------------------------------------------------------------------------------------------------------------------------------------------------------------------------------------------------------------------------------------------------------------------------------------------------------------------------------------------------------------------------------------------------------------------------------------------------------------------------------------------------------------------------------------------------------------------------------------------------------------------------------------------------------------------------------------------------------------------------------------------------------------------------------------------------------------------------------------------------------------------------------------------------------------------------------------------------------------------------------------------------------------------------------------------------------------------------------------------------------------------------|----------------------------------------------------------------------------------------------------------------------------------------------------------------------------------------------------------------------------------------------------------------------------------------------------------------------------------|
| W ₁ | $4 \frac{(n_{is}-1)}{n_{is}^2} \frac{C_l}{3}$; $C_l = \epsilon_r \epsilon_0 \frac{b_w l_{w1}}{d_{eff1}}$; $l_{w1} = \pi(D_i + n_{is}d_{is} + (n_{is}-1)h_{is})$ |
| W ₂ | $4 \frac{(n_{is}-1)}{n_{is}^2} \frac{C_l}{4}$; $C_l = \epsilon_r \epsilon_0 \frac{b_w l_{w1}}{d_{eff1}}$; $b_w = (T_{is}-1)p_{TT} + d_{os}$ |
| W ₃ | $\frac{4(n_{is}-1)}{q_1 n_{is}^2} \frac{C_l}{3}$; $C_l = \epsilon_r \epsilon_0 \frac{b_w l_{w1}}{d_{eff1}}$ |
| W ₄ | $\epsilon_r \epsilon_0 \frac{p_{TT} l_{w1}}{d_{eff2}} \frac{L}{b_w}$; $L = (n_{is}-1)p_{LL} + d_{os}$ [7] |
| W ₅ | $\frac{\epsilon_r \epsilon_0 b_w}{n_{is}^2} \left[\frac{l_{w2}}{d_{eff3}} + \frac{l_{w3}}{d_{eff3}} + \frac{l_{w4}}{d_{eff3} + n_{ip}d_p + (n_{ip}-1)h_{ip}} \right]$ |
| W ₆ | $\epsilon_r \epsilon_0 \left[\frac{p_{TT}(l_{w2} + l_{w3})}{d_{eff4}} \frac{L_1}{b_w} + \frac{p_{TT2}l_{w4}}{d_{eff4} + n_{ip}d_p + (n_{ip}-1)h_{ip}} \frac{L_2}{b_w} \right]$; $L_1 = \left(\frac{n_{is}-1}{2} \right) p_{LL} + d_{os}$; $p_{TT2} = n_{ip}h_p + (n_{ip}-1)h_{ip} + d_{os}$; $L_2 = p_{TT2} + d_{os}$ |
| W ₇ | $\frac{\epsilon_r \epsilon_0 b_w}{n_{is}^2} \left[\frac{l_{w5} + l_{w6} + l_{w7}}{d_{eff5}} \right]$ |
| Parameters interpretation | |
| ϵ_0 / ϵ_r - relative permittivity of vacuum / dielectric material; $\epsilon_r = 4$; b_w - the width of the layer; T_{is} is turns per layer of secondary winding; D_i - inner diameter of the bobbin; $d_{eff1,2,3,4,5}$ - effective thickness of dielectric between two layers [14] [16] for different TWAs; l_{w1} - mean length turn for the TWAs W ₁ , W ₂ , W ₃ and W ₄ ; $l_{w2} / l_{w3} / l_{w4}$ - mean length turn between most inner two secondary (S ₁ , S ₂) / most outer two secondary (S ₃ , S ₄) / most outer secondary and the most inner secondary (S ₂ , S ₃), layers for W ₅ and W ₆ ; $l_{w5} / l_{w6} / l_{w7} / l_{w8} / l_{w9} / l_{w10}$ - mean length turn between most inner two secondary (S ₁ , S ₂) / middle two secondary (S ₂ , S ₃) / most outer two secondary (S ₃ , S ₄) layers for W ₇ q_1 - number of sections for structure W ₃ and $q_1 = 4$; For remaining abbreviations refer Tables 1 and 3; | |

technique as well as the short mean turn length [14]. If the distance between two layers is much less than the mean diameter for the two layers, the cylindrical capacitor can be considered to be a parallel plate capacitor and (3) can be employed to calculate the capacitance by replacing w with πD (see Fig. 3b).

IV. LEAKAGE INDUCTANCE

The leakage inductance in a transformer is calculated using the energy stored in the magnetic field [16]. The total leakage energy stored in the magnetic field is given by

$$E_{Magnetic} = \frac{1}{2} \iiint_{Vol} \mu_0 H^2 dv = \frac{1}{2} L_{lk} I_p^2 \quad (5)$$

where H is the magnetic field strength which is proportional to the number of ampere turns linked by the flux path, L_{lk} is the leakage inductance, and I_p is the peak current in the winding. The fundamental principles used to calculate the leakage inductance are thoroughly investigated in [3], [4],

TABLE III. PRIMARY LEAKAGE INDUCTANCE EQUATIONS FOR DIFFERENT TWAS

| TWA | Leakage inductance expression |
|---------------------------------------------------------------------------------------------------------------------------------------------------------------------------------------------------------------------------------------------------------------------------------------------------------------------------------------------------------------------------------------------------------------------------------------------------------------------------------------------------------------------------------------------------------------------------------------------------------------------------------------------------------------------------------------------------------------------------------------------------------------------------------------------------------------------------------------|------------------------------------------------------------------------------------------------------------------------------------------------------------------------------------------------------------------------------------------------------------------------------------------------------------------------------------------------------------------------------------------------------------------------------------------------------------------------------------------------------------------------------------------------------------|
| W ₁ , W ₂ , W ₃ , W ₄ | $\mu_0 l_w N_p^2 \left[\frac{1}{b_w} \left(\frac{n_p h_p}{3} + \frac{(2n_{lp} - 1)(n_{lp} - 1)}{6} \left(\frac{h_{ip}}{n_{lp}} + h_i \right) + \right) \right] \quad [17]$ |
| W ₅ , W ₆ | $\frac{\mu_0 l_w N_p^2}{b_w} \left[\frac{n_{ls1}^3 + n_{ls2}^3}{3(n_{ls1} + n_{ls2})^3} (n_{lp} h_p + (n_{ls1} + n_{ls2}) h_s) + \frac{n_{ls1}^2 + n_{ls2}^2}{(n_{ls1} + n_{ls2})^2} h_i + \left\{ \frac{n_{ls1}(n_{ls1} - 1)(2n_{ls1} - 1) + n_{ls2}(n_{ls2} - 1)(2n_{ls2} - 1)}{6(n_{ls1} + n_{ls2})^2} \right\} h_{is} + \left\{ (n_{lp} - 1) \left(\frac{n_{ls1} n_{lp}}{n_{ls1} + n_{ls2}} \right)^2 + \frac{n_{lp}(n_{lp} - 1)(2n_{lp} - 1)}{6} \right\} \frac{h_{ip}}{n_{lp}^2} + \frac{n_{ls1}^2 n_{lp}(n_{lp} - 1)}{n_{ls1} + n_{ls2}} \right]$ |
| W ₇ | $\mu_0 \frac{l_w}{b_w} N_p^2 \left[\frac{3h_p + 4h_s}{72} + \frac{7}{36} h_i \right]$ |
| Parameters interpretation μ_0 - permeability of free air; l_w - mean length turn (MLT); b_w - width of the layer; b_{w2} - width of the layer excluding the combined width of the sections walls for TWA W ₃ , $b_{w2} < b_w$; For W ₁ , W ₂ and W ₄ , $b_w = b_{w2}$; $h_p = d_{op}$ and $h_s = d_{os}$; $h_{ip} / h_{is} / h_i$ - insulation thickness between primary-to-primary layer, secondary-to-secondary layer and primary-to-secondary layer; For W ₅ and W ₆ , n_{ls1} and n_{ls2} are the number of secondary layers are at the top and bottom of a primary winding respectively, having n_{lp} primary layers. In Fig. 4c, $n_{ls1}=2$ and $n_{ls2}=2$; For remaining abbreviations refer Tables 1 and 2; | |

and [16]. Based on those methods, the equations for calculating the leakage inductances for TWAs W₁-W₇ have been derived and are summarized in Table 3 [17]. The MMFs in each primary and secondary layer are $T_{lp}I_p$ and $T_{ls}I_s$, respectively. For the winding buildup shown in Fig. 4a, the energy stored in the magnetic field is derived in (AI) in Appendix.

V. AC RESISTANCE

The AC resistance is calculated using equations commonly found in the literature [18]-[19], [26]. The DC resistance of the primary/secondary winding can be calculated by

$$R_{DC} = \frac{\rho l_w N}{A n_{par}}, \quad A = \frac{\pi d_i^2}{4} \quad (6)$$

where ρ is the resistivity of copper at room temperature ($\rho=17.24 \text{ n}\Omega/\text{m}$ at 20°C), N is the total number of primary/secondary turns, l_w is the mean length turn of the winding, n_{par} is the number of parallel wires, A is the cross sectional area of the winding and d_i is the inner diameter of the winding excluding the insulation.

The AC resistance per layer of a given winding is given by

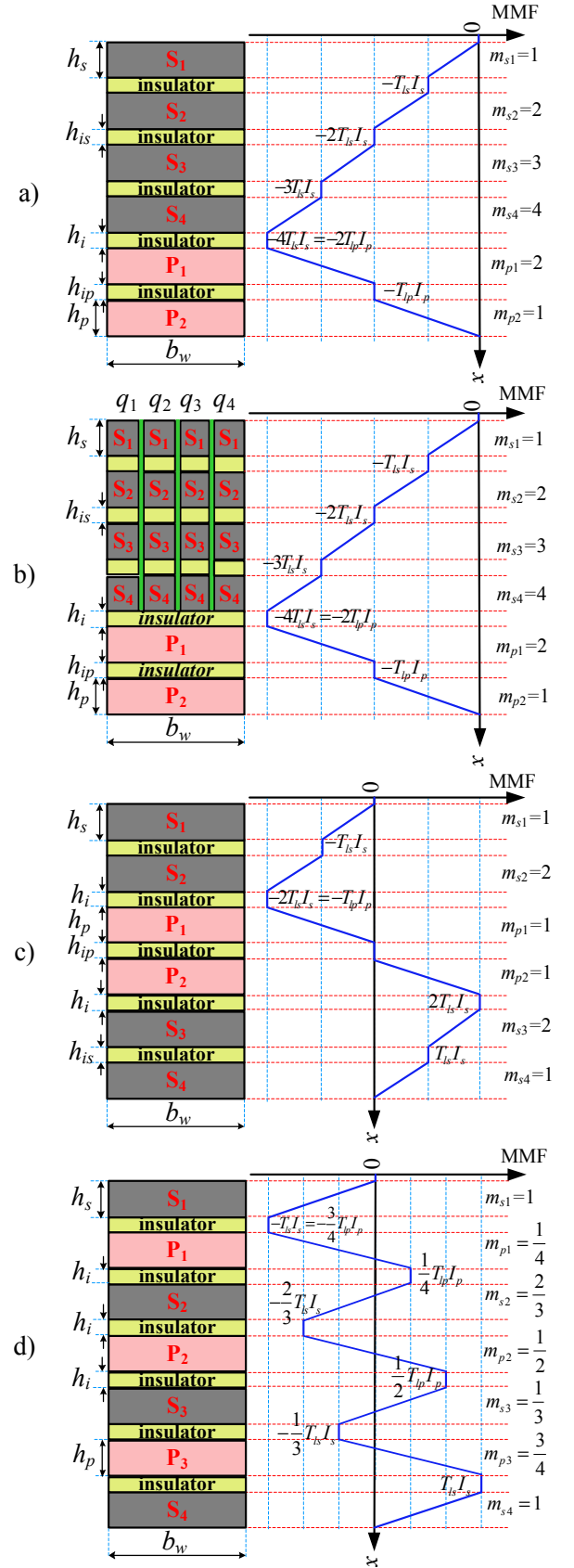


Figure 4. Analytical MMF distribution for, a) non-interleaved structure (S/P – W₁, W₂, W₄), b) non-interleaved structure (S/P – W₃), c) interleaved structure (S/S/P/S/S – W₅, W₆), d) fully interleaved structure (S/P/S/P/S/P/S – W₇)

$$R_{AC,layer} = R_{DC,layer} Q \left\{ \begin{aligned} & \left(2m^2 - 2m + 1 \right) \frac{\sinh(2Q) + \sin(2Q)}{\cosh(2Q) - \cos(2Q)} - \\ & 4(m^2 - m) \frac{\cos(Q) \sinh(Q) - \sin(Q) \cosh(Q)}{\cosh(2Q) + \cos(2Q)} \end{aligned} \right\} \quad (7)$$

Assume the variables Δ_1 , Δ_2 , Δ_3 , and Δ_4 are assigned as in (8)

$$\begin{aligned} \Delta_1 &= \frac{\sinh(2Q) + \sin(2Q)}{\cosh(2Q) - \cos(2Q)}, \quad \Delta_2 = \frac{\cos(Q) \sinh(Q) - \sin(Q) \cosh(Q)}{\cosh(2Q) + \cos(2Q)} \\ \Delta_3 &= \frac{\sinh(Q) + \sin(Q)}{\cosh(Q) - \cos(Q)}, \quad \Delta_4 = \frac{\sinh(Q) - \sin(Q)}{\cosh(Q) + \cos(Q)} \end{aligned} \quad (8)$$

The variable Δ_1 in terms of Δ_3 and Δ_4 , and Δ_2 and Δ_4 is given by [19]

$$\Delta_1 = \frac{1}{2}(\Delta_3 + \Delta_4), \quad \Delta_2 = (2\Delta_2 + \Delta_4) \quad (9)$$

Using (8), (9) in (7), the simplified AC resistance per layer is

$$R_{AC,layer} = R_{DC,layer} Q \left\{ \Delta_1 + 2(m^2 - m) \Delta_4 \right\} \quad (10)$$

$$R_{AC,layer} = R_{DC,layer} \frac{Q}{2} \left\{ \Delta_3 + (2m - 1)^2 \Delta_4 \right\} \quad (11)$$

The total AC resistance of M layers for the non-interleaved TWAs W_1 - W_4 is given by

$$\begin{aligned} R_{AC,total} &= R_{DC,layer} Q \sum_{m=1}^M \left\{ \Delta_1 + 2(m^2 - m) \Delta_4 \right\} \\ &= (R_{DC,layer} M) Q \left\{ \Delta_1 + \frac{2}{3}(M^2 - 1) \Delta_4 \right\} \\ &= R_{DC,total} Q \left\{ \Delta_1 + \frac{2}{3}(M^2 - 1) \Delta_4 \right\} \end{aligned} \quad (12)$$

where $R_{DC,layer}$ and $R_{DC,total}$ are the DC resistance per layer and total DC resistance, respectively. The variable m represents the effective number of layers and is given by

$$m = \frac{F(h)}{F(h) - F(0)} \quad (13)$$

where $F(0)$ and $F(h)$ are the magneto motive forces (MMFs) at the start and end of each layer, respectively. The variable Q is the effective layer thickness normalized with the skin depth and is given by

$$Q = \frac{\text{layer thickness}}{\text{penetration depth}} = \frac{\frac{\pi^{3.5}}{4} d_i \sqrt{\frac{d_o T_l}{b_w}}}{\sqrt{\frac{\rho}{\pi \mu_0 f}}} \quad (14)$$

where d_i is the bare wire diameter, d_o is the overall wire diameter including insulation, T_l is the turns per layer of the given winding and f is the switching frequency.

To calculate the AC resistance per layer for the interleaved TWAs W_5 - W_7 , (10) or (11) needs to be used with the corresponding value of m for each layer. The total AC resistance is the sum of all AC resistances in each layer.

The total AC resistance referred to the primary is given by

$$R_{AC} = R_{AC,total,P} + \frac{R_{AC,total,S}}{n^2} \quad (15)$$

where n is the transformer turns ratio $R_{AC,total,P}$ and $R_{AC,total,S}$ are the total AC resistance of primary and secondary windings, respectively.

TABLE IV. ENERGY LOSS EXPRESSIONS OF TRANSFORMER PARACITICS

| Name of energy loss | Loss expressions | |
|------------------------------------------------------------------------------------------------------------------------------------------------------------------------------------------------------------------------------------------------------------------------------------------------------------------------------------------------------------------------------------------------------------------------------------------------------------------------------------------------------------------------------------------------------------------------------------------------------------------------------------------------------------------------------------------------------------------------------------------------------------------------------------------------------------------------------------------------------------------------------------|---------------------------------------------------------------------------------------------------------------------------------------------------------------------------------------------------------------------------------------------------------------|--------------------------------------------------------------------------------------------------------------------------------------------------------------------------------------------------------------------------------------------------------------|
| | Charge process (J) | Discharge process (J) |
| Switching loss due to self-capacitance | $E_{C1} = 0.5 C_p V_{dsP}^2$ | $E_{C2} = 0.5 C_s V_{dsS}^2$ |
| Snubber loss due to leakage inductance | $E_{L1} = \frac{0.5 L_{lkP} i_{pkP}^2 V_{snLV}}{V_{snLV} - V_{out}}$ | $E_{L2} = \frac{0.5 L_{lkS} i_{pkS}^2 V_{snHV}}{V_{snHV} - V_{in}}$ |
| Winding loss due to AC and DC resistances | $E_{R1} = \left[\begin{aligned} & \left[I_{DCP}^2 R_{DCP} + \right] t_{onC} + \\ & \left[I_{RMSP}^2 R_{ACP} + \right] t_{offC} + \\ & \left[I_{DCS}^2 R_{DCS} + \right] t_{offC} + \\ & \left[I_{RMSS}^2 R_{ACS} \right] t_{offC} \end{aligned} \right]$ | $E_{R2} = \left[\begin{aligned} & \left[I_{DCP}^2 R_{DCP} + \right] t_{offD} + \\ & \left[I_{RMSP}^2 R_{ACP} + \right] t_{offD} + \\ & \left[I_{DCS}^2 R_{DCS} + \right] t_{onD} + \\ & \left[I_{RMSS}^2 R_{ACS} \right] t_{onD} \end{aligned} \right]$ |
| Parameters interpretation | | |
| C_p / C_s – self capacitance referred to primary / secondary; V_{dsP} / V_{dsS} – drain to source voltage of primary / secondary MOSFET; L_{lkP} / L_{lkS} – leakage inductance referred to primary / secondary; i_{pkP} / i_{pkS} – primary / secondary peak current; V_{snLV} / V_{snHV} – RCD snubber capacitor voltage of primary / secondary; V_{out} / V_{in} – output / input voltage of the converter; I_{DCP} / I_{DCS} – DC current of primary / secondary; R_{DCP} / R_{DCS} – DC resistance of primary / secondary; I_{RMSP} / I_{RMSS} – RMS current of primary / secondary; R_{ACP} / R_{ACS} – AC resistance of primary / secondary; t_{onC} / t_{offC} – on / off time of the primary MOSFET during the charge process; t_{onD} / t_{offD} – on / off time of the HV MOSFET during the discharge process; | | |

VI. FINITE ELEMENT ANALYSES

The different winding architectures are simulated in Ansoft Maxwell to extract the value of the leakage inductance, self-capacitance and AC resistance. In Fig. 5 the electrostatic energy between the windings is shown for winding schemes B and D. It is noted that the energy density is high between layer to layer and low between turn to turn as expected in winding scheme B. In winding scheme D there is less electrostatic energy and thus it has lower self-capacitance.

Fig. 6 shows a close-up of the magneto static energy of the three investigated winding buildups. The leakage flux runs approximately vertically through the windings and the magneto static energy is highest in the space between the primary and secondary windings. The heavy interleaved buildup (S/P/S/P/S/P/S) has very low magneto static energy and thus it will have a very low leakage inductance.

The AC resistance at 100 kHz is also simulated for the three winding buildups. A standard mesh which is very fine compared to the skin depth is used to simulate the eddy effects in the winding. A close up plot of the mesh is shown in Fig. 7.a. The diameter of the secondary winding is 0.3 mm and the skin depth at 100 kHz is approximately 0.2 mm. It is

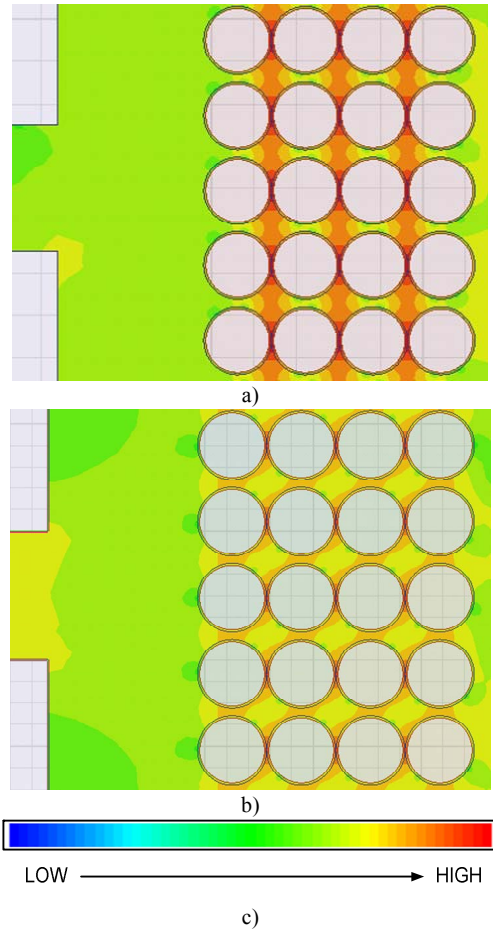


Figure 5. Plots from simulation of self-capacitance.
a) Energy distribution for winding scheme B. b) Energy distribution for winding scheme D. c) Density color bar

noted that the dimensions of the mesh is much lower than the diameter of the winding and the skin depth at 100 kHz. In Fig. 7. b-d, a close up of the current density for the three winding buildups is shown. It is noted that the current density in the non-interleaved buildup is much higher compared to the others and thus the AC resistance will also be higher.

VII. EXPERIMENTAL RESULTS

The simulated, calculated and measured values of the self-capacitance, leakage inductance (measured at 10 kHz frequency using the impedance analyzer PSM1735) and AC resistance for the 7 TWA's are shown in the Tables 5, 6 and 7, respectively, from which it is clear that the measured, calculated and simulated transformer parameters for most of the TWAs closely matches. However, the differences in winding parameters such as an average layer to layer distance and mean length turn may cause errors around $\pm 20\%$. The measurement setup with 5 of the transformer prototypes is shown in Fig. 8. The energy loss expressions due to the transformer parasitics are summarized in Table 4. A plot of the loss distribution of the energy losses caused by the transformer parasitics, in a bi-directional flyback converter, used for charging and discharging an incremental DEAP actuator is shown in Fig. 9. The winding loss calculation for the flyback transformer is different from that of normal

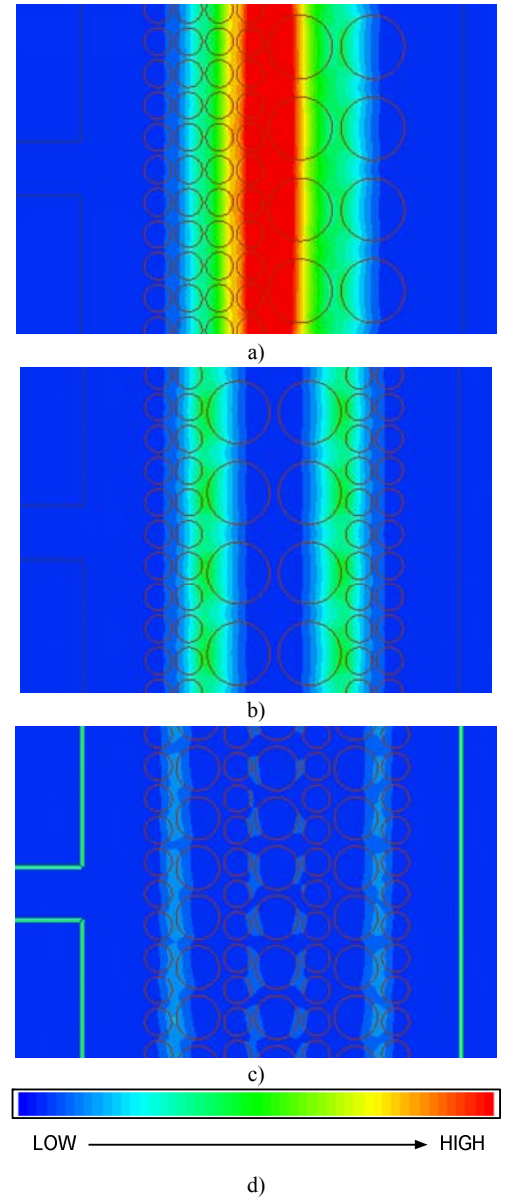


Figure 6. Plots from simulation of leakage inductance.
a) P/S. b) S/P/S. c) S/P/S/P/S/P/S. d) Density color bar.

transformer since the primary and secondary currents are out of phase, in [20] the winding loss is calculated for a flyback transformer with a non-interleaved structure. The same method can be used for the interleaved structures as well. However, due to limited space that is not included in this paper.

The calculated transformer parasitic values are used for calculating all losses, in order to provide a fair and useful comparison of the losses. The following specifications are used to calculate the losses in the bi-directional flyback converter [17], [20]-[23]: input voltage: 24V, output voltage: 1500 V, load capacitance: 200 nF, switching frequency during the charging and discharging process: 20-200 kHz, and 26 kHz, and primary peak current during charge and discharge processes: 2.12 A. The primary magnetizing inductance: 35 μ H. From Fig. 9, it is clear that W_6 has the lowest loss among all TWAs followed by W_4 , W_7 and W_3 .

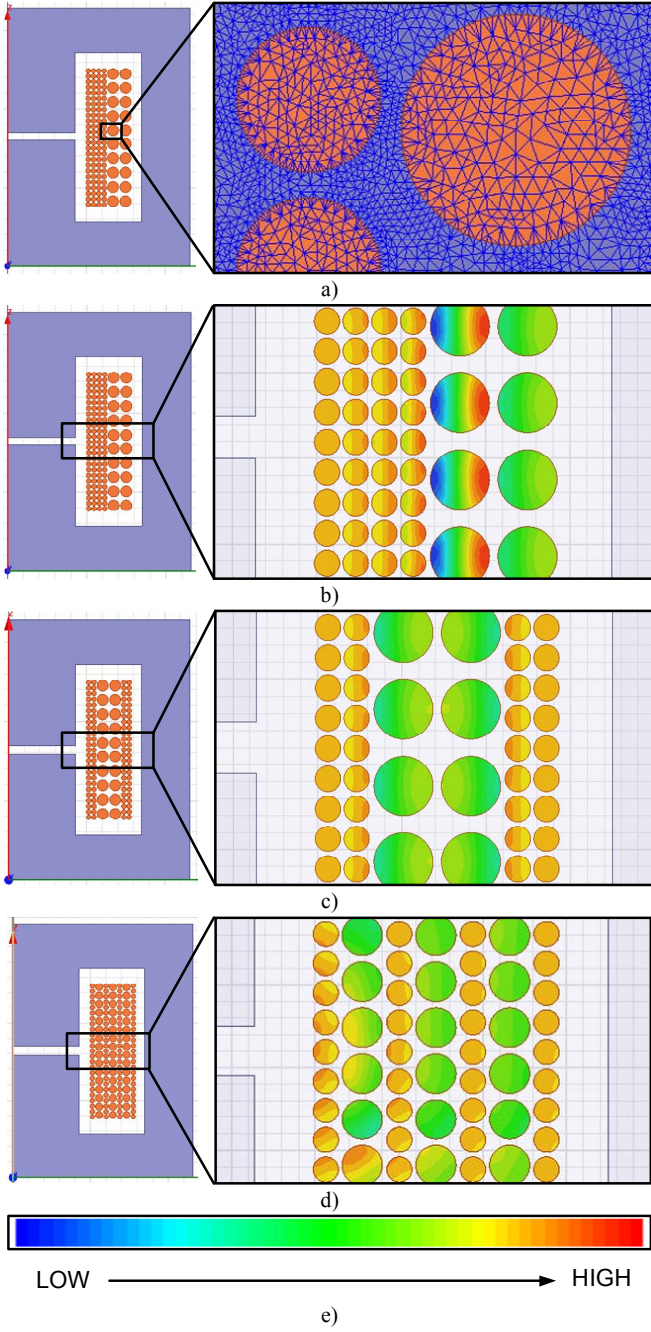


Figure 7. Plots from the simulations of AC resistance.
a) Default mesh, b) Current density of W_1 - W_4 , c) Current density of W_5 - W_6 , d) Current density of W_7 , e) Density color bar

Thus the structure W_6 is highly recommended for high voltage capacitor charging application.

VIII. CONCLUSIONS

The analytical equations for calculating the transformer AC resistance, leakage inductance and self-capacitance for seven different winding architectures have been presented and evaluated experimentally and with FEA simulation. The main contribution to the errors is due to practical winding issues which are not accounted for in the equations. The transformer loss distribution is based on the calculated values, and it clearly shows that transformer winding architectures

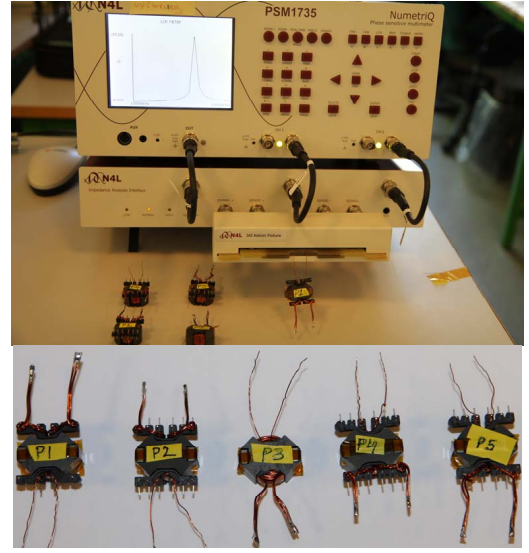


Figure 8. Measurement setup and five transformer prototypes with RM8 core

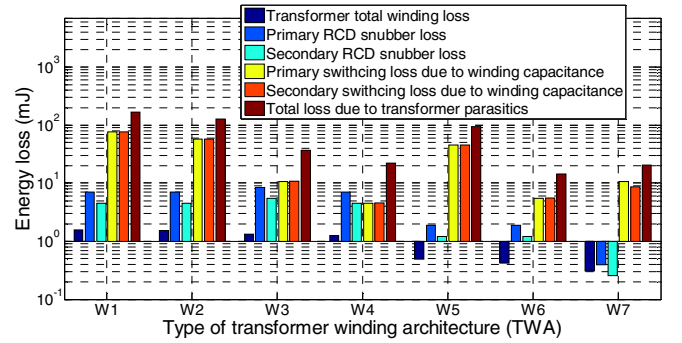


Figure 9. Energy loss distribution of the losses caused by transformer parasitics in the high voltage capacitor charging application.

where the self-capacitance is lowest are particularly suitable for high voltage charging applications. Future work involves the experimental validation of the proposed TWAs in the high voltage bi-directional dc-dc converter.

TABLE V. SELF-CAPACITANCE OF SECONDARY WINDING AT RESONANCE FREQUENCY

| TWA | Buildup | Winding scheme | Sim. (pF) | Calc. (pF) | Meas. (pF) |
|-------|---------------|----------------|-----------|------------|------------|
| W_1 | S/P | A | 33 | 32 | 28 |
| W_2 | S/P | B | 25 | 24 | 26 |
| W_3 | S/P | C | 2.4 | 2 | 4.2 |
| W_4 | S/P | D | 1.9 | 1 | 1.3 |
| W_5 | S/P/S | B | 10 | 20 | 22 |
| W_6 | S/P/S | D | 3.3 | 2.1 | 6 |
| W_7 | S/P/S/P/S/P/S | B | 5 | 3.6 | 15 |

TABLE VI. LEAKAGE INDUCTANCE REFERRED TO PRIMARY

| TWA | Buildup | Winding scheme | Sim. (nH) | Calc. (nH) | Meas. (nH) |
|-------|---------------|----------------|-----------|------------|------------|
| W_1 | S/P | A | 526 | 590 | 550 |
| W_2 | S/P | B | | | 520 |
| W_3 | S/P | C | | | 725 |
| W_4 | S/P | D | | | 580 |
| W_5 | S/P/S | B | 150 | 152 | 181 |
| W_6 | S/P/S | D | | | 208 |
| W_7 | S/P/S/P/S/P/S | B | 30 | 22 | 74 |

TABLE VII. AC RESISTANCE REFERRED TO PRIMARY AT 100 KHZ

| TWA | Buildup | Winding scheme | Sim. (mΩ) | Calc. (mΩ) | Meas. (mΩ) |
|----------------|---------------|----------------|-----------|------------|------------|
| W ₁ | S/P | A | 102 | 110 | 130 |
| W ₂ | S/P | B | | | 127 |
| W ₃ | S/P | C | | | 135 |
| W ₄ | S/P | D | | | 84 |
| W ₅ | S/P/S | B | 35 | 37 | 39 |
| W ₆ | S/P/S | D | | | 42 |
| W ₇ | S/P/S/P/S/P/S | B | 23 | 18 | 22 |

REFERENCES

- [1] R. E. Pelrine, R. D. Kornbluh, Q. Pei, and J. P. Joseph, "High-speed electrically actuated elastomers with strain greater than 100%," in *Proc. Science*, vol. 287, pp. 836–839, 2000.
- [2] R. E. Pelrine, R. D. Kornbluh, and J. P. Joseph, "Electrostriction of polymer dielectric with compliant electrodes as a means of actuation," in *Proc. Sens. Actuators A*, vol. 64, pp. 77–85, 1998.
- [3] W. G. Hurley and D. J. Wilcox, "Calculation of leakage inductance in transformer windings," in *Proc. IEEE Trans. Power Electronics*, vol. 9, pp. 121–126, 1994.
- [4] Z. Ouyang, Z. Zhang, O. C. Thomsen and M. A. E. Andersen, "Planar-integrated magnetics (PIM) module in hybrid bidirectional DC-DC converter for fuel cell application," in *Proc. IEEE Trans. Power Electronics*, vol. 26, pp. 3254–3264, 2011.
- [5] S. R. Cove, M. Ordóñez, F. Luchino, and J. E. Quaiçoe, "Applying Response Surface Methodology to Small Planar Transformer Winding Design," in *Proc. IEEE Trans. Industrial Electronics*, vol. 60, pp. 483–493, 2013.
- [6] J. Zhang, Z. Ouyang, M. Duffy, M. A. E. Andersen and W. G. Hurley "Leakage inductance calculation for planar transformer with magnetic shunt", in *Proc. ECCE USA 2013*.
- [7] F. Blache, J-P. Keradec, B. Cogitore, "Stray capacitances of two winding transformers: equivalent circuit, measurements, calculation and lowering," in *Proc. IEEE Industry Applications Society Annual Meeting*, pp. 1211–1217 vol. 2, 2–6 Oct. 1994.
- [8] W. T. Duerdorth, "Equivalent capacitance of transformer windings," in *Proc. Wireless Eng.*, vol. 23, pp. 161–167, Jun. 1946.
- [9] A. Massarini and M. K. Kazimierzczuk, "Self-capacitance of inductors," in *Proc. IEEE Trans. Power Electron.*, vol. 12, no. 4, pp. 671–676, Jul. 1997.
- [10] T. Duerbaum and G. Sauerlander, "Energy based capacitance model for magnetic devices," in *Proc. APEC*, vol. 1, pp. 109–115, 2001.
- [11] W. T. Duerdorth, "Equivalent capacitance of transformer windings," in *Proc. Wireless Eng.*, vol. 23, pp. 161–167, Jun. 1946.
- [12] T. Duerbaum, "Capacitance model for magnetic devices," in *Proc. Power Electron. Spec. Conf.*, vol. 3, pp. 1651–1656, 2000. H. Y. Lu, J. Zhu, S. Y. R. Hui, and V. S. Ramseden, "Measurement and Modeling of stray capacitances in high frequency transformers," in *Proc. Power Electron. Spec. Conf.*, pp. 763–769, 1999.
- [13] H. Y. Lu, J. G. Zhu, and S. Y. R. Hui, "Experimental determination of stray capacitances in high-frequency transformers," in *Proc. IEEE Trans. Power Electron.*, vol. 18, no. 5, pp. 1105–1112, Sep. 2003.
- [14] L. Dalessandro, F. da Silveira Cavalcante, J. W. Kolar, "Self-Capacitance of High-Voltage Transformers," in *Proc. IEEE Trans. Power Electronics*, vol. 22, no. 5, pp. 2081–2092, Sept. 2007.
- [15] J. Biela, J. W. Kolar, "Using Transformer Parasitics for Resonant Converters—A Review of the Calculation of the Stray Capacitance of Transformers," in *Proc. IEEE Trans. Industry Applications*, vol. 44, no. 1, pp. 223–233, 2008.
- [16] E. C. Snelling, *Soft Ferrites-Properties and applications*, 2nd ed. London, UK, Butterworth, 1988.
- [17] P. Thummala, H. Schneider, Z. Ouyang, Z. Zhang, M. A. E. Andersen, "Estimation of transformer parameters and loss analysis for high voltage capacitor charging application," in *Proc. IEEE ECCE Asia*, pp. 704–710, 3–6 Jun. 2013.
- [18] W.G. Hurley, E. Gath, J. G. Breslin, "Optimizing the AC resistance of multilayer transformer windings with arbitrary current waveforms," in *Proc. IEEE Trans. Power Electronics*, vol. 15, no. 2, pp. 369–376, Mar 2000.
- [19] J. A. Ferreira, "Improved analytical modeling of conductive losses in magnetic components," in *Proc. IEEE Transactions on Power Electronics*, vol. 9, no. 1, pp. 127, 131, Jan 1994.
- [20] P. Thummala, H. Schneider, Z. Zhang, A. Knott, M. A. E. Andersen, "Optimization of a Bi-Directional Flyback Converter for a High Voltage Capacitor Charging Application," in *Proc. IEEE APEC*, pp., 16–20 Mar. 2014.
- [21] K. Venkatesan, "Current Mode Controlled Bidirectional Flyback Converter," in *Proc. IEEE PESC*, pp. 835–842, 1989.
- [22] T. Bhattacharya, V. S. Giri, K. Mathew, L. Umanand, "Multiphase Bidirectional Flyback Converter Topology for Hybrid Electric Vehicles," in *Proc. IEEE Transactions on Industrial Electronics*, vol. 56, no. 1, pp. 78–84, Jan. 2009.
- [23] P. Thummala, Z. Zhang, M. A. E. Andersen, "High Voltage Bi-directional Flyback Converter for Capacitive Actuator," in *Proc. European Power Electronics Conference (EPE)*, pp. 3–6th Sept. 2013.
- [24] G. Chen, Y.-S. Lee, S.Y.R. Hui, D. Xu, Y. Wang, "Actively clamped bidirectional flyback converter," in *Proc. IEEE Trans. Industrial Electronics*, vol. 47, no. 4, pp. 770–779, Aug. 2000.
- [25] M. J. Prieto, A. Fernandez, J. M. Diaz, J. M. Lopera, J. Sebastian, "Influence of transformer parasitics in low-power applications," in *Proc. IEEE APEC*, vol. 2, pp. 1175–1180, 14–18th Mar. 1999.
- [26] R. W. Erickson and D. Maksimovic, "Fundamentals of Power Electronics," 2nd ed. New York: Springer, 2001.
- [27] John R. Barnes, "Robust electronic design reference book," Volume 1, Springer, 2004.

APPENDIX

$$\begin{aligned}
E_{Mag} &= \frac{\mu_0}{2} l_w b_w \int H^2(x) dx = \frac{\mu_0}{2} l_w b_w K_1; K_1 = \left[\sum_{u=1}^{n_{ls}} \int_0^{h_s} H_{su}^2 dx + \sum_{v=1}^{n_p} \int_0^{h_p} H_{pv}^2 dx + \sum_{a=1, b=a+1}^{n_{ls}-1} H_{sab}^2 h_{is} + \sum_{c=1, d=c+1}^{n_p-1} H_{pcd}^2 h_{ip} + H_{sp}^2 h_i \right] \\
H_{su} &= \left[-\frac{(u-1)T_{ls}I_s}{b_w} - \frac{T_{ls}I_s}{b_w} \frac{x}{h_s} \right]; H_{pv} = \left[-\frac{(n_{lp}-v+1)T_{lp}I_p}{b_w} + \frac{T_{lp}I_p}{b_w} \frac{x}{h_p} \right]; H_{sab} = -\frac{uT_{ls}I_s}{b_w}; H_{pcd} = -\frac{vT_{lp}I_p}{b_w}; H_{sp} = -\frac{n_{ls}T_{ls}I_s}{b_w}; \\
K_1 &= \left[\int_0^{h_s} \left(-\frac{T_{ls}I_s}{b_w} \frac{x}{h_s} \right)^2 dx + \int_0^{h_s} \left(-\frac{T_{ls}I_s}{b_w} - \frac{T_{ls}I_s}{b_w} \frac{x}{h_s} \right)^2 dx + \int_0^{h_p} \left(-\frac{2T_{ls}I_s}{b_w} - \frac{T_{ls}I_s}{b_w} \frac{x}{h_s} \right)^2 dx + \int_0^{h_s} \left(-\frac{3T_{ls}I_s}{b_w} - \frac{T_{ls}I_s}{b_w} \frac{x}{h_s} \right)^2 dx + \left(-\frac{T_{lp}I_p}{b_w} \right)^2 h_{ip} \right] \quad (A1) \\
&\quad + \left[\left(-\frac{T_{ls}I_s}{b_w} \right)^2 + \left(-\frac{2T_{ls}I_s}{b_w} \right)^2 + \left(-\frac{3T_{ls}I_s}{b_w} \right)^2 \right] h_{is} + \int_0^{h_p} \left(-\frac{2T_{lp}I_p}{b_w} + \frac{T_{lp}I_p}{b_w} \frac{x}{h_p} \right)^2 dx + \int_0^{h_p} \left(-\frac{T_{lp}I_p}{b_w} + \frac{T_{lp}I_p}{b_w} \frac{x}{h_p} \right)^2 dx + \left(-\frac{2T_{lp}I_p}{b_w} \right)^2 h_i \\
&= \left(\frac{T_{ls}I_s}{b_w} \right)^2 \left[4^3 \frac{h_s}{3} + 14h_{is} \right] + \left(\frac{T_{lp}I_p}{b_w} \right)^2 \left[2^3 \frac{h_p}{3} + h_{ip} + 4h_i \right] = \left(\frac{N_p I_p}{b_w} \right)^2 \left[\frac{2h_p + 4h_s}{3} + \frac{7h_{is}}{8} + \frac{h_{ip}}{4} + h_i \right]; \frac{n_{lp}T_{lp}I_p}{N_p I_p} = \frac{n_{ls}T_{ls}I_s}{N_s I_s};
\end{aligned}$$

APPENDIX G

Detailed Behavior Analysis for High Voltage Bidirectional Flyback Converter Driving DEAP Actuator

39th Annual Conference of the IEEE Industrial Electronics Society (IECON 2013)

Detailed Behavior Analysis for High Voltage Bidirectional Flyback Converter Driving DEAP Actuator

Lina Huang, Zhe Zhang, Michael A. E. Andersen

Technical University of Denmark, Ørsted Plads, Building 349, Kgs. Lyngby, Denmark

huang@elektro.dtu.dk, zz@elektro.dtu.dk, ma@elektro.dtu.dk

Abstract—DEAP (Dielectric Electro Active Polymer) is a new type of smart material. The tubular actuator based on DEAP material has various potential applications and is fundamentally a capacitive load. A high voltage bidirectional converter is required to provide power for the actuator. A bidirectional flyback based converter has been implemented. The parasitic elements have serious influence for the operation of the converter, especially in the high output voltage condition. The detailed behavior analysis has been performed considering the impact of the critical parasitic parameters. The converter has been analyzed for both charging and discharging processes in low and high output voltage operating occasions. The experimental waveforms can validate the analysis.

Keywords—DEAP actuator; bidirectional; flyback; high voltage; behavior analysis

I. INTRODUCTION

As a smart material, DEAP (Dielectric Electro Active Polymer) material started to receive increasing attention among scientists and engineers since early 1990s [1], [2]. DEAP material possesses simple structure - a thin dielectric elastomer sheet sandwiched between two compliant electrodes [2]. Because of the electrostatic pressure, the elastomer is compressed in the thickness direction and expands in the transverse direction by applying voltage to the electrodes [1], [2]. This actuation property makes it possible to develop DEAP material based actuator. In addition, the same construction as capacitor enables the DEAP to be represented by a plate capacitor whose values changes with the geometry [1], [3]. Hence, DEAP has the potential to work as a sensor when applied mechanical or electrical force changes its capacitance. Further, DEAP is a good alternative over other smart materials in the application of energy harvesting [3].

Taking the advantage of light weight, noiseless operation, large strain, high energy density, fast speed of response and high efficiency, DEAP actuators can be a promising replacement for conventional actuators as well as other smart material based actuators [1], [2], [3]. Numerous potential or conceptual applications have already been proposed by material or mechanical researchers in the field of biomimetics, micro electro mechanical systems (MEMS), acoustics, etc. Correspondingly, a variety of configurations is continuously emerging, such as the unimorph, bimorph, diaphragm, tube and roll constructions [1], [2].

Much research concerning DEAP tends to concentrate on the understanding and improvement of the polymer materials as well as the implementation of different configured DEAP actuators in various potential applications. However, not much research related to the development of driving converters for DEAP actuators has been carried out, especially for the driving devices with small size, high efficiency as well as low cost [4]. The object of this paper is to develop a bidirectional flyback based converter in order to drive DEAP actuator and perform a detailed behavior analysis for the operation of this high voltage converter.

This paper is organized as follows. Part II discusses the characteristics of tubular DEAP actuator. Part III addresses the implementation of a low input voltage high output voltage DC-DC driving converter. The corresponding operation behaviors are detailedly analyzed in Part IV. Finally, we make a conclusion in Part V.

II. CHARACTERISTICS OF TUBULAR DEAP ACTUATOR

With a simple configuration, tubular DEAP actuator, shown in Fig. 1, can be applied in a variety of occasions and has attracted considerable concern among researchers [4], [5]. To

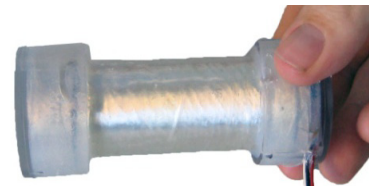


Fig. 1. Tubular DEAP actuator.

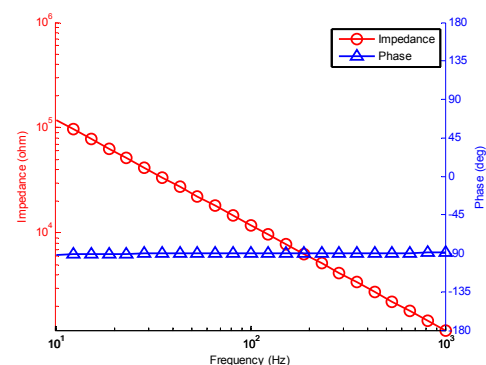


Fig. 2. Impedance versus frequency characteristic of tubular DEAP actuator.

have a better understanding of the characteristics of tubular DEAP actuator is beneficial to design desirable stimulating circuits. Firstly, the impedance versus frequency characteristic is measured using N4L PSM1735 frequency response analyzer with its impedance analysis interface, shown in Fig. 2. The -90° phase angle indicates that the measured tubular DEAP actuator is purely capacitive.

In addition, the stroke and strain versus applied voltage characteristic can be obtained by numerically solving the equations based on [6]. The stroke stands for the absolute elongation distance while strain indicates the relative expansion compared to the initial length of actuator. Corresponding to around 1.8% strain, the maximum displacement 1.05 mm under 2.4 kV implies it is necessary to fully elongate the actuator with a high voltage driving device.

Further, previous research has been performed to validate the capacitance change versus voltage characteristic [7]. According to [7], the capacitance versus strain relationship can be expressed in (1), where C_0 is the capacitance of unstrained actuator and s corresponds to the strain of the actuator.

$$C = C_0 \cdot (1 + s)^{1.83} \quad (1)$$

Together with the strain versus voltage property, we can obtain the capacitance change versus voltage characteristic. Maximum 3.2% capacitance change under 2.4 kV makes it reasonable to assume this tubular DEAP actuator to be a capacitor with constant value. This assumption tends to simplify the consideration concerning the load when designing the driving circuits.

Moreover, the electrical to mechanical efficiency has been discussed and measured in [8]. The low energy conversion ratio indicates that most electrical energy must be stored in the capacitive actuator. Therefore, a high voltage driving converter with the ability to recover the energy back to the power source is beneficial to improve the overall energy utilization ratio [1], [8].

III. IMPLEMENTATION OF HIGH VOLTAGE BIDIRECTIONAL CONVERTER

In general, autonomous actuation system tends to be preferable in the case of biomimetic and MEMS applications. Batteries are more likely to be the principle energy source in these situations. A 3 V battery powered driving converter has been proposed to implement in order to charge a DEAP actuator with 220 nF capacitance to 2.4 kV and discharge to 0 V. The designed power stage of bidirectional flyback converter is shown in Fig. 3. In addition, some critical parasitic elements are depicted as well, which will be used in the detailed behavior analysis later. In fact, the primary and secondary leakage inductors cannot exist at the same time. When energy flow is from power source to secondary side, we use primary leakage inductor to describe the untransferable energy stored in flyback transformer, and vice versa. Two capacitor charger controllers LT3750 from Linear Technology are employed to implement the control for the flyback converter. One is used to realize the charge control for the capacitive load and the discharge control is achieved through the other one. The converter has been built and the picture is shown in Fig. 4. The symbols shown in Fig. 3 and other critical parameters which

will be utilized in the following analysis have been addressed in Table I with the values.

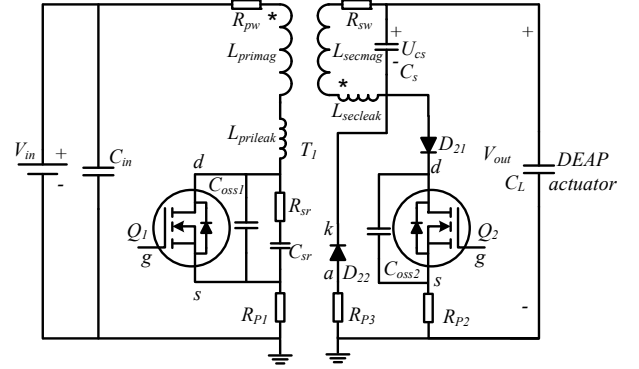


Fig. 3. Schematic of the power stage of bidirectional flyback converter.

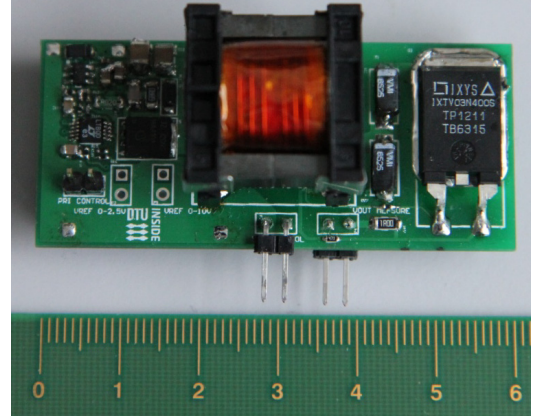


Fig. 4. Picture for the high voltage bidirectional converter.

TABLE I. HIGH VOLTAGE BIDIRECTIONAL FLYBACK CONVERTER PARAMETER DEFINITIONS AND VALUES

| Symbols | Parameters | Values |
|-------------------|---------------------------------------------|--------------------------------------------------------|
| L_{primag} | Primary magnetizing inductance | 13 μ H |
| $L_{prileak}$ | Primary leakage inductance | 300 nH |
| L_{secmag} | Secondary magnetizing inductance | 18.85 mH |
| $L_{secleak}$ | Secondary leakage inductance | 450 μ H |
| C_s | Secondary winding stray capacitance | 14.2 pF |
| R_{pw} | Primary AC resistance | 79.4 m Ω @ 1 kHz 106.81 m Ω @ 100 kHz |
| R_{sw} | Secondary AC resistance | 4.99 Ω @ 1 kHz 29.92 Ω @ 100 kHz |
| R_{dsonQ1} | Q_1 drain to source on-state resistance | 27 m Ω @ $V_{GS}=10$ V |
| C_{oss1} | Q_1 output capacitor | 280 pF @ $V_{DS}=40$ V |
| V_{fdQ1} | Q_1 body diode forward voltage | 0.7 V @ $I_F=4$ A |
| R_{dsonQ2} | Q_2 drain to source on-state resistance | $\leq 290 \Omega$ |
| C_{oss2} | Q_2 output capacitor | 19 pF @ $V_{DS}=2$ V |
| $V_{d21} V_{d22}$ | High voltage diode forward voltage | 7 V @ $I_F=150$ mA |
| R_{P1} | Primary current sensing resistor | 20 m Ω |
| $R_{P2} R_{P3}$ | Secondary current sensing resistor | 1 Ω |
| C_{sr} | Primary snubber capacitor | 220 pF |
| R_{sr} | Primary snubber resistor | 68 Ω |
| C_L | Capacitive load | 220 nF |
| V_{in} | Input voltage | 3 V |
| N | Turns ratio (secondary turns/primary turns) | 232/6 |
| $I_{pripeak}$ | Primary peak current | 4 A |
| $I_{secpeak}$ | Secondary peak current | 103 mA |

IV. DETAILED BEHAVIOR ANALYSIS OF HIGH VOLTAGE BIDIRECTIONAL FLYBACK CONVERTER AND EXPERIMENTAL VALIDATION

Considering the critical parasitic parameters shown in Fig. 3, a detailed behavior analysis has been performed. The converter is analyzed according to the charging and discharging process respectively. In order to verify the analysis and compare analyzed results with experimental ones, the experiments have been performed and the waveforms are shown beside the analyzed waveforms.

A. Charging process

The analyzed model has been built for one single charging cycle, which is applicable for any cycle in the charging process. In fact, the analysis can be carried out based on five different time intervals. In each interval, we create model to mimic the critical behavior of the converter. For certain charging cycle, the initial output voltage is represented as $V_{outInitial}$, which is the starting condition for the current cycle.

[t_0-t_1]: In this period, secondary winding stray capacitor resonates with the secondary inductance until primary MOSFET is switched on. As another point of view, the initial energy stored in C_s oscillates between C_s and $L_{secmag}+L_{seclak}$. Considering the effect of R_{sw} , the voltage over C_s can be obtained through solving (2) with the initial conditions in (3).

$$(L_{secmag} + L_{seclak}) \cdot C_s \cdot \frac{dU_{cs}(t-t_0)}{d^2(t-t_0)} + R_{sw} \cdot C_s \cdot \frac{dU_{cs}(t-t_0)}{d(t-t_0)} + U_{cs}(t-t_0) = 0 \quad (2)$$

$$\begin{cases} U_{cs}(t-t_0)|_{t=t_0} = V_{outInitial} + V_{d22} \\ \frac{dU_{cs}(t-t_0)}{d(t-t_0)}|_{t=t_0} = 0 \end{cases} \quad (3)$$

After obtaining $U_{cs}(t-t_0)$, the current through C_s can be solved through (4).

$$I_{cs}(t-t_0) = C_s \cdot \frac{dU_{cs}(t-t_0)}{d(t-t_0)} \quad (4)$$

In practice, the terminal condition in this stage for low output voltage operation is different from high voltage operation. Q_I is switched on when $U_{cs}(t-t_0)$ reaches the minimum value due to the primary controller for low output voltage. Therefore, half the resonance period can be used to calculate the time interval, represented in (5).

$$t_1 = t_0 + \pi \cdot \sqrt{L_{sec} \cdot C_s} \quad (5)$$

For high voltage operation, when $U_{cs}(t-t_0)$ reaches $-N \cdot (V_{in} + V_{bdQI})$, the body diode of Q_I is forced to conduct first, afterwards, Q_I is switched on. In fact, compared with time interval [t_1-t_3] (Q_I on time), the body diode only conducts for so short time that we can assume Q_I is switched on at exact t_1 to simplify the analysis. Hence, the time interval can be calculated through solving (6). The switchover point from low to high voltage operation is when (6) has solution and happens around when $V_{outInitial}+V_{d22}$ reaches $N \cdot (V_{in} + V_{bdQI})$.

$$U_{cs}(t-t_0)|_{t=t_1} = -N \cdot (V_{in} + V_{bdQI}) \quad (6)$$

With the solved time interval and (2), we can predict the essential behavior in this stage. However, it must be clarified that this stage does not exist for the first charging cycle due to the energy stored in C_s is 0 at the start.

[t_1-t_2]: The analysis for this period needs to be divided into low and high output voltage as well. According to [9], in the low voltage operation, V_{in} starts to magnetize the primary inductance, meanwhile, U_{cs} is charged to $-V_{in} \cdot N$ through the resonance between the $L_{prileak}$ and the reflected capacitance of C_s+C_{oss2} in the primary side. Due to D_{21} , the actual behavior is much more complex, we assume C_{oss2} is in parallel with C_s in order to simplify the model. In this short period, we only consider the resonance and leave the calculation concerning magnetization to the whole [t_1-t_3] period later. Therefore, $U_{cs}(t-t_1)$ can be obtained through solving (7) under the initial conditions in (8).

$$\begin{aligned} & L_{prileak} \cdot N^2 \cdot (C_s + C_{oss2}) \cdot \left(-\frac{d^2 U_{cs}(t-t_1)}{d^2(t-t_1)} \right) + \left(R_{dsonQ1} + R_{P1} + \frac{R_{sw}}{N^2} \right) \cdot N^2 \cdot (C_s + C_{oss2}) \cdot \frac{dU_{cs}(t-t_1)}{d(t-t_1)} - \frac{U_{cs}(t-t_1)}{N} = V_{in} \quad (7) \\ & \begin{cases} U_{cs}(t-t_1)|_{t=t_1} = U_{cs}(t-t_0)|_{t=t_1=t_0+\pi \cdot \sqrt{L_{sec} \cdot C_s}} \\ \frac{dU_{cs}(t-t_1)}{d(t-t_1)}|_{t=t_1} = 0 \end{cases} \quad (8) \end{aligned}$$

After deriving $U_{cs}(t-t_1)$, the current through C_s can be solved through (9).

$$I_{cs}(t-t_1) = (C_s + C_{oss2}) \cdot \frac{dU_{cs}(t-t_1)}{d(t-t_1)} \quad (9)$$

For high voltage operation, at the end of period [t_0-t_1], the body diode in Q_I starts to conduct in order to transfer the energy stored in flyback transformer to primary power source. Owing to the energy stored in L_{seclak} , the resonance between L_{seclak} and (C_s+C_{oss2}) takes place in [t_1-t_2]. Therefore, the similar equation as (7) can be derived to acquire U_{cs} for high voltage operation. However, the initial conditions are different, which are represented in (10).

$$\begin{cases} U_{cs}(t-t_1)|_{t=t_1} = U_{cs}(t-t_0)|_{t=t_1} = -N \cdot (V_{in} + V_{bdQI}) \\ \frac{dU_{cs}(t-t_1)}{d(t-t_1)}|_{t=t_1} = \frac{dU_{cs}(t-t_0)}{d(t-t_0)}|_{t=t_1} \end{cases} \quad (10)$$

[t_1-t_3]: This stage is the on time for Q_I . The current through L_{secmag} can be obtained through solving (11).

$$(L_{primag} + L_{prileak}) \cdot \frac{dI_{primag}(t-t_1)}{d(t-t_1)} + (R_{dsonQ1} + R_{P1} + R_{pw}) \cdot I_{primag}(t-t_1) = V_{in} \quad (11)$$

The initial current for I_{primag} in the low voltage operation is 0, however, the current starts from a minus value for high output voltage, which is represented in (12).

$$I_{primag}(t-t_1)|_{t=t_1} = N \cdot I_{cs}(t-t_0)|_{t=t_1} \quad (12)$$

Because of the fixed peak current control, the time interval for this stage can be acquired by solving (13).

$$I_{primag}(t-t_1)|_{t=t_3} = I_{pripeak} \quad (13)$$

Combining the resonance in [t_1-t_2] and the magnetizing equations for [t_1-t_3], we can build the model to mimic the behavior in the whole [t_1-t_3] period.

[t_3-t_4]: At t_3 , Q_I is switched off. Due to the influence of C_s , D_{22} cannot conduct when Q_I is just turned off. The energy stored in flyback transformer needs to charge C_s until U_{cs} reaches $V_{outInitial}+V_{d22}$. The time interval [t_3-t_4] is used to express this behavior. Replacing $L_{secmag}+L_{seclak}$ with L_{secmag} in (2), we can get the similar differential equation to calculate U_{cs} in this period and the initial conditions are given in (14).

$$\begin{cases} U_{cs}(t-t_3)|_{t=t_3} = -N \cdot V_{in} \\ \frac{dU_{cs}(t-t_3)}{d(t-t_3)}|_{t=t_3} = \frac{I_{pripeak}}{N} \end{cases} \quad (14)$$

The time interval can be obtained through solving (15) with the terminal condition — U_{cs} reaches $V_{outInitial} + V_{d22}$.

$$U_{cs}(t-t_3)|_{t=t_4} = V_{outInitial} + V_{d22} \quad (15)$$

The final current through C_s in this period needs to be calculated as well, represented in (16), which is the actual initial freewheeling current for next time interval.

$$I_{fwInitial} = C_s \cdot \frac{dU_{cs}(t-t_3)}{d(t-t_3)}|_{t=t_4} \quad (16)$$

This period can be neglected in the low voltage operation and tends to become more obvious with the increasing of the output voltage. In fact, when Q_1 is switched off, $L_{pripeak}$ will resonate with C_{oss1} and C_{sr} to dissipate the stored energy. But this phenomenon only exists for a very short time even compared to the time interval $[t_3-t_4]$. Therefore, this resonance behavior has not been modelled. However, in the worst case, all the energy stored in $L_{pripeak}$ is used to charge C_{oss1} , what we need to do is to check the maximum voltage over C_{oss1} will not exceed the voltage rating of Q_1 .

$[t_4-t_5]$: This stage is used to release the energy stored in transformer to the capacitive load. The output voltage V_{out} can be acquired by solving the differential equation in (17) with the initial conditions given in (18).

$$L_{secmag} \cdot C_L \cdot \frac{d^2 V_{out}(t-t_4)}{d^2(t-t_4)} + R_{sw} \cdot C_L \cdot \frac{dV_{out}(t-t_4)}{d(t-t_4)} + V_{out}(t-t_4) + V_{d22} = 0 \quad (17)$$

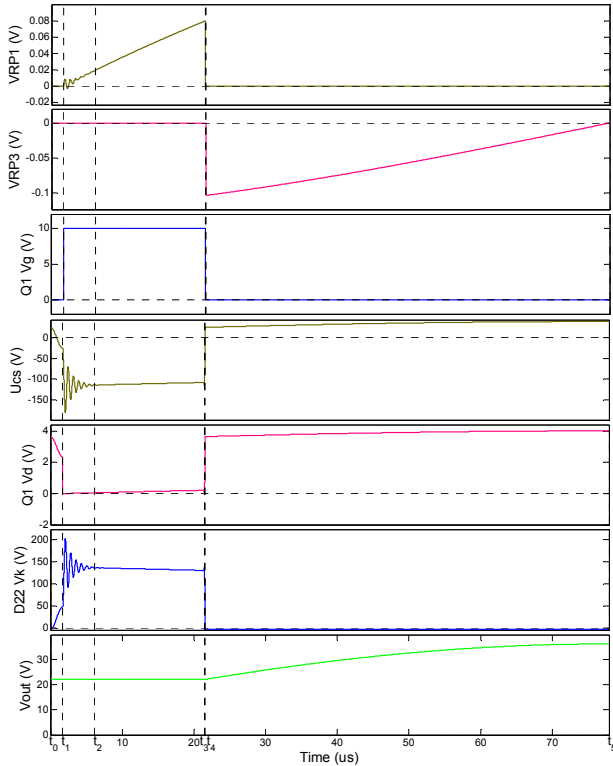


Fig. 5. Calculated critical waveforms of low output voltage operation in charging process.

$$\begin{cases} V_{out}(t-t_4)|_{t=t_4} = V_{outInitial} \\ \frac{dV_{out}(t-t_4)}{d(t-t_4)}|_{t=t_4} = \frac{I_{fwInitial}}{C_L} \end{cases} \quad (18)$$

In addition, the freewheeling current is given by

$$I_{CL}(t-t_4) = C_L \cdot \frac{dV_{out}(t-t_4)}{d(t-t_4)} \quad (19)$$

By solving (20), we can get the freewheeling time and calculate the final output voltage for this charging cycle.

$$I_{CL}(t-t_4)|_{t=t_5} = 0 \quad (20)$$

Based on the analysis mentioned above, a Maple program has been completed to solve all the differential equations with initial conditions. The symbolic solutions have been exported to MATLAB for obtaining the critical waveforms of the converter. In order to validate the model, the calculated critical waveforms for low output voltage operation ($V_{outInitial}=22$ V) in the charging process are shown in Fig. 5 and compared with the corresponding experimental waveforms in Fig. 6 and 7. In addition, the calculated critical waveforms for high voltage operation ($V_{outInitial}=2000$ V), shown in Fig. 8, are compared with the experimental waveforms in Fig. 9 and 10 as well. The good match can verify the analysis as well as the mathematical model.

B. Discharging process

Similarly, the analyzed models based on different time intervals and differential equations have been built for one single cycle in discharging process. And the initial output voltage is represented as $V_{outInitial}$ as well.

$[t_0-t_1]$: Q_2 is switched on in this period. The energy in the capacitive load starts to magnetize flyback transformer until secondary current reaches the preset peak value. The output voltage can be obtained through solving similar differential equation represented in (17) with initial conditions given in (21).

$$\begin{cases} V_{out}(t-t_0)|_{t=t_0} = V_{outInitial} \\ \frac{dV_{out}(t-t_0)}{d(t-t_0)}|_{t=t_0} = 0 \end{cases} \quad (21)$$

Through similar equation as (4), we can calculate the secondary current $I_{sec}(t-t_0)$. Then the time interval can be

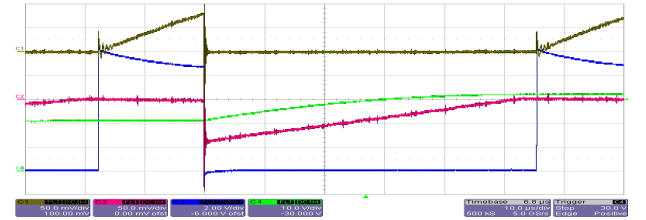


Fig. 6. Experimental waveforms for low output voltage operation in charging process (CH1-VRP1 CH2-VRP3 CH3-Q1 Vg CH4-Vout).

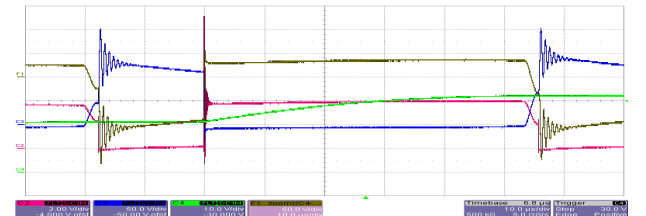


Fig. 7. Experimental waveforms for low output voltage operation in charging process (F1-Ucs CH2-Q1 Vd CH3-D22 Vd CH4-Vout).

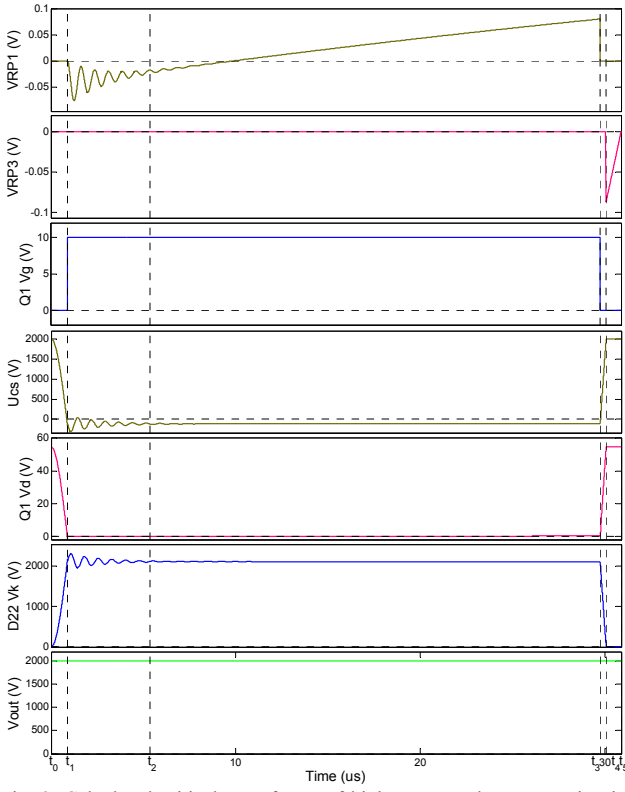


Fig. 8. Calculated critical waveforms of high output voltage operation in charging process.

acquired with analogical equation represented in (13), with which the final output voltage $V_{outFinal}$ can be determined.

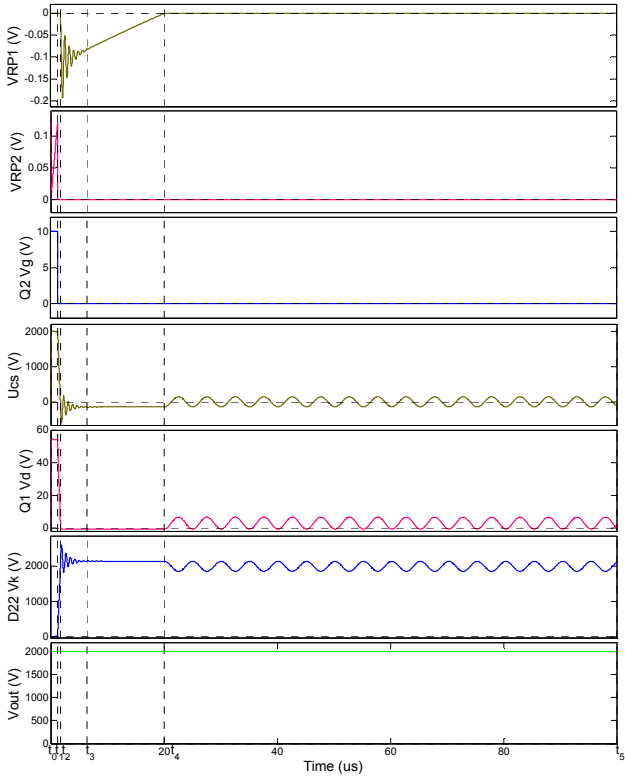


Fig. 11. Calculated critical waveforms of high output voltage operation in charging process.

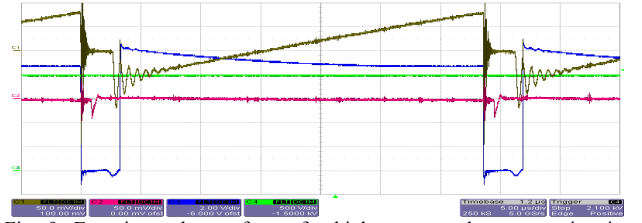


Fig. 9. Experimental waveforms for high output voltage operation in charging process (CH1- V_{RP1} CH2- V_{RP3} CH3- $Q_1 V_g$ CH4- V_{out}).

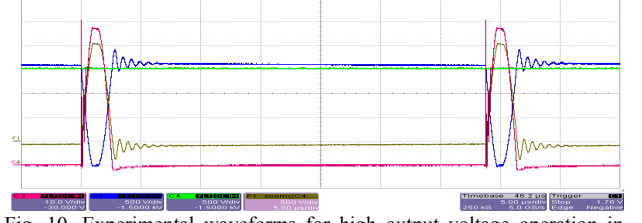


Fig. 10. Experimental waveforms for high output voltage operation in charging process (F1- U_{cs} CH2- $Q_1 V_d$ CH3- $D_{22} V_k$ CH4- V_{out}).

$[t_1-t_2]$: $L_{secmag} + L_{seclak}$ resonate with $C_s + C_{oss2}$ in this period until U_{cs} reaches the $-N \cdot (V_{in} + V_{bdQ1})$. The behaviors are similar as $[t_0-t_1]$ in charging process. Hence, the similar equation as (2) can be derived to calculate U_{cs} with the initial conditions represented in (22).

$$\begin{cases} U_{cs}(t-t_1)|_{t=t_1} = V_{outFinal} \\ \frac{dU_{cs}(t-t_1)}{d(t-t_1)}|_{t=t_1} = -\frac{I_{secpeak}}{C_s + C_{oss2}} \end{cases} \quad (22)$$

$[t_2-t_3]$: L_{seclak} resonate with $C_s + C_{oss2}$ in this period until all the energy stored in L_{seclak} dissipates. This stage has the similar behavior as $[t_1-t_2]$ in charging process. The analysis for high voltage operation in charging cycle is valid here and we can derive (23) to calculate U_{cs} in this period with the initial conditions given in (24).

$$L_{seclak} \cdot (C_s + C_{oss2}) \cdot \frac{d^2 U_{cs}(t-t_2)}{d^2(t-t_2)} + R_{sw} \cdot (C_s + C_{oss2}) \cdot \frac{dU_{cs}(t-t_2)}{d(t-t_2)} + U_{cs}(t-t_2) = 0 \quad (23)$$

$$\begin{cases} U_{cs}(t-t_2)|_{t=t_2} = U_{cs}(t-t_1)|_{t=t_2} \\ \frac{dU_{cs}(t-t_2)}{d(t-t_2)}|_{t=t_2} = \frac{dU_{cs}(t-t_1)}{d(t-t_1)}|_{t=t_2} \end{cases} \quad (24)$$

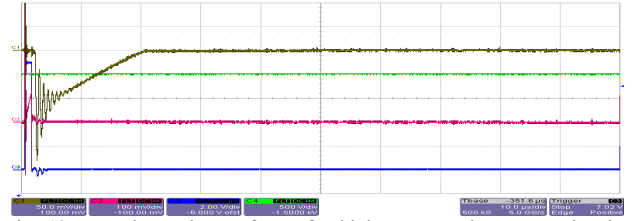


Fig. 12. Experimental waveforms for high output voltage operation in discharging process (CH1- V_{RP1} CH2- V_{RP2} CH3- $Q_2 V_g$ CH4- V_{out}).

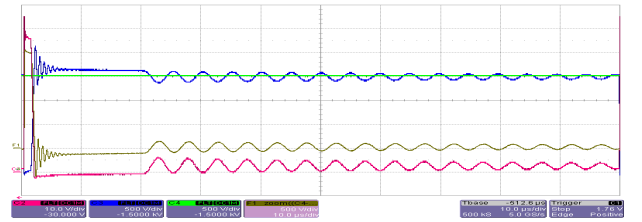


Fig. 13. Experimental waveforms for high output voltage operation in discharging process (F1- U_{cs} CH2- $Q_1 V_d$ CH3- $D_{22} V_k$ CH4- V_{out}).

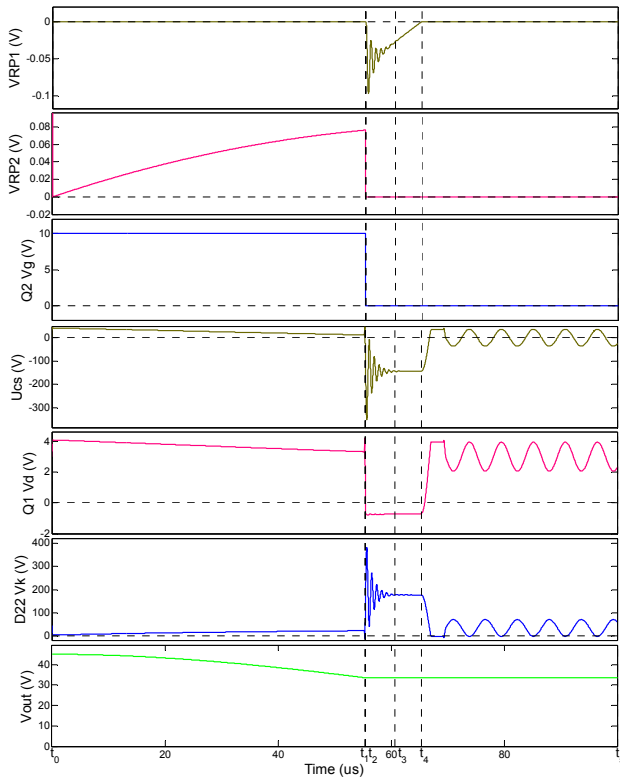


Fig. 14. Calculated critical waveforms of low output voltage operation in charging process.

[t_2 - t_4]: In this whole period, the energy stored in flyback transformer is transferred to primary power source through body diode of Q_1 . Similar behaviors occur in stage [t_1 - t_3] of charging cycle. The derived equation (11) can be applied here with minor changes.

[t_4 - t_5]: This is the discontinuous conduction mode period in discharging cycle. C_s as well as C_{oss2} will resonate with $L_{secmag} + L_{seclak}$ until the start of next cycle. In the high voltage operation, the voltage across C_s can be acquired by solving differential equation (25) with initial conditions in (26).

$$(L_{secmag} + L_{seclak}) \cdot (C_s + C_{oss2}) \cdot \frac{d^2 U_{cs}(t-t_4)}{dt^2(t-t_4)} + R_{sw} \cdot (C_s + C_{oss2}) \cdot \frac{dU_{cs}(t-t_4)}{dt(t-t_4)} + U_{cs}(t-t_4) = 0 \quad (25)$$

$$\begin{cases} U_{cs}(t-t_4)|_{t=t_4} = U_{cs}(t-t_2)|_{t=t_4} \\ \frac{dU_{cs}(t-t_4)}{dt(t-t_4)}|_{t=t_4} = 0 \end{cases} \quad (26)$$

For low output voltage operation, the behavior is more complex because the maximum resonance voltage over C_s is clamped to $V_{outFinal} + V_{d22}$. Similar with charging process, the switchover point occurs when $V_{outFinal} + V_{d22}$ reaches $N \cdot (V_{in} + V_{bdQ1})$.

Another Maple program has been finished to solve all the differential equations for one discharging cycle and the solutions have been transferred to MATLAB in order to draw the critical waveforms as well. The calculated critical waveforms when $V_{outInitial}=46$ V and $V_{outInitial}=2000$ V are shown in Fig. 11 and 14, respectively. The corresponding experimental waveforms, shown in Fig. 12, 13, 15 and 16, indicate the good match with calculated ones.

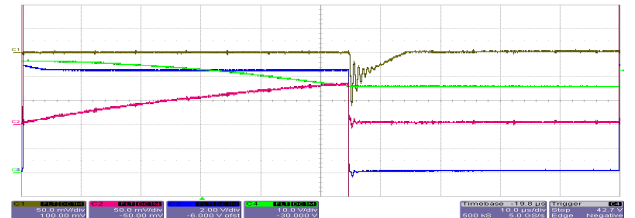


Fig. 15. Experimental waveforms for low output voltage operation in discharging process (CH1-VRP1 CH2-VRP2 CH3-Q2 Vg CH4-Vout).

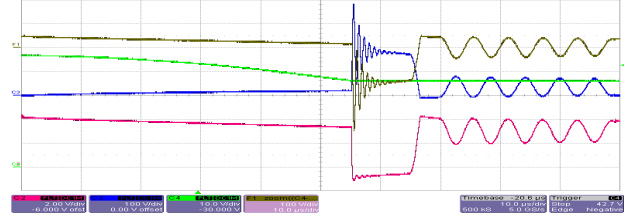


Fig. 16. Experimental waveforms for low output voltage operation in discharging process (F1-Ucs CH2-Q1 Vd CH3-D22 Vd CH4-Vout).

V. CONCLUSION

As a new type of smart material, DEAP material as well as DEAP based tubular actuator are introduced. The essential characteristics have been investigated. A low input voltage bidirectional flyback based converter for driving DEAP actuator has been implemented. The detailed behavior analysis considering the influence of the critical parasitic elements has been performed for the operation of the converter, including the analysis for both charging and discharging processes in the low and high output voltage conditions. The experimental results can provide a good proof for the analysis.

REFERENCES

- [1] Y. Bar-Cohen, Electroactive Polymer (EAP) Actuators as Artificial Muscles: Reality, Potential, and Challenges, 2nd ed. Washington, DC: SPIE, 2004.
- [2] R. Sarban, B. Lassen, and M. Willatzen, "Dynamic electromechanical modeling of dielectric elastomer actuators with metallic electrodes," IEEE/ASME Transactions on Mechatronics, vol. 17, no. 5, pp. 960-967, October 2012.
- [3] Y. Iskandarani and H. R. Karimi, "Sensing capabilities based on dielectric electro active polymers - feasibility and potential state-of-the-art application," IEEE Sensors Journal, vol. 12, no. 8, pp. 2616-2624, August 2012.
- [4] L. Huang, Z. Zhang, and M. A. Andersen, "A review of high voltage drive amplifiers for capacitive actuators," 47th International Universities Power Engineering Conference (UPEC), 2012.
- [5] T. Andersen, M. S. Rødgaard, O. C. Thomsen, and M. A. E. Andersen, "Low voltage driven dielectric electro active polymer actuator with integrated piezoelectric transformer based driver," SPIE, vol. 7976, pp. 79762N-1-79762N-12, 2011.
- [6] R. Sarban, R. W. Jones, B. R. Mace and E. Rustighi, "A tubular dielectric elastomer actuator: Fabrication, characterization and active vibration isolation," Mechanical Systems and Signal Processing, vol. 25, pp. 2879-2891, 2011.
- [7] T. Andersen, L. Huang, M. Andersen, and O. Thomsen, "Efficiency of capacitively loaded converters," 38th Annual Conference on IEEE Industrial Electronics Society (IECON), pp. 368-373, 2012.
- [8] M. J. Tryson, R. Sarban, and K. P. Lorenzen, "The dynamic properties of tubular DEAP actuators," Electroactive Polymer Actuators and Devices (EAPAD), vol. 7642, 2010.
- [9] S.-K. Chung, "Transient characteristics of high-voltage flyback transformer operating in discontinuous conduction mode," IEE Electric Power Applications, vol. 151, no. 5, pp. 628-634, 2004.

APPENDIX H

Analytical Switching Cycle Modeling of Bidirectional High Voltage Flyback Converter for Capacitive Load Considering Core Loss Effect

Submitted to Transactions on Power Electronics (TPEL-Reg-2014-10-1700)

Analytical Switching Cycle Modeling of Bidirectional High Voltage Flyback Converter for Capacitive Load Considering Core Loss Effect

Lina Huang, *Student Member, IEEE*, Zhe Zhang, *Member, IEEE*, and Michael A. E. Andersen, *Member, IEEE*

Department of Electrical Engineering, Technical University of Denmark

Kgs. Lyngby, DK-2800, Denmark

ABSTRACT

With the advancement of material science, various smart materials with intrinsic capacitive property are emerging. The high voltage (HV) power electronics converters with bidirectional energy flow functionality for feeding the capacitive load are highly demanded. A switching cycle based analytical model of HV bidirectional converter driving capacitive load is beneficial in thoroughly understanding the operational behavior, investigating the energy efficiency and optimizing the design. In this paper, a HV bidirectional flyback converter for capacitive load is generally discussed in terms of configuration, working principle and control scheme. Considering the parasitic elements as well as the core loss effect, the converter is modeled with analytical formulas for one switching cycle. The comparison between the model based calculation results and prototype experiments based measurement results are used to validate the analytical model.

Index Terms—Analytical modeling, switching cycle, high voltage, bidirectional, flyback, capacitive load

I. INTRODUCTION

Power electronics technology focuses on processing power in order to feed the load as required with minimum cost in terms of power loss (high efficiency), volume (high power density) and price (low cost) [1]-[3]. Since the equipments or devices with resistive or resistive-inductive

characteristic have been intensively used, such as the electrical heater, motor and lighting appliance, most research in this field pays attention to the resistive or resistive-inductive load. In the past decades, with the rapid development of material science, a variety of smart material with intrinsic capacitive property is constantly emerging. Due to their advantages, such as light weight, compact size, nonmagnetic and the ability to directly generate mechanical motion under external voltage, they tend to become desired candidate in various actuation systems to replace the conventional hydraulic, pneumatic or electromagnetic actuator. In order to feed the capacitive actuators as required, a considerable effort needs to be dedicated to develop the applicable power electronics converters with competitive efficiency, size as well as cost.

Piezoelectric and dielectric electro active polymer (DEAP) materials are two types of smart material with highly capacitive characteristic [4] [5]. They share a similar structure – an insulating layer sandwiched between two compliant conducting electrodes. The ceramic material forms dielectric layer in the piezoelectric case and the soft silicone polymer is employed for DEAP material. Once an electric field is applied to the capacitive materials, the deformation of the insulation layer will be induced due to the inverse piezoelectric effect or electrostatic force. This intrinsic property enables the actuators composed of capacitive materials. One common challenge in driving capacitive actuators is the relatively high stimulating voltage: thanks to the employment of multilayer structure in piezoelectric actuator, this voltage can be reduced to the range of hundred volts; however in DEAP case, the voltage still needs to be in the vicinity of several kilovolts in order to fully elongate the actuator. Normally, this high voltage (HV) cannot be directly available, especially in the autonomous circumstance, which actually will be the most case for the system consisting of capacitive actuator. Thus, a converter with the features of low input voltage and high output voltage needs to be investigated. Besides, to avoid the waste of electrical energy stored in the capacitive actuator, the energy (charge) recovery technique needs to be employed in order to

recycle the energy to the power source when the actuator needs to be released [6]. Hence, a converter which can deal with the bidirectional energy flow tends to be a desired candidate in this case.

As a simple and easily implemented configuration with galvanic isolation functionality, flyback topology has been widely used in power electronics industry, such as the laptop and mobile phone charger, standby power supplies, etc. [7] [8]. Recently, due to the energy crisis, researchers in power electronics community concentrate more on investigating the flyback based inverters for renewable energy applications [9]-[15]. Besides, the investigation regarding the flyback has also been intensively carried out in the field of light-emitting diode (LED) driver [16]-[22]. As a mature technology, flyback is well suited for the high output voltage applications since no extra inductor is needed in the HV side and it had already been successfully applied in the color TVs to generate HV [23]-[25]. Flyback topology can easily achieve the bidirectional energy flow by replacing the rectifier diode with an active semiconductor device in the secondary side [26] [27]. The emerging of smart materials will encourage the research into the HV bidirectional energy conversion for capacitive load in coming years. Preliminary research has been conducted to design and implement the bidirectional HV flyback converter for capacitive actuators [28]-[30]. As a critical part in flyback configuration, the transformer (coupled inductors) considerably affects the operational behavior due to the parasitic elements, especially in the HV condition [7] [31]-[33]. Compared to the converter feeding the resistive load, the capacitive property of the actuators will introduce different operating behavior for the energy conversion. The effect of core loss needs to be taken into account in this capacitive load case, if an accurate model is set to be the ultimate goal. Hence, the operational behavior is worthy to be investigated in the bidirectional energy flow for HV converter with capacitive load in order to thoroughly understand the working principle, which will be beneficial for analyzing the efficiency, providing the design guideline as well as optimizing the

design. This paper will focus on the analytical behavioral modeling of bidirectional HV flyback converter for capacitive load in each switching cycle with the consideration of core loss effect. In Section II, the bidirectional HV flyback converter for capacitive load is described in terms of configuration, fundamental operation principle and basic control schemes. The general discussion, definition and consideration utilized to perform the analytical modeling as well as the detailed analytical switching cycle modeling are presented in Section III. In Section IV, the analyzed model is verified through the comparison between the calculated results and the experimental ones for both charging and discharging mode. The efficiency comparison is applied to verify the importance of considering the core loss. A conclusion is drawn in Section V.

II. DESCRIPTION OF BIDIRECTIONAL HV FLYBACK CONVERTER FOR CAPACITIVE LOAD

A. Topology and configuration

The proposed bidirectional HV flyback converter for capacitive load is depicted in Fig. 1. Due to the poor performance of body diode inside the HV MOSFET (S_2), two extra HV diodes (D_{21} and D_{22}) are employed to block the current through the body diode and to form the freewheeling path for the secondary side current, respectively. The current sensing resistors (RP_1 , RP_2 and RP_3) are applied in order to realize the current loop control. As aforementioned, the parasitic components in flyback transformer will introduce significant influence to the operation of the converter, especially in the HV condition, and must be considered in the analytical modeling. The most critical parasitic element in the HV transformer is the secondary winding stray capacitance caused by a large number of winding turns [31] [34]. Combined with other parasitic capacitances in the HV side, such as the junction capacitance of HV diodes and the output capacitance of the HV MOSFET, an equivalent stray capacitance C_{seq} paralleled to secondary winding of transformer is utilized to represent the effect of parasitic capacitances. In addition, the leakage inductance (L_{pl} and L_{sl}) has always been

focused on by the researchers who want to improve the efficiency [7]. It should be noted that the primary side leakage inductance (L_{pl}) and secondary side leakage inductance (L_{sl}) cannot exist simultaneously. When the energy flow is from primary side to secondary side, L_{pl} is adopted to stand for the untransferrable energy stored in the flyback transformer. The same concept applies to L_{sl} . Furthermore, in order to establish the precise analytical model, the winding resistances (R_{pw} and R_{sw}) cannot be neglected. All the essential parasitic elements are shown in Fig. 1 as well. For precisely analyzing the behavior of the converter feeding capacitive load, the impact of the core loss must be considered as in the conventional converter for resistive load. Resistive element is proved to be an effective means to represent the core loss. An equivalent resistance of core loss reflected to the secondary side (R_{ceqs}), therefore, is employed to stand for the influence of the core loss in each switching cycle.

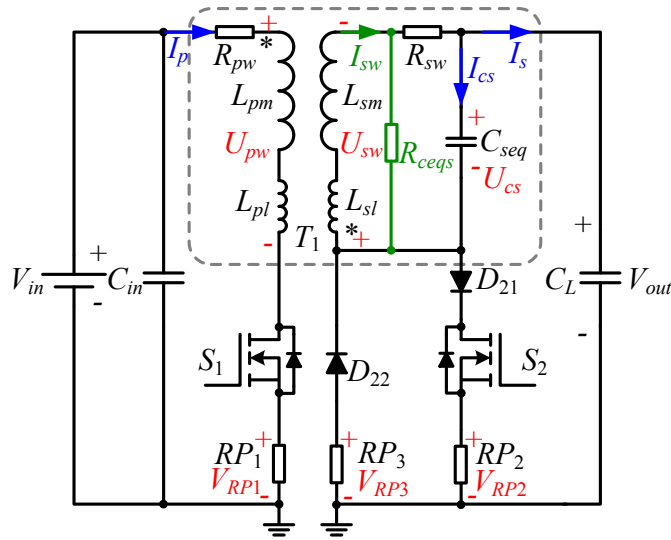


Fig. 1. The configuration of bidirectional HV flyback converter for capacitive load.

B. General operation principle

Unlike the conventional DC-DC converter, the bidirectional HV converter designed for capacitive load normally does not operate in the steady state. The common operating states consist

of the charging mode (the output voltage increases) - energy transfers from source to the capacitive load, and discharging mode (the output voltage decreases) - energy recycles from capacitive load to power source. The entire charging process from zero till the pre-set maximum output voltage is just like the start up process in the conventional converter and consists of a large number of successive switching charging cycles. Similarly, the overall discharging process is comprised of a lot of successive switching cycles to discharge the capacitive load from maximum voltage to zero. The variation of output voltage in the normal operation is shown in Fig. 2 with the identification of entire charging and discharging process as well as switching cycles in charging and discharging mode.

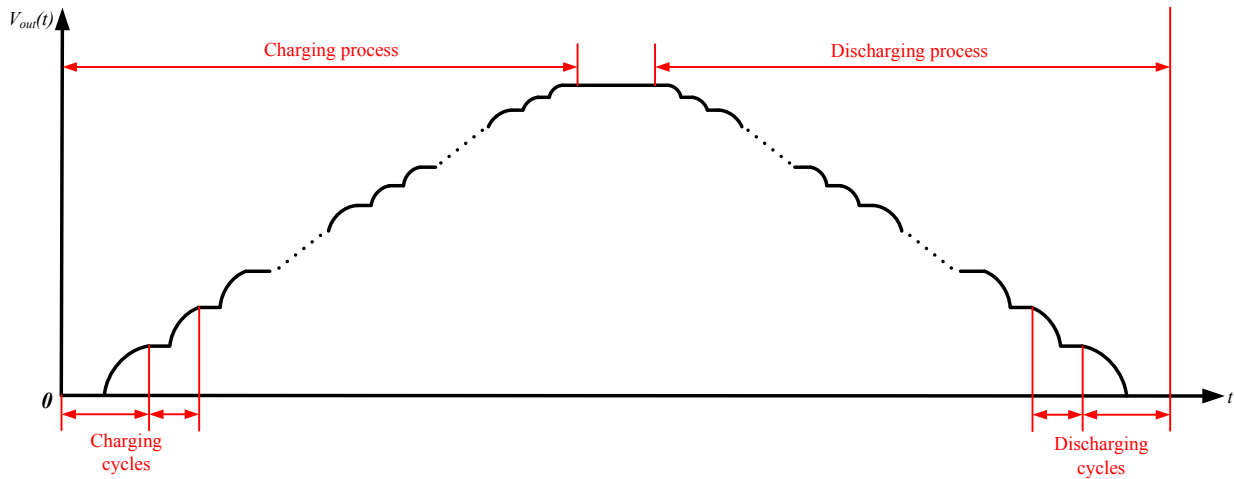


Fig. 2. The output voltage variation in the normal operation.

C. Control schemes

The frequently used double closed loop control schemes, i.e. the inner current loop control and outer voltage loop control, in the conventional switch-mode power converters can be applied for the converter with capacitive load as well.

In terms of current control, there are two commonly implemented strategies – average current mode control and peak current mode control. Compared to the former one, peak current mode control tends to be more desirable in the flyback configuration due to its quick response time,

intrinsic cycle-by-cycle current protection function as well as the easy implementation. In order to achieve the complete energy transfer in each switching cycle, the Boundary Conduction Mode (BCD) or Discontinuous Conduction Mode (DCM) tends to be a good solution.

For most conventional converters, the output voltage is fixed while the input voltage can vary within a certain range. The function of the voltage closed loop is to regulate the output voltage accurately under various load and input voltage conditions. Normally, the small-signal analysis needs to be carried out and the traditional proportional-integral (PI) controller is utilized to guarantee the voltage loop stable at any condition. However, all these mentioned above cannot be applied for the converter with capacitive load. In fact, the pure capacitive characteristic of the load indicates that the output voltage changes only when there is current flowing through the load. Considering the requirement of the variation for the output voltage, the simple hysteresis voltage control tends to be a desirable choice in this case [35].

III. ANALYTICAL MODELING

A. General discussion and definitions

As the typical and long-term operation status in conventional DC-DC converter, the steady state has been traditionally researched in terms of modeling and detailed analysis. Correspondingly, the charging and discharging modes, as the normal operating states, in the converter with capacitive load are necessary to be thoroughly investigated. Referring to Fig. 2, the charging process contains a series of switching cycles and the behavior in one switching cycle differs from that in another one due to the variable initial output voltage. In spite of this, all the switching cycles share the same fundamental analytical model. Hence, the investigation of charging mode can be focused on just one single charging cycle. The same concept can also be applied to the discharging mode. In this paper, the charging mode will be analyzed in BCM while the discharge mode will be modeled in DCM.

In the circuit shown in Fig. 1, as aforementioned, L_{pm} and L_{sm} are primary and secondary magnetizing inductances, respectively. L_{pl} and L_{sl} are primary and secondary leakage inductances, respectively. And $L_p = L_{pm} + L_{pl}$ as well as $L_s = L_{sm} + L_{sl}$ is utilized to stand for the primary and secondary total inductance. RP_1 , RP_2 and RP_3 are the resistances of three current sensing resistors. The secondary side equivalent parasitic capacitance paralleled to transformer winding is denoted as C_{seq} . V_{D21} and V_{D22} are the forward voltage drop of high voltage diodes D_{21} and D_{22} , respectively. In fact, the voltage drop changes with the forward current. To reduce the complexity, the constant forward voltage drop is assumed here. In the discharging mode, the body diode of primary switch (S_1) plays the role of freewheeling and its forward voltage drop is denoted as V_{bdS1} . In order to improve the accuracy of the model, the on resistances of MOSFETs (S_1 and S_2) need to be taken into account, especially that for the HV MOSFET due to its large value. On the other hand, to simplify the analytical model, the on resistances are considered to be a fixed value and denoted as R_{dsonS1} and R_{dsonS2} , respectively. Winding resistances (R_{pw} and R_{sw}) are frequency related parameters and do not have the fixed values, which will be defined in the analytical modeling later. C_L is utilized to stand for the capacitance of the capacitive load. V_{in} is the input voltage source with fixed value, V_o is the output voltage and the initial output voltage for the current switching cycle is denoted as V_{oini} . U_{cs} is used to stand for the voltage over the equivalent parasitic capacitance C_{seq} . Considering the measuring of the current in reality, it is reasonable to use the voltages over the current sensing resistors V_{RP1} , V_{RP2} and V_{RP3} to represent the currents in the circuit. The voltages over transformer windings are denoted as U_{pw} and U_{sw} , respectively. And the positive directions for all the voltages are illustrated in Fig. 1. The primary current I_p and secondary current I_s are also depicted in Fig. 1 with their positive directions. The current through C_{seq} is denoted as I_{cs} with the corresponding positive direction to the voltage. Due to the impact of C_{seq} and the equivalent

resistance of core loss, the secondary current I_s cannot stand for the secondary side winding current, which is then denoted as I_{sw} with the positive direction shown in Fig. 1.

B. Discussion of core loss and its equivalent resistance R_{ceqs}

It is reasonable to discuss the capacitively loaded converter from the energy point of view, since there is no real output power for this type of converter. For charging mode, in a certain switching cycle, the input energy from power source can be assumed to be fixed if the corresponding current control mode is employed, thus, the energy increase over the capacitive load will depend on the energy losses for all the components in the converter. Therefore, in order to accurately predict the voltage variation of the load during this switching period, all the losses need to be taken into account, including the core loss. In terms of energy flow, the discharging mode can be considered to be the reverse process of charging mode. To establish the precise model, the core loss effect cannot be neglected as well.

The most commonly used method to calculate core loss is the Steinmetz equation. It should be noted that this equation is only valid for sinusoidal waveforms and cannot be directly applied in most power electronics systems [36] [37]. In order to overcome this limitation, several methodologies have been proposed. Among them, the widely adopted approach is the improved generalized Steinmetz equation (iGSE) [36] [37]

$$P_v = \frac{1}{T} \int_0^T k_i \left| \frac{dB}{dt} \right|^\alpha (\Delta B)^{\beta-\alpha} dt \quad (1)$$

$$k_i = \frac{k}{(2\pi)^{\alpha-1} \int_0^{2\pi} |\cos \theta|^\alpha 2^{\beta-\alpha} d\theta} \quad (2)$$

where P_v is the time-average power loss per unit volume, T stands for the switching period, $\left| \frac{dB}{dt} \right|$ is the absolute value of change rate of flux density, ΔB is the peak-to-peak flux density and α , β , k are material related parameters, which can be obtained or derived from the datasheet of the material.

As previously stated, resistive element can be utilized to represent the effect of core loss. If the analytical model in one switching cycle is known, the core loss can be calculated through (1), thus the secondary side equivalent resistance of core loss R_{ceqs} can be derived through (3) and the detailed behavior can be predicted [37].

$$R_{ceqs} = \frac{U_{sw}^2}{P_v} \quad (3)$$

However, the contradiction is that without knowing the equivalent resistance of core loss, the accurate analytical model cannot be obtained in advance. One feasible approach is proposed: 1) build the accurate behavior model in one switching cycle considering the impact of R_{ceqs} ; 2) set R_{ceqs} to infinity in order to avoid the consideration of the core loss to achieve the estimated behavior model in one switching cycle; 3) based on the estimated model, through (1) and (3), the equivalent resistance of core loss can be obtained; 4) apply the acquired R_{ceqs} to the accurate model to achieve the precise behavior in one switching cycle. Hence, in the following derivation process, including the charging mode as well as the discharging mode, this methodology will be applied in order to acquire the accurate analytical behavior model in one switching cycle.

C. Analytical behavior modeling of charging mode

In charging mode, due to the employment of BCM, one switching cycle consists of 4 stages. In Fig. 3 (a)-(d), considering the equivalent resistance of core loss, the equivalent circuits of different operation stages with the practical current flow direction are depicted respectively. And the key waveforms concerning the operation stages, including the waveforms for low and high output voltages in the charging process, are shown in Fig. 4.

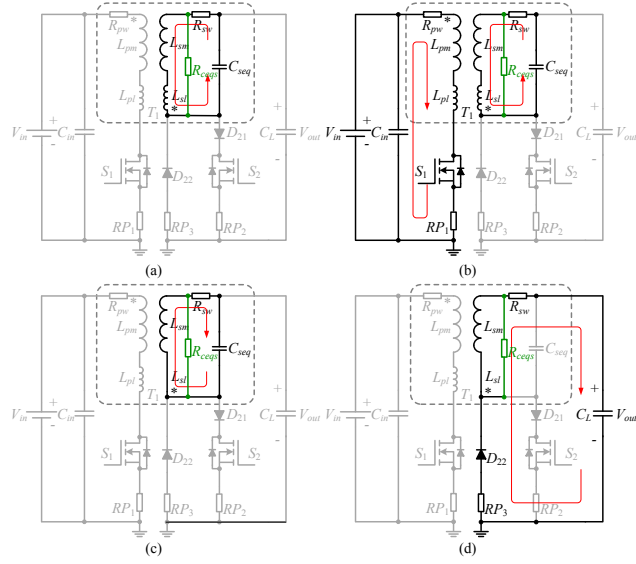


Fig. 3. Equivalent circuit schemes of different operation stages.
 (a) $t_0 < t < t_1$ (b) $t_1 < t < t_2$ (c) $t_2 < t < t_3$ (d) $t_3 < t < t_4 = t_0$.

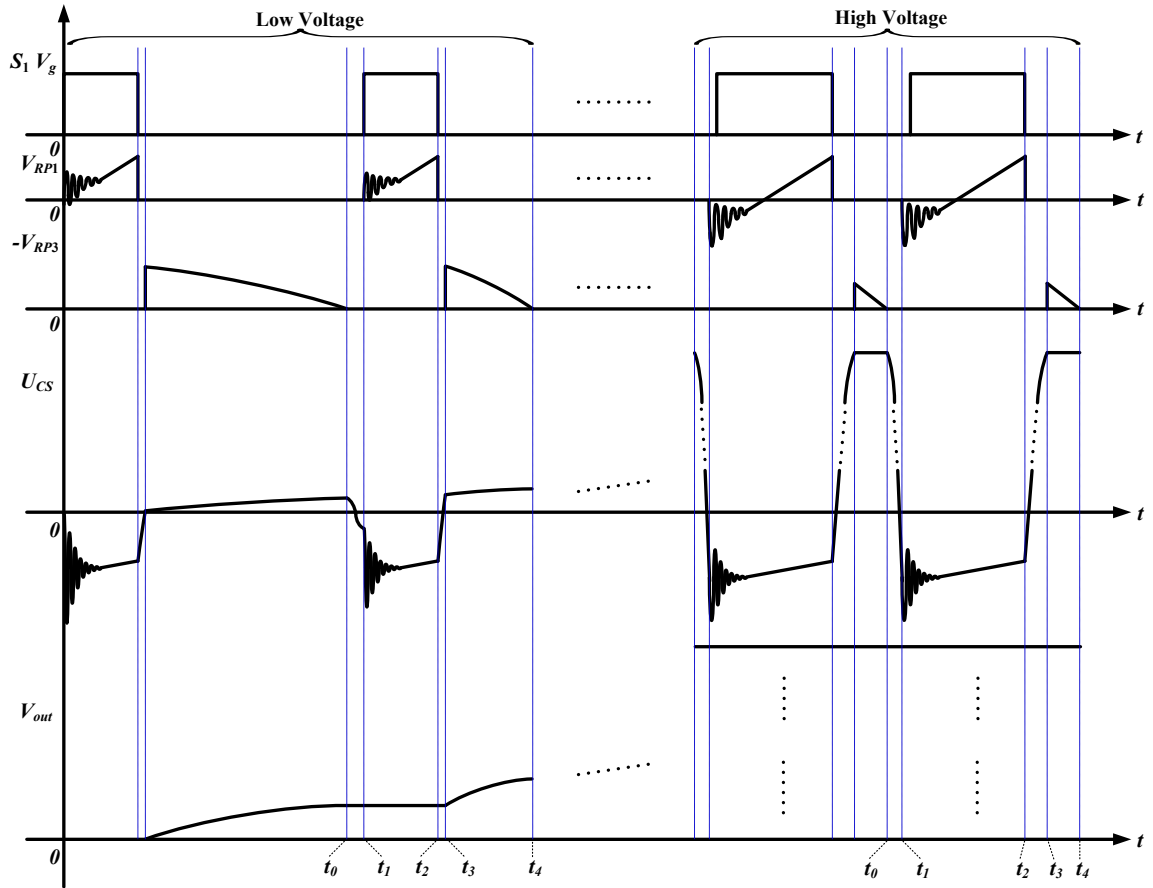


Fig. 4. Key waveforms of the operation stages under different output voltage levels.

Stage 1 [$t_0 < t < t_1$: *Fig. 3 (a)*]: In this stage, the secondary side equivalent stray capacitor C_{seq} resonates with secondary inductance L_s with the initial energy stored in the capacitor. At the beginning of this stage, the voltage over C_{seq} is

$$U_{csc01t0} = V_{oini} + V_{D22} \quad (1)$$

The subscript $c01$ stands for the stage [$t_0 t_1$] in the charging mode and $t0$ represents the time t_0 . This rule for subscript will be applied throughout this paper. Due to the resonance in this stage, the voltage over C_{seq} and the secondary winding current I_{sw} can be derived as

$$U_{cs01}(t) = e^{-\frac{L_s + R_{swc01} \cdot C_{seq} \cdot R_{ceqs}}{2 \cdot L_s \cdot C_{seq} \cdot (R_{swc01} + R_{ceqs})} (t - t_0)} \cdot$$

$$\left\{ U_{csc01t0} \cdot \cos[\omega_{c01} \cdot (t - t_0)] + \frac{R_{ceqs} \cdot C_{seq} \cdot R_{swc01} \cdot U_{csc01t0} - L_s \cdot U_{csc01t0}}{AP_{c01}} \cdot \sin[\omega_{c01} \cdot (t - t_0)] \right\} \quad (2)$$

$$I_{swc01}(t) = -\frac{2 \cdot R_{ceqs} \cdot C_{seq} \cdot U_{csc01t0}}{AP_{c01}} \cdot e^{-\frac{L_s + R_{swc01} \cdot C_{seq} \cdot R_{ceqs}}{2 \cdot L_s \cdot C_{seq} \cdot (R_{swc01} + R_{ceqs})} (t - t_0)} \cdot \sin[\omega_{c01} \cdot (t - t_0)] \quad (3)$$

Then secondary winding voltage can be written as

$$U_{swc01}(t) = L_s \cdot \frac{dI_{swc01}(t)}{dt} \quad (4)$$

In these equations, R_{swc01} is the secondary winding resistance at the resonance frequency in this stage:

$$R_{swc01} = R_{sw} @ \frac{1}{2\pi \cdot \sqrt{L_s \cdot C_{seq}}} \quad (5)$$

In addition,

$$AP_{c01} = \sqrt{4 \cdot L_s \cdot C_{seq} \cdot R_{ceqs}^2 + 2 \cdot L_s \cdot C_{seq} \cdot R_{swc01} \cdot R_{ceqs} - L_s^2 - R_{swc01}^2 \cdot C_{seq}^2 \cdot R_{ceqs}^2} \quad (6)$$

$$\omega_{c01} = \frac{AP_{c01}}{2 \cdot L_s \cdot C_{seq} \cdot (R_{swc01} + R_{ceqs})} \quad (7)$$

are valid.

In low voltage operation, the quasi-resonant characteristic can be achieved if the proper parameters are selected in the control circuits. Then, the end time for this stage can be calculated as

$$t_1 = t_0 + \frac{\pi}{\omega_{c01}} \quad (8)$$

However, this is not the case for other operation voltages. With the increase of the output voltage, the secondary winding voltage $U_{swc01}(t)$ tends to be capable of reaching the threshold voltage, defined as

$$U_{th} = N \cdot (V_{in} + V_{bdS1}) \quad (9)$$

where N is the turns ratio of the transformer and defined as the secondary winding turns N_{sec} divided by primary winding turns N_{pri} . Once the threshold voltage is reached, the body diode of S_1 is forced to conduct. Hence, a minus voltage over RP_1 , which represents the minus primary current, can be observed, as the V_{RP1} waveforms under medium and high voltages in Fig. 4. After an extremely short while (also depending on the parameters in the control circuits), S_1 will be turned on and the minus current will switch to pass through S_1 instead of its body diode due to its low on-resistance. In order to simplify the analysis, it can be assumed that S_1 is turned on at exactly the time the body diode of S_1 is forced to conduct. Therefore, the end time t_1 can be obtained through numerically solving the following equation

$$U_{swc01}(t_1) = U_{th} \quad (10)$$

In fact, it can be summarized that if (10) does not have the real solution, then the converter is working at the low voltage operation; otherwise it is defined to be under non low voltage operations.

Stage 2 [$t_1 < t < t_2$: Fig. 3 (b)]: S_1 is switched on at the beginning of this stage. The dominant behavior in this stage is the primary magnetization. In addition, the resonance due to the primary leakage inductance and C_{seq} in the low voltage operation and the secondary leakage inductance and C_{seq} in other operating voltages cannot be neglected [31]. In fact, the core loss equivalent resistance

is desired to be considered from the primary side in this phase, and from (1) and (3) it is easy to derive the relationship between the primary core loss equivalent resistance R_{ceqp} and its secondary side counterpart R_{ceqs}

$$R_{ceqp} = \frac{R_{ceqs}}{N^2} \quad (11)$$

The magnetizing current during this stage can be written

$$I_{pc12mag}(t) = \frac{V_{in}}{R_{pmeqc12}} + (I_{pc01t1} - \frac{V_{in}}{R_{pmeqc12}}) \cdot e^{-\frac{R_{pmeqc12} \cdot R_{ceqp}}{L_p \cdot (R_{pmeqc12} + R_{ceqp})} (t-t_1)} \quad (12)$$

In this equation, I_{pc01t1} is the initial primary current and can be obtained through

$$I_{pc01t1} = \begin{cases} 0 & \text{if low voltage operation} \\ N \cdot I_{csc01}(t_1) & \text{if non low voltage operation} \end{cases} \quad (13)$$

and $R_{pmeqc12}$ stands for the primary magnetizing equivalent resistance and can be calculated as

$$R_{pmeqc12} = R_{pwc12} + R_{dsonS1} + RP_1 \quad (14)$$

where R_{pwc12} is the primary winding resistance at the switching frequency for the current cycle. So far, the exact switching frequency is unknown. But an estimated value can be achieved by ignoring the influence of the stages (a) and (c) in Fig. 3 and only considering the ideal situations for the stages (b) and (d) in Fig. 3

$$f_{swideal} = \frac{1}{\frac{(I_{pp} - I_{p01t1}) \cdot L_p}{V_{in}} + \tan^{-1} \left(\frac{I_{pp} \cdot \sqrt{L_{sm}}}{N \cdot V_{oini} \cdot \sqrt{CL}} \right) \cdot \sqrt{L_{sm} \cdot CL}} \quad (15)$$

where I_{pp} is the primary peak current set by the inner current loop control. Then,

$$R_{pwc12} \approx R_{pw} @ f_{swideal} \quad (16)$$

The primary winding voltage caused by the magnetization is

$$U_{pwc12mag}(t) = (V_{in} - I_{pc01t1} \cdot R_{pmeqc12}) \cdot e^{-\frac{R_{pmeqc12} \cdot R_{ceqp}}{L_p \cdot (R_{pmeqc12} + R_{ceqp})} (t-t_1)} \quad (17)$$

Concerning the resonance part, if the converter is under low voltage operation, the primary winding resonant voltage and primary resonant current can be written

$$U_{pwc12rl}(t) = -\left(\frac{U_{csc01t1}}{N} + V_{in}\right) \cdot e^{-\frac{R_{preqc12}}{2 \cdot L_{pl}}(t-t_1)} \cdot \left\{ \cos[\omega_{c12rl} \cdot (t - t_1)] + \frac{C_{preq} R_{preqc12}}{AP_{c12rl}} \cdot \sin[\omega_{c12rl} \cdot (t - t_1)] \right\} \quad (18)$$

$$I_{pc12rl}(t) = \frac{2 \cdot C_{preq}}{AP_{c12rl}} \cdot \left(\frac{U_{csc01t1}}{N} + V_{in}\right) \cdot e^{-\frac{R_{preqc12}}{2 \cdot L_{pl}}(t-t_1)} \cdot \sin[\omega_{c12rl} \cdot (t - t_1)] \quad (19)$$

In these equations,

$$U_{csc01t1} = U_{csc01}(t_1) \quad (20)$$

$$C_{preq} = C_{seq} \cdot N^2 \quad (21)$$

$$R_{preqc12} = \frac{R_{swc12rl}}{N^2} + R_{dsonS1} + RP_1 \quad (22)$$

$$R_{swc12rl} = R_{sw} @ \frac{1}{2\pi \cdot \sqrt{L_{pl} \cdot C_{preq}}} \quad (23)$$

$$AP_{c12rl} = \sqrt{4 \cdot L_{pl} \cdot C_{preq} - R_{preqc12}^2 \cdot C_{preq}^2} \quad (24)$$

$$\omega_{c12rl} = \frac{AP_{c12rl}}{2 \cdot L_{pl} \cdot C_{preq}} \quad (25)$$

Likewise, if the converter is working at non low voltage operation, the primary winding resonant voltage and primary resonant current can be derived as

$$U_{pw12rh}(t) = -\frac{2 \cdot L_{sl} \cdot I_{csc01t1}}{N \cdot AP_{c12rh}} \cdot e^{-\frac{R_{swc12rh}}{2 \cdot L_{sl}}(t-t_1)} \cdot \sin[\omega_{c12rh} \cdot (t - t_1)] \quad (26)$$

$$I_{pc12rh}(t) = -I_{pc01t1} \cdot e^{-\frac{R_{swc12rh}}{2 \cdot L_{sl}}(t-t_1)} \cdot \left\{ \cos[\omega_{c12rh} \cdot (t - t_1)] - \frac{C_{seq} R_{swc12rh}}{AP_{c12rh}} \cdot \sin[\omega_{c12rh} \cdot (t - t_1)] \right\} \quad (27)$$

In these equations,

$$I_{csc01t1} = I_{csc01}(t_1) \quad (28)$$

$$R_{swc12rh} = R_{sw} @ \frac{1}{2\pi \cdot \sqrt{L_{sl} \cdot C_{seq}}} \quad (29)$$

$$AP_{c12rh} = \sqrt{4 \cdot L_{sl} \cdot C_{seq} - R_{swc12rh}^2 \cdot C_{seq}^2} \quad (30)$$

$$\omega_{c12rh} = \frac{AP_{c12rh}}{2 \cdot L_{sl} \cdot C_{seq}} \quad (31)$$

Hence, the total primary winding voltage and primary current can be obtained through

$$U_{pwc12}(t) = \begin{cases} U_{pwc12mag}(t) + U_{pwc12rl}(t) & \text{if low voltage operation} \\ U_{pwc12mag}(t) + U_{pwc12rh}(t) & \text{if non low voltage operation} \end{cases} \quad (32)$$

$$I_{pc12}(t) = \begin{cases} I_{pc12mag}(t) + I_{pc12rl}(t) & \text{if low voltage operation} \\ I_{pc12mag}(t) + I_{pc12rh}(t) & \text{if non low voltage operation} \end{cases} \quad (33)$$

Considering no current in the secondary side during this stage, the secondary winding voltage and the voltage over C_{seq} can be calculated through

$$U_{swc12}(t) = -U_{csc12}(t) = N \cdot U_{pwc12}(t) \quad (34)$$

and at the end of this stage

$$I_{pc12}(t_2) = I_{pp} \quad (35)$$

can be written. By numerically solving this equation, the end time t_2 can be acquired.

Stage 3 [$t_2 < t < t_3$: Fig. 3 (c)]: S_1 is switched off at the beginning of this stage. However, the secondary freewheeling diode D_{22} cannot conduct immediately due to the reverse voltage. In this stage, in order to simplify the analysis, the primary side resonance between the leakage inductance and output capacitance of S_1 will not be considered and the dominant behavior tends to be the resonance between secondary magnetizing inductance L_{sm} and stray capacitance C_{seq} . In terms of

energy, C_{seq} is charged in this stage from the energy already stored in the transformer until its voltage can force D_{22} to conduct. The voltage over C_{seq} and the secondary winding current can be derived as

$$U_{csc23}(t) = e^{-\frac{L_{sm}+R_{swc23} \cdot C_{seq} \cdot R_{ceqs}}{2 \cdot L_{sm} \cdot C_{seq} \cdot (R_{swc23}+R_{ceqs})} (t-t_2)} \cdot \{U_{csc12t2} \cdot \cos[\omega_{c23} \cdot (t-t_2)] + \frac{2 \cdot R_{ceqs} \cdot L_{sm} \cdot I_{swc12t2} + R_{ceqs} \cdot C_{seq} \cdot R_{swc23} \cdot U_{csc12t2} - L_{sm} \cdot U_{csc12t2}}{AP_{c23}} \cdot \sin[\omega_{c23} \cdot (t-t_2)]\} \quad (36)$$

$$I_{swc23}(t) = e^{-\frac{L_{sm}+R_{swc23} \cdot C_{seq} \cdot R_{ceqs}}{2 \cdot L_{sm} \cdot C_{seq} \cdot (R_{swc23}+R_{ceqs})} (t-t_2)} \cdot \{I_{swc12t2} \cdot \cos[\omega_{c23} \cdot (t-t_2)] - \frac{2 \cdot R_{ceqs} \cdot C_{seq} \cdot U_{csc12t2} + R_{ceqs} \cdot C_{seq} \cdot R_{swc23} \cdot I_{swc12t2} - L_{sm} \cdot I_{swc12t2}}{AP_{c23}} \cdot \sin[\omega_{c23} \cdot (t-t_2)]\} \quad (37)$$

In these equations,

$$R_{swc23} = R_{sw} @ \frac{1}{2\pi \cdot \sqrt{L_{sm} \cdot C_{seq}}} \quad (38)$$

$$AP_{c23} = \sqrt{4 \cdot L_{sm} \cdot C_{seq} \cdot R_{ceqs}^2 + 2 \cdot L_{sm} \cdot C_{seq} \cdot R_{swc23} \cdot R_{ceqs} - L_{sm}^2 - R_{swc23}^2 \cdot C_{seq}^2 \cdot R_{ceqs}^2} \quad (39)$$

$$\omega_{c23} = \frac{AP_{c23}}{2 \cdot L_{sm} \cdot C_{seq} \cdot (R_{swc23} + R_{ceqs})} \quad (40)$$

And the initial conditions can be obtained through

$$U_{csc12t2} = U_{csc12}(t_2) \quad (41)$$

$$I_{swc12t2} = N \cdot (I_{pc12}(t_2) - \frac{U_{pwc12}(t_2)}{R_{ceqp}}) \quad (42)$$

At the end of the stage,

$$U_{csc23}(t_3) = U_{csc23t3} = V_{oini} + V_{D22} \quad (43)$$

then the end time t_3 can be obtained through numerically solving the equation.

Stage 4 [$t_3 < t < t_4$: Fig. 3 (d)]: D_{22} is forced to conduct at the beginning of this stage and the freewheeling phase starts. The energy still stored in the flyback transformer will be transferred to the capacitive load. Normally, compared to the capacitance of the load, the stray capacitance can be neglected. Hence, in the analysis for this stage, C_{seq} is not considered. In this phase, the output voltage V_{out} and secondary winding current I_{sw} can be expressed as

$$V_{outc34}(t) = e^{-\frac{L_{sm} + R_{fwc34} \cdot C_L \cdot R_{ceqs}}{2 \cdot L_{sm} \cdot C_L (R_{fwc34} + R_{ceqs})} (t - t_3)} \cdot \left\{ U_{csc23t3} \cdot \cos[\omega_{c34} \cdot (t - t_3)] + \frac{2 \cdot R_{ceqs} \cdot L_{sm} \cdot I_{swc23t3} + R_{ceqs} \cdot C_L \cdot R_{fwc34} \cdot U_{csc23t3} - L_{sm} \cdot U_{csc23t3}}{AP_{c34}} \cdot \sin[\omega_{c34} \cdot (t - t_3)] \right\} - V_{D22} \quad (44)$$

$$I_{swc34}(t) = e^{-\frac{L_{sm} + R_{fwc34} \cdot C_L \cdot R_{ceqs}}{2 \cdot L_{sm} \cdot C_L (R_{fwc34} + R_{ceqs})} (t - t_3)} \cdot \left\{ I_{swc23t3} \cdot \cos[\omega_{c34} \cdot (t - t_3)] - \frac{2 \cdot R_{ceqs} \cdot C_L \cdot U_{csc23t3} + R_{ceqs} \cdot C_L \cdot R_{fwc34} \cdot I_{swc23t3} - L_{sm} \cdot I_{swc23t3}}{AP_{c34}} \cdot \sin[\omega_{c34} \cdot (t - t_3)] \right\} \quad (45)$$

And secondary current I_s can be acquired by

$$I_{sc34}(t) = C_L \cdot \frac{dV_{outc34}(t)}{dt} \quad (46)$$

In these equations,

$$I_{swc23t3} = I_{swc23}(t_3) \quad (47)$$

$$R_{fwc34} \approx RP_3 + R_{sw}@f_{swideal} \quad (48)$$

$$AP_{c34} = \sqrt{4 \cdot L_{sm} \cdot C_L \cdot R_{ceqs}^2 + 2 \cdot L_{sm} \cdot C_L \cdot R_{fwc34} \cdot R_{ceqs} - L_{sm}^2 - R_{fwc34}^2 \cdot C_L^2 \cdot R_{ceqs}^2} \quad (49)$$

$$\omega_{c34} = \frac{AP_{c34}}{2 \cdot L_{sm} \cdot C_L \cdot (R_{fwc34} + R_{ceqs})} \quad (50)$$

At the end of this stage, the freewheeling current will reach 0. Hence, the end time of this interval t_4 can be achieved by numerically solving the following equation

$$I_{sc34}(t_4) = 0 \quad (51)$$

So far, the accurate analytical model for one switching cycle during the charging process has been built. However, the unknown parameter – equivalent resistance of core loss R_{ceqs} , prevents the application of the model. As previously stated, an estimated model can be established by setting the R_{ceqs} to infinity in the related equations listed above in order to ignore the influence of the core loss. In this estimated model, the secondary winding voltages and time intervals for each stage can be obtained and utilized to calculate the equivalent resistance of core loss R_{ceqs} .

Referring to (1), the averaged core power loss is determined by $\left| \frac{dB}{dt} \right|$ as well as ΔB . And $\left| \frac{dB}{dt} \right|$ can be obtained through

$$\left| \frac{dB}{dt} \right| = \left| \frac{U_{sw}}{N_{sec} \cdot A} \right| \quad (52)$$

where N_{sec} is the number of turns for the transformer secondary winding and A stands for the cross-sectional area of magnetic core. As previously defined, U_{sw} is winding voltage of transformer secondary side. Neglecting the influence of winding resistances, then through the current waveforms (V_{RP1} and $-V_{RP3}$) and the voltage waveform (U_{cs}) shown in Fig. 4, the rough B - H curves for low and high output voltages with the identification of operation stages can be obtained, depicted in Fig. 5. It can be observed that the peak-to-peak flux density ΔB is, in fact, the flux density change in the stage $[t_1-t_2]$. Hence, it can be calculated with

$$\Delta B = \int_{t_1}^{t_2} \frac{U_{swc12}(t)}{N_{sec} \cdot A} dt \quad (53)$$

as previously illustrated, U_{swc12} is the secondary winding voltage corresponding to stage $[t_1-t_2]$ in the charging mode.

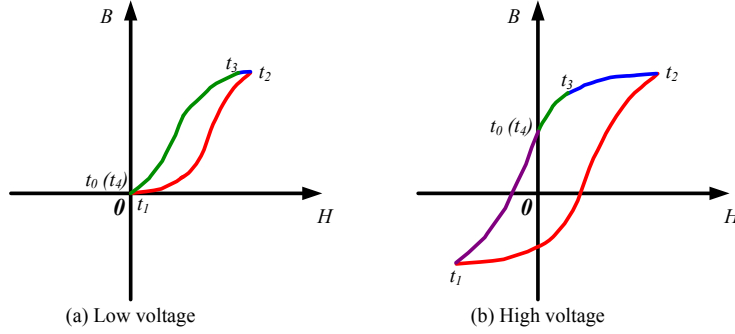


Fig. 5. B - H curves under different output voltage levels.

In addition, the switching period T affects the determination of core loss as well. However, if energy instead of power is chosen to be the standpoint and considering the 4 stages in one charging cycle, the core energy loss per cycle can be expressed as

$$E_v = V_e \cdot \frac{k_i \cdot \Delta B^{\beta-\alpha}}{|N_{sec} \cdot A|^\alpha} \cdot \sum_{m=0,1,2,3} \int_{t_m}^{t_{m+1}} |U_{swcm,m+1}(t)|^\alpha dt \quad (54)$$

where $U_{swcm,m+1}(t)$ ($m=0,1,2,3$) (i.e. $U_{swc01}(t)$, $U_{swc12}(t)$, $U_{swc23}(t)$ and $U_{swc34}(t)$) are the voltages over secondary winding for 4 stages in the charging mode and V_e stands for the volume of the magnetic core. Referring to the general definition of equivalent resistance in terms of power, from secondary side, the core loss equivalent resistance can be derived as

$$R_{ceqs} = \frac{\sum_{m=0,1,2,3} \int_{t_m}^{t_{m+1}} U_{swcm,m+1}^2 dt}{E_v} \quad (55)$$

After applying the achieved equivalent resistance of core loss R_{ceqs} to the established accurate analytical model, the detailed behavior of one switching cycle during the charging process can be acquired.

D. Analytical behavior modeling of discharging mode

As previously stated, the discharging mode is going to be analyzed with DCM working in the fixed operation frequency (denoted as f_{fsd}) and one switching cycle will consist of 5 stages. Similar to the analysis in charging mode, the equivalent circuits for each operation stage are depicted in Fig. 6 (a)-(e) respectively. And the key waveforms for the operation stages, including the waveforms for high as well as low output voltages in the discharging process, are provided in Fig. 7.

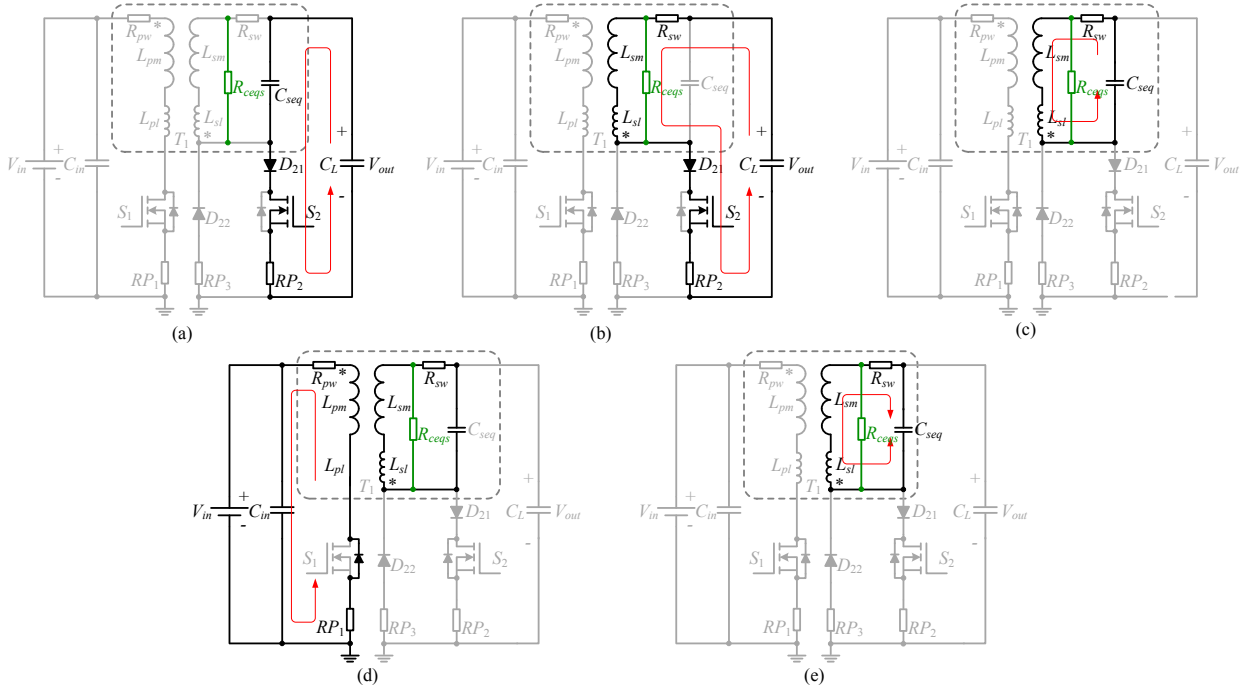


Fig. 6. Equivalent circuit schemes of different operation stages.
(a) $t_0 < t < t_1$ (b) $t_1 < t < t_2$ (c) $t_2 < t < t_3$ (d) $t_3 < t < t_4$ (e) $t_4 < t < t_5 = t_0$.

Similar to the situation in charging mode, the accurate analytical behavior model needs to be established first, which is presented below.

Stage 1 [$t_0 < t < t_1$: Fig. 6 (a)]: At the beginning of this stage, S_2 is switched on and the secondary side equivalent stray capacitor C_{seq} starts to be charged. Normally, the load capacitance is more than thousand times larger than the capacitance of C_{seq} , so in this stage, the capacitive load can be assumed to be a constant voltage source. It should be noted that the equivalent resistance of

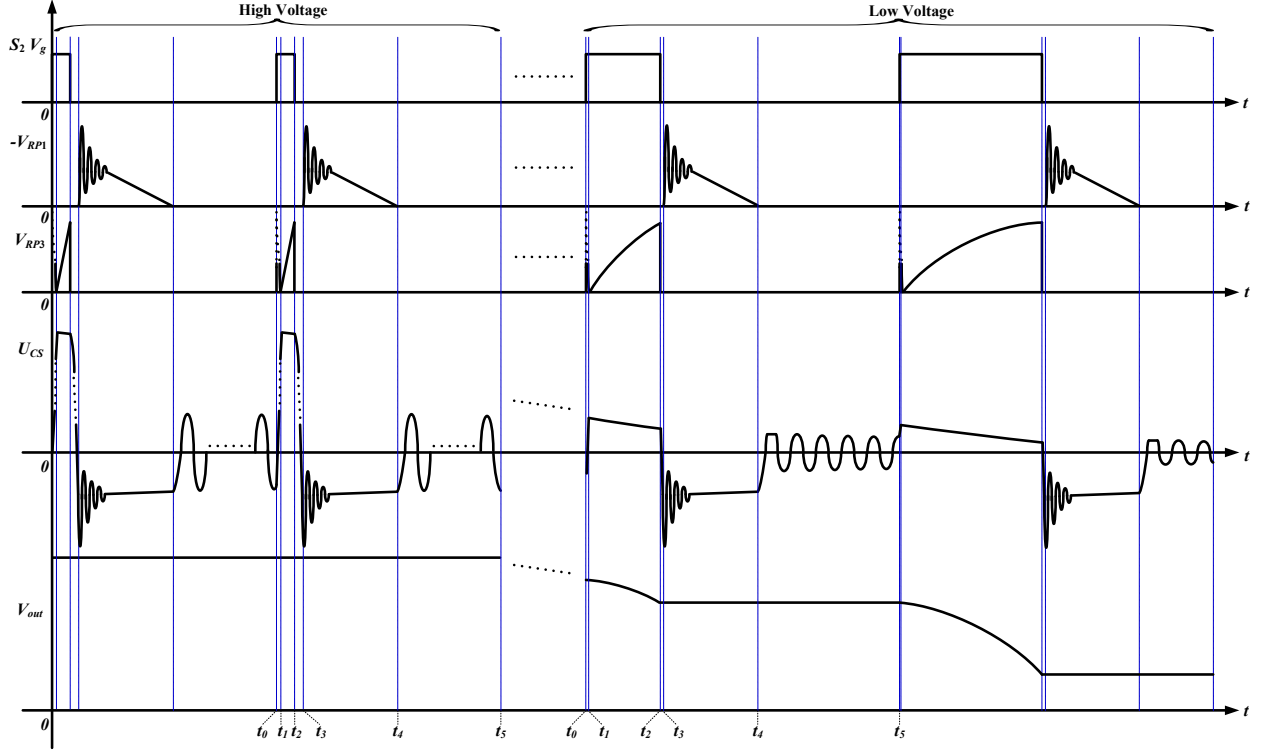


Fig. 7. Key waveforms of the operation stages under different output voltage levels.

core loss R_{ceqs} does not contribute in this period, since only the parasitic capacitor is charged and the core has not been magnetized yet. Thus, in this interval, the voltage over and the current through C_{seq} can be written as

$$U_{csd01}(t) = (V_{oini} - V_{D21}) + (U_{csd01t0} - (V_{oini} - V_{D21})) \cdot e^{-\frac{t-t_0}{T_{ccd01}}} \quad (56)$$

$$I_{csd01}(t) = \frac{V_{oini} - V_{D21} - U_{csd01t0}}{R_{ccd01}} \cdot e^{-\frac{t-t_0}{T_{ccd01}}} \quad (57)$$

In these equations,

$$R_{ccd01} = R_{dsonS2} + RP_2 \quad (58)$$

$$T_{ccd01} = R_{ccd01} \cdot C_{seq} \quad (59)$$

As previously mentioned, the subscript $d0l$ represents the stage $[t_0 \ t_1]$ in the discharging mode and $t0$ stands for the time t_0 . In the entire discharging process, the initial condition of U_{cs} (i.e. $U_{csd01t0}$) for each switching cycle can be obtained through the end condition of last cycle. However, if only one independent switching cycle is investigated, the worst case in terms of charging current (i.e. $I_{csd01}(t)$) needs to be considered, which means the minimum value of $U_{csd01t0}$ needs to be applied in this stage. Considering the stage $[t_4-t_5]$ of last switching cycle and ignoring the damping effect of the winding resistance, in the high voltage operation, U_{cs} can fluctuate between $-N \cdot (V_{in} + V_{bdS1})$ and $N \cdot (V_{in} + V_{bdS1})$. But this is not the case for low voltage operation, due to the voltage clamp caused by the final output voltage of previous cycle (i.e. the initial output voltage for the current cycle) and V_{D22} , the fluctuation range for U_{cs} is $[-(V_{oini} + V_{D22}) \ (V_{oini} + V_{D22})]$. Thus, the initial condition for U_{cs} can be written as

$$U_{csd01t0} = \begin{cases} -(V_{oini} + V_{D22}) & \text{if low voltage operation} \\ -N \cdot (V_{in} + V_{bdS1}) & \text{if non low voltage operation} \end{cases} \quad (60)$$

And the operation status (i.e. low voltage or non voltage operation) can be determined by the comparison of $N \cdot (V_{in} + V_{bdS1})$ and $(V_{oini} + V_{D22})$. If the former one is smaller, then the converter is working under low voltage operation, otherwise, it is defined to be under non low voltage operation.

Theoretically, at the end of this stage, the voltage over C_{seq} needs to reach $V_{oini} - V_{D21}$. However, based on the model built above, this terminal condition will lead to an infinite time for the interval. In order to solve this issue, the final voltage over C_{seq} is assumed to reach only 95% of $(V_{oini} - V_{D21})$. Then, the end time can be written as

$$t_1 = t_0 + \ln\left(\frac{V_{oini} - V_{D21} - U_{csd01t0}}{(1-95\%) \cdot V_{oini} - V_{D21}}\right) \cdot T_{ccd01} \quad (61)$$

In terms of reliability, it is critical to build the model for this stage in order to predict the maximum voltage over the current sensing resistor RP_2 . Thus, the parameters of a RC filter, which

is utilized to suppress this voltage spike before the current signal goes into the control IC, can be determined.

Stage 2 [$t_1 < t < t_2$: Fig. 6 (b)]: The flyback transformer is magnetized during this stage until the magnetizing current reaches the pre-set value of the controller. The energy transfers from the capacitive load to the coupled inductor in this stage. To simplify the model, it is reasonable to neglect the effect of C_{seq} due to its really small value compared to the capacitance of the load. The output voltage, secondary side current I_s as well as the secondary winding current I_{sw} can be expressed as

$$V_{outd12}(t) = (V_{outd12t1} - V_{D21}) \cdot e^{-\frac{L_s + R_{smd12} \cdot C_L \cdot R_{ceqs}}{2 \cdot L_s \cdot C_L \cdot (R_{smd12} + R_{ceqs})}(t-t_1)} \cdot \{\cos[\omega_{d12} \cdot (t - t_1)] + \frac{R_{ceqs} \cdot C_L \cdot R_{smd12} - L_c}{AP_{d12}} \cdot \sin[\omega_{d12} \cdot (t - t_1)]\} + V_{D21} \quad (62)$$

$$I_{sd12}(t) = \frac{(V_{outd12t1} - V_{D21})}{R_{smd12} + R_{ceqs}} \cdot e^{-\frac{L_s + R_{smd12} \cdot C_L \cdot R_{ceqs}}{2 \cdot L_s \cdot C_L \cdot (R_{smd12} + R_{ceqs})}(t-t_1)} \cdot \{-\cos[\omega_{d12} \cdot (t - t_1)] + \frac{L_s - 2 \cdot R_{ceqs}^2 \cdot C_L - R_{ceqs} \cdot C_L \cdot R_{smd12}}{AP_{d12}} \cdot \sin[\omega_{d12} \cdot (t - t_1)]\} \quad (63)$$

$$I_{swd12}(t) = -\frac{2 \cdot R_{ceqs} \cdot C_L \cdot (V_{outd12t1} - V_{D21})}{AP_{d12}} \cdot e^{-\frac{L_s + R_{smd12} \cdot C_L \cdot R_{ceqs}}{2 \cdot L_s \cdot C_L \cdot (R_{smd12} + R_{ceqs})}(t-t_1)} \cdot \sin[\omega_{d12} \cdot (t - t_1)] \quad (64)$$

Then secondary winding voltage can be written as

$$U_{swd12}(t) = L_s \cdot \frac{dI_{swd12}(t)}{dt} \quad (65)$$

In these equations,

$$R_{smd12} = R_{dsonS2} + RP_2 + (R_{sw} @ f_{fsd}) \quad (66)$$

$$AP_{d12} = \sqrt{4 \cdot L_c \cdot C_L \cdot R_{ceqs}^2 + 2 \cdot L_s \cdot C_L \cdot R_{smd12} \cdot R_{ceqs} - L_s^2 - R_{smd12}^2 \cdot C_L^2 \cdot R_{ceqs}^2} \quad (67)$$

$$\omega_{d12} = \frac{AP_{d12}}{2 \cdot L_s \cdot C_L \cdot (R_{smd12} + R_{ceqs})} \quad (68)$$

The capacitive load is assumed to be a constant voltage source in the previous stage and this assumption is beneficial in modeling the behavior in a simple way. However, this is not the real case and the voltage over capacitive load actually slightly decreases since the energy transfers to C_{seq} . Taking this into account, the initial condition of output voltage for stage $[t_1-t_2]$ can be derived through the terminal voltage of C_{seq} , expressed as

$$V_{outd12t1} = U_{csd01}(t_1) + V_{D21} + I_{csd01}(t_1) \cdot R_{ccd01} \quad (69)$$

If the secondary peak current set by the inner current loop control is denoted as I_{sp} , the end time t_2 can be obtained through numerically solving the following equation

$$I_{sd12}(t_2) = -I_{sp} \quad (70)$$

Stage 3 $[t_2 < t < t_3]$: Fig. 6 (c): When S_2 is switched off at the beginning of this stage, the energy stored in the coupled inductor cannot be immediately transferred to the primary side due to the reverse voltage over the body diode of S_1 . In this stage, the behavior is the same as that in the stage $[t_0-t_1]$ of the charging mode. However, the initial conditions are different here, which lead to a more complex model, expressed as

$$U_{csd23}(t) = e^{-\frac{L_s + R_{swd23} \cdot C_{seq} \cdot R_{ceqs}}{2 \cdot L_s \cdot C_{seq} \cdot (R_{swd23} + R_{ceqs})} \cdot (t - t_2)} \cdot \{U_{csd12t2} \cdot \cos[\omega_{d23} \cdot (t - t_2)] + \frac{2 \cdot R_{ceqs} \cdot L_s \cdot I_{swd12t2} + R_{ceqs} \cdot C_{seq} \cdot R_{swd23} \cdot U_{csd12t2} - L_s \cdot U_{csd12t2}}{AP_{d23}} \cdot \sin[\omega_{d23} \cdot (t - t_2)]\} \quad (71)$$

$$I_{swd23}(t) = e^{-\frac{L_s + R_{swd23} \cdot C_{seq} \cdot R_{ceqs}}{2 \cdot L_s \cdot C_{seq} \cdot (R_{swd23} + R_{ceqs})} \cdot (t - t_2)} \cdot \{I_{swd12t2} \cdot \cos[\omega_{d23} \cdot (t - t_2)] - \frac{2 \cdot R_{ceqs} \cdot C_{seq} \cdot U_{csd12t2} + R_{ceqs} \cdot C_{seq} \cdot R_{swd23} \cdot I_{swd12t2} - L_s \cdot I_{swd12t2}}{AP_{d23}} \cdot \sin[\omega_{d23} \cdot (t - t_2)]\} \quad (72)$$

$$U_{swd23}(t) = L_s \cdot \frac{dI_{swd23}(t)}{dt} \quad (73)$$

In these equations,

$$U_{csd12t2} = V_{outd12}(t_2) + I_{sd12}(t_2) \cdot RP_2 - V_{D21} \quad (74)$$

$$I_{swd12t2} = \frac{V_{outd12}(t_2) + I_{sd12}(t_2) \cdot (RP_2 + R_{swd23}) - V_{D21}}{R_{ceqs}} + I_{sd12}(t_2) \quad (75)$$

$$R_{swd23} = R_{sw} @ \frac{1}{2\pi \cdot \sqrt{L_s \cdot C_{seq}}} \quad (76)$$

$$AP_{d23} = \sqrt{4 \cdot L_s \cdot C_{seq} \cdot R_{ceqs}^2 + 2 \cdot L_s \cdot C_{seq} \cdot R_{swd23} \cdot R_{ceqs} - L_s^2 - R_{swd23}^2 \cdot C_{seq}^2 \cdot R_{ceqs}^2} \quad (77)$$

$$\omega_{d23} = \frac{AP_{d23}}{2 \cdot L_s \cdot C_{seq} \cdot (R_{swd23} + R_{ceqs})} \quad (78)$$

When the secondary winding voltage reaches previously defined U_{th} , the body diode of S_I is forced to conduct and this interval ends. Hence, the end time can be obtained by numerically solving the following equation

$$U_{swd23}(t_3) = U_{th} \quad (79)$$

Stage 4 [$t_3 < t < t_4$: *Fig. 6 (d)*]: In this stage, the energy stored in the transformer will be transferred to the primary source. In addition, the energy which cannot be transferred to the primary side (i.e. the energy stored in the secondary side leakage inductance) will result in a resonance between the leakage inductance and the stray capacitance C_{seq} . During this period, it is more reasonable to consider the core loss equivalent resistance in the primary side, which can be calculated through (11). Hence, the primary winding voltage and current can be derived as

$$U_{pwd34}(t) = (U_{pwd23t3} - I_{pd34t3} \cdot R_{dmd34}) \cdot e^{-\frac{R_{dmd34} \cdot R_{ceqp}}{L_{pm}(R_{dmd34} + R_{ceqp})} \cdot (t-t_3)} + \frac{e^{-\frac{R_{swrd34}}{2 \cdot L_{sl}} \cdot (t-t_3)}}{N} \cdot \left\{ -R_{swrd34} \cdot I_{swd23t3} \cdot \cos[\omega_{d34} \cdot (t - t_3)] + \frac{(R_{swrd34}^2 \cdot C_{seq} - 2 \cdot L_{sl}) \cdot I_{swd23t3}}{AP_{d34}} \cdot \sin[\omega_{d34} \cdot (t - t_3)] \right\} \quad (80)$$

$$I_{pd34}(t) = \frac{U_{pwd23t3}}{R_{dmd34}} + e^{-\frac{R_{dmd34} \cdot R_{ceqp}}{L_{pm}(R_{dmd34} + R_{ceqp})} \cdot (t-t_3)} \cdot \left(I_{pd34t3} - \frac{U_{pwd23t3}}{R_{dmd34}} \right) + N \cdot e^{-\frac{R_{swrd34}}{2 \cdot L_{sl}} \cdot (t-t_3)} \cdot \left\{ I_{swd23t3} \cdot \cos[\omega_{d34} \cdot (t - t_3)] - \frac{R_{swrd34} \cdot C_{seq} \cdot I_{swd23t3}}{AP_{d34}} \cdot \sin[\omega_{d34} \cdot (t - t_3)] \right\} \quad (81)$$

The secondary winding voltage can be achieved through

$$U_{swd34}(t) = U_{pwd34}(t) \cdot N \quad (82)$$

In these equations,

$$U_{pwd23t3} = V_{in} + V_{bdS1} \quad (83)$$

$$I_{swd23t3} = I_{swd23}(t_3) \quad (84)$$

$$I_{pd34t3} = I_{swd23t3} \cdot N + \frac{U_{pwd23t3}}{R_{ceqp}} \quad (85)$$

$$R_{dmd34} = RP_1 + (R_{pw} @ f_{fsd}) \quad (86)$$

$$R_{swrd34} = R_{sw} @ \frac{1}{2\pi \cdot \sqrt{L_{sl} \cdot C_{seq}}} \quad (87)$$

$$AP_{d34} = \sqrt{4 \cdot L_{sl} \cdot C_{seq} - R_{swrd34}^2 \cdot C_{seq}^2} \quad (88)$$

$$\omega_{d34} = \frac{AP_{d34}}{2 \cdot L_{sl} \cdot C_{seq}} \quad (89)$$

At the end of this stage, the primary current reaches 0. Thus, the end time t_4 can be obtained by numerically solving the following equation

$$I_{pd34}(t_4) = 0 \quad (90)$$

Stage 5 [$t_4 < t < t_5$: *Fig. 6 (e)*]: This stage is the discontinuous conduction phase in the discharging mode and equivalent resistance of core loss does not affect in this stage. Due to the energy stored in the secondary side stray capacitor C_{seq} at the beginning of this stage, the secondary side inductance L_s starts to resonate with C_{seq} . The voltage over C_{seq} can be written as

$$U_{csd45}(t) = U_{csd34t4} \cdot e^{-\frac{R_{swd45}}{2 \cdot L_s} \cdot (t-t_4)} \cdot \left\{ \cos[\omega_{d45} \cdot (t - t_4)] + \frac{R_{swd45} \cdot C_{seq}}{AP_{d45}} \cdot \sin[\omega_{d45} \cdot (t - t_4)] \right\} \quad (91)$$

In the equation,

$$U_{csd34t4} = -N \cdot U_{pwd34}(t_4) \quad (92)$$

$$R_{swd45} = R_{sw} @ \frac{1}{2\pi \cdot \sqrt{L_s \cdot C_{seq}}} \quad (93)$$

$$AP_{d45} = \sqrt{4 \cdot L_s \cdot C_{seq} - R_{swd45}^2 \cdot C_{seq}^2} \quad (94)$$

$$\omega_{d45} = \frac{AP_{d45}}{2 \cdot L_s \cdot C_{seq}} \quad (95)$$

Similar to the approach in analytical modeling for charging mode, based on the above derived accurate model, the estimated model can be achieved through setting the equivalent resistance of core loss R_{ceqs} to infinity to ignore the influence of core loss. The secondary winding voltages and time intervals for each stage of the estimated model can be acquired and utilized to calculate the equivalent resistance of core loss.

According to the current and voltage waveforms in Fig. 7, the rough B - H curves for high and low output voltages in the discharging process can be acquired, shown in Fig. 8.

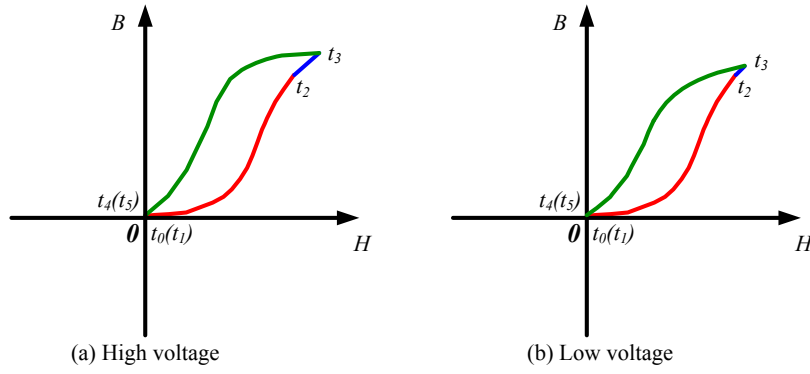


Fig. 8. B - H curves under different output voltage levels.

Thus, in discharging mode, the peak-to-peak flux density ΔB , core energy loss per cycle and the secondary side core loss equivalent resistance can be derived as

$$\Delta B = \int_{t_3}^{t_4} \frac{U_{swd34}(t)}{N_{sec} \cdot A} dt \quad (96)$$

$$E_v = V_e \cdot \frac{k_i \cdot \Delta B^{\beta-\alpha}}{|N_{sec} \cdot A|^{\alpha}} \cdot \sum_{m=1,2,3} \int_{t_m}^{t_{m+1}} |U_{swdm,m+1}(t)|^{\alpha} dt \quad (97)$$

$$R_{ceqs} = \frac{\sum_{m=1,2,3} \int_{t_m}^{t_{m+1}} U_{swdm,m+1}^2 dt}{E_v} \quad (98)$$

where $U_{swdm,m+1}(t)$ ($m=1,2,3$) (i.e. $U_{swd12}(t)$, $U_{swd23}(t)$ and $U_{swd34}(t)$) are the voltages over secondary winding in stages $[t_1-t_2]$, $[t_2-t_3]$ and $[t_3-t_4]$ in the discharging mode. It should be noted that stage $[t_0-t_1]$ corresponds to the inrush charge of stray capacitance C_{seq} and does not contribute to the core loss. In stage $[t_4-t_5]$, if neglecting the effect of winding resistance, the symmetric sinusoidal AC voltage of U_{cs} leads to the average zero change of the flux density (i.e. $\Delta B_{[t_4-t_5]} = 0$). Hence, this stage does not need to be considered in the core loss equivalent resistance calculation as well.

The achieved equivalent resistance of core loss R_{ceqs} then can be applied to the established accurate analytical model to obtain the detailed behavior of one switching cycle during the discharging process.

IV. EXPERIMENTAL VERIFICATION OF ANALYTICAL MODELING

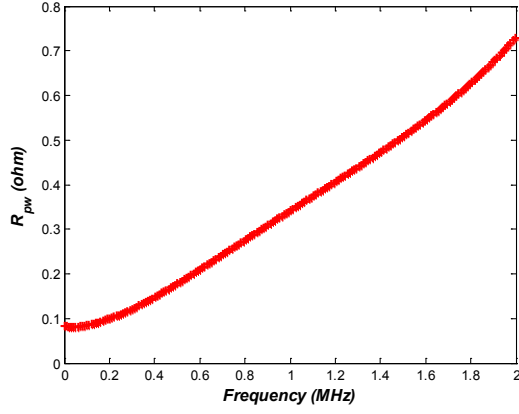
A prototype of bidirectional HV flyback converter was performed in order to validate the theoretical analytical switching cycle modeling of the converter in terms of charging as well as discharge mode. The specifications, design parameters and the employed components are summarized in Table I. The implemented and measured data for the HV flyback transformer as well as the parameters for the core loss calculation are listed in Table II. The primary and secondary winding ac resistance of the transformer are frequency dependent and the measured resistance versus frequency characteristic up to 2 MHz are shown in Fig. 9 (a) and (b), respectively. The photograph of the prototype is shown in Fig. 10.

TABLE I. HV FLYBACK CONVERTER SPECIFICATIONS AND COMPONENTS LIST

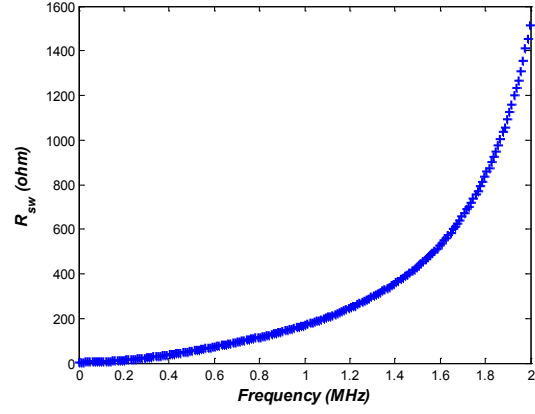
| Parameters | Values |
|---------------------|-------------------|
| V_{in} | 3 V |
| Maximum V_{out} | 2 kV |
| C_L | 220 nF |
| I_{pp} | 4 A |
| I_{sp} | 100 mA |
| S_1 | BSC320N20NS3 G |
| S_2 | IXTV03N400S |
| D_{21} & D_{22} | VMI6525 |
| RP_1 | 20 m Ω 1 % |
| RP_2 & RP_3 | 1 Ω 1 % |

TABLE II. HV FLYBACK TRANSFORMER IMPEMENTED AND MEASURED PARAMETERS

| Parameters | Values |
|------------|----------------------|
| N_{pri} | 6 |
| N_{sec} | 232 |
| N | 38.7 |
| L_{pm} | 12.7 μ H |
| L_{pl} | 300 nH |
| L_{sm} | 18.4 mH |
| L_{sl} | 450 μ H |
| C_{seq} | 30 pF |
| k | 12.97 |
| α | 1.26 |
| β | 2.02 |
| A | 32.8 mm ² |
| V_e | 1564 mm ³ |



(a) Primary winding ac resistance



(b) Secondary winding ac resistance

Fig. 9. HV flyback transformer winding ac resistance.

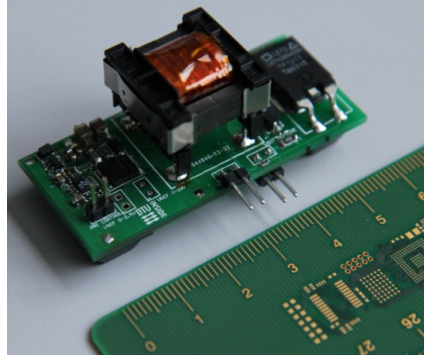


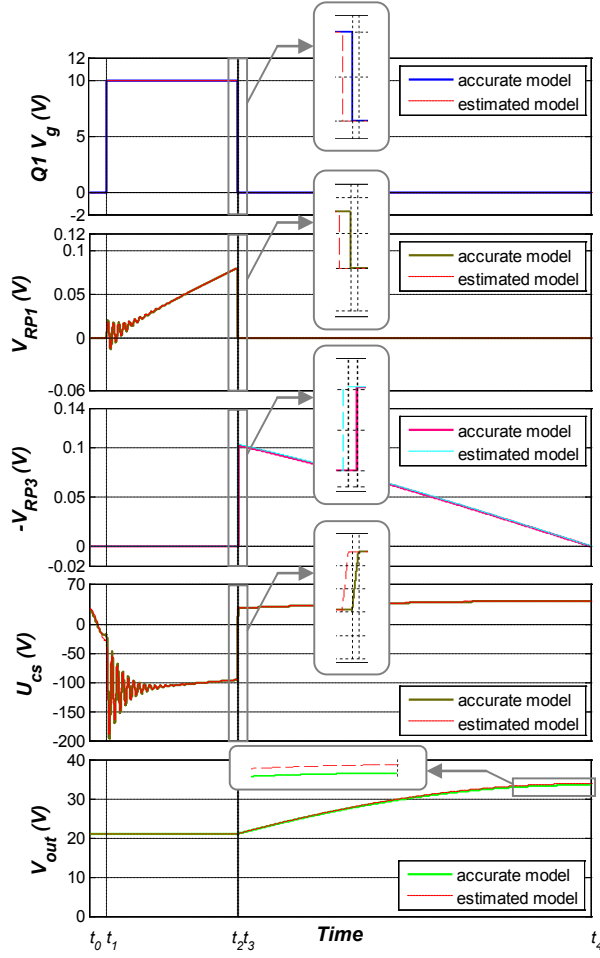
Fig. 10. Picture of the implemented bidirectional HV flyback converter.

A. Validation of analytical model of charging mode

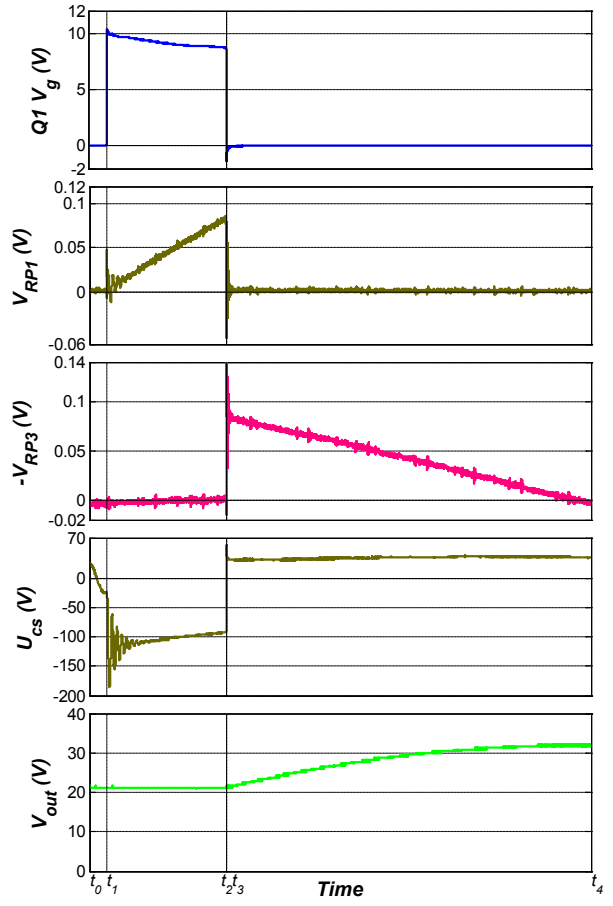
In charging mode, the analytical model is verified for both low voltage and high voltage operations. Fig. 11 (a) and (b) show the estimated and accurate analytical model based calculation waveforms, which are represented with dash line and solid line respectively, and experiments based measurement waveforms for low voltage operation. The end time for each stage of accurate model based waveforms in Fig. 11 (a) and measured waveforms in Fig. 11 (b) as well as the time intervals are summarized in Table III. Likewise, the estimated and accurate calculated waveforms and measured waveforms in high operation voltage are shown in Fig. 12 (a) and (b), respectively. The corresponding end time and time intervals for high voltage operation are listed in Table IV.

The waveforms in Fig. 11 (a) indicate that, in the entire switching cycle, the estimated model based waveforms are almost equal to that based on the accurate model. Only slight differences can be observed in the gray zoom boxes. During the high voltage operation (Fig. 12 (a)), the waveforms based on estimated model are obviously different from that based on accurate model due to the severe influence of core loss. Even in the cases with slight differences, it is still crucial to build the accurate model for each cycle. Since the whole charging process consists of large number of switching cycles, the slight error in one cycle tends to be accumulated accordingly, which eventually leads to the large error in the efficiency evaluation. The measured efficiency as well as the analytical model based efficiency is shown in Fig. 13, which can effectively prove the necessity to build the accurate model.

Even with the accurate model, due to the difficulty in accurately calculating the core loss, the parasitic capacitance introduced by the measuring probes in the high voltage side as well as the measuring errors caused by the oscilloscope, the calculated secondary side current and the output voltage cannot be exactly the same as the measured ones. In addition, the measurement error in the winding resistances will greatly affect the damping phenomenon in stage $[t_1 < t < t_2]$. In the high voltage operation, since the on time for the body diode of S_l in stage $[t_1 < t < t_2]$ is neglected in the calculation for simplifying the model, thus, the time t_l in the measurement is much larger than the time in the calculation. Furthermore, as previously stated, the resonance phenomenon when S_l is switched off is ignored in the analytical model as well. Moreover, due to the intrinsic property of the control IC, the driving voltage for S_l has a slight decline. However, in general, the mismatch between the calculated time data and the measured ones are under acceptable range and the analytical model can well represent the behavior in one switching cycle for charging mode.



(a) Analytical model based calculated waveforms

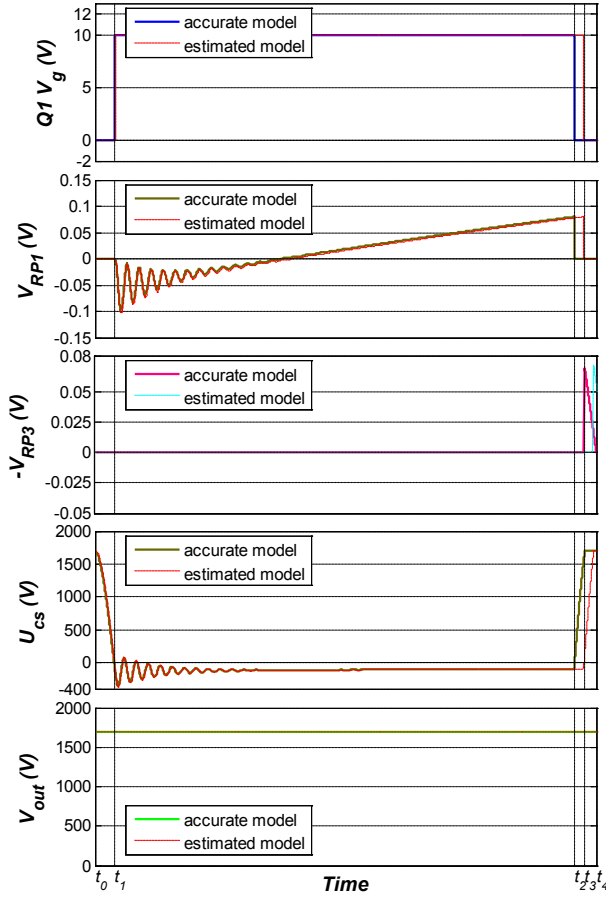


(b) Experimental waveforms

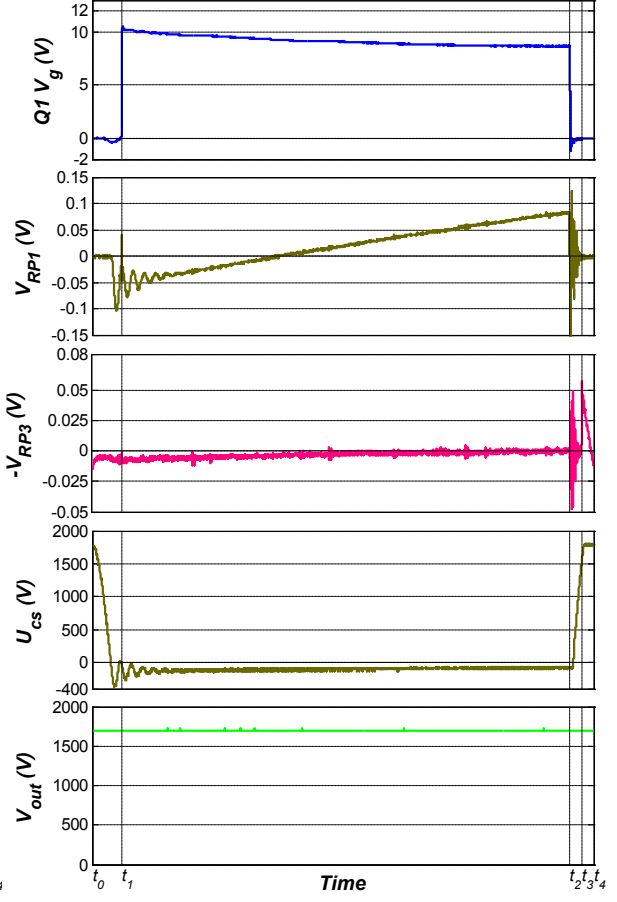
Fig. 11. Low voltage operational key waveforms of charging mode.

TABLE III. TIME DATA AND TIME INTERVALS IN FIG. 12

| Time or Time Intervals | Accurate Model based Calculated Time / μs | Measured Time / μs |
|------------------------|---------------------------------------------------------|-------------------------------|
| t_0 | 0 | 0 |
| t_1 | 2.58 | 2.52 |
| t_2 | 21.70 | 19.75 |
| t_3 | 21.75 | 19.79 |
| t_4 | 73.23 | 72.43 |
| $t_{01} = t_1 - t_0$ | 2.58 | 2.52 |
| $t_{12} = t_2 - t_1$ | 19.12 | 17.23 |
| $t_{23} = t_3 - t_2$ | 0.05 | 0.04 |
| $t_{34} = t_4 - t_3$ | 51.48 | 52.64 |



(a) Analytical model based calculated waveforms



(b) Experimental waveforms

Fig. 12. High voltage operational key waveforms of charging mode.

TABLE IV. TIME DATA AND TIME INTERVALS IN FIG. 13

| Time or Time Intervals | Accurate Model based Calculated Time / μs | Measured Time / μs |
|------------------------|---------------------------------------------------|-------------------------|
| t_0 | 0 | 0 |
| t_1 | 1.32 | 1.84 |
| t_2 | 31.37 | 29.76 |
| t_3 | 32.07 | 30.50 |
| t_4 | 32.82 | 31.24 |
| $t_{01} = t_1 - t_0$ | 1.32 | 1.84 |
| $t_{12} = t_2 - t_1$ | 30.05 | 27.92 |
| $t_{23} = t_3 - t_2$ | 0.7 | 0.74 |
| $t_{34} = t_4 - t_3$ | 0.75 | 0.74 |

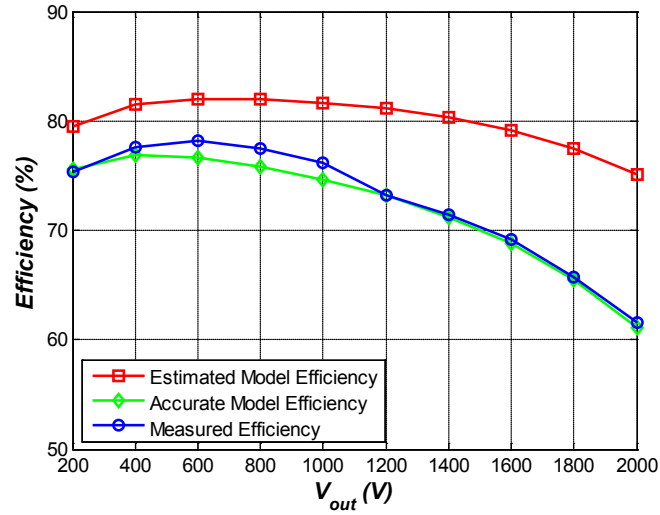


Fig. 13. Comparison of analytical model based charging efficiency and experimentally measured efficiency.

B. Validation of analytical model of discharging mode

The analytical model is also validated for both high and low operational voltages in the discharging mode. Fig. 14 (a) and (b) illustrate both the estimated model and accurate model based calculation waveforms and experiment waveforms for high voltage operation. The end time for each stage based on accurate model in Fig. 14 and the time intervals are summarized in Table V. Similarly, the calculated and measured waveforms in low operational voltage are shown in Fig. 15 (a) and (b), respectively. The corresponding end time and time intervals for low voltage operation are listed in Table VI. Similar to the situation in charging mode, the estimated model based waveforms in Fig. 14 (a) and Fig. 16 (a) look nearly the same to that based on accurate model and only slight difference can be observed in the gray zoom boxes. Since the discharging process also consists of a lot of successive switching cycles, the slight error in one switching cycle tends to result in the large error between the estimated model based discharging efficiency and its measured counterpart, which are illustrated in Fig. 16. It should be noted that, in the discharging process, the secondary side peak current varies with the output voltage due to the intrinsic issue of the control IC. Even with the accurate model based calculated waveforms, end time and time intervals cannot

exactly match with the measured counterparts. The reasons for the mismatch have already been stated in the charging mode verification. In general, the difference can be accepted and the analytical model can also well represent the behavior in one switching cycle for discharging mode.

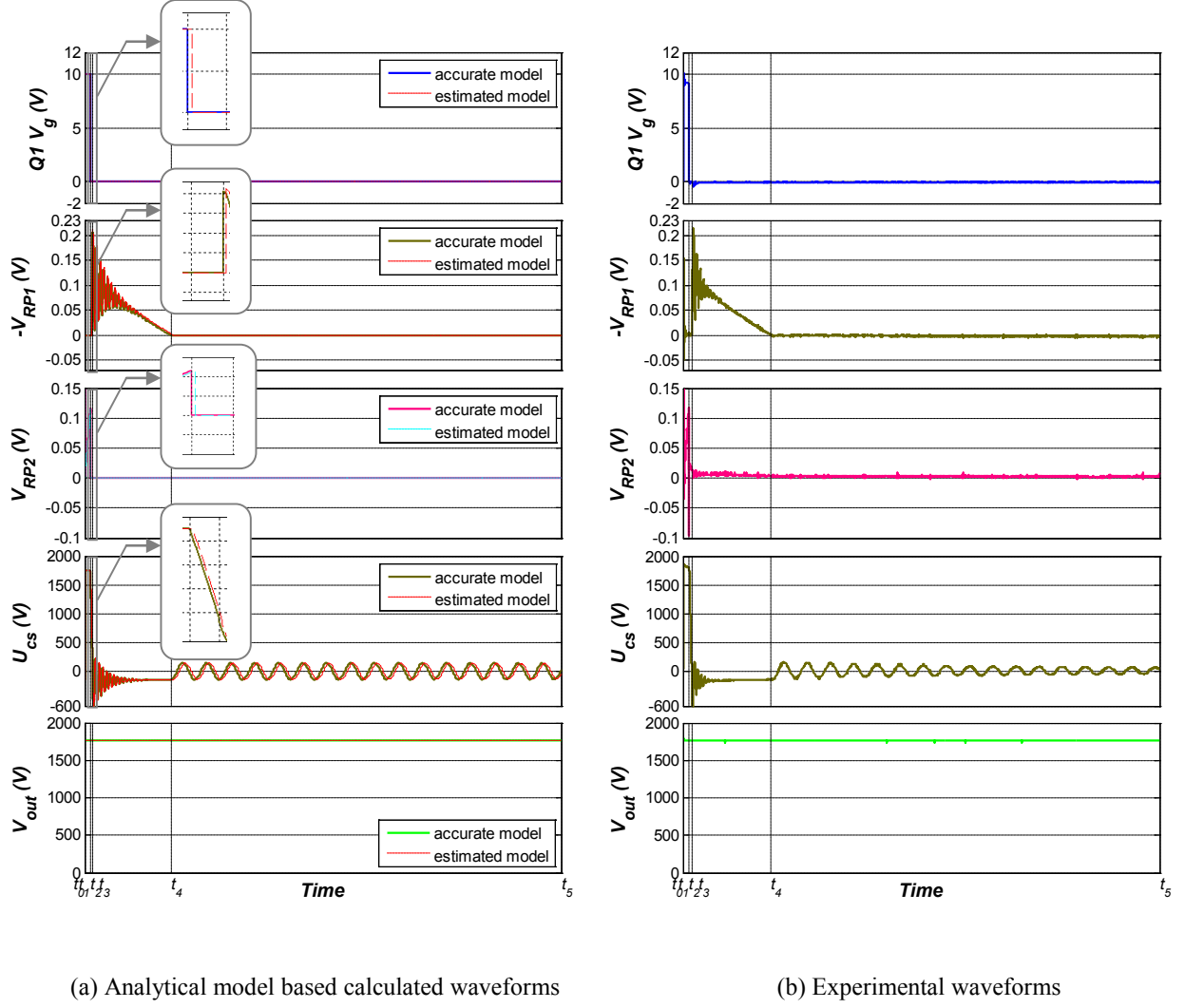
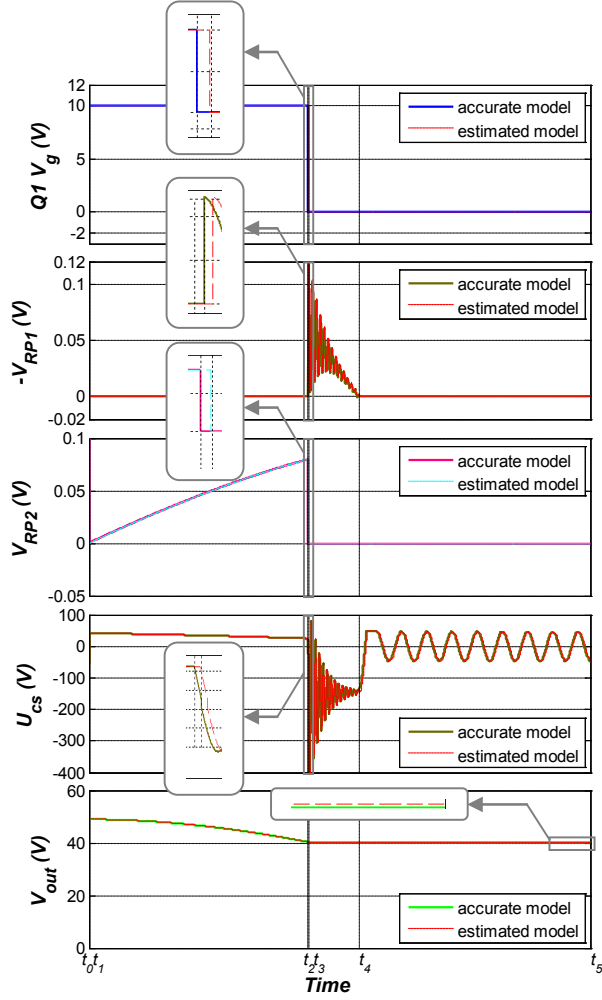


Fig. 14. High voltage operational key waveforms of discharging mode.

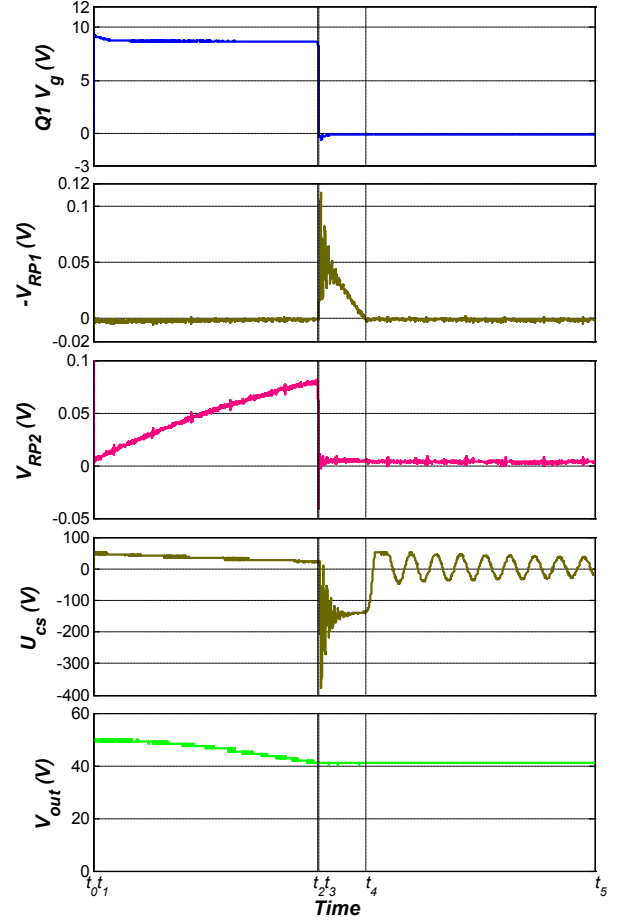
TABLE V. TIME DATA AND TIME INTERVALS IN FIG. 14

| Time or Time Intervals | Calculated Time / μs | Measured Time / μs |
|------------------------|---------------------------------|-------------------------------|
| t_0 | 0 | 0 |
| t_1 | 0.011 | 0.0120 |
| t_2 | 1.21 | 1.25 |
| t_3 | 1.71 | 1.85 |
| t_4 | 18.11 | 18.39 |

| | | |
|----------------------|-------|-------|
| t_5 | 100 | 99.39 |
| $t_{01} = t_1 - t_0$ | 0.011 | 0.012 |
| $t_{12} = t_2 - t_1$ | 1.199 | 1.238 |
| $t_{23} = t_3 - t_2$ | 0.5 | 0.6 |
| $t_{34} = t_4 - t_3$ | 16.4 | 16.54 |
| $t_{45} = t_5 - t_4$ | 81.89 | 81 |



(a) Analytical model based calculated waveforms



(b) Experimental waveforms

Fig. 15. Low voltage operational key waveforms of discharging mode.

TABLE VI. TIME DATA AND TIME INTERVALS IN FIG. 15

| Time or Time Intervals | Calculated Time / μs | Measured Time / μs |
|------------------------|---------------------------------|-------------------------------|
| t_0 | 0 | 0 |
| t_1 | 0.013 | 0.016 |
| t_2 | 43.73 | 44.6 |
| t_3 | 43.8 | 44.66 |

| | | |
|----------------------|--------|--------|
| t_4 | 53.8 | 53.93 |
| t_5 | 100 | 99.43 |
| $t_{01} = t_1 - t_0$ | 0.013 | 0.016 |
| $t_{12} = t_2 - t_1$ | 43.717 | 44.584 |
| $t_{23} = t_3 - t_2$ | 0.07 | 0.06 |
| $t_{34} = t_4 - t_3$ | 10 | 9.27 |
| $t_{45} = t_5 - t_4$ | 46.2 | 45.5 |

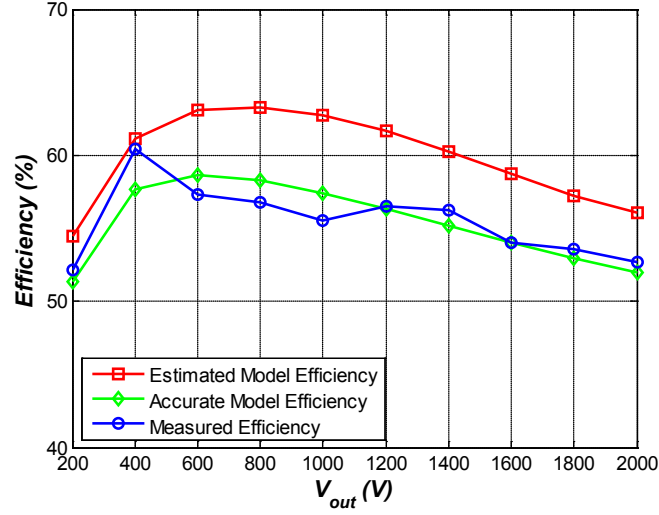


Fig. 16. Comparison of analytical model based discharging efficiency and experimentally measured efficiency.

V. CONCLUSION

In this paper, the HV bidirectional flyback converter utilized to drive the capacitive load is introduced in terms of configuration, basic operational principle and control schemes. For both charging and discharging mode, an accurate behaviour model is established first. By ignoring the effect of core loss in accurate model, an estimated model is achieved in order to derive the core loss equivalent resistance. Afterwards, an accurate behaviour can be predicted with the accurate model as well as the derived core loss equivalent resistance. The analytical model is verified by the comparison between the model based calculation waveforms and the experiment based measurement waveforms. Even though the accuracy of the parasitic parameters and the core loss calculation affect the agreement between the calculated and measured results, the difference is still

under accepted level and the analytical model can well represent the behavior in one switching cycle for both charging and discharging mode. The estimated and accurate model based calculated efficiency as well as the measured data are compared to verify the necessity of employing the accurate model as well as to validate the importance of considering the core loss. The switching cycle based analytical model has been dedicated to the components stress analysis, energy efficiency investigation and optimizing the design for HV bidirectional converter driving capacitive load.

REFERENCES

- [1] T. G. Wilson, "The evolution of power electronics," *Power Electronics, IEEE Transactions on*, vol. 15, no. 3, pp. 439-446, 2000.
- [2] J. Popović-Gerber, J. A. Oliver, N. Cordero, T. Harder, J. A. Cobos, M. Hayes, S. C. O'Mathuna and E. Prem, "Power Electronics Enabling Efficient Energy Usage: Energy Savings Potential and Technological Challenges," *Power Electronics, IEEE Transactions on*, vol. 27, no. 5, pp. 2338-2353, 2012.
- [3] Y. Song and B. Wang, "Survey on Reliability of Power Electronic Systems," *Power Electronics, IEEE Transactions on*, vol. 28, no. 1, pp. 591-604, 2013.
- [4] D. Campolo, M. Sitti and R. S. Fearing, "Efficient charge recovery method for driving piezoelectric actuators with quasi-square waves," *IEEE Transactions on Ultrasonics, Ferroelectrics and Frequency Control*, vol. 50, no. 3, pp. 237-244, 2003.
- [5] R. Sarban, B. Lassen and M. Willatzen, "Dynamic Electromechanical Modeling of Dielectric Elastomer Actuators With Metallic Electrodes," *IEEE/ASME Transactions on Mechatronics*, vol. 17, no. 5, pp. 960-967, 2012.
- [6] C. Wallenhauer, B. Gottlieb, R. Zeichfusl and A. Kappel, "Efficiency-Improved High-Voltage Analog Power Amplifier for Driving Piezoelectric Actuators," *IEEE Transactions on Circuits and Systems I Regular Papers*, vol. 57, no. 1, pp. 291-298, 2010.
- [7] A. Abramovitz, C.-S. Liao and K. Smedley, "State-Plane Analysis of Regenerative Snubber for Flyback Converters," *IEEE Transactions on Power Electronics*, vol. 28, no. 11, pp. 5323-5332, 2013.

- [8] J.-H. Jung and S. Ahmed, "Flyback converter with novel active clamp control and secondary side post regulator for low standby power consumption under high-efficiency operation," *IET Power Electronics*, vol. 4, no. 9, pp. 1058 - 1067, 2011.
- [9] Z. Zhang, X.-F. He and Y.-F. Liu, "An Optimal Control Method for Photovoltaic Grid-Tied-Interleaved Flyback Microinverters to Achieve High Efficiency in Wide Load Range," *Power Electronics, IEEE Transactions on*, vol. 28, no. 11, pp. 5074-5087, 2013.
- [10] S. Zengin, F. Deveci and M. Boztepe, "Decoupling Capacitor Selection in DCM Flyback PV Microinverters Considering Harmonic Distortion," *Power Electronics, IEEE Transactions on*, vol. 28, no. 2, pp. 816-825, 2013.
- [11] Y.-H. Kim, Y.-H. Ji, J.-G. Kim, Y.-C. Jung and C.-Y. Won, "A New Control Strategy for Improving Weighted Efficiency in Photovoltaic AC Module-Type Interleaved Flyback Inverters," *Power Electronics, IEEE Transactions on*, vol. 28, no. 6, pp. 2688-2699, 2013.
- [12] H. Hu, S. Harb, N. H. Kutkut, Z. J. Shen and I. Batarseh, "A Single-Stage Microinverter Without Using Electrolytic Capacitors," *Power Electronics, IEEE Transactions on*, vol. 28, no. 6, pp. 2677-2687, 2013.
- [13] Y. Li and R. Oruganti, "A Low Cost Flyback CCM Inverter for AC Module Application," *Power Electronics, IEEE Transactions on*, vol. 27, no. 3, pp. 1295-1303, 2012.
- [14] A. C. Nanakos, E. C. Tatakis and N. P. Papanikolaou, "A Weighted-Efficiency-Oriented Design Methodology of Flyback Inverter for AC Photovoltaic Modules," *Power Electronics, IEEE Transactions on*, vol. 27, no. 7, pp. 3221-3233, 2012.
- [15] H. Hu, S. Harb, X. Fang, D. Zhang, Q. Zhang, Z. J. Shen and I. Batarseh, "A Three-port Flyback for PV Microinverter Applications With Power Pulsation Decoupling Capability," *Power Electronics, IEEE Transactions on*, vol. 27, no. 9, pp. 3953-3964, 2012.
- [16] S. Moon, G.-B. Koo and G.-W. Moon, "A New Control Method of Interleaved Single-Stage Flyback AC x2013;DC Converter for Outdoor LED Lighting Systems," *Power Electronics, IEEE Transactions on*, vol. 28, no. 8, pp. 4051-4062, 2013.
- [17] X. Wu, Z. Wang and J. Zhang, "Design Considerations for Dual-Output Quasi-Resonant Flyback LED Driver With Current-Sharing Transformer," *Power Electronics, IEEE Transactions on*, vol. 28, no. 10, pp. 4820-4830, 2013.

- [18] H.-H. Chou, Y.-S. Hwang and J.-J. Chen, "An Adaptive Output Current Estimation Circuit for a Primary-Side Controlled LED Driver," *Power Electronics, IEEE Transactions on*, vol. 28, no. 10, pp. 4811-4819, 2013.
- [19] Y. Hu, L. Huber and M. M. Jovanović, "Single-Stage, Universal-Input AC/DC LED Driver With Current-Controlled Variable PFC Boost Inductor," *Power Electronics, IEEE Transactions on*, vol. 27, no. 3, pp. 1579-1588, 2012.
- [20] J. Zhang, H. Zeng and T. Jiang, "A Primary-Side Control Scheme for High-Power-Factor LED Driver With TRIAC Dimming Capability," *Power Electronics, IEEE Transactions on*, vol. 27, no. 11, pp. 4619-4629, 2012.
- [21] C.-S. Moo, Y.-J. Chen and W.-C. Yang, "An Efficient Driver for Dimmable LED Lighting," *Power Electronics, IEEE Transactions on*, vol. 27, no. 11, pp. 4613-4618, 2012.
- [22] X. Xie, J. Wang, C. Zhao, Q. Lu and S. Liu, "A Novel Output Current Estimation and Regulation Circuit for Primary Side Controlled High Power Factor Single-Stage Flyback LED Driver," *Power Electronics, IEEE Transactions on*, vol. 27, no. 11, pp. 4602-4612, 2012.
- [23] P. Davari, F. Zare, A. Ghosh and H. Akiyama, "High-Voltage Modular Power Supply Using Parallel and Series Configurations of Flyback Converter for Pulsed Power Applications," *IEEE Transactions on Plasma Science*, vol. 40, no. 10, pp. 2578 -2587, 2012.
- [24] A. Emrani, E. Adib and H. Farzanehfard, "Single-Switch Soft-Switched Isolated DC-DC Converter," *Power Electronics, IEEE Transactions on*, vol. 27, no. 4, pp. 1952-1957, 2012.
- [25] A. Rahimi, F. F. Rahimi and I. Hassanzadeh, "Analysis of high-voltage flyback converter in color TVs, and its regulation," in *The Fifth International Conference on Power Electronics and Drive Systems 2003 (PEDS 2003)*, Singapore, 2003.
- [26] G. Chen, Y.-S. Lee, S. Y. R. Hui, D. Xu and Y. Wang, "Actively clamped bidirectional flyback converter," *IEEE Transactions on Industrial Electronics*, vol. 47, no. 4, pp. 770 -779, 2000.
- [27] J. Park, Y.-S. Roh, Y.-J. Moon and C. Yoo, "A CCM/DCM Dual-Mode Synchronous Rectification Controller for a High-Efficiency Flyback Converter," *Power Electronics, IEEE Transactions on*, vol. 29, no. 2, pp. 768-774, 2014.
- [28] M. Karpelson, G.-Y. Wei and R. J. Wood, "Milligram-scale high-voltage power electronics for piezoelectric microrobots," in *Robotics and Automation, 2009. ICRA '09. IEEE International Conference on*, 2009.

- [29] L. Huang, P. Thummala, Z. Zhang and M. A. E. Andersen, "Battery powered high output voltage bidirectional flyback converter for cylindrical DEAP actuator," in *2012 IEEE International Power Modulator and High Voltage Conference (IPMHVC 2012)*, San Diego, USA, 2012.
- [30] L. Eitzen, C. Graf and J. Maas, "Cascaded bidirectional flyback converter driving DEAP transducers," in *37th Annual Conference on IEEE Industrial Electronics Society (IECON 2011)*, Melbourne, Australia, 2011.
- [31] S.-K. Chung, "Transient characteristics of high-voltage flyback transformer operating in discontinuous conduction mode," *IEE Proceedings - Electric Power Applications*, vol. 151, no. 5, pp. 628 - 634, 2004.
- [32] L. Dalessandro, F. da Silveira Cavalcante and J. W. Kolar, "Self-Capacitance of High-Voltage Transformers," *Power Electronics, IEEE Transactions on*, vol. 22, no. 5, pp. 2081 -2092, 2007.
- [33] J. Biela and J. W. Kolar, "Using Transformer Parasitics for Resonant Converters x2014;A Review of the Calculation of the Stray Capacitance of Transformers," *Industry Applications, IEEE Transactions on*, vol. 44, no. 1, pp. 223 -233, 2008.
- [34] L. Dalessandro, F. da Silveira Cavalcante and J. W. Kolar, "Self-Capacitance of High-Voltage Transformers," *IEEE Transactions on Power Electronics*, vol. 22, no. 5, pp. 2081 -2092, 2007.
- [35] T. Andersen, M. S. Roedgaard, O. C. Thomsen and M. A. E. Andersen, "Low voltage driven dielectric electro active polymer actuator with integrated piezoelectric transformer based driver," in *Electroactive Polymer Actuators and Devices (EAPAD) 2011*, San Diego, USA, 2011.
- [36] J. Muhlethaler, J. Biela, J. W. Kolar and A. Ecklebe, "Improved Core-Loss Calculation for Magnetic Components Employed in Power Electronic Systems," *Power Electronics, IEEE Transactions on*, vol. 27, no. 2, pp. 964-973, 2012.
- [37] J. Muhlethaler, J. Biela, J. W. Kolar and A. Ecklebe, "Core Losses Under the DC Bias Condition Based on Steinmetz Parameters," *Power Electronics, IEEE Transactions on*, vol. 27, no. 2, pp. 953-963, 2012.

APPENDIX I

Efficiency of Capacitively Loaded Converters

38th Annual Conference of the IEEE Industrial Electronics Society (IECON 2012)

Efficiency of Capacitively Loaded Converters

T. Andersen, L. Huang, M. A. E. Andersen, O. C. Thomsen

Technical University of Denmark, DTU Elektro, Ørsted's Plads, building 349, DK-2800 Kgs. Lyngby, Denmark
ta@elektro.dtu.dk, huang@elektro.dtu.dk, ma@elektro.dtu.dk, oct@elektro.dtu.dk

Abstract- This paper explores the characteristic of capacitance versus voltage for dielectric electro active polymer (DEAP) actuator, 2kV polypropylene film capacitor as well as 3kV X7R multi layer ceramic capacitor (MLCC) at the beginning. An energy efficiency for capacitively loaded converters is introduced as a definition of efficiency. The calculated and measured efficiency curves for charging DEAP actuator, polypropylene film capacitor and X7R MLCC are provided and compared. The attention has to be paid for the voltage dependent capacitive load, like X7R MLCC, when evaluating the charging efficiency of converter. Based on the capacitance-voltage curve, the correct capacitance should be chosen when calculating the stored energy; otherwise misleading optimistic efficiency can always be obtained. Actually, when DEAP actuator is not available at the early developing stage, the voltage independent polypropylene film capacitor can be the equivalent capacitive load. Because of the voltage dependent characteristic, X7R MLCC cannot be used to replace the DEAP actuator. However, this type of capacitor can be used to substitute the capacitive actuator with voltage dependent property at the development phase.

Index Terms- DEAP actuator, capacitance voltage characteristic, voltage independent capacitor, voltage dependent capacitor, energy efficiency

I. INTRODUCTION

DEAP actuators is made of a thin polymer coated with an electrode on each side [1]. The actuator utilizes the Coulomb's force that appears between the electrodes when a voltage is applied to obtain a strain. Applications of DEAP are not limited to low magnetic environments as electromagnetic actuators.

Efficiency of power converters relate input and output power together. High efficiency is attractive in any ordinary application and is therefore a key parameter when comparing power converters. Converters for driving dielectric electro active polymer (DEAP) actuators are no exception.

A cylindrical DEAP push actuator is seen at Fig. 1. A typical curve for the strain as a function of voltage is illustrated in Fig. 2. The elongation of DEAP actuator is a function of the voltage squared. A high voltage is needed to fully elongate a DEAP actuator. For most application this requires a converter with high step-up voltage ratio from input to output.

In the development phase of the converter the actual DEAP actuator might not be available when testing the converter efficiency. A load equivalent to the DEAP is needed.

This work explores the DEAP impedance and trends the non-trivial issue of efficiency measurement of DEAP and capacitively loaded converters.

II. IMPEDANCE OF THE DEAP ACTUATOR

To equate the DEAP actuator the impedance must be known within the range of interest. The geometry of DEAP material itself is closely related to a plate capacitor. Using the DEAP material as an actuator the frequency range of interest is generally limited to low frequency operation.

At low frequency the impedance of the DEAP material is purely capacitive. This is verified by the impedance measurement of an actuator in Fig. 3 where the phase angle is -90 degrees. Furthermore the capacitance is independent of frequency.

The DEAP material changes shape according to the applied voltage [2, 3]. The DEAP materials surface area (S) increases and the thickness (d) decrease with voltage. This has influence on the capacitance; from the definition equation of a parallel plate capacitor, shown in (1), the increase in surface area and the decrease of thickness both give rise to an increase of the capacitance.



Fig. 1. Cylindrical DEAP push Actuator

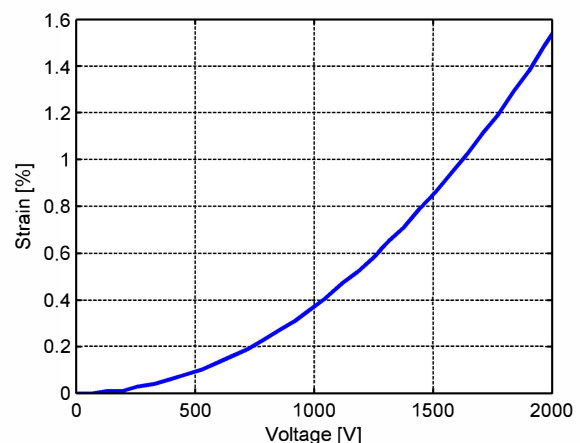


Fig. 2. Typical strain curve of an unloaded cylindrical DEAP actuator as a function of applied voltage

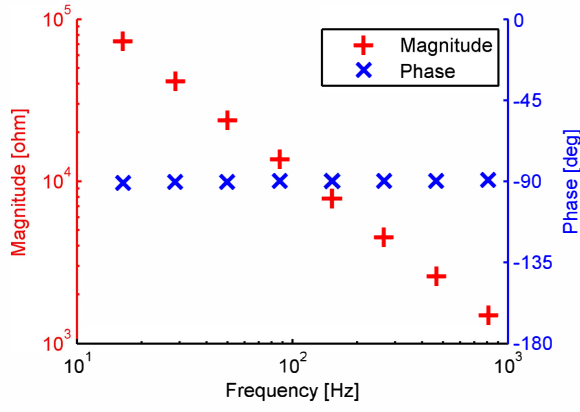


Fig. 3. Impedance measurement of the cylindrical DEAP push actuator at low frequency

$$C = \epsilon \frac{S(V)}{d(V)} \quad (1)$$

A. Capacitance vs. Voltage Test Method

An increase in capacitance with voltage is expected. From [2] the capacitance increase is related to the strain of the DEAP actuator material by a power function, shown in (2), where C_0 is the none stretched capacitance and x is the strain of the material.

$$C = C_0 \cdot (1 + x)^{1.83} \quad (2)$$

The typical strain of the DEAP actuator is seen in Fig. 2. A strain of 1.6% gives an estimated capacitive increase of 3%. To verify the capacitance change of the DEAP actuator, the actual capacitance is measured as a function of voltage.

To measure capacitance-voltage curve of a given capacitor, the circuit in Fig. 4 is used. The capacitance is calculated from the relation between voltage and current, shown in (3). The voltage across the capacitor (V_C) is measured with an oscilloscope. The current into the capacitor is calculated from (4).

$$i_C = C \cdot \frac{dV_C}{dt} \quad (3)$$

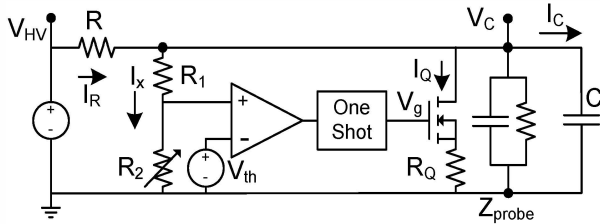


Fig. 4. Circuit for measuring the capacitance of capacitors (C) as function of voltage

$$i_C = \frac{(V_{HV} - V_C)}{R} - \frac{V_C}{R_1 + R_2} - \frac{V_C}{R_{probe}} \quad (4)$$

The capacitor under test is discharged through the MOSFET when the voltage across the capacitor (V_C) reach a predefined threshold set by the voltage divider R_1 and R_2 . When the comparator is triggered a one-shot circuit insures that the MOSFET stays on long enough for the capacitor to fully discharge before the next charge cycle starts.

B. Capacitance vs. Voltage Measurements

The capacitance of the DEAP actuator together with a four parallel 33nF 2kV polypropylene film capacitor and nine parallel 15nF 3kV X7R multi layer ceramic capacitor (MLCC) is measured and plotted in Fig. 5. The capacitance of the DEAP actuator and the film capacitor is similar up to around 1.5kV. Above 1.5kV the capacitance of the DEAP actuator increases, 4% at 2kV. The measured increase is one percent point higher than the estimated value of 3 %.

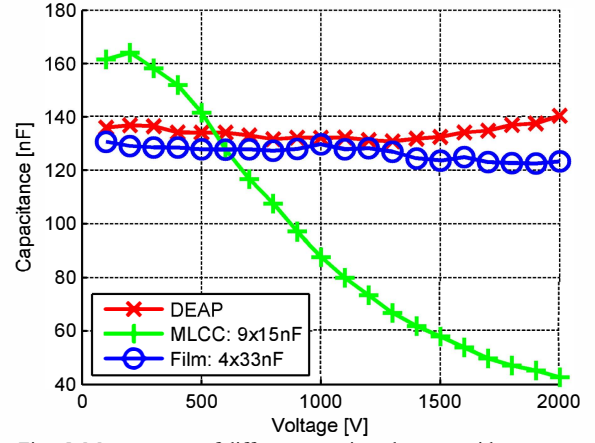


Fig. 5. Measurement of different capacitor elements with same stated capacitance as function of voltage: DEAP actuator, X7R MLCC and polypropylene film.

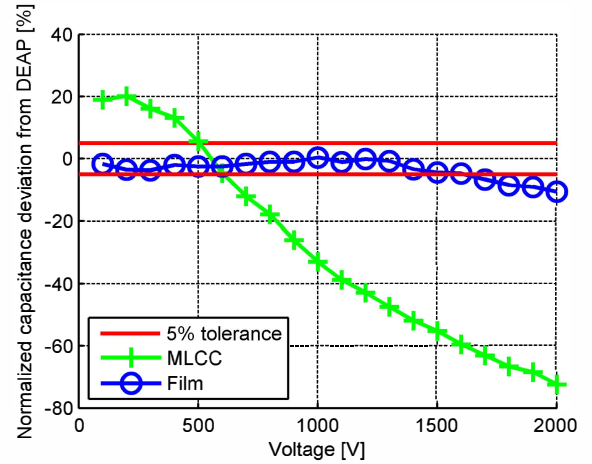


Fig. 6. Deviation of normalized capacitance compared to DEAP material as function of applied voltage for X7R MLCC and polypropylene film

difference might be related to both the actual strain of the actuator being more than 1.6% and that the estimation capacitance increase is based on the DEAP material being stretched rather than compressed as in an actuator application. The capacitance value of the X7R MLCC [4, 5] is highly dependent on the DC voltage with an increase of more than 20% at 200V and a decrease of 70% at 2kV compared to the stated value of datasheet from vendor.

Fig. 6 compares the normalized capacitance deviation from the DEAP actuator. Up to 1.5kV the polypropylene film equivalents the DEAP actuator within 5%, at 2kV the deviation is 10%. From this point of view, polypropylene film capacitor can be the substitute for DEAP actuator. However, the huge capacitance deviation of X7R MLCC prevents it becoming the alternative.

III. EFFICIENCY OF CAPACITIVELY LOADED CONVERTER

For stimulating DEAP actuator a 3V input, 2kV output boundary mode working flyback converter was designed and realized. However, how to evaluate the efficiency of the converter with only capacitive load is an interesting issue deserving of attention.

The method to measure the efficiency of a DC-DC converter for resistive load is well known. Equation (5) shows how the efficiency can be obtained through measuring the voltages and currents at input and output terminals.

$$\eta = \frac{\langle P_{out} \rangle}{\langle P_{in} \rangle} = \frac{V_{out} \cdot I_{out}}{V_{in} \cdot I_{in}} \quad (5)$$

However, for the capacitive load like the DEAP actuator, the situation is different, because there is no power consumption in the load. If (5) is still adopted, then the efficiency is always zero. Therefore, the concept of energy efficiency is proposed, defining the efficiency as energy stored in the capacitive load divided by the total energy feed into the converter.

For measuring the efficiency, the test setup shown in Fig. 7 is utilized. If the capacitance of the load is known, the energy stored in the capacitive load can be achieved through measuring the output voltage. For a certain output voltage, the input voltage and input current as well as the charge time will determine the total input energy. The efficiency can then be expressed by (6).

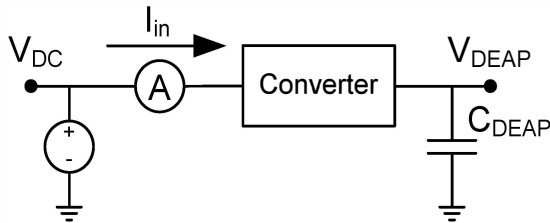


Fig. 7. Setup for measuring efficiency of capacitive loaded converters

$$\eta = \frac{E_{out}}{E_{in}} = \frac{\frac{1}{2} C_{load} \cdot V_{out}^2}{\int_0^{t_{charge}} V_{DC} \cdot I_{in} \cdot dt} \quad (6)$$

The load capacitance (C_{load}) is a critical factor in calculating the efficiency. When capacitor load is being charged, if C_{load} has considerable change, much attention should be paid to get the correct efficiency.

A. Voltage Independent Capacitive Load

Based on the former discussion, for DEAP actuator and polypropylene film capacitor, despite the capacitances have slight variation above 1.5kV, they can generally be considered as voltage independent capacitors.

From Equation (6), if load capacitance (C_{load}) always keeps the same value, it is easy to analyze energy loss of the converter and measure the efficiency.

After building the prototype converter, some parameters, such as flyback transformer inductances, leakage inductance, transformer winding AC resistances and winding self capacitance can be measured for the efficiency calculation.

For capacitively loaded converter, the analysis of energy efficiency in a charging process is quite different from that of power efficiency for an ordinary DC-DC converter in steady state. Since charging is a continuous procedure including many switching cycles, the energy loss for each cycle needs to be recorded separately in order to calculate the energy efficiency for a certain output voltage. In addition, with the increasing of output voltage, the freewheeling time of secondary diode decreases. Thus, in boundary mode, the operating frequency of each cycle differs from one another, which results in variable core loss as well as winding loss, and finally influences the number of switching cycles to reach a predetermined output voltage. Furthermore, the switching times will also affect the energy loss for primary components, i.e. primary MOSFET, winding and current sensing resistor. Therefore, to analyze energy efficiency for a capacitive load converter is a relative complicated subject. In spite of this, the efficiency calculation still needs to be carried out for the purpose of inspecting the correctness of measured energy efficiencies. So a loss analysis and efficiency calculation program has been realized with MATLAB [6, 7]. The basic calculating thought is illustrated in Fig. 8.

When the converter is used to drive DEAP actuator, through the program, the calculated energy efficiency curve with respect to output voltage can easily be achieved, as shown in Fig. 9. While the measured efficiency curve, also shown in Fig. 9, can be obtained through experimental waveforms. For example, Fig. 10 gives the waveforms for charging the DEAP actuator from 0V to 2kV, from which the energy feed into the converter and final stored energy in DEAP can be acquired. With (6), the energy efficiency can be figured out.

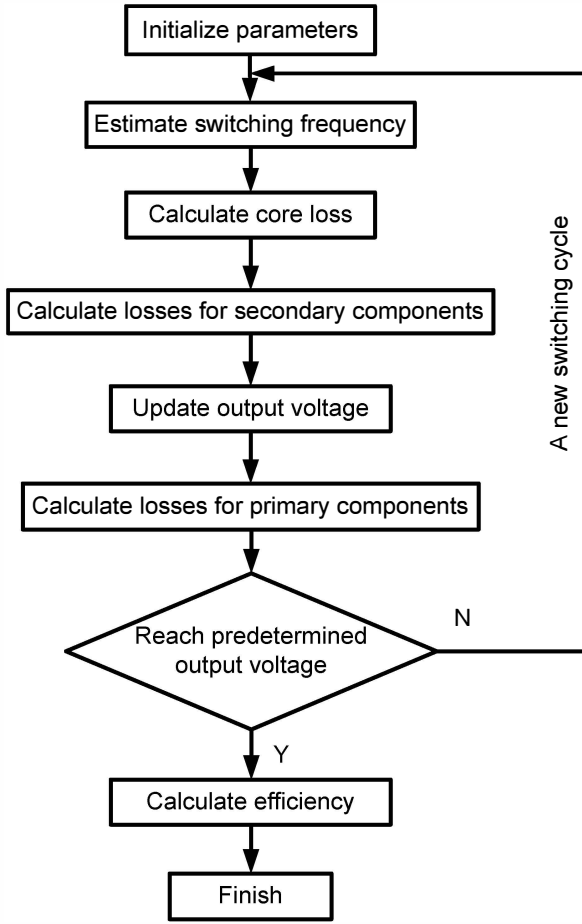


Fig. 8. Flow chart of loss and efficiency computational process

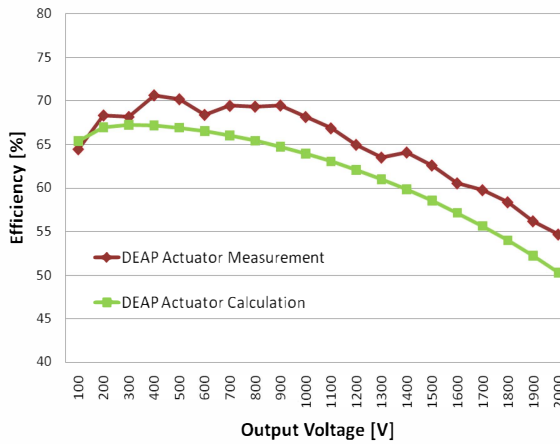


Fig. 9. Calculated and measured efficiency comparison for DEAP actuator

From Fig. 9, it can be seen that the calculated efficiencies cannot completely match with the measured ones. This is mainly because some approximations are supposed in the calculation program. For example, the core loss is evaluated through vendor's loss curve, which is usually measured under sinusoidal excitation. However, in flyback converter, the current waveforms are far from sinusoidal. Furthermore, the successive computational procedure will also accumulate the

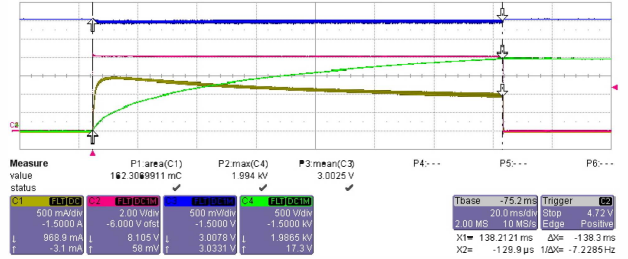


Fig. 10. Waveforms of charging process (CH1-input current, CH2-charge signal, CH3-input voltage, CH4-output voltage)

error step by step, since the outcomes of former cycle will be the inputs for the latter step. In general, it is very difficult to build up an accurate calculation model and consider all practical factors in computation. Therefore, the deviation of the efficiencies occurs. However, Fig. 9 also shows that the two efficiency curves have the same trend and the deviation slightly increases with the switching cycles, which can, to some extent, prove the measured data is credible.

The same calculation and measurement have been implemented for 132nF polypropylene film capacitor. Like DEAP actuator, similar results are presented through Fig.11.

If the measured energy efficiencies for DEAP actuator and film capacitor are placed in the same figure, it can be found out that the efficiencies are nearly the same, shown in Fig.12. So, it is proved again, when the DEAP actuator is not available, that the polypropylene film capacitor with approximate capacitance can be an alternative in evaluating the efficiency for the converter.

B. Voltage Dependent Capacitive Load

Unlike DEAP and polypropylene film capacitor, the capacitance of X7R MLCC is greatly affected by the biased voltage. Therefore, in order to calculate the correct efficiency of the converter, the estimation of the output energy must be calculated with the capacitance of the load at the specific output voltage of interest. The correct equation for calculating the efficiency must include the load capacitors voltage

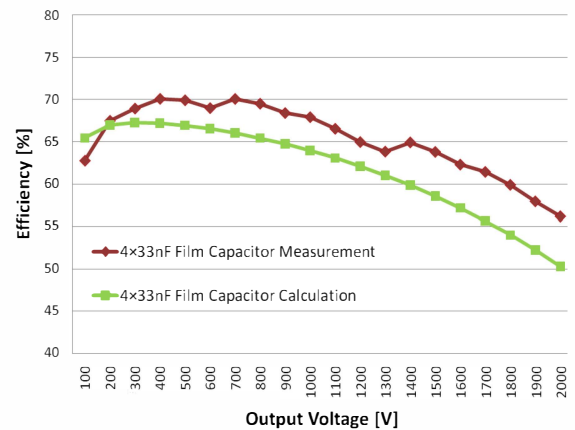


Fig. 11. Calculated and measured efficiency comparison for 132nF polypropylene film capacitor

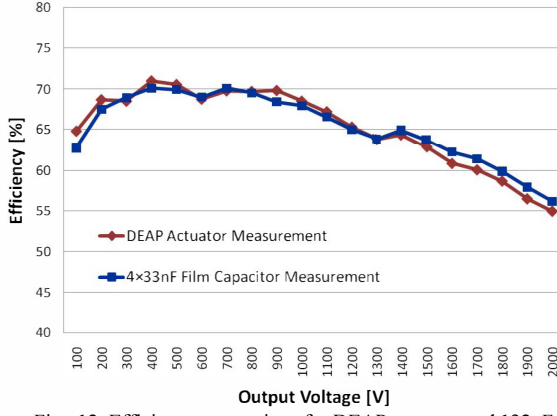


Fig. 12. Efficiency comparison for DEAP actuator and 132nF polypropylene film capacitor

dependency as measured in Fig. 5. Equation (7) thereby gives the correct efficiency.

$$\eta = \frac{E_{out}}{E_{in}} = \frac{\frac{1}{2} C_{load} (V_{out}) \cdot V_{out}^2}{\int_0^{T_{charge}} V_{DC} \cdot I_m \cdot dt} \quad (7)$$

If the capacitance was assumed as constant value with biased voltage for X7R MLCC, a misleading efficiency can easily be obtained in calculation and measurement. The calculated and measured efficiency curves shown in Fig.13 can indicate that the constant capacitance assumption is totally wrong. Since, for any converter, the efficiency cannot exceed 100%.

When the biased voltage increases, considering the great decrease of capacitance, the efficiency analysis will become more complex. For each cycle, not only the output voltage needs recalculation, but the capacitance also should be updated based on the current output voltage.

After correcting the capacitance through data in Fig.5, the efficiency curves for both calculation and measurement are presented in Fig.14. While the differences between calculated efficiencies and measured ones has already been addressed in last section.

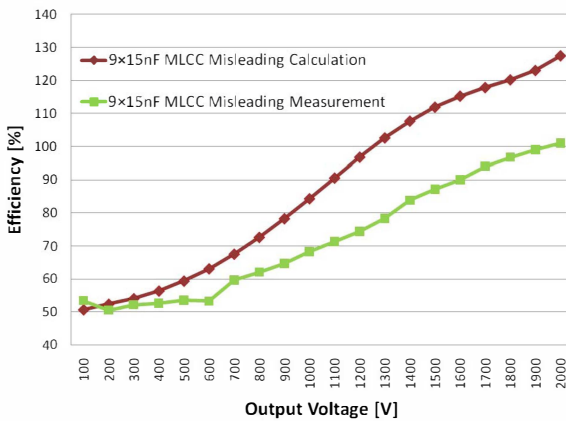


Fig. 13. Misleading calculated and measured efficiency comparison for 135nF X7R MLCC

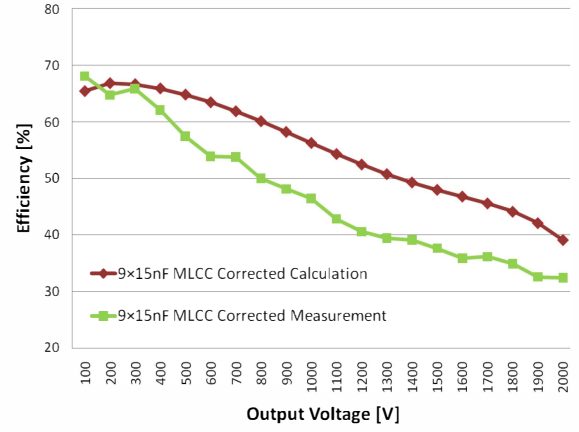


Fig. 14. Calculated and measured efficiency comparison for 135nF X7R MLCC with capacitance correction

For X7R MLCC, despite the correct efficiency can be acquired through Fig. 5 and (7); however, when measured efficiency curve of DEAP actuator is plotted with that of MLCC with capacitance correction in Fig. 15, it is easy to come to the conclusion again that MLCC cannot be the substitute for DEAP actuator. In spite of this, the discussion of this section can provide the reference for voltage dependent capacitive actuator in order to obtain the correct efficiency.

IV. CONCLUSION

Efficiency of a purely capacitive load converter cannot be calculated by power ratio. Instead the energy ratio is used.

However, care has to be taken when estimating the stored energy for voltage dependent capacitive loads. Before measuring the efficiency, the characteristic of load capacitance versus voltage should be obtained first. Otherwise, if the stated value in the datasheet is always employed, the over 100% efficiency may occur. Thus the capacitance-voltage curve must be used in order to obtain the correct energy efficiency.

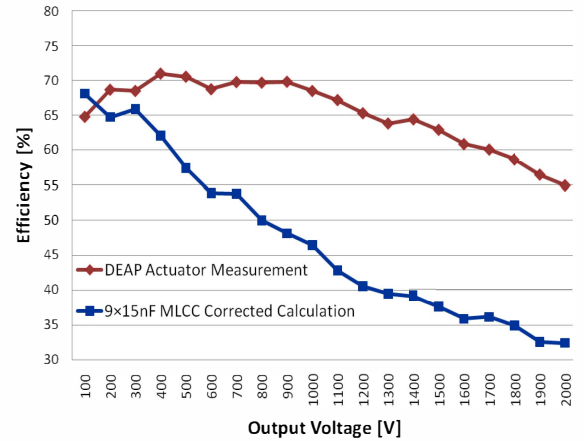


Fig. 15. Efficiency comparison for DEAP actuator and 135nF X7R MLCC with capacitance correction

DEAP material is capacitive and the capacitance can approximately be considered as voltage independent. And the polypropylene film capacitor can also be regarded as voltage independent capacitor. Therefore, DEAP actuator can be equated with polypropylene film capacitors to evaluate the efficiency of converter when actuator is not available.

REFERENCES

- [1] M. Y. Benslimane, H. E. Kiil, and M. J. Tryson, "Dielectric electro-active polymer push actuators: performance and challenges," *Polymer International*, vol. 59, pp. 415-421, 2010.
- [2] M. Benslimane, H. E. Kiil, and M. J. Tryson, "Electromechanical properties of novel large strain PolyPower film and laminate components for DEAP actuator and sensor applications," in *SPIE*, 2010, p. 764231.
- [3] M. Tryson, H. E. Kiil, and M. Benslimane, "Powerful tubular core free dielectric electro activate polymer (DEAP) push actuator," in *SPIE*, 2009, p. 72871F.
- [4] T. Sun, X. Wang, H. Wang, Z. Cheng, X. Zhang and L. Li "A Theoretical Model on Size Effect of Dielectric Response in DC Bias Field in Barium Titanate Ceramic System," *Journal of the American Ceramic Society*, vol. 93, no. 11, pp. 3808-3813, 2010.
- [5] L. E. Wojewoda, M. J. Hill K. Radhakrishnan and N. Goyal, "Use Condition Characterization of MLCC," *IEEE Trans. Advanced Packaging*, vol. 32, no. 1, pp. 109-115, 2009.
- [6] R. W. Erickson and D. Maksimovic, *Fundamentals of power electronics*, 2nd Edition, Kluwer Academic Publishers, 2004.
- [7] E.C. Snelling, *Soft Ferrites*, 1st Edition, Iliffe Books Ltd. 1969.

APPENDIX J

Energy Efficiency Investigation of Bidirectional High Voltage Flyback Converter for DEAP Actuator

Submitted to Transactions on Power Electronics (TPEL-Reg-2014-10-1701)

Energy Efficiency Investigation of Bidirectional High Voltage Flyback Converter for DEAP Actuator

Lina Huang, *Student Member, IEEE*, Zhe Zhang, *Member, IEEE*, and Michael A. E. Andersen, *Member, IEEE*

Department of Electrical Engineering, Technical University of Denmark

Kgs. Lyngby, DK-2800, Denmark

ABSTRACT

One type of smart material, which can be used to form artificial muscles, called Dielectric Electro Active Polymer (DEAP), is attracting attention from researchers in the material, mechanical and electrical field. The high voltage bidirectional flyback converter is proposed to achieve the driving for DEAP actuator with capacitive property. In order to build up the accurate behavior model to calculate the energy efficiency for the charging and discharging process of the bidirectional converter, the core loss effect and essential parasitic elements need to be taken into account. The established model has been validated through the comparison between the calculated efficiencies and measured ones in both charging and discharging process. The loss distribution indicates that most losses are on the primary side. Through optimizing the transformer and employing the synchronous rectifier technique in the primary side for the discharging phase, the efficiencies can be improved.

Index Terms—Energy efficiency, high voltage, bidirectional, flyback, DEAP actuator, core loss

I. INTRODUCTION

Over the past two decades, the scientists in the field of material have been dedicated to the fundamental research concerning the smart material to form the artificial muscles [1]. Compared to other potential materials, one type of the material called Dielectric Electro Active Polymer (DEAP)

demonstrates good performances, such as light weight, fracture tolerant and pliable, which are similar to the natural properties of biological muscles [1] [2]. Along with the advancement of the smart material, mechanical researchers are gradually getting involved in the field to investigate the possible configuration and to search for the potential application fields in addition to the artificial muscle. In order to commercialize this kind of smart material in suitable areas, the electronics system for driving the material or sensing its parameters cannot be absent, which makes the electronics engineer to take part in this research as well.

When placing the dielectric silicone polymer between two compliant electrodes, the basic DEAP film is constituted. The structure of the DEAP material is shown in Fig. 1 (a). Obviously, it has the similar configuration to that of the parallel-plate capacitor, which also features the sandwich structure with the dielectric element in the middle and the conducting material to form the electrodes. This implies the capacitive property of the DEAP film.

When a certain amount of voltage is applied over the compliant electrodes, the electrostatic force is induced, as indicated in Coulomb's law. This mechanical force can compress the soft silicone polymer in thickness and correspondingly expand the size. This principle of the

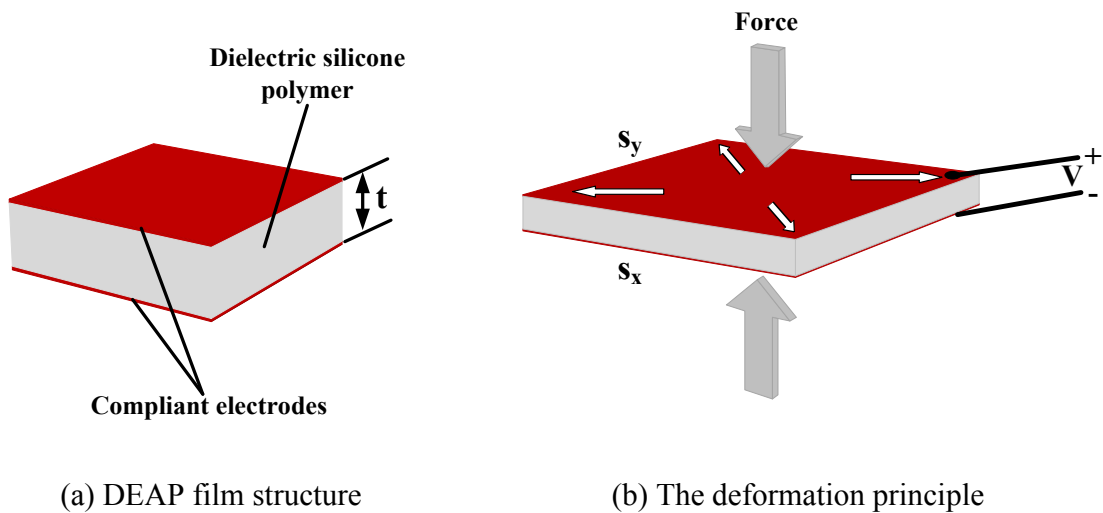


Fig 1. Structure and deformation principle of DEAP material

deformation is illustrated in Fig. 1 (b). The mechanism of deducing the deformation enable the DEAP film based actuator [3] [4]. Compared to conventional counterparts, such as hydraulic, pneumatic and electromagnetic actuators, DEAP actuator can demonstrate better performance in terms of weight, energy density, operation noise and response time, thus leading to the potential application in various fields besides the artificial muscle.

To achieve a certain amount of force, either large amount of DEAP film or the high voltage over the electrodes needs to be applied. In fact, the relationship among electrostatic force $F_{e.static}$, film size S and applied voltage V can be expressed as [2]

$$F_{e.static} = \varepsilon_0 \cdot \varepsilon_r \cdot \frac{V^2}{t^2} \cdot S \quad (1)$$

where ε_0 and ε_r are the vacuum permittivity and the relative permittivity of the DEAP material, respectively. And t stands for the thickness of the film, which cannot be adjusted if the film has been manufactured. The trend to reduce the element volume in various applications, similarly, makes a low volume DEAP actuator more attractive, thus resulting in the high applied voltage over the electrodes. The current version material indicates that 2 – 2.5 kV is required to achieve the fully elongation of the actuator.

Normally, the high voltage in the range of kilovolts cannot be acquired directly. A voltage transformation device, which can boost the low voltage to high voltage, is required. In recognition of the energy saving in the current situation, the switched mode power or energy conversion device can be a desired solution. The topology comparison indicates that, currently, there are two feasible approaches to achieve both the very high step up ratio and the relatively high efficiency. One is the newly developed piezoelectric transformer based power converter, which normally features complex control scheme to ensure the proper operation. The other solution, which is more mature and had been extensively applied in the old-fashioned cathode ray tube (CRT) TVs and monitors to

generate high voltage, is the magnetic transformer based flyback power converter, which will be adopted in this paper to achieve the low to high voltage transformation [5].

To further confirm the capacitive characteristic of the DEAP film, especially in the high voltage operation, some experiments had been carried out, which are illustrated in [6]. The transformation ratio of DEAP actuator from electrical energy to mechanical force is very low, around 2% in the performed experiments in [7]. This phenomenon indicates that most energy is still stored in the actuator electrically. When the actuator needs to be released, if all the stored energy can be recovered back to the energy source rather than be dissipated through the energy consumption element, the overall efficiency can be improved. If the battery is selected to be the power source, this strategy can significantly extend the battery life. Thus the converter with bidirectional energy flow functionality can be an expected solution [8]-[11]. When applying the bidirectional flyback topology to control the energy conversion between the source and the capacitive actuator to achieve the charge and discharge of the load, the working principle and the design considerations are considerably different from that of the normal steady-state operation flyback converter. The investigation of the flyback topology employed in the DEAP actuator driving applications need to be carried out in order to understand the detailed operating behavior, analyze the energy efficiency and finally to propose the optimal design guidelines. Furthermore, the achieved research results can also provide the references for other capacitive actuators, such as piezoelectric actuator [12]. When conducting the behavior and efficiency analysis, the parasitic elements involved in the converter cannot be neglected since they significantly affect the operating behavior of the converter, especially under the high voltage operation. These parameters include the stray capacitance of high voltage flyback transformer, parasitic capacitance of the high voltage semiconductors in the secondary side and the leakage inductance [13]-[16]. Normally, core loss can affect the efficiency analysis in the power electronics converter with magnetic components. In this

high voltage converter driving the capacitive actuator application, the existence of core loss not only affect the analysis concerning the energy efficiency, but also influence the switching cycle behavior, which must be considered in the analytical modeling and efficiency investigation.

In this paper, the practical configuration with the essential parasitic elements as well as the normal operating modes of the high voltage bidirectional flyback converter will be presented in Section II. In Section III, the approach to consider the core loss in this special application will be discussed. Afterwards, the switching cycle based behavior and loss model will be established for two typical operating modes in Section IV. Based on the achieved behavior model and components losses in switching cycles, the efficiency for the entire charging and discharging phases and the corresponding loss distribution can be derived in Section V. The energy efficiency analytical model is verified through comparing the calculated efficiencies with the measured ones in Section VI. Finally, the conclusions are drawn in Section VII.

II. HIGH VOLTAGE FLYBACK CONVERTER FOR DEAP ACTUATOR

A. Practical configuration with parasitic elements

The proposed high voltage bidirectional flyback converter with the essential parasitic components is illustrated in Fig. 2. The poor performance of body diode inside the high voltage MOSFET (S_2) necessitates two extra high voltage diodes (D_{21} and D_{22}) to block the current through the body diode and to provide the freewheeling path for the secondary side current, respectively. To achieve the current loop control, three current sensing resistors (RP_1 , RP_2 and RP_3) in both primary and secondary side are applied. In practice, the most critical parasitic element in the high voltage transformer is the secondary winding stray capacitance caused by a large number of winding turns [14], [16]. In recognition of other parasitic capacitances in the high voltage side, such as the junction capacitance of high voltage diodes and the output capacitance of the high voltage MOSFET, an equivalent stray capacitance C_{seq} paralleled to secondary winding of transformer is

proposed to represent the effect of parasitic capacitances. The leakage inductances (L_{pl} and L_{sl}) have always been a factor which prevents the achievement of higher efficiency. It should be noted that the primary side leakage inductance (L_{pl}) and secondary side leakage inductance (L_{sl}) cannot exist simultaneously. When the energy flow is from primary side to secondary side, L_{pl} is adopted to stand for the untransferrable energy stored in the flyback transformer. The same concept applies to L_{sl} . Moreover, in order to achieve the accurate energy efficiency, the winding resistances (R_{pw} and R_{sw}) cannot be neglected. Resistive element is proved to be an effective approach to represent the core loss [17] [18]. Thus an equivalent resistance of core loss reflected to the secondary side (R_{ceqs}) is employed, which will be discussed in detail in Section III.

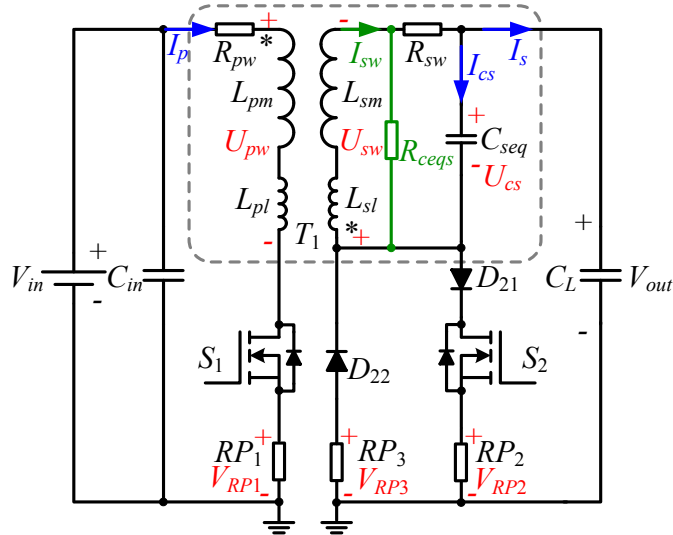


Fig. 2. The configuration of bidirectional HV flyback converter for capacitive load.

B. The definition of variables

It is necessary to define the variables before establishing the switching cycle based behavior and loss model. L_{pm} and L_{sm} are primary and secondary magnetizing inductances, respectively. L_{pl} and L_{sl} are primary and secondary leakage inductances, respectively. And $L_p = L_{pm} + L_{pl}$ as well as $L_s = L_{sm} + L_{sl}$ is utilized to stand for the primary and secondary total inductance. RP_1 , RP_2 and RP_3

are the resistances of three current sensing resistors. The secondary side equivalent parasitic capacitance paralleled to transformer winding is denoted as C_{seq} . V_{D21} and V_{D22} are the forward voltage drop of high voltage diodes D_{21} and D_{22} , respectively. In fact, the voltage drop changes with the forward current. To reduce the complexity, the constant forward voltage drop is assumed here. In the discharging mode, the body diode of primary switch (S_1) plays the role of freewheeling and its forward voltage drop is denoted as V_{bdS1} . In order to improve the accuracy of the model, the on resistances of MOSFETs (S_1 and S_2) need to be taken into account, especially that for the high voltage MOSFET due to its large value. On the other hand, to simplify the model, the on resistances are considered to be a fixed value and denoted as R_{dsonS1} and R_{dsonS2} , respectively. Winding resistances (R_{pw} and R_{sw}) are frequency related parameters and do not have the fixed values, which will be defined in the modeling later. C_L is utilized to stand for the capacitance of the DEAP actuator. V_{in} is the input voltage source with fixed value, V_o is the output voltage and the initial output voltage for one switching cycle is denoted as V_{oini} . U_{cs} is used to stand for the voltage over the equivalent parasitic capacitance C_{seq} . Considering the measurement of the current in reality, it is reasonable to use the voltages over the current sensing resistors V_{RP1} , V_{RP2} and V_{RP3} to represent the currents in the circuit. The voltages over transformer windings are denoted as U_{pw} and U_{sw} , respectively. And the positive directions for all the voltages are illustrated in Fig. 2. The primary current I_p and secondary current I_s are also depicted in Fig. 2 with their positive directions. The current through C_{seq} is denoted as I_{cs} with the corresponding positive direction to the voltage. Due to the impact of C_{seq} and the equivalent resistance of core loss, the secondary current I_s cannot stand for the secondary side winding current, which is then denoted as I_{sw} with the positive direction shown in Fig. 2.

C. Operating modes

The typical operating modes of the bidirectional flyback converter for capacitive actuator are the charging mode (the output voltage increases) - energy transfers from source to the capacitive load, and discharging mode (the output voltage decreases) - energy recycles from capacitive load to power source. To achieve the pre-determined output voltage, a series of successive switching cycles working in the charging mode need to be applied. In each cycle, the output voltage increases due to positive current to the capacitive load. The accumulation of the voltage in each switching cycle during the entire charging process enables the achievement of the pre-set output voltage. Likewise, in each switching cycle operated in the discharging mode, the output voltage decreases. The reduction of the output voltage in a series of successive cycles can lead to the fully discharge of the actuator. To achieve the complete energy transfer in one switching cycle, for the current control scheme in the bidirectional flyback converter, either the boundary conduction mode (BCD) or the discontinuous conduction mode (DCM) needs to be applied. In this paper, the charging mode will be analyzed in BCM while the discharge mode will be modeled in DCM.

1) Switching cycle in the charging mode

Due to the employment of BCM current control in the charging process, one switching cycle in the charging mode consists of 4 intervals. The key waveforms of one charging cycle are illustrated in Fig. 3.

$[t_0 < t < t_1]$: In this interval, the secondary side equivalent stray capacitor C_{seq} resonates with secondary inductance L_s with the initial energy stored in the capacitor. Under the low voltage operation, the control IC normally makes this interval last for half of the resonance period. While under high voltage operation, when the voltage over the primary winding can force the body diode of S_1 to conduct, this interval is assumed to be finished.

$[t_1 < t < t_2]$: S_1 is switched on at the beginning of this interval. The dominant behavior in this interval is the primary magnetization. Moreover, the resonance due to the primary leakage

inductance and C_{seq} under the low voltage operation and the secondary leakage inductance and C_{seq} under high operating voltage needs to be taken into account. When the magnetizing current reaches the pre-set value of the control IC, this interval terminates.

$[t_2 < t < t_3]$: S_1 is switched off at the beginning of this interval. However, the secondary freewheeling diode D_{22} cannot conduct immediately due to the reverse voltage. In this interval, C_{seq} is charged from the energy stored in the transformer until its voltage can force D_{22} to conduct.

$[t_3 < t < t_4]$: D_{22} is forced to conduct at the beginning of this interval and the freewheeling phase starts. The energy still stored in the flyback transformer will be transferred to the capacitive load. The interval terminates when the freewheeling current reaches zero.

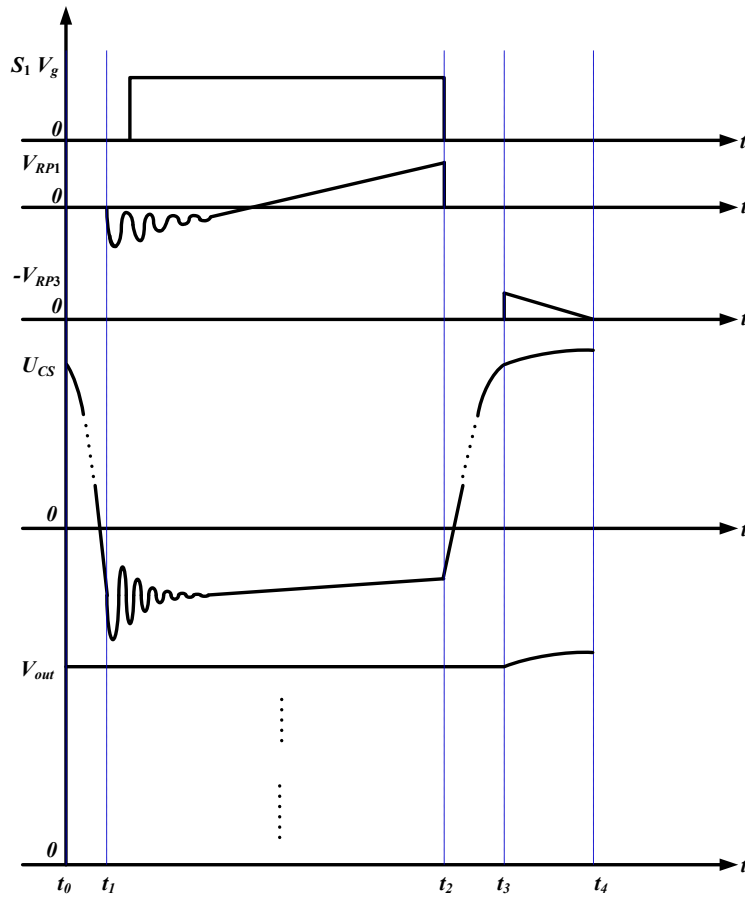


Fig. 3. The key waveforms of one switching cycle in charging mode under high voltage operation.

2) Switching cycle in the discharging mode

In comparison, the application of the DCM in the discharging process makes the switching cycle normally feature a DCM interval, thus leading to 5 intervals in one discharging cycle. The key waveforms of one discharging cycle are illustrated in Fig. 4.

$[t_0 < t < t_1]$: At the beginning of this interval, S_2 is switched on and the secondary side equivalent stray capacitor C_{seq} starts to be charged. Until the voltage over C_{seq} and the high voltage diode D_{21} reaches the current output voltage, this interval terminates.

$[t_1 < t < t_2]$: The flyback transformer is magnetized during this interval until the magnetizing current reaches the pre-set value of the controller. The energy transfers from the capacitive load to the flyback transformer in this interval. Correspondingly, the output voltage decreases during this period.

$[t_2 < t < t_3]$: When S_2 is switched off at the beginning of this interval, the energy stored in the coupled inductor cannot be immediately transferred to the primary side due to the reverse voltage over the body diode of S_1 . In this interval, the behavior is similar to that in the stage $[t_0-t_1]$ of the charging mode. When the primary winding voltage reaches the value, which can force the body diode of S_1 to conduct, this interval ends.

$[t_3 < t < t_4]$: In this interval, the energy stored in the transformer will be transferred to the primary source. Moreover, the energy which cannot be transferred to the primary side (i.e. the energy stored in the secondary side leakage inductance) will result in a resonance between the leakage inductance and the stray capacitance C_{seq} . When all the energy stored in the transformer is recovered to the source, this interval terminates.

$[t_4 < t < t_5]$: This interval is the discontinuous conduction phase in the discharging mode. The fixed frequency control is applied in the discharging process. When next switching cycle starts, this interval automatically ends.

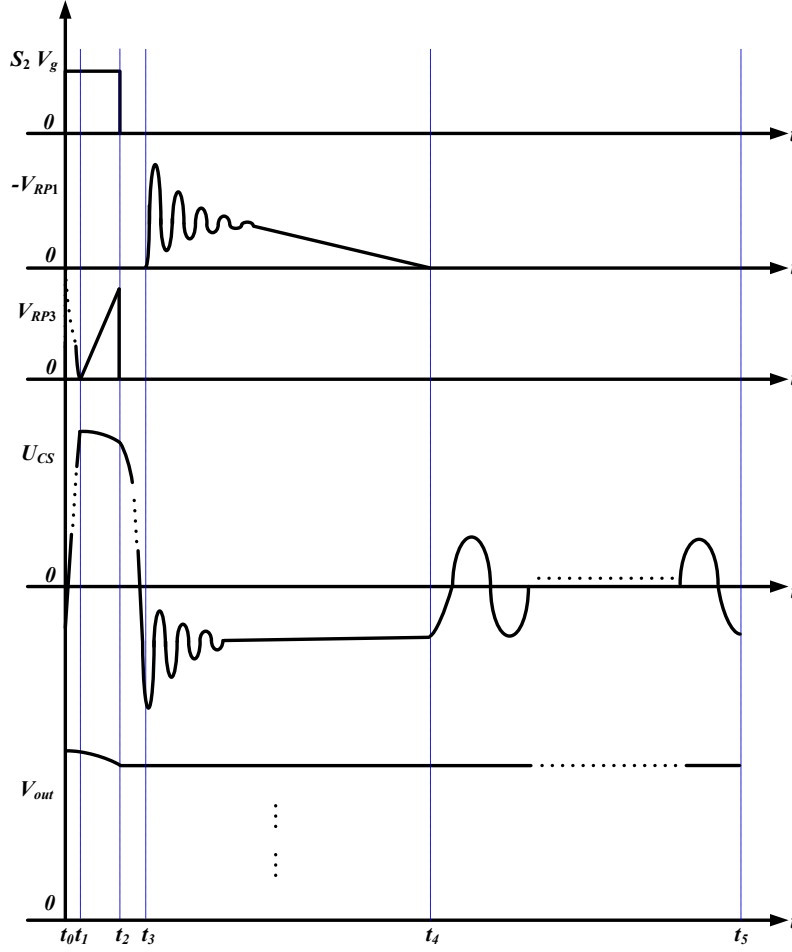


Fig. 4. The key waveforms of one switching cycle in discharging mode under high voltage operation.

III. CORE LOSS CONSIDERATION

The most commonly used method to calculate core loss is the Steinmetz equation. It should be noted that this equation is only valid for sinusoidal waveforms and cannot be directly applied in most power electronics systems. In order to overcome this limitation, several methodologies have been proposed. Among them, the widely adopted approach is the improved generalized Steinmetz equation (iGSE) [17] [18]

$$P_v = \frac{1}{T} \int_0^T k_i \left| \frac{dB}{dt} \right|^\alpha (\Delta B)^{\beta-\alpha} dt \quad (2)$$

$$k_i = \frac{k}{(2\pi)^{\alpha-1} \int_0^{2\pi} |\cos \theta|^\alpha 2^{\beta-\alpha} d\theta} \quad (3)$$

where P_v is the time-average power loss per unit volume, T stands for the switching period, $\left|\frac{dB}{dt}\right|$ is the absolute value of change rate of flux density, ΔB is the peak-to-peak flux density and α , β , k are material related parameters, which can be obtained or derived from the datasheet of the material.

As previously stated, resistive element can be utilized to represent the effect of core loss. If the analytical behavioral model in one switching cycle is known, the core loss can be calculated through (2), thus the secondary side equivalent resistance of core loss R_{ceqs} can be derived through (4)

$$R_{ceqs} = \frac{U_{sw}^2}{P_v} \quad (4)$$

In practice, in order to achieve the R_{ceqs} , when calculating the winding voltages, the effect of core loss needs to be neglected first. Afterwards, the acquired R_{ceqs} can be used to establish the precious behavioral and loss models.

IV. SWITCHING CYCLE BASED BEHAVIORAL AND LOSS MODELS

Taking the pure capacitive property of DEAP actuator into account, it is rational to establish the switching cycle based behavioral and loss model of the bidirectional flyback converter from the energy point of view. As indicated in Section II, no matter in the charging mode or discharging mode, there are several intervals in one switching cycle, the achievement of the behavior and loss model in each interval can help to acquire the total energy loss in one cycle.

A. Charging mode

$[t_0 < t < t_1]$: Considering the effect of core loss, the behavior in this interval can be expressed as

$$L_s \cdot C_{seq} \cdot \left(\frac{R_{swc01}}{R_{ceqs}} + 1 \right) \cdot \frac{dI_{swc01}^2(t-t_0)}{dt^2} + \left(\frac{L_s}{R_{ceqs}} + R_{swc01} \cdot C_{seq} \right) \cdot \frac{dI_{swc01}(t-t_0)}{dt} + I_{swc01}(t-t_0) = 0 \quad (5)$$

The initial conditions are

$$\begin{cases} I_{swc01}(t - t_0)|_{t=t_0} = 0 \\ \frac{dI_{swc01}(t-t_0)}{dt}|_{t=t_0} = \frac{-U_{csc01t_0}}{L_s \cdot \left(\frac{R_{swc01}}{R_{ceqs}} + 1\right)} \end{cases} \quad (6)$$

where R_{swc01} is the secondary winding resistance at the resonance frequency in this interval

$$R_{swc01} = R_{sw} @ \frac{1}{2\pi \cdot \sqrt{L_s \cdot C_{seq}}} \quad (7)$$

At the beginning of this interval, the voltage over C_{seq} is

$$U_{csc01t_0} = V_{oini} + V_{D22} \quad (8)$$

It should be noted that the subscript $c01$ stands for the interval $[t_0 \ t_1]$ in the charging mode and t_0 represents the time t_0 . This rule for subscript will be applied throughout this paper.

The differential equations in (5) can be solved with the initial conditions in (6) to achieve the secondary side winding current in this interval first. Correspondingly, other parameters, such as the voltage over C_{seq} and the current through C_{seq} can be obtained. During this period of time, not only the secondary winding resistance consumes energy, under the high voltage operation, the energy stored in the secondary leakage inductance L_{sl} also will be lost. Thus, the energy loss in this interval can be expressed as

$$E_{swc01} = \int_{t_0}^{t_1} I_{csc01}(t - t_0)^2 \cdot R_{swc01} \cdot dt \quad (9)$$

$$E_{slc01} = \frac{1}{2} \cdot L_{sl} \cdot (I_{csc01}(t - t_0)|_{t=t_1})^2 \quad (10)$$

$[t_1 < t < t_2]$: In this magnetizing stage, it is convenient to consider the core loss effect from the primary side through representing the core loss with primary equivalent resistance R_{ceqp} . According to (4), the relationship between the primary and secondary equivalent resistance of core loss can be derived as

$$R_{ceqp} = \frac{R_{ceqs}}{N^2} \quad (11)$$

where N is the turns ratio of the transformer and defined as the secondary winding turns N_{sec} divided by primary winding turns N_{pri} . Thus the magnetizing behavior in this interval can be derived as

$$L_p \cdot \left(\frac{R_{pwc12} + R_{dsonS1} + RP_1}{R_{ceqp}} + 1 \right) \cdot \frac{dI_{pc12mag}(t-t_0)}{dt} + (R_{pwc12} + R_{dsonS1} + RP_1) \cdot I_{pc12mag}(t-t_0) = 0 \quad (12)$$

The initial condition depends on the operation voltage and can be expressed as

$$I_{pc12magt1} = \begin{cases} I_{pc12mag}(t-t_1)|_{t=t_1} = 0 & \text{if low voltage operation} \\ N \cdot I_{csc01}(t-t_0)|_{t=t_1} & \text{if high voltage operation} \end{cases} \quad (13)$$

where R_{pwc12} is the primary winding resistance at the switching frequency for the current cycle. So far, the exact switching frequency is unknown. But an estimated value can be achieved by ignoring the influence of the intervals $[t_0 < t < t_1]$ and $[t_2 < t < t_3]$ and only considering the ideal situations for the intervals $[t_1 < t < t_2]$ and $[t_3 < t < t_4]$

$$f_{swideal} = \frac{1}{\frac{(I_{pp} - I_{pc12magt1}) \cdot L_p}{V_{in}} + \tan^{-1} \left(\frac{I_{pp} \cdot \sqrt{L_{sm}}}{N \cdot V_{oini} \cdot \sqrt{C_L}} \right) \cdot \sqrt{L_{sm} \cdot C_L}} \quad (14)$$

where I_{pp} is the primary peak current set by the inner current loop control. Then,

$$R_{pwc12} \approx R_{pw} @ f_{swideal} \quad (15)$$

In addition, if under high voltage operation, the secondary leakage inductance resonates with C_{seq} , the behavior can be expressed as

$$L_{sl} \cdot C_{seq} \cdot \left(\frac{R_{swc12rh}}{R_{ceqs}} + 1 \right) \cdot \frac{dI_{swc12}^2(t-t_1)}{dt^2} + \left(\frac{L_s}{R_{ceqs}} + R_{swc12rh} \cdot C_{seq} \right) \cdot \frac{dI_{swc12}(t-t_1)}{dt} + I_{swc12rh}(t-t_1) = 0 \quad (16)$$

The initial conditions are

$$\begin{cases} I_{swc12}(t - t_1)|_{t=t_1} = I_{swc01}(t - t_0)|_{t=t_1} \\ \frac{dI_{swc12}(t-t_1)}{dt}\bigg|_{t=t_1} = \frac{-U_{csc01t1}}{L_{sl} \cdot \left(\frac{R_{swc12rh}}{R_{ceqs}} + 1\right)} \end{cases} \quad (17)$$

where $R_{swc12rh}$ is the secondary winding resistance at the resonance frequency of L_{sl} and C_{seq} in this interval

$$R_{swc12rh} = R_{sw} @ \frac{1}{2\pi \cdot \sqrt{L_{sl} \cdot C_{seq}}} \quad (18)$$

If under low voltage operation, the primary leakage inductance resonates with C_{seq} , the corresponding behavior can be expressed as

$$\begin{aligned} L_{pl} \cdot C_{seq} \cdot N \cdot \frac{dU_{csc12rl}^2(t-t_1)}{dt^2} + \left(C_{seq} \cdot N \cdot \left(\frac{R_{swc12rl}}{N^2} + R_{dsonS1} + RP_1 \right) \right) \cdot \frac{dU_{csc12rl}(t-t_1)}{dt} + \\ \frac{U_{csc12rl}(t-t_1)}{N} = V_{in} \end{aligned} \quad (19)$$

The initial conditions are

$$\begin{cases} U_{csc12rl}(t - t_1)|_{t=t_1} = U_{csc01t1} \\ \frac{dU_{csc12rl}(t-t_1)}{dt}\bigg|_{t=t_1} = 0 \end{cases} \quad (20)$$

where $R_{swc12rl}$ is the secondary winding resistance at the resonance frequency of L_{pl} and C_{seq} in this interval

$$R_{swc12rl} = R_{sw} @ \frac{1}{2\pi \cdot \sqrt{L_{pl} \cdot C_{seq} \cdot N^2}}} \quad (21)$$

By solving the magnetizing and the corresponding resonance differential equations with initial conditions, the magnetizing and resonance current and other variables can be achieved. Thus the total primary current in this interval can be obtained through

$$I_{pc12}(t) = \begin{cases} I_{pc12mag}(t) + I_{pc12rl}(t) & \text{if low voltage operation} \\ I_{pc12mag}(t) + I_{pc12rh}(t) & \text{if high voltage operation} \end{cases} \quad (22)$$

In this interval, the primary winding consumes energy and can be expressed as

$$E_{pwc12} = \int_{t_1}^{t_2} I_{pc12}(t)^2 \cdot R_{pwc12} \cdot dt \quad (23)$$

The energy stored in the primary leakage inductance is assumed to be fully lost

$$E_{plc12} = \frac{1}{2} \cdot L_{pl} \cdot I_{pp}^2 \quad (24)$$

In general, when calculating the loss of MOSFET, the conduction loss and switching loss need to be considered. In the switching loss calculation, the turn on loss depends on the current and voltage of the MOSFET at the turn on transient. It is really challenging to achieve the accurate calculation. When calculating the turn off loss, normally, only the loss caused by the output capacitor of MOSFET needs to be taken into account [19]. However, in this flyback converter case, this energy, in fact, comes from the leakage inductance, thus it is not necessary to consider once again. Therefore, the conduction loss can represent the total loss of S_I in this interval and can be expressed as

$$E_{S_1c12} = \int_{t_1}^{t_2} I_{pc12}(t)^2 \cdot R_{dsonS_1} \cdot dt \quad (25)$$

Similarly, the energy consumption in the current sensing resistor can be derived as

$$E_{RP_1c12} = \int_{t_1}^{t_2} I_{pc12}(t)^2 \cdot RP_1 \cdot dt \quad (26)$$

$[t_2 < t < t_3]$: In this interval, the behavior is the same as in $[t_0 < t < t_I]$ and can be expressed with similar equations as (5). In addition, the initial conditions are similar to that expressed in (6). Thus the equations are not necessary to be repeated here. During this period of time, only secondary winding consumes energy and can be expressed as

$$E_{swc23} = \int_{t_2}^{t_3} I_{csc23}(t - t_2)^2 \cdot R_{swc23} \cdot dt \quad (27)$$

where R_{swc23} is the secondary winding resistance at the resonance frequency of L_{sm} and C_{seq} in this interval

$$R_{swc23} = R_{sw} @ \frac{1}{2\pi \cdot \sqrt{L_{sm} \cdot C_{seq}}} \quad (28)$$

$[t_3 < t < t_4]$: In this interval, the energy still stored in the transformer is transferred to the capacitive actuator, the behavior can be expressed as

$$L_{sm} \cdot C_L \cdot \left(\frac{R_{fwc34}}{R_{ceqs}} + 1 \right) \cdot \frac{dI_{swc34}^2(t-t_3)}{dt^2} + \left(\frac{L_{sm}}{R_{ceqs}} + R_{fwc34} \cdot C_L \right) \cdot \frac{dI_{swc34}(t-t_3)}{dt} + I_{swc34}(t-t_3) = 0 \quad (29)$$

The initial conditions are

$$\begin{cases} I_{swc34}(t-t_3)|_{t=t_3} = I_{swc23}(t-t_2)|_{t=t_3} \\ \frac{dI_{swc34}(t-t_3)}{dt} \Big|_{t=t_3} = \frac{-(V_{oini} + V_{D22}) - R_{fwc34} \cdot I_{swc23}(t-t_2)|_{t=t_3}}{L_{sm} \cdot \left(\frac{R_{fwc34}}{R_{ceqs}} + 1 \right)} \end{cases} \quad (30)$$

where

$$R_{fwc34} = RP_3 + R_{swc34} = RP_3 + R_{sw} @ f_{swideal} \quad (31)$$

By solving the differential equations in (29) with the initial conditions, all the variables in this interval can be achieved. Thus, the energy consumed by secondary winding, freewheeling diode and current sensing resistor can be expressed as

$$E_{swc34} = \int_{t_3}^{t_4} I_{sc34}(t)^2 \cdot R_{swc34} \cdot dt \quad (32)$$

$$E_{D22c34} = \int_{t_3}^{t_4} I_{sc34}(t) \cdot V_{D22} \cdot dt \quad (33)$$

$$E_{RP3c34} = \int_{t_3}^{t_4} I_{sc34}(t)^2 \cdot RP_3 \cdot dt \quad (34)$$

B. Discharging mode

$[t_0 < t < t_l]$: In this interval, the capacitive actuator can be assumed to be a voltage source, since its capacitance value is much larger than the C_{seq} , and the behavior can be expressed as

$$(R_{dsonS2} + RP_2) \cdot C_{seq} \cdot \frac{dU_{csd01}(t-t_0)}{dt} + U_{csd01}(t-t_0) - (V_{oini} - V_{D21}) = 0 \quad (35)$$

and the initial condition is

$$U_{csd01}(t-t_0)|_{t=t_0} = U_{csd01t1} \quad (36)$$

where $U_{csd01t1}$ can be achieved by the terminal condition of last cycle.

In practice, this interval is too tiny, it is not necessary to consider the energy consumption in the components. Thus, it is reasonable to assume that no loss is induced during this period of time.

$[t_l < t < t_2]$: The behavior in this interval is similar to the resonance between the L_{sm} and C_L in $[t_3 < t < t_4]$ of the charging mode. While in the discharging mode, the high voltage MOSFET S_2 and high voltage diode D_{2l} are involved instead of the freewheeling diode D_{22} in the charging mode. Similar differential equation as (29) can be achieved. Combined with the corresponding initial conditions, all the variables can be obtained in this interval. And the energy consumption of secondary winding resistance, leakage inductance, S_2 , current sensing resistor and D_{2l} can be expressed

$$E_{swd12} = \int_{t_1}^{t_2} I_{sd12}(t)^2 \cdot R_{swd12} \cdot dt \quad (37)$$

$$E_{sl12} = \frac{1}{2} \cdot L_{sl} \cdot I_{sp}^2 \quad (38)$$

$$E_{S_2d12} = \int_{t_1}^{t_2} I_{sd12}(t)^2 \cdot R_{dsonS2} \cdot dt \quad (39)$$

$$E_{RP_2d12} = \int_{t_1}^{t_2} I_{sd12}(t)^2 \cdot RP_2 \cdot dt \quad (40)$$

$$E_{D_{21}d12} = \int_{t_1}^{t_2} I_{sd12}(t) \cdot V_{D21} \cdot dt \quad (41)$$

$[t_2 < t < t_3]$: In practice, the behavior in this interval is similar to that in $[t_0 < t < t_1]$ of the charging mode. And the energy consumption of the secondary winding resistance during this period of time can be expressed as

$$E_{swd23} = \int_{t_2}^{t_3} I_{csd23}(t)^2 \cdot R_{swd23} \cdot dt \quad (42)$$

$[t_3 < t < t_4]$: Similarly, the differential equation of the interval $[t_2 < t < t_3]$ of charging mode can be used to represent the behavior here. In this interval, the energy consumption of primary winding resistance, current sensing resistor and body diode of S_l can be expressed as

$$E_{pw34} = \int_{t_3}^{t_4} I_{pri34}(t)^2 \cdot R_{w34} \cdot dt \quad (43)$$

$$E_{RP134} = \int_{t_3}^{t_4} I_{pri34}(t)^2 \cdot RP_1 \cdot dt \quad (44)$$

$$E_{bdS134} = \int_{t_3}^{t_4} I_{pri34}(t) \cdot V_{bdS1} \cdot dt \quad (45)$$

$[t_4 < t < t_5]$: This interval is the DCM stage and the behavior can be expressed as

$$L_s \cdot C_{seq} \cdot \frac{dU_{csd45}^2(t-t_4)}{dt^2} + R_{swd45} \cdot \frac{dU_{csd45}(t-t_4)}{dt} + U_{csd45}(t-t_4) = 0 \quad (46)$$

The initial conditions can be derived from last interval. During this period of time, the energy consumption of the secondary winding resistance can be expressed as

$$E_{swd45} = \int_{t_4}^{t_5} I_{csd45}(t)^2 \cdot R_{swd45} \cdot dt \quad (47)$$

V. ENERGY EFFICIENCY AND LOSS DISTRIBUTION ANALYSIS

A. Charging mode

As indicated in Fig. 3, in one switching cycle, only in interval $[t_1 < t < t_2]$, the energy is transferred from the source to the converter. Therefore, the input energy in one cycle can be expressed as

$$E_{in_charge_cycle} = \int_{t_1}^{t_2} I_{pc12}(t) \cdot V_{in} \cdot dt \quad (48)$$

By adding the input energy of every switching cycle in the charging process, the total input energy E_{in} can be achieved. The final energy stored in the DEAP actuator can be derived as

$$E_{stored} = \frac{1}{2} \cdot C_L \cdot V_{omax}^2 \quad (49)$$

where V_{omax} is the pre-determined maximum output voltage. So, the charging efficiency can be expressed as

$$\eta_{charge} = \frac{E_{stored}}{E_{in}} \quad (50)$$

As illustrated in Fig. 2, the loss elements in the bidirectional flyback converter operated in the charging mode include primary winding resistance R_{pwc} , primary leakage inductance L_{pl} , S_1 , RP_1 , secondary winding resistance R_{swc} , secondary leakage inductance L_{sl} , secondary freewheeling diode D_{22} , RP_3 and core. The losses in each interval of charging mode have been achieved in Section IV. For each element, by adding the losses of all intervals in one switching cycle, the energy consumption of this component in one cycle can be achieved. If the losses are added up for all the cycles during the entire charging process, the total loss of this element can be achieved, which will be beneficial to carry out the loss distribution analysis.

B. Discharging mode

Fig. 4 indicates, in one switching cycle, only in interval $[t_3 < t < t_4]$, the energy is recovered to the energy source from the converter. Therefore, the recovered energy in one cycle can be expressed as

$$E_{recovered_discharge_cycle} = \int_{t_3}^{t_4} I_{pd34}(t) \cdot V_{in} \cdot dt \quad (48)$$

The total recovered energy $E_{recovered}$ can be achieved through adding the recovered energy of every switching cycle in the discharging process. Thus, the discharging efficiency can be expressed as

$$\eta_{discharge} = \frac{E_{recovered}}{E_{stored}} \quad (50)$$

Likewise, the loss elements in the bidirectional flyback converter operated in the discharging mode include secondary winding resistance R_{swd} , secondary leakage inductance L_{sl} , S_2 , secondary high voltage diode D_{21} , RP_2 , primary winding resistance R_{pwd} , body diode of S_1 , RP_1 and core. The same approach stated in the charging mode in this section can be applied to achieve the loss distribution during the discharging process.

VI. EXPERIMENTAL VERIFICATION

A prototype of bidirectional high voltage flyback converter was performed in order to validate the energy efficiency model in terms of charging as well as discharging process. The specifications, design parameters and the employed components are summarized in Table I. The implemented and measured data for the high voltage flyback transformer as well as the parameters for the core loss calculation are listed in Table II. The primary and secondary winding ac resistance of the transformer are frequency dependent and the measured resistance versus frequency characteristic up to 2 MHz are shown in Fig. 5 (a) and (b), respectively.

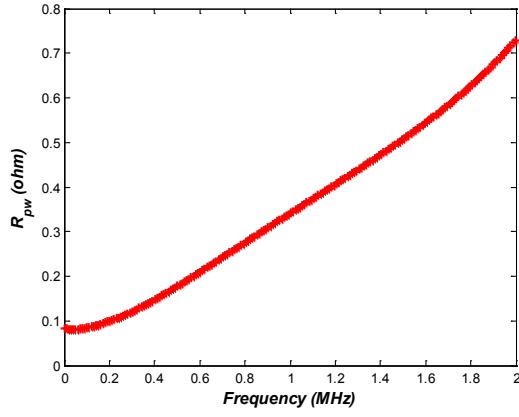
TABLE I. HV FLYBACK CONVERTER SPECIFICATIONS AND COMPONENTS LIST

| Parameters | Values |
|---------------------|----------------|
| V_{in} | 3 V |
| Maximum V_{out} | 2 kV |
| C_L | 220 nF |
| I_{pp} | 4 A |
| I_{sp} | 100 mA |
| S_1 | BSC320N20NS3 G |
| S_2 | IXTV03N400S |
| D_{21} & D_{22} | VMI6525 |
| RP_1 | 20 mΩ 1 % |

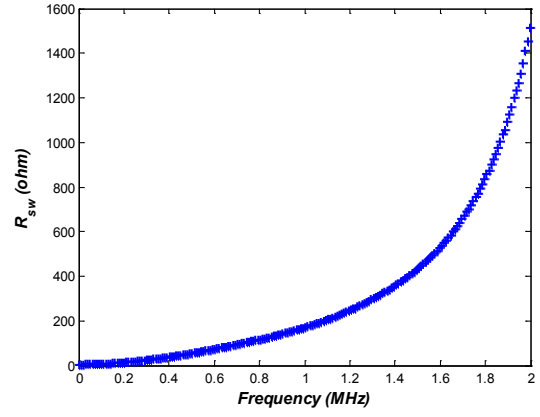
| | |
|-----------------|----------------|
| RP_2 & RP_3 | 1 Ω 1 % |
|-----------------|----------------|

TABLE II. HV FLYBACK TRANSFORMER IMPEMENTED AND MEASURED PARAMETERS

| Parameters | Values |
|------------|----------------------|
| N_{pri} | 6 |
| N_{sec} | 232 |
| N | 38.7 |
| L_{pm} | 12.7 μ H |
| L_{pl} | 300 nH |
| L_{sm} | 18.4 mH |
| L_{sl} | 450 μ H |
| C_{seq} | 30 pF |
| k | 12.97 |
| α | 1.26 |
| β | 2.02 |
| A | 32.8 mm ² |
| V_e | 1564 mm ³ |



(a) Primary winding ac resistance



(b) Secondary winding ac resistance

Fig. 5. HV flyback transformer winding ac resistance.

A. Validation of charging mode

Based on the efficiency calculation model, the charging energy efficiencies versus output voltage can be achieved, which are shown in Fig. 6. In comparison, the experiments based measured efficiencies are illustrated in Fig. 6 as well. Obviously, the calculated efficiencies can well match the measured ones, which can validate the behavior and efficiency calculation model of charging mode. Moreover, for charging process, the loss breakdown for different elements is

illustrated in Fig. 7. It can be observed that losses are mostly on the primary side and the flyback transformer core.

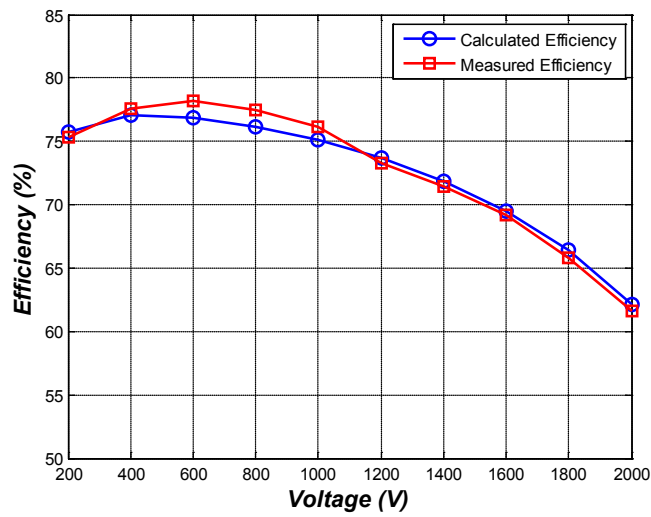


Fig. 6. Comparison of calculated and measured charging efficiency.

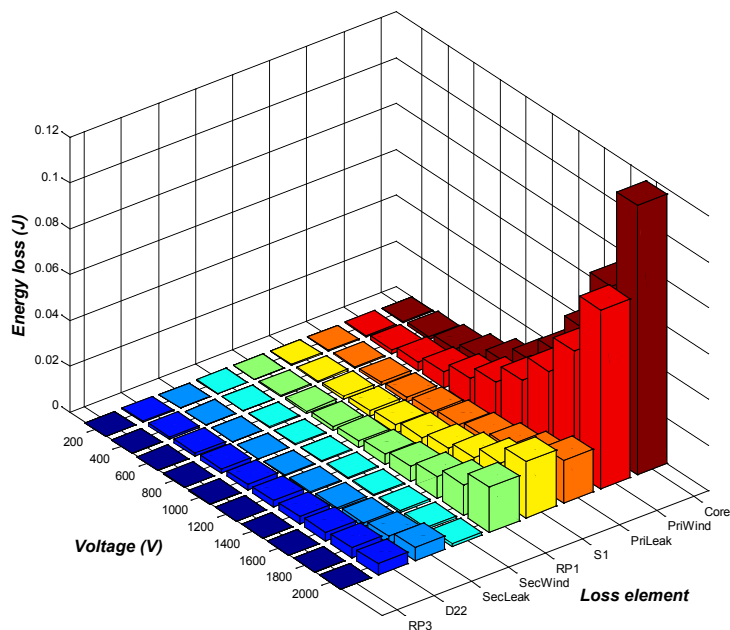


Fig. 7. Loss distribution of charging process.

B. Validation of discharging mode

Likewise, the calculated and measured efficiencies are obtained for discharging process, which are shown in Fig. 8. It can be seen that the calculated efficiencies can well match the measured ones in the discharging process as well, which can verify the behavior and loss model of the discharging mode. The loss distribution shown in Fig. 9, indicates that, in the discharging process, most losses are consumed in the primary side.

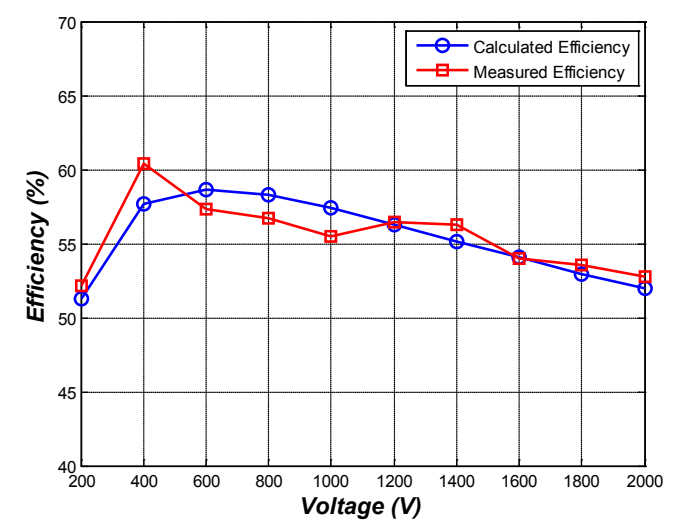


Fig. 8. Comparison of calculated and measured discharging efficiency.

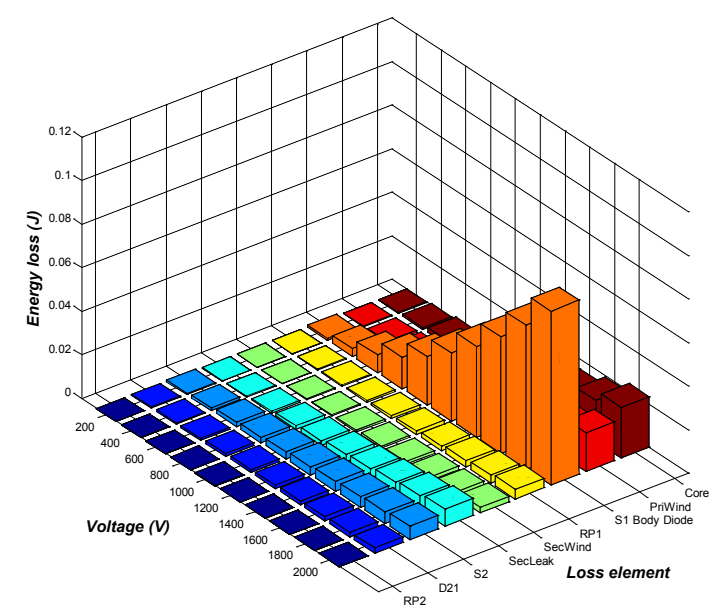


Fig. 9. Loss distribution of discharging process.

V. CONCLUSION AND FUTURE WORKS

In this paper, the Dielectric Electro Active Polymer (DEAP) material and its actuator are introduced first. The high voltage bidirectional flyback converter is proposed to realize the driving for the DEAP actuator. The practical flyback configuration with essential parasitic elements is illustrated. In order to understand the behaviour and carry out the energy efficiency analysis for the converter supplying capacitive load, the behaviour and loss model need to be established. Core loss significantly affects the accuracy of the model, it is necessary to integrate the core loss effect into the analytical behaviour and energy calculation model. Finally, the match between the calculated efficiencies and measured ones in both charging and discharging process validates the behaviour as well as the efficiency calculation model. The loss distribution indicates that, no matter in the charging or discharging mode operation, most losses are on the primary side. By optimizing the transformer and using synchronous rectifier in the discharging mode, the efficiency can be improved, which can be one of the future works.

REFERENCES

- [1] Y. Bar-Cohen, "Electroactive polymer (EAP) actuators as artificial muscles: reality, potential, and challenges," *SPIE Press*, 2004.
- [2] P. Brochu and Q. Pei, "Advances in dielectric elastomers for actuators and artificial muscles," *Macromolecular Rapid Communications*, vol. 31, no. 1, pp. 10-36, 2010.
- [3] D. De Rossi, R. Pelrine, F. Carpi, and R. Kornbluh, "Dielectric elastomers as electromechanical transducers". *Elsevier Science*, 2008.
- [4] M. Y. Benslimane, H.-E. Kiil, and M. J. Tryson, "Dielectric electro-active polymer push actuators: performance and challenges," *Polymer International*, vol. 59, no. 3, pp. 415–421, 2010.
- [5] A. Rahimi, F. F. Rahimi and I. Hassanzadeh, "Analysis of high-voltage flyback converter in color TVs, and its

regulation," in *The Fifth International Conference on Power Electronics and Drive Systems 2003 (PEDS 2003)*, Singapore, 2003.

- [6] T. Andersen, L. Huang, Z. Zhang and M. A. E. Andersen, "Efficiency of Capacitively Loaded Converters," *38th Annual Conference of the IEEE Industrial Electronics Society (IECON 2012)*, 2012.
- [7] M. J. Tryson, R. Sarban, and K. P. Lorenzen, "The dynamic properties oftubular DEAP actuators," *Proceedings of SPIE*, vol. 7642, pp. 76420O-1 - 76420O-10, March 2010.
- [8] C. Wallenhauer, B. Gottlieb, R. Zeichfusl and A. Kappel, "Efficiency-Improved High-Voltage Analog Power Amplifier for Driving Piezoelectric Actuators," *IEEE Transactions on Circuits and Systems I Regular Papers*, vol. 57, no. 1, pp. 291-298, 2010.
- [9] A. Abramovitz, C.-S. Liao and K. Smedley, "State-Plane Analysis of Regenerative Snubber for Flyback Converters," *IEEE Transactions on Power Electronics*, vol. 28, no. 11, pp. 5323-5332, 2013.
- [10] G. Chen, Y.-S. Lee, S. Y. R. Hui, D. Xu and Y. Wang, "Actively clamped bidirectional flyback converter," *IEEE Transactions on Industrial Electronics*, vol. 47, no. 4, pp. 770 -779, 2000.
- [11] J. Park, Y.-S. Roh, Y.-J. Moon and C. Yoo, "A CCM/DCM Dual-Mode Synchronous Rectification Controller for a High-Efficiency Flyback Converter," *Power Electronics, IEEE Transactions on*, vol. 29, no. 2, pp. 768-774, 2014.
- [12] M. Karpelson, G.-Y. Wei and R. J. Wood, "Milligram-scale high-voltage power electronics for piezoelectric microrobots," in *Robotics and Automation, 2009. ICRA '09. IEEE International Conference on*, 2009.
- [13] S.-K. Chung, "Transient characteristics of high-voltage flyback transformer operating in discontinuous conduction mode," *IEE Proceedings - Electric Power Applications*, vol. 151, no. 5, pp. 628 - 634, 2004.
- [14] L. Dalessandro, F. da Silveira Cavalcante and J. W. Kolar, "Self-Capacitance of High-Voltage Transformers," *Power Electronics, IEEE Transactions on*, vol. 22, no. 5, pp. 2081 -2092, 2007.
- [15] J. Biela and J. W. Kolar, "Using Transformer Parasitics for Resonant Converters: A Review of the Calculation of the Stray Capacitance of Transformers," *Industry Applications, IEEE Transactions on*, vol. 44, no. 1, pp. 223 -233, 2008.
- [16] L. Dalessandro, F. da Silveira Cavalcante and J. W. Kolar, "Self-Capacitance of High-Voltage Transformers," *IEEE Transactions on Power Electronics*, vol. 22, no. 5, pp. 2081 -2092, 2007.

- [17] J. Muhlethaler, J. Biela, J. W. Kolar and A. Ecklebe, "Improved Core-Loss Calculation for Magnetic Components Employed in Power Electronic Systems," *Power Electronics, IEEE Transactions on*, vol. 27, no. 2, pp. 964-973, 2012.
- [18] J. Muhlethaler, J. Biela, J. W. Kolar and A. Ecklebe, "Core Losses Under the DC Bias Condition Based on Steinmetz Parameters," *Power Electronics, IEEE Transactions on*, vol. 27, no. 2, pp. 953-963, 2012.
- [19] M. Hartmann, H. Ertl and J. W. Kolar, "On the Tradeoff Between Input Current Quality and Efficiency of High Switching Frequency PWM Rectifiers," *Power Electronics, IEEE Transactions on*, vol. 27, no. 7, pp. 3137-3149, 2012.

APPENDIX K

Design and Development of Autonomous High Voltage Driving System for DEAP Actuator in Radiator Thermostat

2014 IEEE Applied Power Electronics Conference and Exposition(APEC 2014)

Design and Development of Autonomous High Voltage Driving System for DEAP Actuator in Radiator Thermostat

Lina Huang, Zhe Zhang and Michael A. E. Andersen

Department of Electrical Engineering

Technical University of Denmark

Oersteds Plads, Building 349, Kgs. Lyngby, Denmark

Email: huang@elektro.dtu.dk, zz@elektro.dtu.dk, ma@elektro.dtu.dk

Abstract— In radiator thermostat applications, DEAP (Dielectric Electro Active Polymer) actuator tends to be a good candidate to replace the conventional self-actuating or step motor based actuator due to its intrinsic advantages. The capacitive property and high voltage (HV) driving demand of DEAP actuator make a high voltage capacitive load driving system to be necessary. The only energy source battery determines it needs to be an autonomous system. The detailed system specifications have been introduced and the corresponding system level design has been proposed. In addition, the detailed design and implementation information has been provided as well, including the power and control stage inside the high voltage converter, the output voltage measurement circuit, the feedback control, etc. Finally, the experimental results have been provided to validate the capability and performance of the driving system.

I. INTRODUCTION

Radiator thermostat is a device, which can automatically adjust the position of heating valve to control the hot water flow in the pipe according to the indoor ambient temperature. It has been employed in the heating system with the purpose of saving energy since the seventies of last century. Currently, inside the thermostat, there are two types of actuator, one is the self-actuating actuator with the issue of inaccurate temperature control as well as the unrealizable remote control, and the other is the step motor actuator with the issue of mechanical noise as well as short battery life time.

With the emergence of various new materials, a class of material, called smart material, has gradually aroused the interest of researchers and engineers due to the intrinsic good properties. As a kind of smart material, DEAP (Dielectric Electro Active Polymer) consisting of a soft silicone elastomer and two compliant metallic electrodes on both sides of the elastomer, can produce large strain when an external electric field is applied [1]. Because of the advantageous characteristics, such as high-resolution motion capability, light

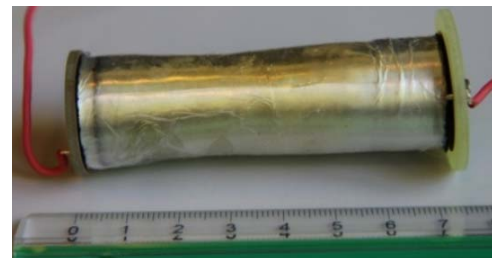


Fig. 1. Current version cylindrical DEAP actuator.

weight and noise-free operation, DEAP material based actuator can be a prosperous alternative to the self-actuating and step motor actuators in the thermostat [2]. With a simple and practical configuration, a cylindrical DEAP actuator, shown in Figure 1, tends to be an appropriately shaped actuator for the thermostat application.

The structure of DEAP implies it is fundamentally a capacitor, which has also been validated through the impedance measurements in [3]. Although the dielectric elastomer is ultra thin, a high stimulating voltage on the electrodes still tends to be necessary to generate a certain amount of electric field in order to produce enough electrostatic force for the deformation [4]. For fully elongating the current version DEAP actuator, the maximum voltage around 2 kV needs to be employed [3]. In order to drive the actuator, a high voltage (HV) driving system with the capability to charge capacitive load to 2 kV and discharge to 0 V needs to be explored, which forms the discussion topic of this paper.

The design specifications as well as the system level based solution are presented in Section II. Based on the system level design, in Section III, detailed design proposals concerning power and control stages inside the HV DC-DC converter, high voltage measurement circuit, super capacitor charger circuit and output voltage tracking control are discussed. The

experimental results in Section IV are used to validate the design as well as the implementation. Finally, a conclusion is given in Section V.

II. DESIGN SPECIFICATIONS AND SYSTEM LEVEL PROPOSAL

A. Design Specifications Discussion

In the electromechanical system, the characteristics and requirements of the mechanical components lead to the acquisition of the design specifications concerning electrical parts.

Inside the radiator thermostat, the 1.5 V AA batteries tend to be the only power source. Two batteries in series can provide 3 V input voltage. The volume of DEAP actuator is a critical criterion from the mechanical point of view. In fact, the mechanical force (F), the applied voltage for actuator (V) and the size of DEAP material (S) have the following relationship

$$F = \varepsilon_0 \cdot \varepsilon_r \cdot S \cdot \left(\frac{V}{d}\right)^2 \quad (1)$$

where ε_0 and ε_r are the permittivity of vacuum and the DEAP material, respectively. d stands for the thickness of the DEAP material. In order to generate enough amount of mechanical force to actuate the heating valve with the minimum volume of the actuator, the stimulating voltage needs to reach the breakdown voltage of the material. For the current version material, it is around 2 kV. Then the size of DEAP material (S) can be used to determine the capacitance of the actuator through the following equation

$$C = \varepsilon_0 \cdot \varepsilon_r \cdot \frac{S}{d} \quad (2)$$

TABLE I. SYSTEM DESIGN SPECIFICATIONS

| Parameters | Specifications |
|------------------------------------------------|--------------------------|
| Input voltage | 3 V |
| Maximum output voltage | 2 kV |
| Capacitance of DEAP actuator | 200 nF |
| Change of output voltage | Follow reference voltage |
| Maximum continuous charging / discharging time | 5 s |
| Energy recovery | Necessary |
| Total system size | As small as possible |

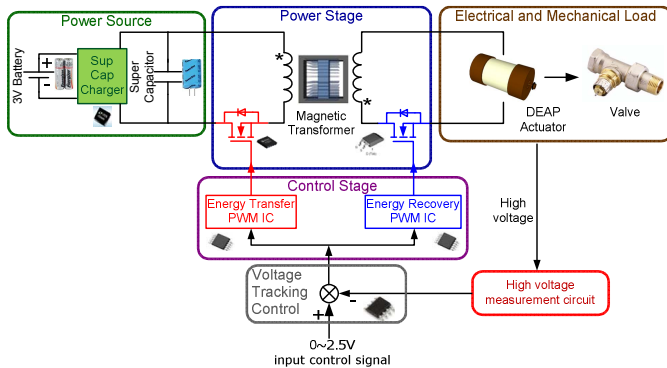


Fig. 2. System level block diagram.

The ambient temperature is the ultimate control object, which can be adjusted through controlling the hot water volume in the radiator. In fact, the position of the heating valve determines the hot water flow in the pipe and can be regulated by the deformation of DEAP actuator. The stroke of actuator versus applied voltage characteristic in [5] indicates that the stimulating voltage is the direct control parameter to the motion position of DEAP actuator. Therefore, the output voltage of the HV DC-DC converter cannot be fixed at a certain value and needs to vary according to the feedback of the temperature close loop control.

Although the heating valve system does not put much pressure on dynamic changes, the system response time still needs to be confined within certain limits. In terms of specifications for the HV driving system, the continuous capacitive load charging or discharging time is demanded in limited time. Considering the intrinsic capacitive property of DEAP actuator, the energy recovery technique is desirable in order to recycle the energy stored in the actuator back to the source when it needs to be released, with the final goal of extending the lifetime of the batteries [5] [6]. The DEAP actuator as well as the entire HV driving system, eventually, needs to be placed inside the thermostat. Due to the limited space, the size of the HV driving system is required to be as small as possible. The specific design requirements are summarized in Table I.

B. Proposal for System Level Solution

According to the aforementioned demands, a system level design solution is proposed and illustrated in Fig. 2. The entire system consists of HV DC-DC converter, including power stage as well as control stage, high voltage measurement circuit, super capacitor and its charger circuit, output voltage tracking control part and the DEAP actuator as well as the heating valve load. From the electrical point of view, the actuator tends to be the terminal load instead of the valve in the mechanical part.

A HV DC-DC converter with the ability to charge and discharge the actuator is the most critical part in this HV driving system. In the case of high step up ratio requirement as well as the capacitive load driving demand, the flyback or piezoelectric transformer (PT) based converter tends to be the appropriate candidates for power stage [7]-[9]. Considering the necessity of recycling the energy back to the power source and maturity of the technology, flyback based solution tends to be more feasible [10] [11]. In addition, in terms of the size issue, the bidirectional flyback topology with only two active semiconductor components is, in fact, a good choice as well. Furthermore, the control for this uncomplicated configuration tends to be more simple and reliable compared to that of the half bridge in PT based solution. Moreover, the flyback solution only needs a low side driver or even an integrated driver inside the control ICs, which is not only beneficial for the space saving, but also for improving the reliability.

Inside the HV converter, the control stage needs to fulfill the energy transfer control, which corresponds to the charging of the actuator, as well as the energy recovery control, which refers to the discharging of the actuator. Due to the limited space as well as the reliability consideration, the commercial

control ICs are suitable to be employed here. When selecting the device, the IC with the ON/OFF function tends to be more desirable, due to the consideration for the voltage feedback loop control. In fact, the control for this HV converter is different from that of normal steady state working converter. Small signal modeling cannot be applied here because of the unfixed output voltage as well as the capacitive property of the load. An ON/OFF control methodology for energy transfer as well as energy recovery, therefore, tends to be more reasonable, as long as the output voltage ripple is within the acceptable limited value.

In order to realize the reference tracking control for the output voltage and considering it is impossible to directly sense the output voltage of HV converter, the HV measurement circuit needs to be designed and implemented. In addition, the measurement circuit tends to play the role of the isolation part between the high output voltage side and the low voltage control side, which is important from the safety point of view.

Currently, the batteries inside the radiator thermostat in the living room are non-rechargeable components, in order to keep consistence, the batteries in this HV driving system are considered to be normal primary cells as well. When actuator needs to be released, the energy stored in actuator is going to be recovered to the primary energy source. Due to the non-rechargeable characteristic of battery cells, another energy storage element - super capacitor, can be employed in the primary side so as to store the recycled energy as well as stabilize the input voltage. However, if the batteries are going to be directly connected to the super capacitor, in the transient time, the unlimited charging current tends to be harmful to both battery cells and super capacitor. In order to avoid this issue, a super capacitor charging circuit with current limit function, therefore, needs to be employed.

Output voltage tracking control part is different from the PI controller in the steady state working converter, which mainly focuses on regulating the output voltage to the set point. Since the only load for this HV driving system is a purely capacitive actuator, the output voltage will increase only if there is current to charge the load, and vice versa. Theoretically, the output voltage will not drop since there is no resistive load to discharge the energy stored in the actuator if the leakage current through the actuator itself, the HV measurement circuit as well as the HV semiconductor devices inside HV converter is neglected. Actually, the output of the voltage tracking control part tends to provide the control signal for HV converter. Combining the aforementioned description of control stage inside the HV converter, the control signal needs to be high-low level signal in order to start or stop the working of the energy transfer control IC as well as energy recovery control IC.

Due to the necessity of driving active semiconductor devices inside the HV converter and considering the only 3 V battery source, a commercial boost converter IC with the ability to boost 3 V input voltage to 10 V is employed with the purpose of saving space. In addition, in order to provide power for other ICs which need 5 V supply voltage, another boost converter IC is employed as well. However, the

auxiliary power part tends to be simple as a result of adopting the commercial ICs, which will not be discussed in the detailed design and implementation section in this paper.

III. DETAILED DESIGN PROPOSAL AND IMPLEMENTATION

The detailed design and implementation part tends to discuss the realization of the HV converter, including the power stage as well as the control stage, the design of HV measurement circuit, the selection of the super capacitor and its charger circuit and the implementation of the output voltage tracking control in detail.

A. High Voltage Converter Power Stage

In the system level discussion, compared to other alternative solutions, the bidirectional flyback topology tends to be more reasonable for the power stage in the HV converter. The configuration of the power stage with critical parasitic elements is shown in Fig. 3 and the fundamental working principles can refer to [5].

As the steady state working bidirectional flyback or synchronous rectifier based flyback converter, two active semiconductor devices Q_1 and Q_2 are employed. In the secondary side, due to the poor performance of body diode inside HV MOSFET Q_2 , D_{21} is adopted in order to block the current through the body diode of Q_2 and D_{22} provides the freewheeling path for the secondary current.

Considering the voltage stress issue for semiconductor components in a flyback converter caused by parasitic elements, in general, RC snubber or RCD clamp circuit needs to be employed. Due to the limited space constraint, RC snubber methodology tends to be more desirable for the primary side. Therefore, R_{sr} and C_{sr} are introduced. In terms of charging ability, i.e. the maximum achievable charging output voltage, as well as the efficiency, any extra capacitor needs to be avoided in the secondary side. Therefore, neither RC snubber nor RCD clamp is employed in the secondary side. In order to guarantee the reliable operation, HV MOSFET with sufficient voltage rating needs to be selected.

As the normal steady state working DC-DC converters, two loops based control, i.e. the outer output voltage control loop and inner current control loop, is employed for this autonomous system as well, in spite of the variable output voltage. Considering the reliability as well as the easy implementation, peak current control tends to be desirable here. Two current sensing resistors RP_1 and RP_2 , therefore, are

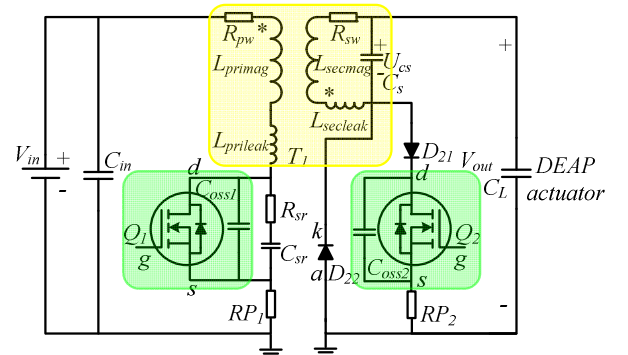


Fig. 3. Configuration of power stage in HV converter.

employed in primary and secondary side, respectively.

In fact, for the uncomplicated flyback based converter, the flyback transformer, i.e. the coupled inductor, tends to be the most critical part in the converter in terms of complexity of design as well as implementation.

In general, it is not reasonable to design the transformer alone without considering the limitation of control IC. It is well known that all the ICs have finite bandwidth and take time to react in spite of the increasingly tiny response time. When operating in the energy recovery mode under maximum output voltage, the time to achieve the set point of secondary peak current $I_{secpeak}$, i.e. $T_{secpeakmin}$, needs exceed the minimum response time $T_{responsemin}$ of the control IC, illustrated in the following equation

$$T_{secpeakmin} = \frac{L_{sec}}{V_{outmax}} \cdot I_{secpeak} \geq T_{responsemin} \quad (3)$$

where V_{outmax} is the maximum output voltage and L_{sec} stands for the secondary inductance. In fact, (3) provides a constraint for the design of the transformer, and considering the high output voltage, the value of L_{sec} cannot be too small.

Due to the energy storage requirement in the flyback transformer, the air gap in the core is needed. If neglecting the magnetic resistance introduced by magnetic material and only considering the magnetic resistance caused by the air gap, the secondary inductance L_{sec} can be expressed by

$$L_{sec} = \frac{N_{sec}^2 \mu_0 A}{l_{gap}} \quad (4)$$

where N_{sec} is the number of turns for secondary winding, μ_0 stands for the vacuum permeability, A and l_{gap} are the core cross-sectional area and the length of the air gap, respectively.

In order to have large value of L_{sec} , increasing N_{sec} or A or decreasing l_{gap} tends to be possible solutions. It is not desired to have a large number of turns or big size core, because of the small size requirement. In addition, considering the same bobbin space, less secondary turns may lead to lower stray capacitance of secondary winding, which will be beneficial for the charging ability as well as the efficiency. The decrease of length of the air gap seems to be more feasible. Yet, this will increase the risk of saturating the core if other parameters are kept the same, illustrated in the following equation

$$B_{max} = \frac{N_{sec} I_{secpeak}}{l_{gap}} \quad (5)$$

where B_{max} stands for the maximum flux density.

In addition, if N_{sec} has been decided, turns ratio N_{ratio} , with the definition in the (6), tends to be a critical parameter in terms of determining the voltage rating of Q_I , shown in (7), as well as calculating the turn-on time of Q_I in the charging process, shown in (8).

$$N_{ratio} = \frac{N_{sec}}{N_{pri}} \quad (6)$$

$$V_{Q1dsmax} = V_{in} + \frac{V_{outmax}}{N_{ratio}} \quad (7)$$

$$T_{Q1on} = \frac{L_{pri} I_{pripeak}}{V_{in}} = \frac{L_{sec} I_{pripeak}}{N_{ratio}^2 V_{in}} \quad (8)$$

where N_{pri} is the number of turns for primary winding. $V_{Q1dsmax}$ and V_{in} are the theoretical maximum drain to source voltage of Q_I without considering the transient behavior and input voltage, respectively. L_{pri} and $I_{pripeak}$ stand for primary inductance, including magnetizing inductance L_{primag} as well as leakage inductance $L_{pripeak}$ and set point of primary peak current, respectively.

Through (7) and (8), it seems that a larger number of turns ratio tends to be beneficial for the voltage rating of the primary MOSFET as well as to increase the operating frequency in the charging process if boundary control mode scheme is employed in the control IC. However, this will lead to smaller amount of stored transferrable energy in the transformer per switching cycle if $I_{pripeak}$ keeps constant and eventually the inequality (9) cannot be satisfied.

$$\frac{1}{2} \cdot L_{primag} \cdot I_{pripeak}^2 > \frac{1}{2} \cdot C_s \cdot V_{outmax}^2 \quad (9)$$

where C_s stands for the stray capacitance of the transformer secondary winding. The right part of (9) indicates the energy stored in C_s under maximum output voltage. Actually, if the energy stored in the transformer is not sufficient to charge C_s to the current output voltage, the voltage will not increase any longer. The selection of N_{ratio} , therefore, tends to be a trade off issue as well.

According to the aforementioned design constraints of flyback transformer, combining with the try-and-error methodology, a transformer design proposal without optimization has been achieved. The detailed design parameters are listed in Table II.

When implementing this HV transformer, how to arrange the winding and guarantee the insulation need to be taken into consideration. Between adjacent layers, the 0.1 mm kapton tape is introduced. And between windings, two layers of kapton tape are employed in order to provide a reinforced insulation. In addition, considering the easy realization for the winding structure as well as the insulation, 0.15 mm margin tape is adopted at both edges of the bobbin. Furthermore, compared with U-winding structure, Z-winding methodology tends to be more beneficial in terms of reducing C_s and has been applied in this case. AWG32 and AWG 29 wires are employed for primary and secondary winding, respectively. Because the insulation occupied more space than estimated,

TABLE II. HV FLYBACK TRANSFORMER DESIGN PROPOSAL

| Parameters | Values |
|---------------|------------------------|
| N_{pri} | 6 |
| N_{sec} | 240 |
| N_{ratio} | 40 |
| l_{gap} | 90 μ m |
| $I_{pripeak}$ | 4 A |
| $I_{secpeak}$ | 100 mA |
| B_{max} | 266 mT |
| L_{pri} | 13.9 μ H |
| L_{sec} | 22.2 mH |
| Core type | EF20 |
| Core material | Ferrite N27 from EPCOS |

eventually, only 232 turns of secondary winding can be arranged inside the bobbin. The final winding configuration of HV flyback transformer has been depicted in Fig. 4.

After the realization of the transformer, the actual values of the inductances, winding resistances, including primary winding resistance R_{pw} and secondary winding resistance R_{sw} , as well as the critical parasitic elements can be measured and has been summarized in Table III. Actually, the primary leakage inductance $L_{prileak}$ and secondary leakage inductance $L_{secleak}$ cannot exist simultaneously. $L_{prileak}$ is the indication for the untransferrable energy stored in transformer when energy flows from primary to secondary side. The same applies to $L_{secleak}$.

In fact, the measured values of leakage inductances can be used to estimate the maximum voltage spikes. In the worst case consideration, all the energy stored in leakage inductance will transfer to the output capacitance of MOSFETs and eventually generate a voltage spike in the transient time when switching off the active semiconductor components. The spike voltage evaluation equations are illustrated in (10) and (11) for

Q_1 and Q_2 , respectively.

$$V_{Q1spike} = \sqrt{\frac{L_{prileak}}{C_{oss1}}} \cdot I_{pripeak} \quad (10)$$

$$V_{Q2spike} = \sqrt{\frac{L_{secleak}}{C_{oss2}}} \cdot I_{secpeak} \quad (11)$$

where $V_{Q1spike}$ and $V_{Q2spike}$ are the estimated maximum spike voltage for Q_1 and Q_2 . C_{oss1} and C_{oss2} stand for the output capacitances of Q_1 and Q_2 , respectively.

Considering the spike voltage, it is possible to predict the maximum drain to source voltage for MOSFETs and finally provide a guide in the selection of the proper semiconductor devices. The current sensing resistor tends to be chosen based on the consideration of its power dissipation as well as the requirement of the control IC. The methodology for determining the parameters of the RC snubber circuit can refer to [12]. Eventually, all the components in the power stage of HV converter are summarized in Table IV.

B. High Voltage Converter Control Stage

As previously mentioned, the HV converter control stage is responsible for the energy transfer control as well as energy recovery control. The commercial IC with the function of ON/OFF and peak current control tends to be a desirable candidate in this case. Considering the similarity of charging a photoflash capacitor and a pure capacitive actuator, the on shelf capacitor charger controller LT3750 from Linear Technology must be a good choice in terms of space saving as well as easy implementation [13].

1) Energy Transfer Control

According to the datasheet of LT3750, its default boundary mode control scheme tends to be desirable for the energy transfer control in terms of maximizing the charging efficiency as well as reducing the continuous charging time. The detailed configuration for LT3750 in energy transfer control is illustrated in Fig. 5 and values for the components are listed in Table V.

Normally, whether the IC is working, i.e. whether the converter is charging the capacitive load is dependent on the voltage level of CHARGE pin. The IC, however, can also stop working when the set-up maximum output voltage is reached, which is determined by the resistors R_{I1} and R_{I2} . Although this voltage limitation function will not be expected to work in the normal operation, the proper parameter selection of R_{I1} and R_{I2} will provide an over voltage protection when the overcharging of the output voltage happens to the converter. The boundary current control is realized by means of detecting the discontinuous mode through R_{I3} from the drain of Q_1 and starting a new switching cycle. The suitable value of R_{I3} is desired in order to guarantee the proper detection of discontinuous mode.

When implementing this charging control circuit, the bypass capacitors C_{I4} and C_{I5} need to be as close as possible to the corresponding IC pins in the layout of the PCB. The same rule applies to C_{I1} , C_{I2} and C_{I3} , which are responsible for filtering the interference spike into the IC with the final purpose of guaranteeing the normal operation of the IC.

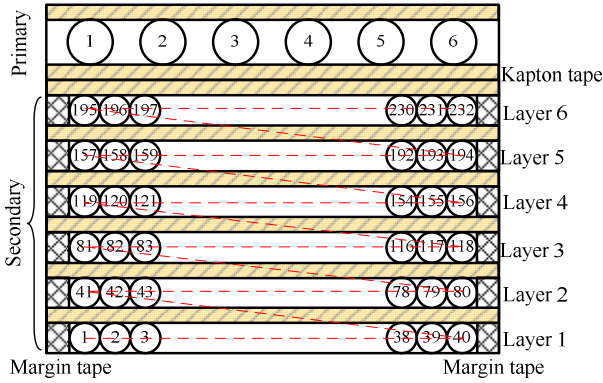


Fig. 4. Winding configuration of HV flyback transformer.

TABLE III. HV FLYBACK TRANSFORMER MEASUREMENT DATA

| Parameters | Values |
|---------------|-----------------------------------------------------------|
| L_{pri} | 13 μ H |
| L_{sec} | 18.85 mH |
| R_{pw} | 79.4 m Ω -106.81 m Ω @ f = 1kHz-100kHz |
| R_{sw} | 4.99 Ω -29.92 Ω @ f = 1kHz-100kHz |
| $L_{prileak}$ | 300 nH |
| $L_{secleak}$ | 450 μ H |
| C_s | 14.2 pF |

TABLE IV. HV CONVERTER POWER STAGE COMPONENTS LIST

| Component Name | Device | Critical Parameters | Vendor |
|----------------------|-----------------|---------------------|----------|
| Q_1 | BSC320N20NS3 G | V_{DSS} = 200 V | INFINEON |
| Q_2 | IXTV03N400S | V_{DSS} = 4 kV | IXYS |
| D_{21} D_{22} | VMI6525 | V_{RWM} =5 kV | VMI |
| RP_1 | LVK12R020FER | 20 m Ω 1% | OHMITE |
| RP_2 | RC1206FR-101RL | 1 Ω 1% | YAGEO |
| R_{sr} | RE1206DR-0768RL | 68 Ω 0.5% | YAGEO |
| C_{sr} | 12062A221JAT2A | 220 pF 200 V | AVX |

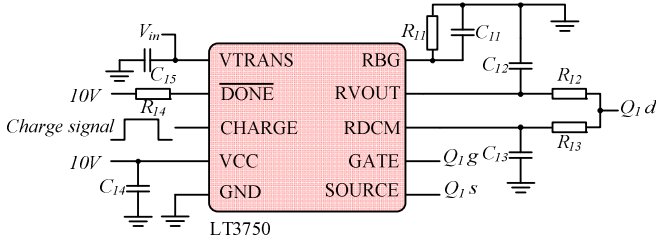


Fig. 5. Energy transfer control configuration scheme.

TABLE V. COMPONENTS LIST FOR ENERGY TRANSFER CONTROL

| Components | Values |
|----------------------------|-------------------------|
| R_{11} | 2.49 k Ω 1% 0402 |
| C_{11} | 100 pF 50 V 0402 |
| R_{12} R_{13} R_{14} | 100 k Ω 1% 0402 |
| C_{12} C_{13} | 10 pF 500 V 1206 |
| C_{14} C_{15} | 10 μ F 16 V 0603 |

2) Energy recovery control

LT3750 tends to be desirable candidate in the energy recovery control as well due to its ON/OFF as well as peak current control function.

Unlike energy transfer control, the default boundary mode control scheme of LT3750 cannot be the desired solution for energy recovery control. Firstly, the very high drain to ground voltage of Q_2 prevents RDCM pin from connecting to the drain of Q_2 . In addition, when recycling the energy from the DEAP actuator, the load in the energy transfer control is switched to be energy source and needs to provide the voltage signal through VTRANS pin. However, this configuration cannot be achieved due to the extremely high output voltage compared to the voltage rating of IC pins. Furthermore, suppose RDCM and VTRANS pin can endure the high voltage, the detection of discontinuous mode in the boundary mode control may fail due to the sensitivity and noise issues in the high voltage side. Moreover, the continuous discharging time is not important concern and the discharging efficiency will be hardly affected by the control methodology in this case.

In fact, compared to the continuous conduction mode (CCM) control scheme, the fixed frequency discontinuous conduction mode (DCM) control method is more feasible for energy recovery control, considering the complete energy transfer characteristic in each switching cycle. It is, however, not straightforward to apply LT3750 to fixed frequency mode. Actually, an additional oscillator LTC1799 from Linear Technology as well, has been employed in order to achieve the fixed frequency control [14]. The detailed configuration for energy recovery control is shown in Fig. 6 and values for corresponding components are summarized in Table VI.

In order to guarantee the DCM operation in the entire discharging process, the fixed switching frequency f_{sw} needs to be less than the estimated lowest cyclical working frequency, illustrated in (12).

$$f_{sw} \leq \frac{8 \cdot \pi \cdot \sqrt{L_{sec} \cdot C_L} \cdot V_{in}}{V_{in} + 8 \cdot \pi \cdot \sqrt{L_{sec} \cdot C_L} \cdot L_{primag} \cdot N_{ratio} \cdot I_{sepeak}} \quad (12)$$

where C_L stands for the capacitance of DEAP actuator.

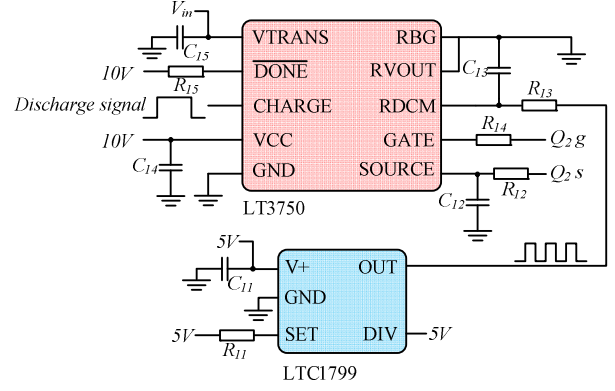


Fig. 6. Energy transfer control configuration scheme.

TABLE VI. COMPONENTS LIST FOR ENERGY RECOVERY CONTROL

| Components | Values |
|-------------------|------------------------|
| R_{11} R_{15} | 100 k Ω 1% 0402 |
| C_{11} | 100 nF 25 V 0603 |
| R_{12} | 68.1 Ω 1% 0402 |
| C_{12} | 1 nF 50 V 0402 |
| R_{13} | 1 k Ω 1% 0402 |
| C_{13} | 100 pF 50 V 0402 |
| R_{14} | 30.1 Ω 1% 1206 |
| C_{14} C_{15} | 10 μ F 16 V 0603 |

The nonnegligible secondary winding stray capacitance C_s as well as the high output voltage will introduce a huge voltage spike RP_2 due to the large transient charging current through C_s when switching on the secondary MOSFET Q_2 . Through SOURCE pin, this spike is very likely to fail the IC and must be suppressed before going into it. One of the feasible and space saving solutions tends to be the RC filter. In order to effectively filter the spike without severely affecting the normal peak current detection, the proper parameters need to be determined. In addition, the introduction of the gate drive resistor can be beneficial for reducing the spike voltage.

The PCB layout considerations mentioned in the energy transfer control part need to be satisfied for energy recovery control as well.

C. High Voltage Measurement Circuit

In general, resistor divider tends to be suitable in the voltage measurement circuit. In this HV application, however, the capacitor divider needs to be employed in parallel with the resistor divider in order to eliminate the influence caused by the parasitic capacitors [15]. The configuration for HV measurement circuit is depicted in Fig. 7. In order to realize the frequency independent operation for the circuit, the following equation needs to be fulfilled [15].

$$R_1 \cdot C_1 = R_2 \cdot C_2 \quad (13)$$

where R_1 and R_2 are the resistances for the resistor divider, and C_1 and C_2 are the capacitances for the capacitor divider. The component values for HV measurement circuit are summarized in Table VII.

Due to the low impedance introduced by the output voltage tracking controller, it is unreasonable to directly

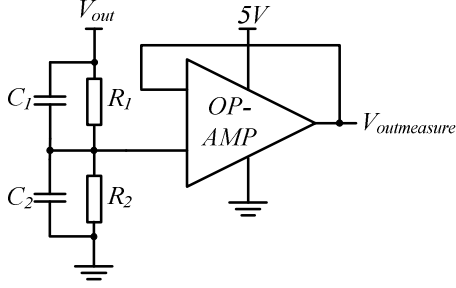


Fig. 7. Schematic of HV measurement circuit.

TABLE VII. COMPONENTS LIST FOR ENERGY TRANSFER CONTROL

| Components | Values |
|------------|---------------------------|
| R_1 | 5 G Ω 3 kV 1% 2512 |
| C_1 | 47 pF 3 kV NPO 1808 |
| R_2 | 5 M Ω 1% 0805 |
| C_2 | 47 nF COG 0805 |
| OP-AMP | OPA365AIDBVT |

connect the measured output voltage to the controller. Therefore, an OP-AMP with high input impedance needs to be employed between the dividers and controller as a buffer.

D. Super Capacitor Selection and its Charger Circuit

The necessity to employ the super capacitor has already been declared in the system level design. The capacitance of the super capacitor, C_{supcap} , can be determined by the maximum energy stored in the actuator, the energy recovery efficiency $\eta_{recovery}$ as well as the maximum allowed voltage rise over the super capacitor ΔV_{supcap} , illustrated in (14).

$$C_{supcap} \geq \frac{\frac{1}{2} C_L V_{outmax}^2 \eta_{recovery}}{\frac{1}{2} (V_{supcap} + \Delta V_{supcap})^2 - \frac{1}{2} V_{supcap}^2} \quad (14)$$

where V_{supcap} is the stable voltage for super capacitor and nearly equals to voltage from the batteries.

In order to limit the inrush current when connecting the batteries to the super capacitor, a super capacitor charger IC, LTC4425, with the function of current limitation from Linear Technology is necessary to be employed. The typical configuration in the datasheet can be directly applied, therefore, no detailed information concerning the super capacitor charger circuit will be shown here [16].

E. Output Voltage Tracking Control

In terms of size as well as flexibility, microcontroller tends to be a proper candidate to fulfill output voltage tracking control. Considering the space constraint, an 8-pin low-cost microcontroller MSP430G2230 from Texas Instrument tends to be suitable in this case [17].

Due to the ON/OFF control requirement of the HV converter control stage, the hysteresis control methodology with only high-low signal output, tends to be a good choice for the output voltage tracking control. The detailed implementation of the control algorithm can be illustrated in Fig. 8. The used parameters and registers need to be defined in initialization part and the delay part is introduced to guarantee the fully charge of the super capacitor. An infinite loop needs

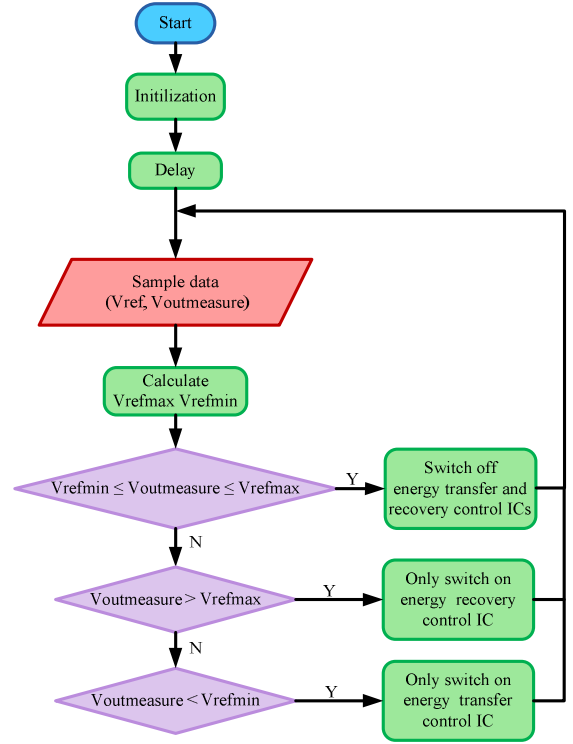


Fig. 8. Flow diagram for output voltage tracking control.

to be employed in order to achieve the continuous operation of the program. At the beginning of each loop, the reference voltage V_{ref} as well as the measured output voltage $V_{outmeasure}$ needs to be sampled. Thus, the upper limit and lower limit of reference voltage in a hysteresis control can be obtained through calculation. The fundamental idea of this algorithm is simple: if $V_{outmeasure}$ is within the limitation of hysteresis, the energy transfer as well as energy recovery control IC needs stop operation; otherwise if $V_{outmeasure}$ is larger than the upper limit, the energy recovery IC starts to work; and once $V_{outmeasure}$ is smaller than the lower limit, the energy transfer IC needs to operate in order to charge the capacitive load.

F. System Integration

For the whole system, there are two PCBs: one is for the super capacitor and its charger circuits, all the other parts including the HV converter power as well as control stage, HV measurement circuit, microcontroller and auxiliary power circuits are accommodated in another PCB. The implemented autonomous HV driving system for DEAP actuator is shown in Fig. 9.

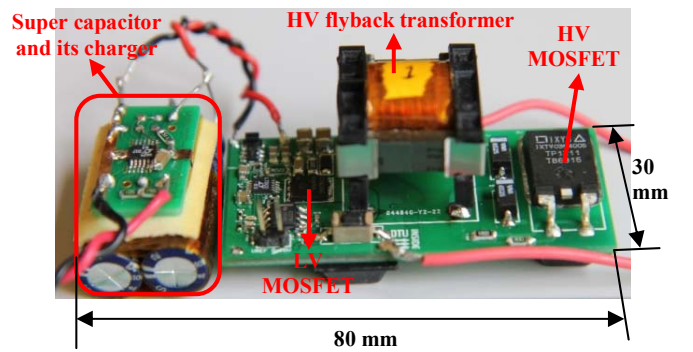


Fig. 9. Picture of the autonomous HV driving system.

IV. EXPERIMENTAL VALIDATION

Experiments need to be carried out in order to verify the design as well as the implementation of this HV driving system.

The charging as well as the discharging ability of the HV converter can be validated through Fig. 10. In order to achieve maximum 2 kV for the output voltage, the continuous charging time is around 600 ms, and the corresponding continuous discharging time is nearly 300 ms. The input voltage has a slight decrease in the energy transfer process and has nearly no increase in the energy recovery process due to the low energy recovery efficiency.

The output voltage tracking ability can be verified in Fig. 11. It is obvious that the measured output voltage $V_{outmeasure}$ can follow the reference voltage V_{ref} well. However, due to the inaccuracy issue caused by the HV measurement circuit, the real output voltage V_{out} is slightly lower than the corresponding $V_{outmeasure}$. The magnitude of the error is around 100 V under 2 kV output voltage condition, which can still be accepted.

V. CONCLUSION

DEAP actuator tends to be a good choice to replace conventional actuators in the radiator thermostat applications due to the intrinsic good properties. This paper presents the design and implementation of an autonomous HV driving

system for DEAP actuator in system level as well as in detailed design level.

Different parts in the driving system, including the HV converter power and control stage, HV measurement circuit, input super capacitor and its charger circuit as well as the realization of the output voltage tracking control is discussed in detailed.

Finally, the experiments have been performed to validate the charging and discharging ability for the HV converter as well as the output voltage tracking function for the entire HV driving system.

REFERENCES

- [1] R. Jones, P. Wang; B. Lassen, and R. Sarban, "Dielectric elastomers and compliant metal electrode technology," in *IEEE 15th Mediterranean Electrotechnical Conference*, 2010, pp. 368-373.
- [2] R. Sarban, B. Lassen, and M. Willatzen, "Dynamic Electromechanical Modeling of Dielectric Elastomer Actuators With Metallic Electrodes," *IEEE/ASME Transactions on Mechatronics*, vol. 17, pp. 960-967, 2012.
- [3] T. Andersen, L. Huang, M. A. E. Andersen, and O. C. Thomsen, "Efficiency of capacitively loaded converters," in *38th Annual Conference on IEEE Industrial Electronics Society (IECON)*, 2012, pp. 368-373.
- [4] R. Sarban, and R. W. Jones, "Physical model-based active vibration control using a dielectric elastomer actuator," *Journal of Intelligent Material Systems and Structures*, vol. 23, pp. 473-483, 2012.
- [5] L. Huang, L.; P. Thummala, Z. Zhang, and M. A. E. Andersen, "A Battery powered high output voltage bidirectional flyback converter for cylindrical DEAP actuator," in *IEEE International Power Modulator and High Voltage Conference (IPMHVC)*, 2012, pp. 454-457.
- [6] M. J. Tryson; R. Sarban, and K. P. Lorenzen, "The dynamic properties of tubular DEAP actuators," in *Proceedings of SPIE*, vol. 7642, 2010.
- [7] L. Huang, Z. Zhang, and M. A. E. Andersen, "A review of high voltage drive amplifiers for capacitive actuators," in *47th International Universities Power Engineering Conference (UPEC)*, 2012, pp. 1-6.
- [8] J. Elmes; C. Jourdan; O. Abdel-Rahman, and I. Batarseh, "High-Voltage, High-Power-Density DC-DC Converter for Capacitor Charging Applications," in *IEEE 2009 Applied Power Electronics Conference and Exposition (APEC)*, 2009, pp. 433-439.
- [9] S. Y. Tseng; C. M. Yang; K. C. Wang, and G. W. Hsu, "High voltage generator using boost/flyback hybrid converter for stun gun applications," in *IEEE 2010 Applied Power Electronics Conference and Exposition (APEC)*, 2010, pp. 1849-1856.
- [10] H. H. Chung; W. L. Cheung, and K. S. Tang, "A ZCS bidirectional flyback DC/DC converter," *IEEE Transactions on Power Electronics*, vol. 19, no. 6, pp. 1426-1434, Nov. 2004.
- [11] G. Chen; Y. S. Lee; S. Hui, D. Xu, and Y. Wang, "Actively clamped bidirectional flyback converter," *IEEE Transactions on Industrial Electronics*, vol. 47, no. 4, pp. 770-779, Aug. 2000.
- [12] R. Ridley, "Flyback converter snubber design," *Switching Converter Magazine*, 2005.
- [13] "LT3750 capacitor charger controller datasheet", *Linear Technology Corporation*, USA.
- [14] "LTC1799 1kHz to 33MHz resistor set SOT-23 oscillator datasheet", *Linear Technology Corporation*, USA.
- [15] T. Andersen, M. S. Rødgaard, O. C. Thomsen, and M. A. E. Andersen, "Low voltage driven dielectric electro active polymer actuator with integrated piezoelectric transformer based driver," in *Proceedings of SPIE*, vol. 7976, 2011.
- [16] "LTC4425 linear supercap charger with current-limited ideal diode and V/I monitor datasheet", *Linear Technology Corporation*, USA.
- [17] "MSP430G22x0 mixed signal microconller datasheet", *Texas Instruments Incorporated*, USA.

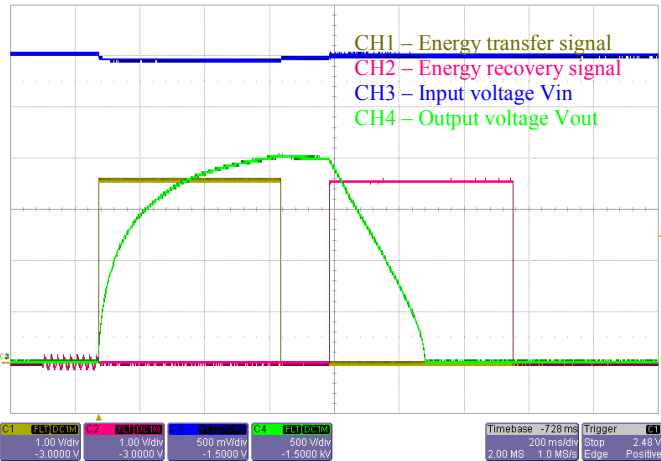


Fig. 10. Continuous charging and discharging process of HV converter.

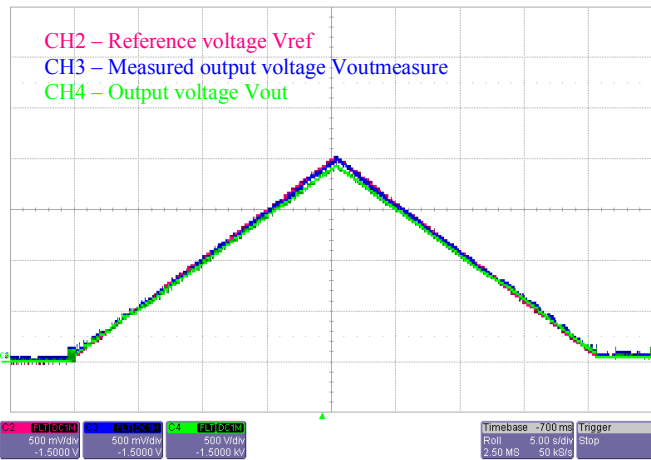


Fig. 11. Output voltage tracking ability validation for HV driving system.

APPENDIX L

Design Comparison of Autonomous High Voltage Driving System for DEAP Actuator

*2014 International Power Electronics and Application Conference and Exposition
(PEAC 2014)*

Design Comparison of Autonomous High Voltage Driving System for DEAP Actuator

Lina Huang, Riccardo Pittini, Zhe Zhang and Michael A. E. Andersen

Department of Electrical Engineering

Technical University of Denmark

Oersteds Plads, Building 349, Kgs. Lyngby, Denmark

Email: huang@elektro.dtu.dk, ripit@elektro.dtu.dk, zz@elektro.dtu.dk, ma@elektro.dtu.dk

Abstract—As a new type of smart material, the Dielectric Electro Active Polymer (DEAP) is introduced in terms of configuration, working principle and potential applications. The design of an autonomous high voltage driving system for DEAP actuator is investigated. The system configuration and the design methodology of a high voltage converter are discussed in detail. Based on the heating valve application, three different high voltage converter solutions have been proposed. The different proposals have been compared in terms of energy loss, volume and cost. Finally, the design selection suggestions are provided to be a reference for the future designers.

Keywords—high voltage, driving system, DEAP actuator, autonomous, design comparison

I. INTRODUCTION

With the advancement of material science, recently, a new kind of smart material, called DEAP (Dielectric Electro Active Polymer) material, increasingly arouses concerns from academia and industry [1-2]. The chemists and material scientists are focusing on improving the performance of the material. Mechanical researchers are investigating possible configurations based on the material as well as the various application occasions. Mathematicians are making effort to establish the math model for DEAP and to build the simulation toolbox. In order to properly utilize the DEAP material, electrical researchers are trying to design and develop highly efficient, small size and low cost electronics circuits.

DEAP material has similar structure to that of the capacitor – the soft dielectric silicone polymer is placed between the compliant electrodes. In most operation cases, the material can be considered with purely capacitive property. When voltage difference is applied on the conducting plates, according to Coulomb's law, a certain amount of electrostatic force is induced, which compresses the flexible insulation layer in thickness direction and expands the size of the polymer. The basic configuration and the working principle are illustrated in Fig. 1. According to this characteristic, DEAP material can be utilized to form an actuator [3]. In addition, when the material is stretched, the capacitance changes accordingly, which enables the material to be a sensor. Furthermore, by using the reverse energy conversion of actuation, the material can be used to constitute a generator, which can transform the mechanical energy to electrical energy.

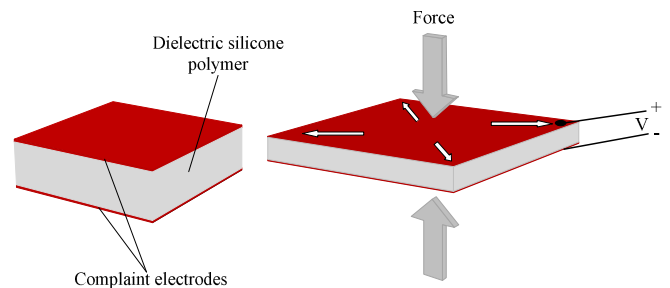


Fig. 1. Basic structure of DEAP material and the illustration of its fundamental working principle.

When applying DEAP based actuator, compared to its conventional counterparts, such as the hydraulic, pneumatic and electromagnetic actuators, it is much lighter and with noise free operation as well as faster electromechanical response speed [4]. This kind of actuator is especially suitable for weight and noise sensitive applications, such as aerospace industry, automobile industry and dwelling space.

In order to design and develop a feasible DEAP actuation system especially in the autonomous applications, not only the compact DEAP actuator is needed, but the highly efficient, small size and low cost driving system for the actuator is required as well. The recent research progress of the material indicates, for the current version of DEAP material, the voltage to fully elongate the actuator needs to reach 2 kV. A high output voltage converter with high efficiency, compact size and low cost design, therefore, needs to be investigated. These general requirements for power electronics converters, however, are normally contradictory. In general, it is impossible to achieve the small volume converter with lowest cost and highest efficiency. The trade-off evaluation needs to be carried out in order to achieve the optimum design. The high driving voltage and the capacitive load property make the design methodology of DEAP actuator driving converter diverse from that of the conventional low output voltage steady-state operation converters.

In this paper, the autonomous driving system and the high voltage converter design are discussed. Different design solutions are proposed for a specific application. The solutions are compared in terms of energy consumption, volume and cost to summarize the design selection suggestions for future use.

II. AUTONOMOUS HIGH VOLTAGE CAPACITIVE ACTUATOR DRIVING SYSTEM DESIGN METHODOLOGY DISCUSSION

A. System Configuration

The autonomous high voltage DEAP actuator driving system consists of five major parts: the power source, the high voltage converter, a DEAP actuator, a terminal mechanical load and the system level sensing and control unit. Considering different terminal application cases, the entire driving system is depicted in Fig. 2.

In autonomous situation, battery normally tends to be the only energy source. The capacitive property of the actuator and the low electrical energy to mechanical work transformation efficiency result in that most effective energy is stored in the actuator [5]. In such case, the introduction of the energy recovery technique is beneficial in improving the energy utilization on the system level. In order to deal with the recycled energy in a highly dynamic condition and to stabilize the input voltage for the high voltage converter, a dynamic energy storage element, such as a super capacitor, need to be employed.

A high voltage DC-DC converter transforms the low voltage from the power source to high output voltage in order to drive the DEAP actuator. The converter consists of three parts: the power stage to provide the energy path, the control stage to generate the PWM signal and realize the inner current loop control and the auxiliary power supplies to provide power for the ICs employed in the control stage.

As an electromechanical device, a DEAP actuator transform the electrical energy from high voltage converter to mechanical force in order to actuate the terminal mechanical load, such as the aircraft wind flap, automotive mirror or indoor heating valve, etc. The connection between the high voltage converter and the actuator is electrical, while actuator and mechanical load are mechanically coupled.

The ultimate goal of the system is to regulate the terminal control parameter, such as the displacement, rotation angle or temperature according to the requirement. To achieve this goal, the feedback control of terminal parameter needs to be implemented with the help of corresponding sensors. Alternatively, if the relationship between the terminal control parameter and the output voltage of high voltage converter is known, and the terminal parameter cannot easily be obtained, with the help of high voltage sensing circuit, the output voltage closed loop control can be employed to replace the terminal parameter based feedback control. The measurement of high voltage normally consumes large amount of energy and is not desired in the autonomous system with limited energy resource. If the output voltage has the relationship with other parameter, such as the charging time considering the capacitive property of the actuator, the other parameter based open loop control can be beneficial for saving energy.

In this paper, the attention will be focused on the critical electrical part in this entire electromechanical coupling system, i.e. the high voltage DC-DC converter.

B. High Voltage Converter Design Discussion

Traditionally, flyback converter has been employed to achieve high output voltage and high step-up ratio. Recently, with the penetration of piezoelectric technology, the piezoelectric transformer (PT) based converter tends to be another option in the field of low power high voltage generation. Even though, for the same output voltage level, the PT can be much smaller than the traditional flyback transformer, the extra space and cost for more active semiconductor devices and the complex control circuits in the PT based solution make the flyback topology to be a more reasonable choice in the current stage of product development.

1) High voltage flyback topology discussion

As aforementioned, the energy recovery technique can be applied to improve the overall efficiency. Shown in Fig. 3 a),

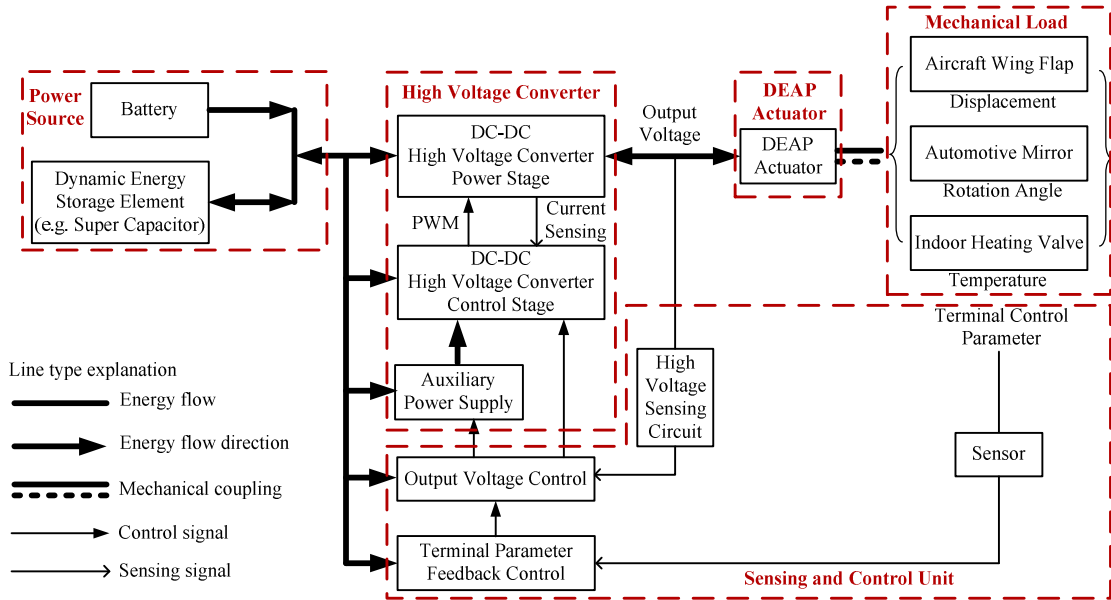
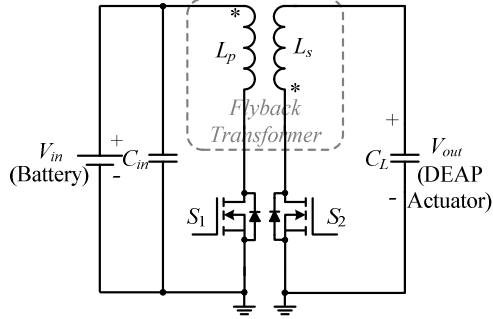


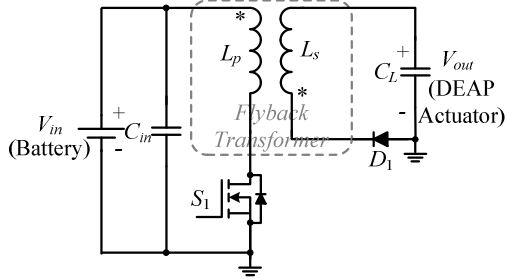
Fig. 2. System level configuration of autonomous high voltage DEAP actuator driving system with terminal loads.

the traditional bidirectional flyback topology which can provide the path for the energy flow back and forth, therefore, can be one option for the power stage in the high voltage converter. However, the active semiconductor component in the secondary side and the control circuits to realize the energy recovery introduce extra cost, space occupation and energy consumption. The unidirectional flyback topology, shown in Fig. 3 b), therefore, tends to be another option in some cases.

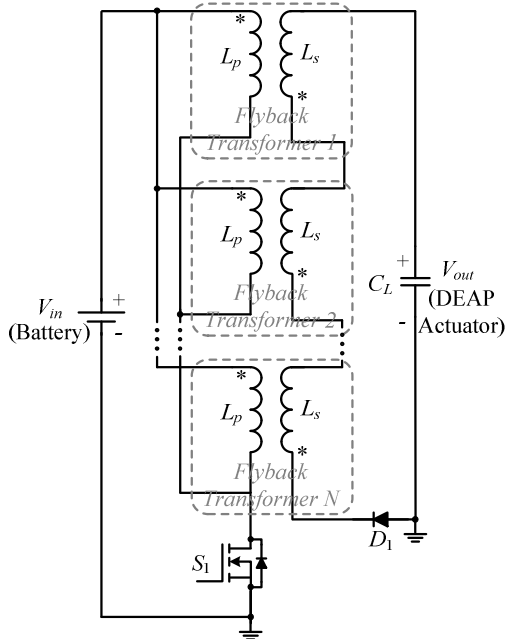
The large number of windings in the high voltage transformer leads to high self-capacitance of the winding [6].



a) Bidirectional flyback topology



b) Unidirectional flyback topology



c) Primary parallel secondary series flyback topology

Fig 3. High voltage converter topologies.

In the capacitive load charging application, the high winding stray capacitance results in lower achievable output voltage, longer charging time as well as lower charging efficiency. One possible solution to weaken the influence of this capacitance is proposed, i.e. the multiple flyback transformer based topology with primary windings in parallel and secondary windings in series, shown in Fig. 3 c) [7]. If the self-capacitance of secondary winding for one transformer is denoted as C_s , the equivalent secondary side stray capacitance of N transformers based configuration can be calculated as

$$C_{seq} = \frac{C_s}{N} \quad (1)$$

In addition, this structure can provide more flexibility in space utilization if small size flyback transformer is applied compared to one single transformer based configuration.

The high output voltage and the capacitive feature of the actuator load limits the utilization of the commercial flyback transformer. As the most critical part in the power stage, the high voltage flyback transformer, therefore, needs to be designed and implemented on one's own. The detailed design methodology and the practical skills to implement the transformer can refer to [8]. Compared to single transformer structure, the lower secondary side winding voltage of each transformer in multiple transformers based configuration enable the adoption of the small size commercial flyback transformer. The parallel configuration in the primary side can guarantee the equal voltage sharing over secondary windings. If the output voltage is denoted as V_{out} , the voltage over the secondary winding of each transformer is expressed as

$$V_{sw} = \frac{V_{out}}{N} \quad (2)$$

2) High voltage flyback converter control strategy discussion

In capacitive load charging applications, the flyback based configuration has simple working principle. In each switching cycle, when primary active semiconductor is turned on, the electrical field energy is transferred to the magnetic field energy and stored in the flyback transformer. When the primary MOSFET is turned off, the stored magnetic energy is automatically released to the capacitive load through the freewheeling diode in the secondary side, which corresponds to the increase of the output voltage. The successive switching cycles leads to the accumulation of the output voltage until it reaches the preset value. If the energy recovery technique is employed, the same working concept is applied to the discharging process of capacitive load, which corresponds to the release of the actuator.

With the help of current sensing circuits, the current closed loop control can be implemented to generate PWM signals for driving the MOSFETs in the power stage. Compared to the average current control, the peak current control is more suitable due to its quick response and cycle-by-cycle current limit to avoid the saturation of magnetic core.

In each switching cycle, in order to achieve the complete transfer of the stored energy in the flyback transformer to the capacitive actuator, the current Discontinuous Conduction Mode (DCM) or Boundary Conduction Mode (BCM) needs to

be adopted. Some commercial ICs with the BCM or DCM function can be directly applied in the control stage of the high voltage converter.

3) Auxiliary power supplies

For the high input voltage and fixed low output voltage DC-DC converter, normally, the auxiliary power comes from the output voltage instead of input voltage to achieve lower power loss. This strategy, however, cannot be applied for high output voltage converter with capacitive load, since the output voltage is high and variable. In this case, the switching power supply based commercial ICs, which can directly be powered by the battery, tends to be good candidates in terms of size and efficiency.

III. CASE STUDY AND DESIGN SOLUTIONS COMPARISON

In an indoor heating valve application, a 3 V battery powered autonomous high voltage DEAP actuator driving system needs to be investigated. The design specifications of high voltage converter are summarized in Table I.

A. Power Stage

The high voltage topologies shown in Fig. 3 can lead to three different solutions for the autonomous high voltage DEAP actuator driving system: solution 1 can be the system with bidirectional flyback topology; solution 2 corresponds to the traditional single transformer based unidirectional flyback topology as the power processing stage; solution 3 is the multiple flyback transformers topology based driving system. Solution 1 is with intrinsic discharging ability to release the energy stored in the DEAP actuator when it is needed. Solution 2 and 3, however, need extra discharging circuits to realize the controllable energy release for the actuator. The circuits can be formed by the series connection of the high voltage resistors and active high voltage MOSFET and are connected to the actuator in parallel. When the MOSFET is triggered on, the energy in actuator can be discharged through the high voltage resistors. The configuration information for solution 1, 2 and 3 are summarized in Table II.

Concerning the critical flyback transformer design, solution 1 and 2 can share the same design and implementation. The detailed design and implemented parameters can refer to [8]. 6 small size commercial flyback transformers CJ5143 from Coilcraft are adopted in solution 3. The detailed transformer

TABLE I. HIGH VOLTAGE CONVERER DESIGN SPECIFICATIONS

| Parameters | Specifications |
|------------------------------------------------|----------------|
| Input voltage | 3 V |
| Maximum output voltage | 1.8 kV - 2 kV |
| Capacitance of DEAP actuator | 200 nF |
| Maximum continuous charging / discharging time | 5 s |

TABLE II. CONFIGURATION SUMMARY OF DIFFERENT SOLUTIONS

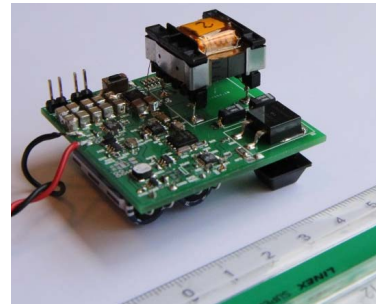
| Solutions | Topology | Discharging Circuit |
|------------|-----------|-------------------------|
| Solution 1 | Fig. 3 a) | Intrinsic with topology |
| Solution 2 | Fig. 3 b) | Discharge resistor |
| Solution 3 | Fig. 3 c) | Discharge resistor |

parameters can refer to [9].

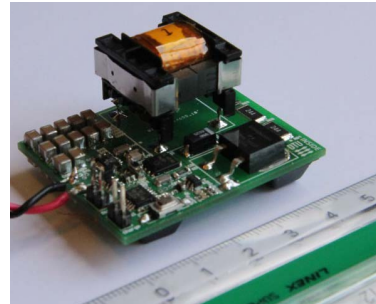
B. Control Stage

As stated before, the terminal parameter feedback control can be employed to regulate the terminal control parameter. The output voltage closed loop control can also be utilized to indirectly regulate the terminal parameter. However, this approach tends to be inefficient in terms of energy utilization. System level burst mode control, therefore, is proposed to save energy as well as to directly regulate the terminal control parameter.

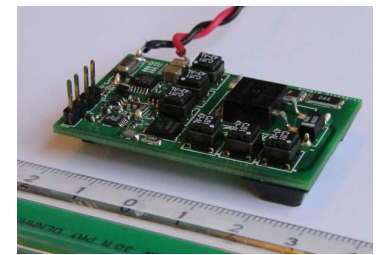
In the burst control mode, the terminal parameter tends to be sensed at regular intervals instead of continuously. The output voltage closed loop control is absent in order to save energy and improve overall energy efficiency. Instead, the high voltage converter only works when there are trigger commands from the terminal parameter closed loop control. When the charging trigger signal is captured, the high voltage converter starts to charge the actuator until the output voltage reaches the preset voltage. Then the entire driving system shuts down to save energy. In the same way, the converter needs to discharge the actuator to 0 V when the discharging trigger signal is



a) Solution 1 (bidirectional flyback) prototype (50mm×50mm×32mm)



b) Solution 2 (unidirectional flyback + discharge resistor) prototype (50mm×40mm×20mm)



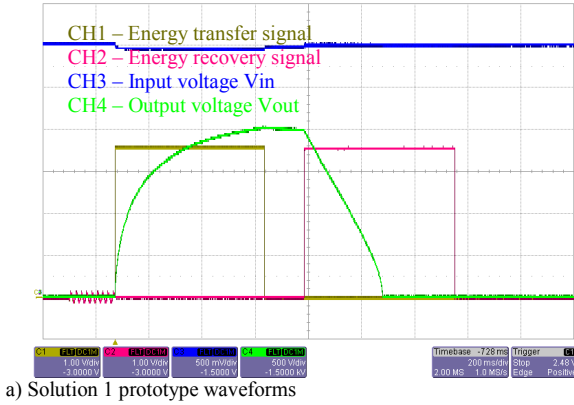
c) Solution 3 (multiple transformer based unidirectional flyback + discharge resistor) prototype (50mm×30mm×6mm)

Fig 4. High voltage converter prototypes.

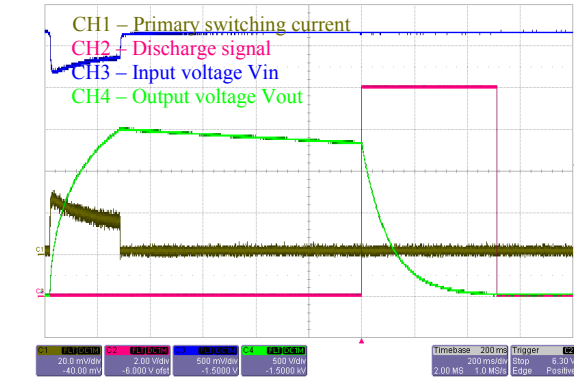
captured. Then the whole system goes to the sleep mode again until the arrival of next trigger signal. This strategy is especially beneficial for heating valve applications, since temperature control system is normally with large inertia constant and does not need to regulate so frequently.

C. High Voltage Converter Implementation

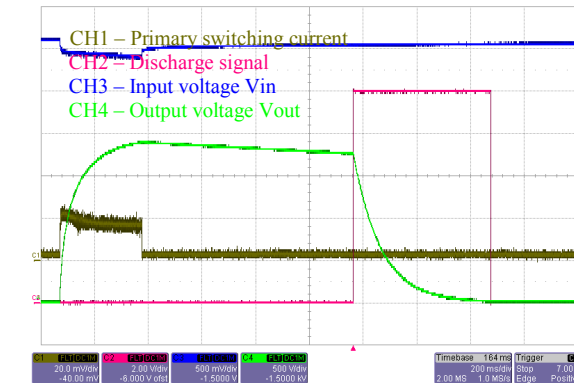
Corresponding to three different solutions mentioned above, three prototypes have been implemented and the pictures are shown in Fig. 4 a) b) and c), respectively. In addition, the converter dimensions are indicated in the figure caption. The functionality of each solution has been experimentally verified and the experimental waveforms are shown in Fig. 5 a) b) and c), respectively.



a) Solution 1 prototype waveforms



b) Solution 2 prototype waveforms



c) Solution 3 prototype waveforms

Fig. 5. Experimental waveforms of prototypes.

D. Aquasition of Critical Evaluation Parameters

In order to evaluate the performance of different solutions, some critical assessment indicators need to be obtained experimentally. One important indicator tends to be the efficiency of the power stage in the high voltage converter. The capacitive property of the actuator calls for the energy efficiency rather than the power efficiency for the converter powering resistive load. In this case, for charging process, the energy efficiency is defined as the final stored energy in the actuator (E_{stored}) divided by the total input energy to the converter (E_{in}) and is expressed as

$$\eta_{charge} = \frac{E_{stored}}{E_{in}} \quad (3)$$

Likewise, for the bidirectional topology, the discharge efficiency is defined as the total recovered energy ($E_{recovered}$) divided by the energy stored in the actuator

$$\eta_{discharge} = \frac{E_{recovered}}{E_{stored}} \quad (4)$$

The measured efficiency for different solutions is shown in Fig. 6. Since solution 1 and 2 share the same high voltage transformer and have used the same components in the power stage, the charging efficiency of these two solutions tends to be equal. Due to the large secondary series resistance of flyback transformers in solution 3, the charging efficiency is much lower than that of solution 1 and 2. The dramatic efficiency drop in the high voltage is caused by the self-capacitance of secondary winding.

E. High Voltage Converter Comparison

For battery operated autonomous system, one of the primary concerns tends to be the battery life time. This parameter can be evaluated through calculating the energy consumption of the high voltage converter. The efficiency data, charging and discharging time and maximum output voltage

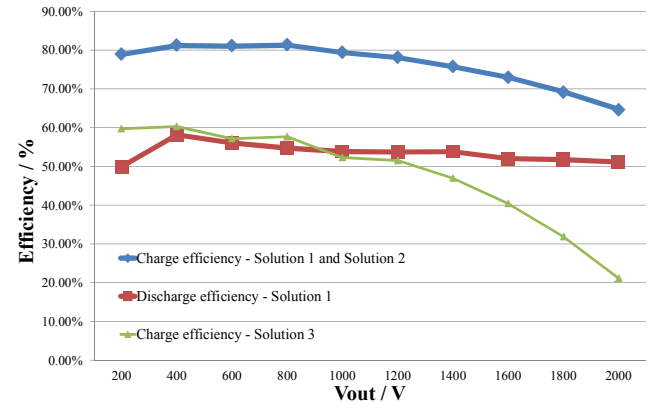
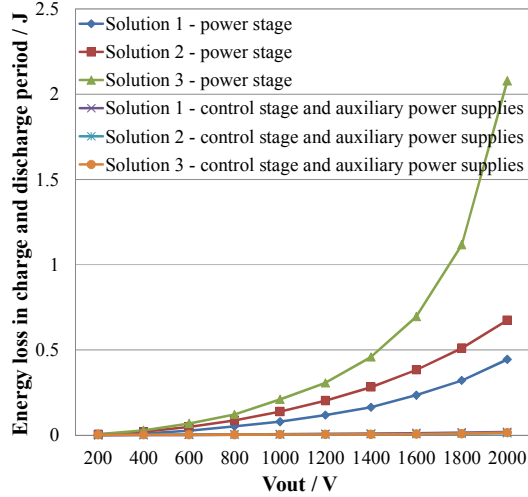


Fig. 6. Measured efficiency of three solutions.

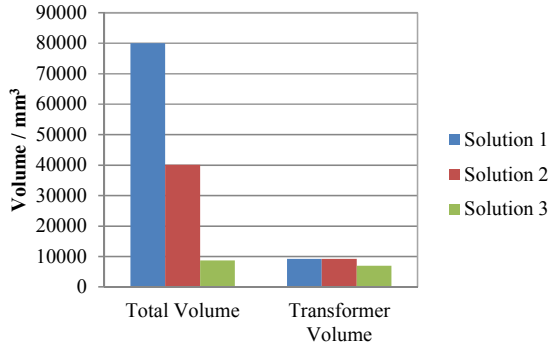
TABLE III. CHARGING AND DISCHARGING TIME AND MAXIMUM OUTPUT VOLTAGE OF HIGH VOLTAGE CONVERTER

| Solutions | Charging Time / ms | Discharging Time / ms | Maximum Voltage / kV |
|------------|--------------------|-----------------------|----------------------|
| Solution 1 | 500 | 300 | 2 |
| Solution 2 | 300 | 500 | 2 |
| Solution 3 | 300 | 500 | 1.9 |

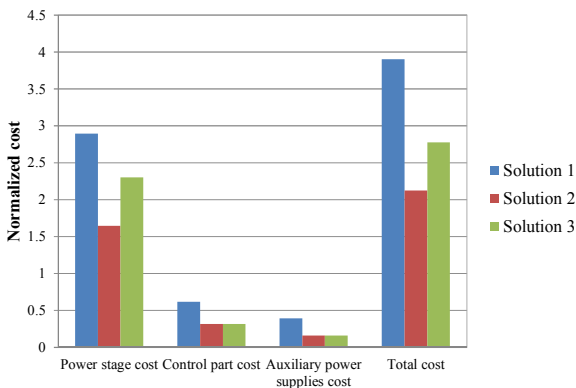
can be applied to obtain the total energy loss for the entire charging and discharging period. The energy consumption comparison of 3 solutions is shown in Fig. 7 a), which indicates that energy dissipated in the control stage and auxiliary power supplies can be neglected when compared to the energy dissipation in the power stage, and this is mainly due to the employment of the system level burst mode control. The curves of the power stage for solution 1 and 2 prove that if the battery life time is with the highest priority, the energy recovery technique is worthy to be implemented.



a) Energy consumption comparison



b) Volume comparison



c) Cost comparison

Fig. 7. Implemented prototypes comparison.

In order to achieve high power density, a low volume power converter is desired. The volume comparison for 3 three solutions is shown in Fig. 7 b). The converter volume is defined as length×width×height. The transformer volume in solution 3 is the total volume of 6 small transformers. Combining the energy loss information in Fig. 7 a), it can be concluded that the volume reduction corresponds to the increases of the energy loss in the power stage. This phenomenon becomes more and more severe with the increase of the output voltage. Fig. 7 b) also indicates that if volume distribution can be practically implemented, such as replacing the large single transformer with several small independent transformers, whose total volume is similar to that of single transformer, it will be greatly beneficial for the reduction of the total volume.

The cost comparison of different solutions is illustrated in Fig. 7 c), which indicates that the cost of the power stage dominates the cost of the entire high voltage converter, since normally high voltage semiconductor devices tend to be more expensive compared to other components.

IV. CONCLUSION

The structure, working principle and application fields of the DEAP material are introduced first. The design of the autonomous high voltage driving system for DEAP actuator is discussed in the second part in detailed, especially the most critical part in the system, i.e. high voltage converter. Then the investigation of autonomous system for heating valve application has been carried out and three possible solutions have been proposed. Finally, the different solutions are compared in terms of energy consumption, volume and cost. The design selection suggestions are provided to be a reference for the future designers to achieve optimum design.

REFERENCES

- [1] R. Sarban, B. Lassen, and M. Willatzen, "Dynamic Electromechanical Modeling of Dielectric Elastomer Actuators With Metallic Electrodes," *IEEE/ASME Transactions on Mechatronics*, vol. 17, pp. 960-967, 2012.
- [2] L. Huang, L.; P. Thummala, Z. Zhang, and M. A. E. Andersen, "A Battery powered high output voltage bidirectional flyback converter for cylindrical DEAP actuator," in *IEEE International Power Modulator and High Voltage Conference (IPMHVC)*, 2012, pp. 454-457.
- [3] M. J. Tryson; R. Sarban, and K. P. Lorenzen, "The dynamic properties of tubular DEAP actuators," in *Proceedings of SPIE*, vol. 7642, 2010.
- [4] R. Sarban, and R. W. Jones, "Physical model-based active vibration control using a dielectric elastomer actuator," *Journal of Intelligent Material Systems and Structures*, vol. 23, pp. 473-483, 2012.
- [5] M. J. Tryson; R. Sarban, and K. P. Lorenzen, "The dynamic properties of tubular DEAP actuators," in *Proceedings of SPIE*, vol. 7642, 2010.
- [6] L. Dalessandro, F. da Silveira Cavalcante, and J. Kolar, "Self-Capacitance of High-Voltage Transformers," *IEEE Transactions on Power Electronics*, vol. 22, no. 5, pp. 2081-2092, 2007.
- [7] R. Pittini, L. Huang, Z. Zhang, and M. A. E. Andersen, "Primary Parallel Secondary Series Flyback Converter (PPSSFC) with Multiple Transformers for Very High Step-Up Ratio in Capacitive Load Charging Applications," in *IEEE 2014 Applied Power Electronics Conference and Exposition (APEC)*, 2014, pp. 1440-1447.
- [8] L. Huang, Z. Zhang, and M. A. E. Andersen, "Design and Development of Autonomous High Voltage Driving System for DEAP Actuator in Radiator Thermostat," in *IEEE 2014 Applied Power Electronics Conference and Exposition (APEC)*, 2014, pp. 1633-1640.
- [9] "CJ5143 flyback transformer datasheet", *Coilcraft, Inc.*, USA.

APPENDIX M

DEAP actuator and its high voltage driver for heating valve application

SPIE Smart Structures/NDE on Electroactive Polymer Actuators and Devices (EAPAD) 2014

DEAP actuator and its high voltage driver for heating valve application

L. Huang^{a1}, L. F. Nørmølle^{b2}, R. Sarban^{c3}, E. N. Christiansen^{d4}, Z. Zhang^{a5}, M. A. E. Andersen^{a6}
^aTechnical University of Denmark, Oersteds Plads Building 349, DK-2800 Kgs. Lyngby, Denmark;
^bLanoe Electronics, Oesterbordingvej 47, DK-8600 Silkeborg, Denmark;
^cDanfoss PolyPower A/S, Nils Koppel Allé, Building 404, DK-2800 Kgs. Lyngby, Denmark;
^dDanfoss A/S, Heating Solutions Division, Jens Juuls Vej 9, DK-8260 Viby J, Denmark

ABSTRACT

Due to the advantages of DEAP (Dielectric Electro Active Polymer) material, such as light weight, noise free operation, high energy and power density and fast response speed, it can be applied in a variety of applications to replace the conventional transducers or actuators. This paper introduces DEAP actuator to the heating valve system and conducts a case study to discuss the feasible solution in designing DEAP actuator and its driver for heating valve application. First of all, the heating valves under study are briefly introduced. Then the design and the development for DEAP actuator is illustrated in detail, and followed by the detailed investigation of the HV driver for DEAP actuator. In order to verify the implementation, the experimental measurements are carried out for DEAP actuator, its HV driver as well as the entire heating valve system.

Keywords: DEAP actuator, high voltage, driver, heating valve system

1. INTRODUCTION

As a smart material, since emerging in the early 90s, DEAP (Dielectric Electro Active Polymer) has obtained enormous attention from the researchers and engineers [1] [2] [3] [4]. The structure of DEAP material is simple: that is a thin and soft dielectric sheet sandwiched between two compliant electrodes. From electrical point of view, DEAP material has the similar configuration of plate capacitor, so that, can be considered to be a variable capacitor. When a high voltage (HV) is applied over the electrodes, DEAP will be compressed in thickness and expand in the perpendicular direction due to the electrostatic force, which means the material can be used to form actuators [6]. Due to the advantages such as light weight, noise free operation, high energy and power density and fast response speed, DEAP based actuators tend to replace the conventional counterparts, especially in the cases where weight, volume or noise are critical.

In the modern heating system, valves are widely employed to control the hot water flow in pipes. Currently, self-actuating actuator and step motor based actuator are applied to actuate the heating valve. Due to their drawbacks, such as inaccurate temperature control and short battery life time, and considering the advantages of DEAP material, DEAP based actuator is proposed to replace the conventional actuators in the heating valve application [6] [7].

Chemical and material scientists are focusing on improving performance of DEAP material, while the mechanical researchers are trying to investigate various feasible configurations for different applications [8] [9] [10] [11]. In comparison, the research and development of drivers for DEAP transducers or actuators seems lag behind since only few literatures are available [12] [13] [14]. Unlike other papers in the DEAP field focusing on the detailed investigation for certain issues, this paper will, from an application perspective, carry out a case study to illustrate the feasible solution when designing and applying DEAP actuator and its driver in the heating valve system.

¹ huang@elektro.dtu.dk, ² lars@lanoe.dk, ³ sarban@danfoss.com, ⁴ enc@danfoss.com, ⁵ zz@elektro.dtu.dk, ⁶ ma@elektro.dtu.dk

This paper is organized in the following structure: the overall system illustration will be provided in Section 2; in Section 3, the terminal load – heating valve and its specifications will be briefly introduced; the design and implementation of DEAP actuator will be discussed in detail in Section 4; in Section 5, the HV driver will be investigated in terms of design and development; the experimental results are provided in Section 6 to verify the design and implementation for DEAP actuator as well as its HV driver; eventually, a conclusion and future work is presented in Section 7.

2. SYSTEM LEVEL OVERVIEW

The heating valve system under study consists of three main parts, i.e. heating valve, DEAP actuator and its HV driver. From electrical point of view, the overall system level diagram is depicted in Figure 1.

The terminal load of the whole system is the heating valve. The capacitive load of the HV driver - DEAP actuator is used to actuate the valve in order to adjust the hot water flow in the pipe. The most essential part for the entire system tends to be the HV driver, which consists of five sub-parts. Due to the capacitive property of the DEAP actuator and in order to improve the energy efficiency, a power stage with bidirectional energy flow characteristic is applied. A control stage is adopted to realize the control for the energy transfer (energy is from power source to DEAP load) as well as the energy recovery (energy is from DEAP load to power source). To keep consistence with the current valve actuation products, two non-rechargeable 1.5V AA batteries are employed as the energy source for the HV driver. Considering energy recycling and non-rechargeable batteries, another energy storage element – a super capacitor needs to be applied. The ultimate goal of the heating valve system is to control the ambient temperature according to the requirements of the users. According to the basic operation principle of the heating valve system, the motion position of the heating valve controls the hot water flow and indirectly determines the temperature, while the position can be regulated by the deformation of DEAP actuator. The displacement of actuator versus applied voltage property measured in reference [14] indicates that the stimulating voltage can adjust the position of DEAP actuator. It should be noted that, to realize the temperature control, a closed loop needs to be implemented, which is not shown in Figure 1 but provides the input control signal for the system. A HV measurement circuit is employed to monitor the voltage over the actuator and a voltage tracking control is implemented in a microcontroller in order to follow the input control signal coming from the temperature closed loop.

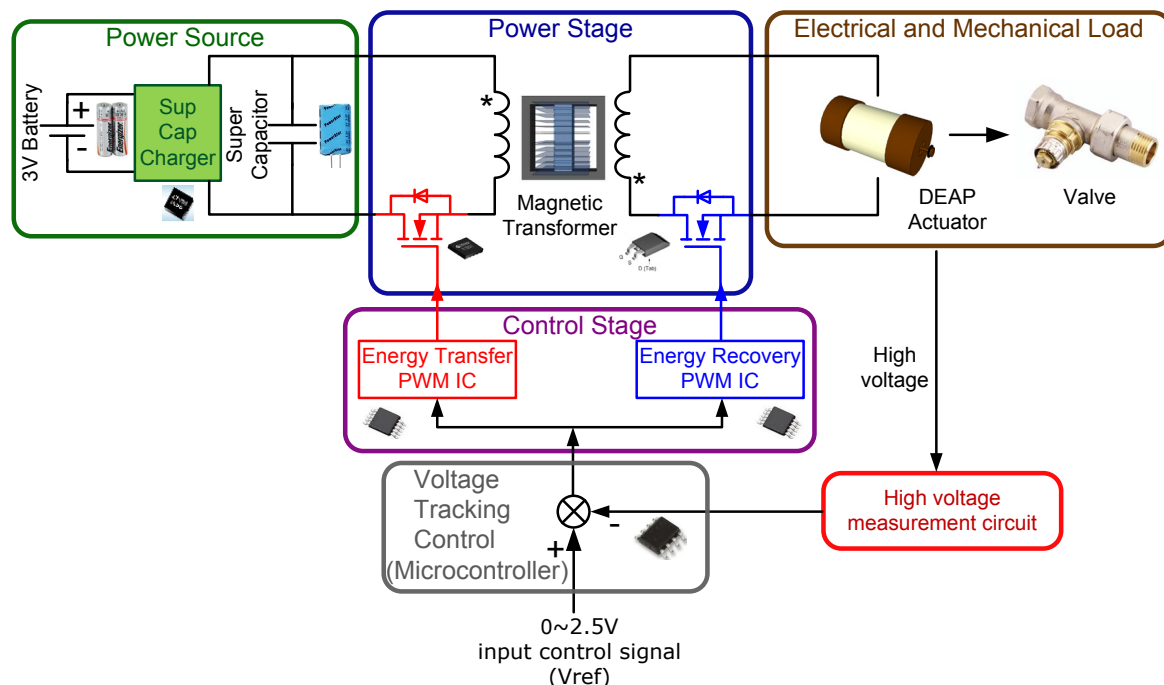


Figure 1. System level block diagram.

3. VALVE BODY INTRODUCTION

As previously stated, the heating valves are employed to be the terminal load for the whole system. Two types of valve are investigated in this case study. They have the same parameters in terms of dimension, maximum working pressure and applied water temperature, and only differ from each other in their shapes. One type is the straight design, shown in Figure 2 (a), and the other is the angle design, shown in Figure 2 (b) [15] [16].



(a) Straight design



(b) Angle design

Figure 2. Heating valves employed in the system.

As the mechanical load to the DEAP actuator, the valves need to be specified in terms of the actuation requirements in order to provide the design information for the actuator. The requirements are provided in terms of force, actuating frequency, stroke and noise level, which are summarized in Table 1.

Table 1. The actuation requirements of the heating valve.

| Actuation requirements | Values |
|------------------------|--------------------|
| Force | 25 N |
| Frequency | 0.2 Hz |
| Stroke | 1 mm |
| Noise level | As low as possible |

4. DEAP ACTUATOR

4.1 Design specifications discussion

The DEAP actuator is specified to provide 25N closing force to the valve when no voltage is applied. This is a normally closed configuration of a valve operation. The actuator has to release the valve by 1 mm, allowing flow in the system, when charged to 2 kV. The closing force and the required stroke define the cross sectional area and length of the actuator respectively. The cross sectional area is calculated as:

$$A = \frac{F}{2 \cdot C_M ((1+S_p)^2 - (1+S_p)^{-2})} \quad (1)$$

C_M is the elastic constant of the DEAP material and S_p represents the pre-strain of the actuator required to provide the closing force of 25N. The pre-strain in this case was chosen to be 10% which allows the calculation of actuators cross section area. Having calculated the cross section of the actuator, the length of the actuator can be calculated by the following force equilibrium equation:

$$2 \cdot C_M ((1+S)^2 - (1+S)^{-2}) = \varepsilon_0 \varepsilon_r \left(\frac{V}{d} \right)^2 (1+S)^2 + \frac{F}{A} (1+S) \quad (2)$$

where ε_0 and ε_r are the vacuum and material permittivity respectively. V and d are the applied voltage and the thickness of the DEAP sheet respectively. For the current version of DEAP material, the operating stimulus voltage is 2 kV. Solving Eq. 2 yields $S > S_p$ where the additional strain is the actuation strain due to electrostatic stimulation. By isolating the actuation strain the length of actuator can be dimensioned to provide 1 mm stroke.

Considering the fast response speed and silent operation properties of the material, the DEAP actuator can easily fulfill the requirements of actuating frequency and noise level. Due to the large strain capability of the material, 1 mm stroke can easily be realized as well [3][17].

4.2 Conceptual actuator design

Figure 3 illustrates the conceptual design and integration of the DEAP actuator in the valve system. The actuator has a center rod pressuring against the valve pin when the actuator is fixed on a valve. As the spring of the valve compresses its counterforce stretches the actuator, hence the elastic force of the DEAP actuator has initially a downward force closing the valve (normally closed operation). When a voltage is applied to the actuator, it generates electrostatic forces counteracting the elastic force of the actuator resulting in an upward motion hence opening the valve.

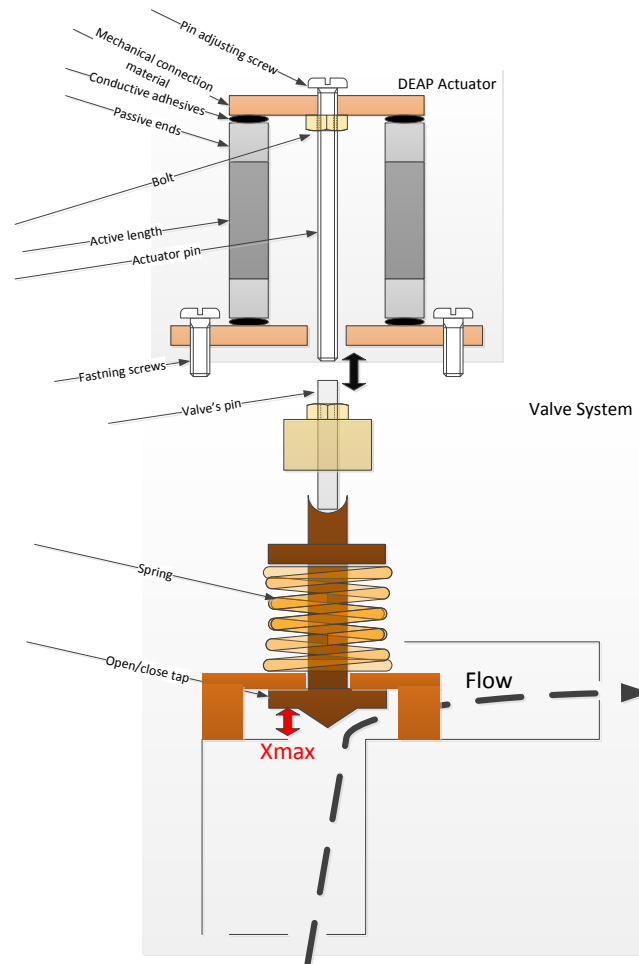


Figure 3. Conceptual design of the DEAP actuator and its integration in the valve.

4.3 Detailed actuator design

The cross sectional area of the actuator is dimensioned such that it should exhibit a downward elastic force of 25 N when it is stretched by 10% of its initial length. This condition resulted in using 5 m of DEAP film. The actuator length is dimensioned such that it provides a stroke of approximately 1 mm when the maximum electric field is applied. Here the maximum strain of the actuator was calculated to be 2% of its length hence resulting in an active length of 50 mm to provide 1 mm stroke.

Figure 4 shows the detailed drawing of the actuator. The DEAP laminate is rolled and the ends are cut to provide flat surface. Conductive adhesives are applied on either ends and PCBs are glued to the either end by the conductive adhesives. Wires are soldered on PCBs such that electrical charges from the HV driver can be transferred through wires to PCB and then through the conductive adhesives to the DEAP laminate electrodes resulting in elongation of the

actuator. The top PCB is attached to a thread house and the lower PCB has a hole. The center rod is mounted from top and goes through the body of the actuator and comes out of the bottom. The position of the rod is adjusted to by the thread house. This adjustment provides the fine tuning of the actuator’s downward force.

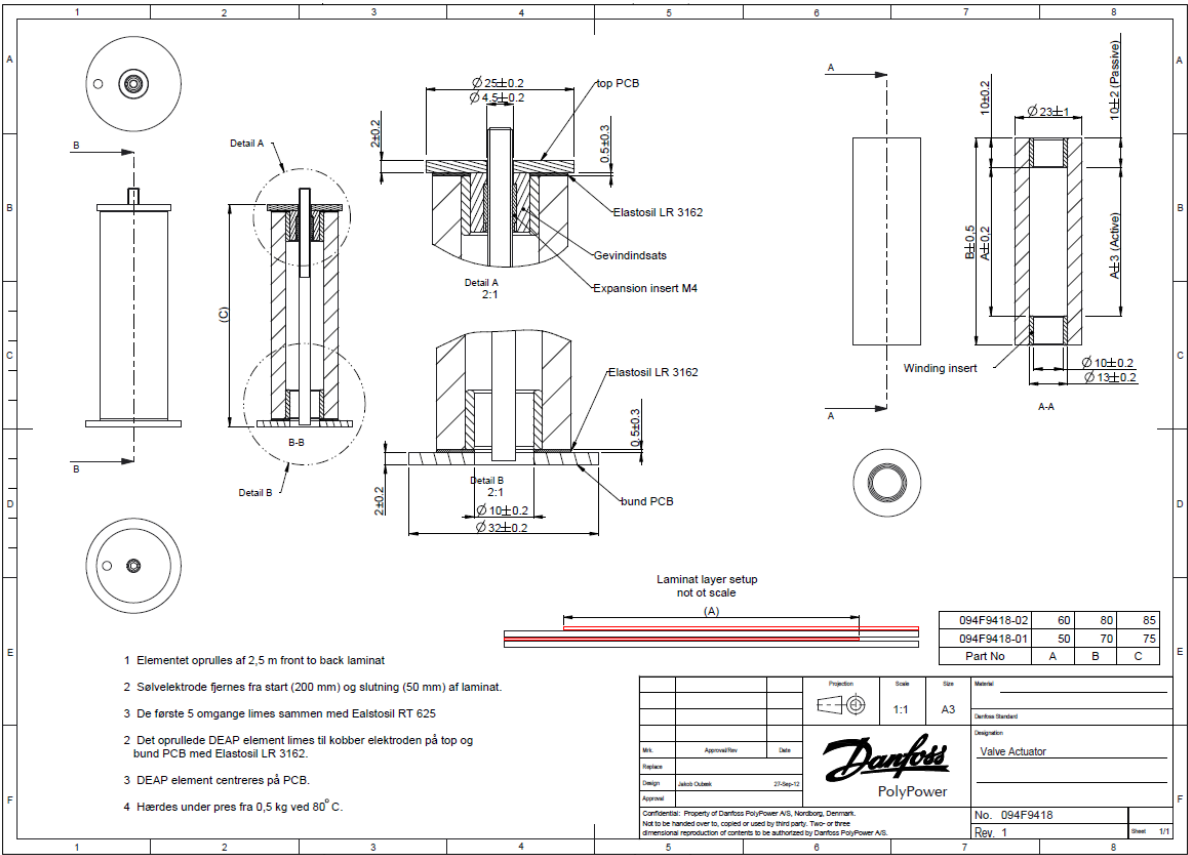


Figure 4. Detailed design drawing of the actuator.

4.4 Implemented actuator and its integration to the heating valve

The realized DEAP actuator and its integration to the valve are shown in Figure 5.

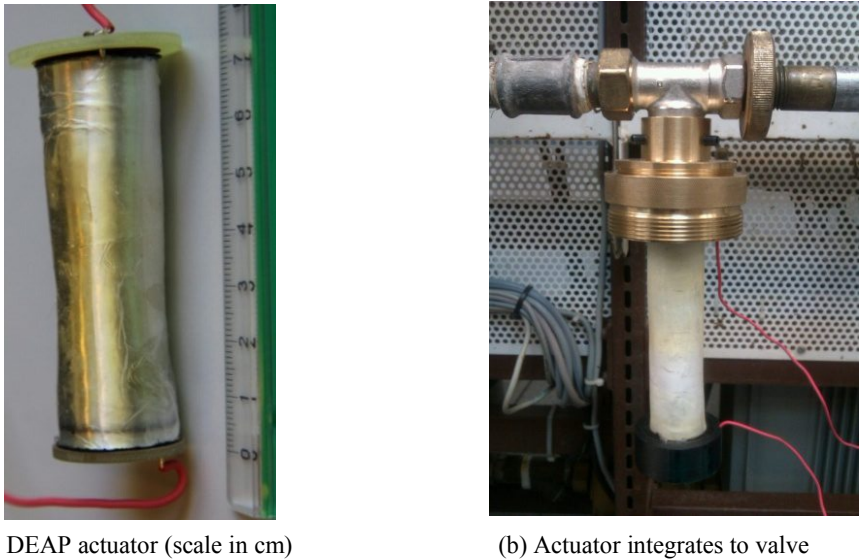


Figure 5. Final implemented DEAP actuator and its integration to heating valve.

5. HIGH VOLTAGE DRIVER

5.1 Design specifications discussion

Once the size of the DEAP sheet (S) is determined, the capacitance of the actuator (C) can be calculated through the following equation

$$C = \varepsilon_0 \cdot \varepsilon_r \cdot \frac{S}{d} \quad (3)$$

Combining with other requirements from the load - DEAP actuator, the design specifications for HV driver are summarized in Table 2.

Table 2. HV driver design specifications.

| Parameters | Specifications |
|------------------------------------------------|----------------------------------------------------|
| Input voltage | 3 V |
| Maximum output voltage | 2 kV |
| Capacitance of DEAP actuator | 200 nF |
| Change of output voltage | Follow control signal from temperature closed loop |
| Maximum continuous charging / discharging time | 2.5 s |
| Energy recovery | Necessary |
| Size | As small as possible |

As previously discussed, the HV driver system consists of five sub-parts – HV power stage, HV control stage, power source, HV measurement circuit and output voltage tracking control part. And they will be illustrated in detail in terms of design and implementation, as follows.

5.2 HV power stage

Among the various configurations, Flyback topology has been widely used in the consumer electronics as well as in the telecommunication industry due to the low cost, simple configuration and low components count [18] [19]. In the past decades, this topology has been successfully applied in the high voltage generation situations, such as the power supply for CRT displays, high voltage capacitor charging applications, etc [20] [21] [22]. In addition, the reversible energy flow can easily be achieved through a bidirectional flyback configuration [23].

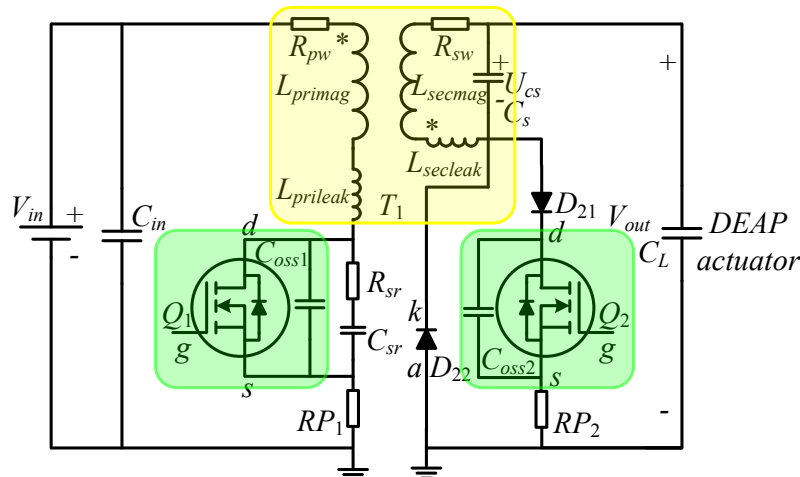


Figure 6. Schematic of HV flyback converter.

The schematic for the power stage is illustrated in Figure 6 and selected components are listed in Table 3.

Table 3. HV power stage component list.

| Component Name | Device | Critical Parameters |
|-----------------------|-----------------|------------------------------------|
| Q_1 | BSC320N20NS3 G | $V_{DSS} = 200 \text{ V}$ |
| Q_2 | IXTV03N400S | $V_{DSS} = 4 \text{ kV}$ |
| D_{21} and D_{22} | VMI6525 | $V_{RWM} = 5 \text{ kV}$ |
| RP_1 | LVK12R020FER | $20 \text{ m}\Omega \text{ } 1 \%$ |
| RP_2 | RC1206FR-101RL | $1 \Omega \text{ } 1 \%$ |
| R_{sr} | RE1206DR-0768RL | $68 \Omega \text{ } 0.5 \%$ |
| C_{sr} | 12062A221JAT2A | $220 \text{ pF } 200 \text{ V}$ |

The most essential element in power stage tends to be the HV flyback transformer, i.e. T_1 in Figure 6. The detailed design and implementation information can refer to previous investigation in [24].

5.3 HV control stage

One commercial photoflash capacitor charger controller LT3750 has been employed in order to achieve the peak current control for the HV flyback configuration [25]. It is applied in the primary side for the energy transfer control as well as in the secondary side for the energy recovery control. The ON/OFF function of the controller makes it desirable for the output voltage tracking control.

The default boundary mode control scheme of LT3750 can be directly applied for the energy transfer control. The configuration of the controller is shown in Figure 7 and the selected components are summarized in Table 4.

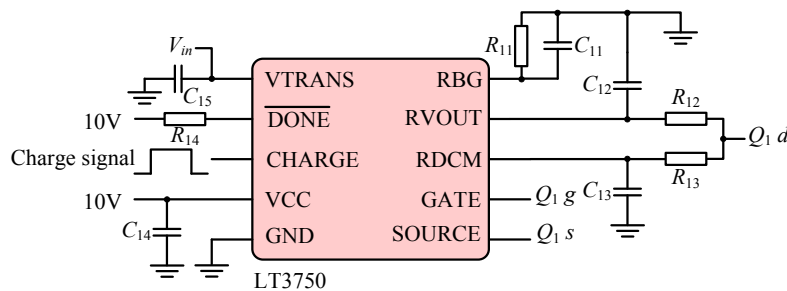


Figure 7. Energy transfer control configuration scheme.

Table 4. Component list for energy transfer control.

| Components | Values |
|----------------------------|----------------------------------------------------|
| R_{11} | $2.49 \text{ k}\Omega \text{ } 1 \% \text{ } 0402$ |
| C_{11} | $100 \text{ pF } 50 \text{ V } 0402$ |
| $R_{12} \ R_{13} \ R_{14}$ | $100 \text{ k}\Omega \text{ } 1 \% \text{ } 0402$ |
| $C_{12} \ C_{13}$ | $10 \text{ pF } 500 \text{ V } 1206$ |
| $C_{14} \ C_{15}$ | $10 \mu\text{F } 16 \text{ V } 0603$ |

From: <http://proceedings.spiedigitallibrary.org/> on 03/29/2014 Terms of Use: <http://spiedigitallibrary.org/terms>

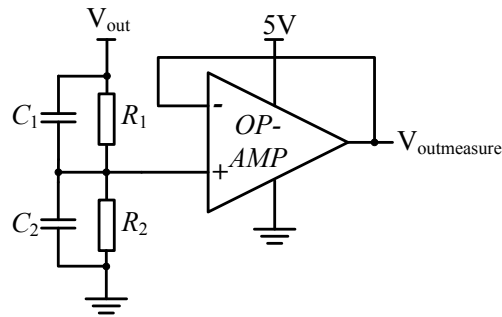


Figure 9. Schematic of HV measurement circuit.

Table 6. Component list for HV measurement circuit.

| Components | Values |
|------------|----------------------------|
| R_1 | 5 G Ω 3 kV 1 % 2512 |
| C_1 | 47 pF 3 kV NPO 1808 |
| R_2 | 5 M Ω 1 % 0805 |
| C_2 | 47 nF COG 0805 |
| OP-AMP | OPA365AIDBVT |

5.6 Output voltage tracking control

The output voltage tracking control is realized in an 8-pin low-cost microcontroller MSP430G2230 [28]. The flow diagram of the control program is illustrated in Figure 10. After the initialization of the controller, a delay is applied to ensure the fully charge of the super capacitors. Then a hysteresis algorithm is adopted to realize the voltage tracking control.

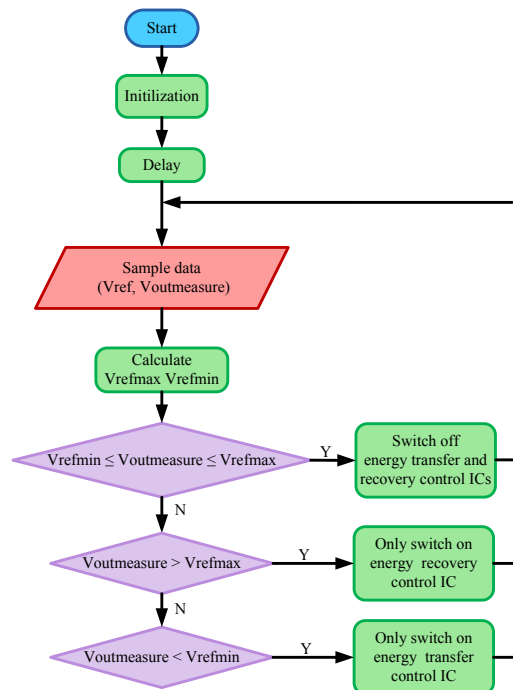


Figure 10. Flow diagram for output voltage tracking control program.

5.7 The implemented HV driver

For the whole HV driver, there are two PCBs: one is used to accommodate the power source, all the other parts including HV power stage as well as control stage, microcontroller and HV measurement circuit are placed in another PCB. The implemented HV driver for DEAP actuator is shown in Figure 11.

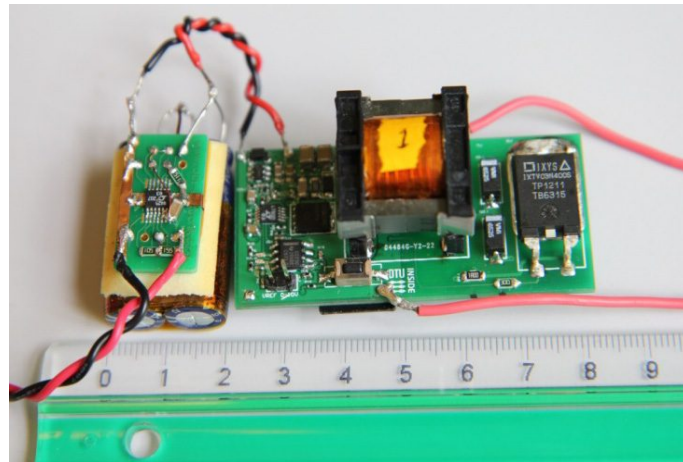


Figure 11. Picture of the HV driver.

6. EXPERIMENTAL VERIFICATION

The heating valves are already put on the market. That means the necessary tests had already been carried out. Therefore, in this paper, only DEAP actuator and its HV driver need to be verified through experiments. Certainly, the performance of the entire heating valve system is an important concern as well, which will be checked through the system level measurement.

6.1 Experimental validation for DEAP actuator

The stroke versus applied voltage characteristic of the actuator has been measured and the curve is shown in Figure 12. It can be observed the stroke is 1 mm when the stimulating voltage reaches around 2 kV. That means the design requirement can be fully satisfied.

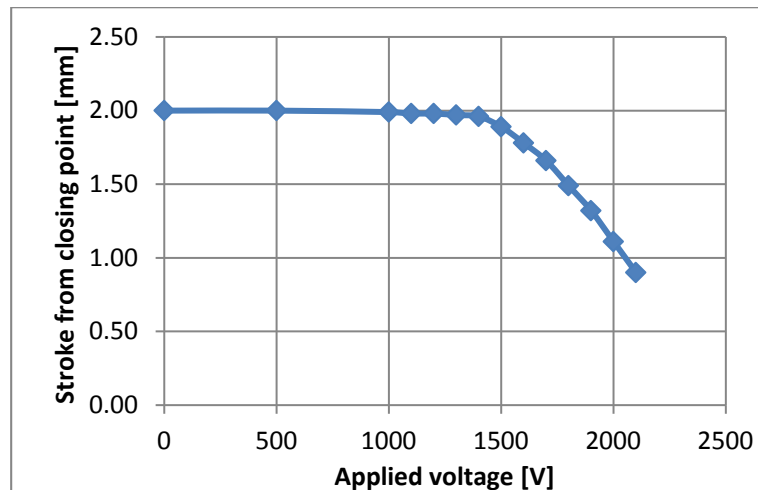
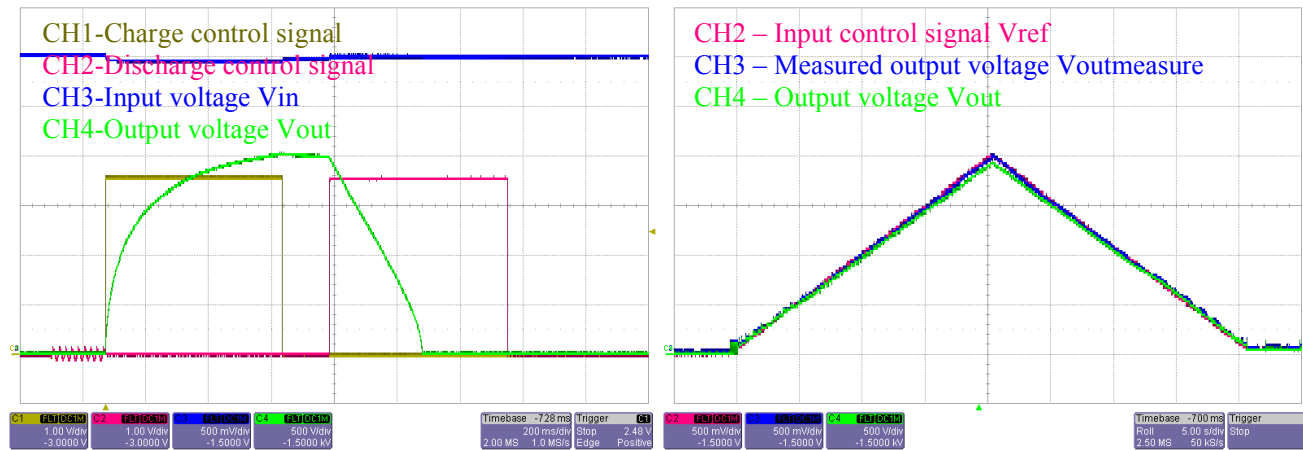


Figure 12. Stroke versus applied voltage characteristic of DEAP actuator.

6.2 Experimental validation for HV driver

The continuous charging and discharging waveforms of HV driver are shown in Figure 13 (a). It can be observed that the maximum voltage 2 kV is achieved. The duration time for the whole charging process and discharging process are around 520 ms and 300 ms, respectively. All the measured data indicate the fulfillment for the requirements. The output voltage tracking capability has been checked as well, shown in Figure 13 (b). It can be seen that the output voltage can follow the reference voltage well, which can validate the functionality of the voltage tracking program.



(a) Continuous charging and discharging process (b) Output voltage tracking ability validation

Figure 13. Experimental results of HV driver.

6.3 Experimental validation for entire heating valve system

The water flow versus applied voltage characteristic, which comes from the standard test bench in Danfoss A/S, is shown in Figure 14. It can be observed the DEAP actuator can regulate the water flow well by changing the applied voltage of the actuator.

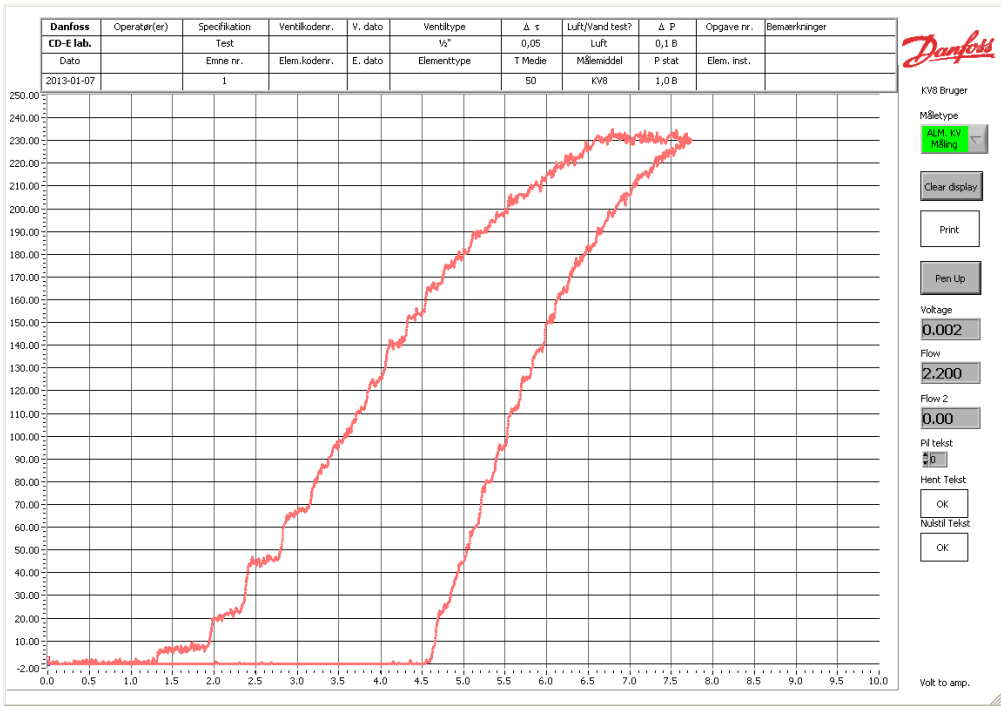


Figure 14. Water flow versus applied voltage characteristic of entire heating valve system. (The x-axis corresponds to the applied voltage over actuator and the values in the figure times 300 is the actual stimulating voltage in Volts. The y-axis expresses the water flow in the pipe and the unit is Liter/hour.)

7. CONCLUSION AND FUTURE WORK

In this paper, an application based case study concerning the design and development of DEAP actuator and its high voltage driver for heating valve system has been carried out. The heating valves under study are briefly introduced. The design concept as well as the detailed mechanical drawing of DEAP actuator is provided. The HV driver, including HV power and control stages, power source part, HV measurement circuit and output voltage tracking control part, are investigated in detail. The experimental results are provided to validate the design as well as implementation for DEAP actuator, its HV driver as well as the entire heating valve system.

Although the DEAP actuator and its driver are successfully applied in the heating valve system, compared to the existing counterparts, until now, this new technology is not so competing in terms of compactness as well as cost. In the future, more research needs to be conducted in order to reduce the size. DEAP material is cheap itself, but the HV driver introduces high cost. Once the maximum applied voltage for the actuator is reduced, the cost for the driver can decrease dramatically. Therefore, more effort needs to be dedicated to improving the performance of the material.

REFERENCES

- [1] Bar-Cohen, Y. "Electro-active polymers current capabilities and challenges," in *Smart Structures and Materials 2002: Electroactive Polymer Actuators and Devices (EAPAD)*, San Diego, USA, (2002).
- [2] Benslimane, Y. M., Kiil, H.-E. and Tryson, M. J., "Dielectric electro-active polymer push actuators performance and challenges," *Polymer International*, Wiley-Blackwell, 59, 415-421 (2010).
- [3] Sarban, R., Lassen, B. and Willatzen, M., "Dynamic Electromechanical Modeling of Dielectric Elastomer Actuators With Metallic Electrodes," *IEEE/ASME Transactions on Mechatronics*, 17(5), 960-967 (2012).
- [4] Truong, B. N. M., Nam, D. N. C. and Ahn, K. K., "Hysteresis modeling and identification of a dielectric electro-active polymer actuator using an APSO-based nonlinear Preisach NARX fuzzy model," *Smart Materials and Structures*, IOP Publishing Ltd., 22, 1-15 (2013).
- [5] Iskandarani, Y. and Karimi, H. R., "Sensing Capabilities Based on Dielectric Electro Active Polymers - Feasibility and Potential State-of-the-Art Application," *IEEE Sensors Journal*, 12(8), 2616-2624 (2012).
- [6] York, A., Dunn, J. and Seelecke, S., "Experimental characterization of the hysteretic and rate-dependent electromechanical behavior of dielectric electro-active polymer actuators," *Smart Materials and Structures*, IOP Publishing Ltd., 19, 1-9 (2010).
- [7] York, A., Dunn, J. and Seelecke, S., "Systematic approach to development of pressure sensors using dielectric electro-active polymer membranes," *Smart Materials and Structures*, IOP Publishing Ltd., 22, 1-10 (2013).
- [8] Singh, U., Davis, F., Mohan, S. and Mitchell, G., "Electro-active nanofibres electrospun from blends of poly-vinyl cinnamate and a cholesteric liquid crystalline silicone polymer," *Journal of Materials Science*, Springer, 48, 7613-7619 (2013).
- [9] Liu, H., Zhang, L., Yang, D., Ning, N., Yu, Y., Yao, L., Yan, B. and Tian, M., "A new kind of electro-active polymer composite composed of silicone elastomer and polyethylene glycol," *Journal of Physics D: Applied Physics*, IOP Publishing Ltd., 45, 1-9 (2012).
- [10] Berardi, U., "Modelling and testing of a dielectric electro-active polymer (DEAP) actuator for active vibration control," *Journal of Mechanical Science and Technology, Korean SOC Mechanical Engineers*, 27, 1-7 (2013).
- [11] Murray, C., McCoul, D., Sollier, E. and Ruggiero, T., "Electro-adaptive microfluidics for active tuning of channel geometry using polymer actuators," *Microfluidics and Nanofluidics*, Springer Heidelberg, 14, 345-358 (2013).
- [12] Andersen, T., Roedgaard, M. S., Thomsen O. C. and Andersen, M. A. E., "Low voltage driven dielectric electro active polymer actuator with integrated piezoelectric transformer based driver," in *Electroactive Polymer Actuators and Devices (EAPAD) 2011*, San Diego, USA, (2011).
- [13] Eitzen, L., Graf, C. and Maas, J., "Cascaded bidirectional flyback converter driving DEAP transducers," in *37th Annual Conference on IEEE Industrial Electronics Society (IECON 2011)*, Melbourne, Australia, (2011).
- [14] Huang, L., Thummala, P., Zhang, Z. and Andersen, M. A. E., "Battery powered high output voltage bidirectional flyback converter for cylindrical DEAP actuator," in *2012 IEEE International Power Modulator and High Voltage Conference (IPMHVC 2012)*, San Diego, USA, (2012).

- [15] "Danfoss radiator valves 013G0016," [Online]. Available:
<http://www.danfoss.com/Products/Categories/Detail/HE/Radiator-Thermostats/Radiator-Valves/Pre-Setting-Valves/013G0016/364135e4-3f64-45c5-a1ea-af888bc4a88d/58d2710f-1a41-466d-8818-8bb22ab7db92.html>.
- [16] "Danfoss radiator valves 013G0016," [Online]. Available:
<http://www.danfoss.com/Products/Categories/Detail/HE/Radiator-Thermostats/Radiator-Valves/Pre-Setting-Valves/013G0016/364135e4-3f64-45c5-a1ea-af888bc4a88d/58d2710f-1a41-466d-8818-8bb22ab7db92.html>.
- [17] Castaneda, P. P. and Siboni, M. N., "A finite-strain constitutive theory for electro-active polymer composites via homogenization," *International Journal of Non-linear Mechanics*, Pergamon-Elsevier Science Ltd., 47, 293-306 (2012).
- [18] Jung, J.-H. and Ahmed, S., "Flyback converter with novel active clamp control and secondary side post regulator for low standby power consumption under high-efficiency operation," *IET Power Electronics*, 4(9), 1058 -1067 (2011).
- [19] Abramovitz, A., Liao, C.-S. and Smedley, K., "State-Plane Analysis of Regenerative Snubber for Flyback Converters," *IEEE Transactions on Power Electronics*, 28(11), 5323-5332 (2013).
- [20] Rahimi, A., Rahimi, F. F. and Hassanzadeh, I., "Analysis of high-voltage flyback converter in color TVs, and its regulation," in *The Fifth International Conference on Power Electronics and Drive Systems 2003 (PEDS 2003)*, Singapore, (2003).
- [21] Elmes, J., Jourdan, C., Abdel-Rahman, O. and Batarseh, I., "High-Voltage, High-Power-Density DC-DC Converter for Capacitor Charging Applications," in *IEEE 2009 Applied Power Electronics Conference and Exposition (APEC)*, Washington DC, USA, (2009).
- [22] Tseng, S. Y., Yang, C. M., Wang, K. C. and Hsu, G. W., "High voltage generator using boost/flyback hybrid converter for stun gun applications," in *IEEE 2010 Applied Power Electronics Conference and Exposition (APEC)*, Palm Springs, USA, (2010).
- [23] Chen, G., Lee, Y.-S., Hui, S. Y. R., Xu, D. and Wang, Y., "Actively clamped bidirectional flyback converter," *IEEE Transactions on Industrial Electronics*, 47(4), 770 -779 (2000).
- [24] Huang, L., Zhang, Z., Andersen, M. A. E. and Sarban, R., "High Voltage Bidirectional Flyback Converter Driving DEAP Actuator for Automotive Applications," in *2013 IEEE Vehicle Power and Propulsion Conference (VPPC)*, Beijing, China, (2013).
- [25] "LT3750 capacitor charger controller datasheet," Linear Technology Corporation, USA.
- [26] "LTC1799 1kHz to 33MHz resistor set SOT-23 oscillator datasheet," Linear Technology Corporation, USA.
- [27] "LTC4425 linear supercap charger with current-limited ideal diode and V/I monitor datasheet," Linear Technology Corporation, USA.
- [28] "MSP430G22x0 mixed signal microcontroller datasheet," Texas Instruments Incorporated, USA.

www.elektro.dtu.dk

Department of Electrical Engineering
Electronics Group (ELE)
Technical University of Denmark
Oersteds Plads Building 349
DK-2800 Kgs. Lyngby
Denmark
Tel: (+45) 45 25 38 00
Fax: (+45) 45 93 16 34
Email: info@elektro.dtu.dk